Université de Toulouse

# THÈSE

**En vue de l'obtention du**

## DOCTORAT DE L'UNIVERSITÉ DE TOULOUSE

**Délivré par :**

Institut Supérieur de l'Aéronautique et de l'Espace (ISAE)

---

**Présentée et soutenue par :**
**Jean-Michel LUCAS**

**le** lundi 13 octobre 2014

**Titre :**

Étude et modélisation du phénomène de croissance transitoire et de son lien avec la transition Bypass au sein des couches limites tridimensionnelles

Spatial optimal perturbations for transient growth analysis in three-dimensional boundary layers

---

**École doctorale et discipline ou spécialité :**

ED MEGeP : Dynamique des fluides

**Unité de recherche :**

Équipe d'accueil ISAE-ONERA EDyF

**Directeur(s) de Thèse :**

M. Daniel ARNAL (directeur de thèse)
M. Olivier VERMEERSCH (co-directeur de thèse)

**Jury :**

M. Carlo COSSU - Président du jury
M. Alessandro BOTTARO - Rapporteur
M. Grégoire CASALIS - Examinateur
M. Yann DOUTRELEAU - Examinateur
M. Ardeshir HANIFI - Rapporteur
M. Olivier VERMEERSCH - Co-directeur de thèse

## Spatial optimal perturbations for transient growth analysis in three-dimensional boundary layers

**Abstract**
The transition from a laminar to a turbulent flow strongly modifies the boundary layer properties. Understanding the mechanisms leading to transition is crucial to reliably predict aerodynamic performances. For boundary layers subjected to high levels of external disturbances, the natural transition due to the amplification of the least stable mode is replaced by an early transition, called Bypass transition. This is the result of non-normal mode interactions that lead to a phenomenon of transient growth of disturbances. These disturbances are known as Klebanoff modes and take the form of streamwise velocity streaks.
This thesis aims at understanding this linear mechanism of transient growth and quantifying its influence on the classical modal amplification of disturbances. This is done by computing the so-called optimal perturbations, *i.e.* the initial disturbances that undergo maximum amplification in the boundary layer.
These optimal perturbations are first determined for two-dimensional compressible boundary layers developing over curved surfaces. In particular, we show that Klebanoff modes naturally evolve towards Görtler vortices that occur over concave walls. Three-dimensional boundary layers are then considered. In such configurations, transient growth provides an initial amplitude to crossflow vortices. Finally, applying the tools developed in this thesis to new flow cases such as swept wings provides further understanding of the phenomenon of transient growth for realistic geometries.

**Keywords:** boundary layer, laminar/turbulent transition, transient growth, Bypass transition, streaks, Klebanoff modes, Görtler vortices, crossflow vortices.

---

## Étude et modélisation du phénomène de croissance transitoire et de son lien avec la transition Bypass au sein des couches limites tridimensionnelles

**Résumé**
Le passage du régime laminaire au régime turbulent s'accompagne d'importantes modifications des propriétés physiques de la couche limite. La détermination précise de la transition est donc cruciale dans de nombreux cas pratiques. Lorsque la couche limite se développe dans un environnement extérieur faiblement perturbé, la transition est gouvernée par l'amplification du mode propre le moins stable. Lorsque l'intensité des perturbations extérieures augmente, des interactions multimodales entraînent une amplification transitoire des perturbations. Ce phénomène peut conduire à une transition prématurée, appelée transition Bypass. Les perturbations prennent alors la forme de stries longitudinales de vitesse appelées modes de Klebanoff.
L'objectif de cette thèse est d'étudier ce mécanisme linéaire de croissance transitoire et son influence sur l'amplification modale classique des perturbations. Cela passe par la détermination des perturbations les plus amplifiées au sein de la couche limite, appelées perturbations optimales. Ces perturbations optimales sont d'abord calculées pour des couches limites bidimensionnelles et compressibles se développant sur des surfaces courbes. En particulier, on montre que les modes de Klebanoff évoluent vers les tourbillons de Görtler qui se forment sur des parois concaves. Le cas plus général de couches limites tridimensionnelles est ensuite envisagé. Pour de telles configurations, la croissance transitoire fournit une amplitude initiale aux instabilités transversales. Enfin, l'application des outils développés dans cette thèse fournit de nouveaux résultats pour des cas d'écoulements autour de géométries réalistes comme une aile en flèche.

**Mots clés :** couche limite, transition laminaire/turbulent, croissance transitoire, transition Bypass, stries, modes de Klebanoff, tourbillons de Görtler, instabilités transversales.

# Remerciements

Il est difficile de résumer les nombreuses rencontres qui ont émaillé ces trois années de thèse, et qui ont parfois été déterminantes sur le plan humain et professionnel. Je vais tâcher de faire mon possible pour n'oublier personne, tout en essayant de ne pas ennuyer le lecteur à qui il reste encore quelques 130 pages à lire (courage !).

Quelques phrases ne me suffiront pas pour remercier suffisamment Olivier Vermeersch. Je voudrais commencer par lui exprimer toute ma gratitude pour la confiance qu'il m'a accordée en m'acceptant comme son premier doctorant. Je voudrais aussi, et surtout, le remercier pour l'encadrement extraordinaire dont j'ai eu la chance de bénéficier et pour sa disponibilité au quotidien. Cette thèse n'aurait certainement pas été la même sans lui et j'espère avoir le privilège de travailler de nouveau avec lui dans les années à venir. J'ai également eu l'honneur et la chance d'être l'un des derniers doctorants de Daniel Arnal, que je remercie énormément pour sa gentillesse et sa disponibilité. J'ai toujours eu grand plaisir à profiter de son immense connaissance de la couche limite lors de nos réunions. Si je l'ai parfois obligé à revenir à l'Onera après son départ, je lui souhaite de profiter désormais pleinement de sa retraite !

Je pense avoir eu la chance de bénéficier du meilleur jury possible lors de ma soutenance de thèse. Aussi, je souhaite exprimer toute ma reconnaissance à Alessandro Bottaro et Ardeshir Hanifi pour avoir accepté de relire mon manuscrit et de participer à l'évaluation de ma thèse. Leurs commentaires et appréciation de mon travail m'ont beaucoup apporté. Je remercie tout particulièrement Ardeshir Hanifi pour son accueil lors de mon passage au KTH et le temps qu'il m'a consacré. Merci également à Carlo Cossu pour avoir présidé mon jury, ainsi qu'à Grégoire Casalis et Yann Doutreleau qui m'ont fait l'honneur de participer à une discussion scientifique des plus enrichissantes.

J'ai eu le plaisir d'effectuer cette thèse au département Modèles pour l'Aérodynamique et l'Énergétique (DMAE) de l'Onera, et je souhaite en remercier tout son personnel, et notamment son directeur Pierre Milan pour m'y avoir accueilli. Je voudrais également remercier les différents membres de l'unité Instabilités, Transition et ACoustique (ITAC). En particulier, un grand merci à Grégoire Casalis pour les nombreux conseils qu'il m'a prodigués au cours de cette thèse et à Estelle Piot pour l'intérêt qu'elle a porté à mon travail.

Un immense merci bien sûr à tous les doctorants que j'ai pu côtoyer et qui ont rendu ces trois années aussi plaisantes ! Merci donc aux "anciens" qui m'ont accueilli (Hélène Parisot-Dupuis, Julien Primus, Olivier Léon, Sheddia Didorally, Cécile Dutrion, David Vanpouille, Lucas Pascal, Javier Rodriguez Sanchez, Farid Benyoucef), à mes compagnons de route (Ghislain Blanchard,

Baptiste Dejean, Lokman Bennani, Valentin Biasi, Gianluca Lavalle et Bertrand Gazanion), ainsi qu'aux futurs docteurs (Gustavo Arroyo-Callejo, Vincent Popie, Alexandre Minot, Maxime Itasse, Natacha Szulga, François Laurendau, Pierre Grenson, François Nicolas, Rémi Chauvin) et aux petits nouveaux (Stéphanie Béguet, Maxime Bouyges, Jérémie Derre, Guillaume Begou) à qui je souhaite toute la réussite possible ! Je n'oublie pas les stagiaires de passage, au premier rang desquels je ne peux que mentionner Julien Deborde.
Merci également à Ludivine Gougeon, Maxime Forte et Hugues Deniau qui resteront associés à mes meilleurs souvenirs à l'Onera, et en dehors !
Je me dois de remercier plus particulièrement mes différents co-bureaux qui m'ont supporté pendant ces trois années ! Une grosse pensée surtout à Sheddia, dont le sourire et la bonne humeur ont éclairé mon bureau pendant plus de deux ans. Et merci à Gustavo pour tous les bons moments que nous avons partagés, notamment toutes les parties de coinche remportées ensemble ! Et comme j'ai parfois l'impression que lui aussi a été mon co-bureau, je remercie aussi tout spécialement Bertrand pour tout le temps que nous avons passé ensemble à ne pas faire avancer la science !

Merci également à toutes les personnes qui ne connaissent rien à la mécanique des fluides et qui ne liront sans doute jamais cette thèse, mais qui m'ont permis de me changer les idées de temps à autre et dont les encouragements et le soutien m'ont été très précieux.

Une tendre pensée toute particulière pour Cécile : merci pour tout.

Enfin, je termine par un énorme merci à ma Maman, qui m'a toujours soutenu dans tout ce que j'ai entrepris. Et un énorme merci aussi à Carine, ma grande sœur qui m'a toujours montré le chemin.

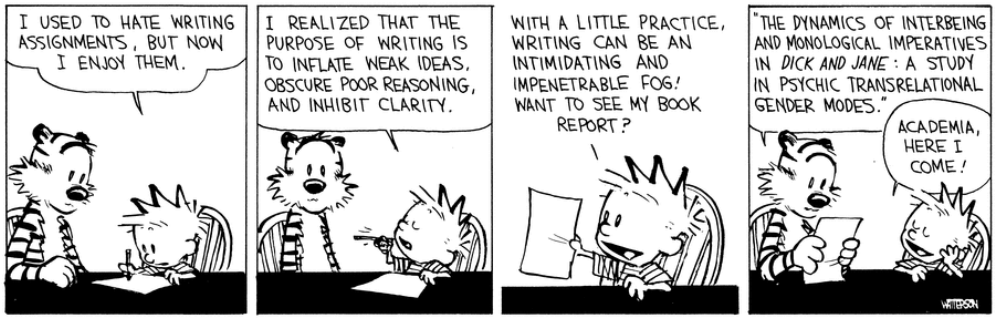


Bill Watterson
*Homicidal Psycho Jungle Cat: A Calvin and Hobbes Collection* (1994)

# Contents

# List of figures

# Nomenclature

| | |
|---|---|
| $x$ | chordwise coordinate |
| $y$ | wall-normal coordinate |
| $z$ | spanwise coordinate |
| $L$ | reference length in the chordwise direction |
| $Re_L$ | Reynolds number based on $L$ |
| $\delta$ | reference length in the wall-normal direction: $\delta = {}^{L}/\sqrt{Re_L}$ |
| $Re_\delta$ | Reynolds number based on $\delta$: $Re_\delta = \sqrt{Re_L}$ |
| $Tu$ | external disturbance level |
| $U$ | mean chordwise velocity |
| $V$ | mean normal velocity |
| $W$ | mean spanwise velocity |
| $T$ | mean temperature |
| $P$ | mean pressure |
| $\rho$ | mean density |
| $M$ | Mach number |
| $Pr$ | Prandtl number |
| $\gamma$ | specific heat ratio |
| $\mu$ | dynamic viscosity |
| $\nu$ | kinematic viscosity |
| $K_p$ | pressure coefficient |
| $\alpha$ | chordwise wavenumber |
| $\beta$ | spanwise wavenumber |

| | |
|---|---|
| $u'$ | chordwise disturbance velocity |
| $v'$ | normal disturbance velocity |
| $w'$ | spanwise disturbance velocity |
| $\theta'$ | disturbance temperature |
| $p'$ | pressure disturbance |
| $r'$ | disturbance density |
| $E$ | disturbance energy |
| $G$ | gain: $G = E_{\text{out}}/E_{\text{in}}$ |
| $N$ | $N$ factor: $N = 0.5\ln(G)$ |
| $R_c$ | radius of curvature |
| $\mathsf{G}$ | Görtler number: $\mathsf{G} = {}^{L}/_{R_c}\sqrt{Re_L}$ |
| $\beta_H$ | Hartree parameter |
| $\Lambda$ | sweep angle |

**Subscripts**

| | |
|---|---|
| d | dimensioned quantity |
| in | inlet quantity |
| out | outlet quantity |

**Superscripts**

| | |
|---|---|
| $*$ | complex conjugate |
| $+$ | adjoint operator |
| $H$ | complex conjugate transpose |
| $T$ | transpose |

**Acronyms**

| | |
|---|---|
| CF | Crossflow |
| PSE | Parabolised Stability Equations |
| TS | Tollmien-Schlichting |
| DNS | Direct Numerical Simulations |
| FS(C) | Falkner-Skan(-Cooke) |

# Introduction

Boundary-layer stability and the prediction of the onset of transition remain major challenges in today's aerodynamics. The transition from a laminar to a turbulent regime strongly modifies the flow properties. Laminar boundary layers are characterised by an undisturbed and well ordered flow, while turbulent boundary layers display three-dimensional fluctuations and random fluid motions. Such modifications may be profitable for industrial applications, for example by enhancing mixing and heat transfers. However, this is not the case in aerodynamics where transition to turbulence is accompanied by a strong increase in skin friction, which is responsible for a large part of the aerodynamic drag of modern airplanes. One approach to improve aircraft efficiency is to reduce this aerodynamic drag, thus reducing fuel consumption, by extending the laminar region over the wing surface. This can be done with a specific design of the wing or the use of control techniques to shift transition towards the trailing edge. A complete understanding of the mechanisms leading to transition is thus required to reliably predict aerodynamic performances.
For low external disturbance levels, the first step in the transition process is called receptivity. It describes how these external disturbances interact with the boundary layer to generate instabilities. These instabilities are then amplified linearly in the boundary layer before leading to the formation of turbulent spots through non-linear interactions. These spots can then grow and overlap until the boundary layer becomes fully turbulent. Most criteria used to determine the onset of transition from laminar to turbulent are based on the linear stability theory that describes the amplification of the least stable mode. Natural transition occurs once this dominant mode reaches a given amplitude. However, there are many cases where transition in shear flows is triggered for Reynolds numbers smaller than the critical Reynolds number given by the linear stability theory. These observations suggest that another mechanism also plays a role in the amplification of disturbances in boundary layers. This mechanism has first been highlighted by Ellingsen and Palm (1975) who studied the evolution of a transverse perturbation in a shear flow. They showed that these perturbations could grow and evolve into streamwise velocity streaks, also known as Klebanoff modes. These streaks can be amplified over a short distance (or time) before being damped by viscosity. This phenomenon is called transient growth. Early transition, compared to the natural one, might be triggered if the streaks are sufficiently amplified. This is referred to as Bypass transition (Morkovin, 1969), meaning that the linear amplification process of the least stable mode is bypassed. Landahl (1980) showed that the formation of the streaks in the boundary layer is due to the so-called lift-up effect: fluid particles keeping their horizontal momentum while being displaced vertically due to the interaction between longitudinal vortices and the mean shear flow lead to the formation of streamwise velocity fluctuations. Unlike linear stability theory, which focuses on the amplification of the least stable mode, a multimodal analysis is needed to study transient growth in order to account for the interactions between non-normal modes. In practice, when considering an evolving

flow, the aim is to compute the optimal perturbation. This term refers to the initial disturbance that undergoes the maximum amplification in the boundary layer. The spatial growth of optimal perturbations was first studied by Andersson *et al.* (1999) and Luchini (2000) in a Blasius boundary layer. They showed that the maximum transient growth is associated with stationary streamwise vortices that form streamwise streaks further downstream. Using the results from the optimal perturbation theory, Biau (2006) and Vermeersch (2009) developed transition criteria in order to determine the onset of Bypass transition. In the case of Bypass transition, the external disturbances level is such that transition is governed by transient growth only. However, when the external disturbance level is moderate, both transient growth and modal amplification can occur. This raises the question of the influence of transient growth on the modal amplification of disturbances.

In this context, the present work aims at computing optimal perturbations in boundary layers developing over complex geometries in order to quantify the influence of transient growth on the modal amplification of disturbances. The relation with practical transition criteria employed in such configurations is of particular interest throughout this study.

The thesis is organised as follows: the first chapter reviews the principal instability mechanisms that can be found in boundary layers. The mechanisms involved in transient growth are also introduced and previous studies of spatial optimal growth in two- and three-dimensional boundary layers are presented to detail the context of this work (chapter 1). The next chapter focuses on the method used in two-dimensional flows to compute optimal perturbations, *i.e.* initial disturbances associated with maximum energy growth. The parabolised equations in the case of a Blasius boundary layer are presented. When considering a non-parallel flow, the optimisation problem is solved using iterations of the direct and adjoint equations (chapter 2).
This method is then used to determine optimal disturbances in two-dimensional compressible boundary layers over curved surfaces. A set of parabolised equations is derived to take curvature effects into account. A new criterion is established to select the optimal disturbance that attains the largest growth at the shortest chordwise location. Such an optimal perturbation is considered for a boundary layer over a wall with a constant concave curvature in order to compute the neutral curve for the Görtler problem, which strongly depends on the initial conditions. By employing the optimal perturbation approach, the corresponding neutral curve should delimit a unique envelope for the unstable domain. The spatial optimal growth of Görtler vortices is determined and compressibility effects are discussed. The parallel-flow approximation is then adopted to compute the spectrum and pseudospectrum of the operators. These sets are used to analyse the sensitivity of the eigenvalues to non-normality and the influence of curvature on transient growth. A multimodal approach, based on the most non-normal modes, is used to quantify the disturbance amplification and study the potential for transient growth before recovering an exponential amplification (chapter 3). After considering a constant curvature, transition for compressible boundary-layer flows over wavy surfaces is investigated. The link between transient growth and practical transition criteria for surface waviness is explored. Optimal perturbations are computed for surfaces with a periodic curvature in order to study the evolution from Klebanoff modes into Görtler vortices. Multiple oscillations, which are representative of realistic surface imperfections encountered in industrial applications, are then considered. The link between the region of transient growth over the first chordwise locations and the initial amplitude for the amplification of the Görtler instability is particularly discussed. To this end, disturbance amplifications computed with the optimal perturbation approach are compared with results obtained with the Parabolised Stability Equations method. The question of the importance of transient growth effects in the accurate prediction of transition locations

is also addressed (chapter 4). The results of these last two chapters were communicated at two international conferences and an article has been accepted for publication (Lucas *et al.*, 2013, 2014). The last part of this thesis focuses on transient growth in three-dimensional boundary layers that are characteristic of swept-wing flows. A modification of the classic Parabolised Stability Equations, which are employed to describe the evolution of crossflow instabilities, is presented in order to account for both modal and non-modal disturbances. Stationary optimal disturbances propagating in a Falkner-Skan-Cooke boundary layer are then studied using this method. The evolution of the optimal disturbance into the corresponding eigenmode when exponential amplification occurs is of particular interest in the context of this work. This relation is investigated by comparing both the amplification and the shape functions of optimal initial disturbances and crossflow modes. The influence of transient growth on the initial amplification of crossflow vortices is specifically explored in both accelerated and decelerated boundary layers (chapter 5). This potential for an initial amplification of crossflow modes through transient growth is then explored for boundary-layer flows developing on more complex geometries. The Onera DTP-B airfoil is considered and detailed comparisons are made between modal and non-modal disturbances amplification. Finally, the attachment-line flow over a swept cylinder is considered. This flow is typical of boundary layers that develop along the leading edge of a swept wings. The practical transition criterion used to determine the onset of leading-edge contamination is discussed in the framework of transient growth in three-dimensional boundary layers (chapter 6). To that end, optimal perturbations are computed along and in the vicinity of the attachment line using the numerical tools developed in the previous chapters.

The principal results are finally discussed in order to draw conclusions from the work presented throughout the thesis and offer some outlook for future research.

# Part I

# Transition in boundary layers and optimal perturbation theory

Chapter 1

# State of the art

This chapter deals with transition mechanisms in two- and three-dimensional boundary layers. Different roads to turbulence are first presented, depending on the external disturbances level, to establish the context for this work. Several instability mechanisms are then detailed. Each of these instabilities is characteristic of specific conditions such as surface curvature or pressure gradient. Local and non-local approaches to study the modal stability of boundary layers are introduced. Moving beyond the behaviour of eigenvalues, the phenomenon of transient growth is introduced. Such algebraic growth arises from interactions between non-orthogonal modes for non-normal operators. Finally, transient growth mechanisms in boundary layers are presented.

## Contents

## 1.1 Different paths to turbulence

Transition to turbulence has first been highlighted by Reynolds (1883). His experiments on dye dispersion in a pipe flow revealed different motions for the fluid. For low fluid speeds, no dye dispersion is visible and the flow is laminar. Increasing the speed leads to turbulent motion, characterised by the dispersion of the dye in the whole pipe. Reynolds experiments were repeated for a range of diameters ($d$), speeds ($U$) and kinematic viscosity ($\nu$). A dimensionless number, namely the Reynolds number, can be defined as $Re = {}^{Ud}/_{\nu}$. Laminar flow occurs at low Reynolds numbers where viscous forces are dominant, while turbulent flow arises at higher Reynolds number where inertial forces prevail. However, the critical Reynolds number for which the flow undergoes transition is not universal and depends on many parameters, such as surface roughness, wall temperature, or free-stream disturbances.
The transition from laminar to turbulent flow is due to an instability of the base flow. Considering the process of transition for boundary layers in external flows, the first step focuses on how free-stream disturbances enter the boundary layer. This step is referred to as *receptivity*, a term first coined by Morkovin (1969). Receptivity describes how external disturbances provide the initial characteristics (*e.g.* amplitude, frequency) for the onset of instabilities in the boundary layer. Depending on the flow characteristics, these instabilities will either grow and lead to transition, or decay.
Reshotko (2008) reviews the process of transition in wall bounded shear flows. The initial growth of instabilities is usually described by linear stability theory. The weak linear growth of the perturbations is followed by a rapid amplification in the form of three-dimensional or non-linear interactions. These so-called secondary instabilities then lead to the breakdown to turbulence. For a long time, this scenario based on the growth of linear disturbances has constituted the dominant view of laminar-turbulent transition. The most common example is the amplification of Tollmien-Schlichting waves leading to a turbulent flow.
However, some flows exhibit a strong initial amplification of disturbances, quickly followed by secondary instabilities and transition to turbulence. In such flows, disturbance growth can be observed when linear theory predicts dampened eigenmodes and hence linear stability. Morkovin (1969) introduced the term *Bypass transition* to label this type of transition, meaning that the linear amplification is bypassed by the strong initial growth of disturbances. Bypass transition has consistently been explained by the transient growth phenomenon (Reshotko, 2001), which is due to interactions between damped non-orthogonal eigenmodes. The role of the non-orthogonality of the eigenfunctions in transient amplification of disturbances is further detailed in section 1.3.1. Bypass transition has been observed in cases of surface roughness or high free-stream turbulence levels. The external disturbances level thus plays an important role in this transition process. Morkovin *et al.* (1994) propose different paths to transition, which are shown in fig. 1.1.

- Path A corresponds to transition due to modal amplification. This situation arises for low disturbance environments where modal growth is important. The growth of Tollmien-Schlichting (TS) waves or crossflow (CF) waves (for three-dimensional boundary layers over swept wings) leads to the breakdown to turbulence. Görtler instabilities also follow this path for flows over concave surfaces. Transition prediction is based on the evolution of the least stable mode, as detailed in section 1.2.2. A comprehensive review of the mechanisms involved in this path can also be found in Reed *et al.* (1996).

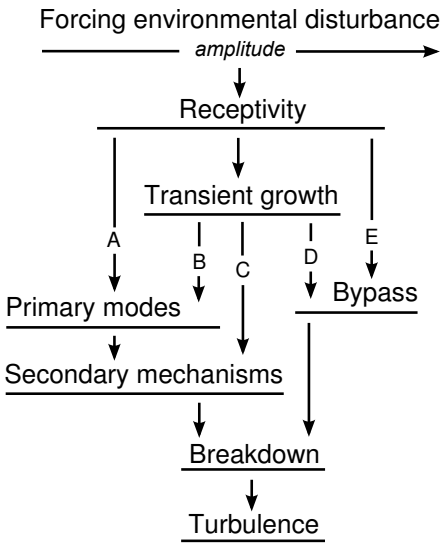


Figure 1.1: Different paths leading to turbulence, from Morkovin *et al.* (1994).

- When the external disturbance level increases, transient growth becomes significant. In path B, the disturbances level is still sufficiently low so that both modal and non-modal growth occur. As depicted in fig. 1.1, transient growth provides a higher initial amplitude to the eigenmode growth before crossing into an exponentially unstable domain. A possible scenario for two-dimensional boundary layers is the non-modal growth preceding a Görtler instability, as both mechanisms involve disturbances of comparable wavelength. This particular scenario will be further investigated in chapters 3 and 4. For three-dimensional boundary layers, the connection between transient growth and stationary crossflow waves would also be representative of path B, as detailed in chapter 5.
  Kosorygin and Polyakov (1990) observed concurrent growth of both Tollmien-Schlichting waves and Klebanoff modes (see section 1.4.1) for an external disturbance level $0.1\% \leqslant Tu \leqslant 0.7\%$. Transition is determined by the presence and interaction of both types of instability.

- In path C, the external disturbances level is now high enough so that transient growth overrides modal amplification. Optimal perturbation theory shows that initial perturbations that correspond to longitudinal vortices lead to the formation of streaks in the boundary layer, as detailed in section 1.4. These optimal disturbances can exhibit large transient energy growth.

- As in path C, external disturbances enter the boundary layer at the leading edge to form streaks. In path C transition is caused by a secondary instability, *i.e.* an instability of the modified boundary layer flow distorted by the propagation of Klebanoff modes. In path D, transient growth results in a full spectrum of disturbances, and high frequencies—which were filtered by the boundary layer in path C due to the slow amplification of the streaks—interact with Klebanoff modes to speed up the transition.

- Path E represents cases of very large external disturbances levels. The amplitude forcing is so large that there is no linear regime. The boundary layer is fully turbulent from the start, and the notion of laminar region and transition is questionable in this case.

## 1.2 Boundary layer instability mechanisms

Several instability mechanisms can be identified depending on the nature of the boundary layer. A comprehensive review can be found *e.g.* in Arnal and Casalis (2000). In the following, modal instabilities for two- and three-dimensional boundary layers are detailed (*i.e.* Tollmien-Schlichting and crossflow waves respectively). Modal stability analysis and transition prediction methods based on the evolution of the least stable mode are also introduced. Görtler vortices that arise on concave walls are then presented. Finally, attachment-line phenomena that take place at the leading edge are also reviewed.

### 1.2.1 Modal instabilities

#### 1.2.1.1 Tollmien-Schlichting waves

Tollmien (1929) and Schlichting (1933) first computed the amplification of the least stable disturbances in a two-dimensional incompressible boundary layer. These viscous instabilities take the form of travelling waves and are called *Tollmien-Schlichting* (TS) waves. They were first observed experimentally by Schubauer and Skramstad (1948). Figure 1.2 shows TS waves propagating in a two-dimensional incompressible boundary layer observed in a water channel at low speed. Streamwise wave-like disturbances can be observed, which break down into turbulent spots at some distance downstream the leading edge. The transition is governed by the amplification of the least stable mode and has historically been labelled natural transition. Tollmien-Schlichting waves are relevant in a number of transition scenarios, both in two and three-dimensional boundary layers.

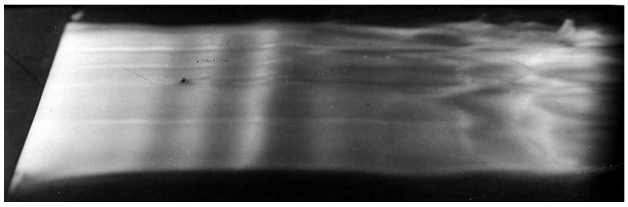

Figure 1.2: Tollmien-Schlichting waves propagating in a two-dimensional incompressible boundary layer (Werlé, ONERA, 1980). The flow goes from left to right.

At first, TS waves exhibit an exponential growth which can be computed by the linear stability analysis (Mack, 1984). An important result from the linear stability analysis is the existence of a critical Reynolds number below which all disturbances are damped. For a Blasius boundary layer developing on a flat plate, this Reynolds number is $Re_{\delta_1} = 520$, based on the displacement thickness $\delta_1$. The first unstable mode then corresponds to the TS waves. Further downstream, three-dimensional and non-linear effects become important. A secondary instability develops when TS waves reach an amplitude of around 1% of the free-stream velocity. This secondary instability leads to the formation of various vortical structures which eventually break down into smaller vortices and finally take a random character to form turbulent spots. The distance between the end of the region where TS waves amplification is accurately described by the linear stability analysis and the breakdown to turbulence is short. For this reason, most of the practical transition prediction methods are solely based on linear stability.

#### 1.2.1.2 Crossflow vortices

For three-dimensional boundary-layer flows, *e.g.* on swept wings or rotating disks, the mean velocity profile can be decomposed into two components: a streamwise and a crossflow velocity profile ($U$ in the direction of the external streamline, and $W$ in the direction normal to the streamline respectively, as illustrated in fig. 1.3). Outside the boundary layer, the sweep and pressure gradient lead to the formation of curved streamlines at the edge of the boundary layer. The crossflow profile comes from the imbalance between the pressure gradient in the crossflow direction and the centripetal acceleration inside the boundary layer where the streamwise velocity is reduced while the pressure gradient is unchanged. This secondary flow is perpendicular to the direction of the inviscid streamline.

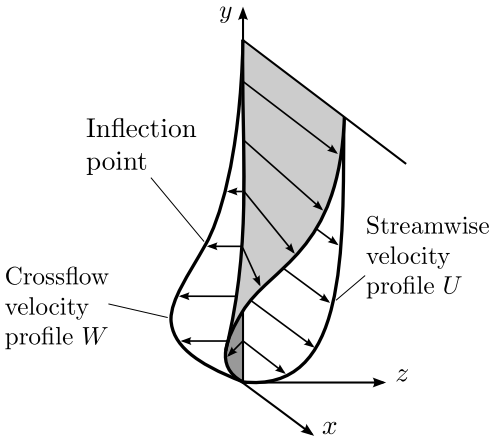


Figure 1.3: Three-dimensional boundary layer profiles (Saric *et al.*, 2003).

The crossflow profile vanishes at the wall and at the boundary-layer edge, which results in an inflection point. Rayleigh (1879) found that an inflection point is necessary for the onset of inviscid instabilities. The inviscid instabilities which take place in three-dimensional boundary layers are *crossflow vortices* (CF), first identified theoretically by Gregory *et al.* (1955). Crossflow vortices take the form of co-rotating vortices when superposed to the mean flow, but the instability alone is formed of contra-rotating vortices. A comprehensive review of crossflow instability is provided by Reed and Saric (1989); Saric *et al.* (2003).
Crossflow waves are unstable in regions where the flow is accelerated in the streamwise direction (alternatively where the pressure gradient is negative), *e.g.* close to the leading edge of a swept-wing. Both stationary and travelling waves can then be observed, although transition is generally caused by one type of instability only. Stationary waves dominate at low turbulence levels while travelling waves, which are more amplified according to linear theory, prevail for high turbulence levels. From a receptivity point of view, stationary CF waves are caused by micron-sized roughness, while their travelling counterparts are initiated by external turbulence (Bippes, 1990). Although stationary crossflow waves are usually weak, the normal and spanwise velocity disturbances produce an important modification of the streamwise velocity profile, which can lead to the formation of a secondary instability.

### 1.2.2 Modal stability analysis

#### 1.2.2.1 Local stability theory

Linear stability theory first requires the introduction of small perturbations into the Navier-Stokes equations. These equations are then linearised and quadratic terms of the disturbances are neglected. Mean-flow quantities are assumed to be functions of the normal direction $y$ only. This constitutes the parallel-flow approximation and implies that the stability of the flow at a given location can be determined by the local conditions at that location only (*i.e.* independently of all others). Perturbations $\boldsymbol{q}'$ are written as normal modes

$$\boldsymbol{q}'(x,y,z,t) = \boldsymbol{q}(y)\exp[i(\alpha x + \beta z - \omega t)], \tag{1.1}$$

where $\alpha$ and $\beta$ are the streamwise and transverse wavenumbers respectively, and $\omega$ is the angular frequency. The linearised Navier-Stokes equations together with the normal mode decomposition represents a system of ordinary differential equations in the wall-normal coordinate $y$ for the amplitude function $\boldsymbol{q}$. Numerically, it constitutes a temporal or spatial eigenvalue problem: when the mean flow is specified, non-trivial solutions exist only for particular combinations of ($\alpha$, $\beta$, $\omega$) which are related through a dispersion relation.

- A temporal eigenvalue problem is obtained if $\alpha$ and $\beta$ are real. Then $\omega$ is complex, with a real part representing the angular frequency and an imaginary part specifying the temporal growth of the eigenmode.

- A spatial eigenvalue problem is obtained if $\omega$ is real, and $\alpha$ and $\beta$ are complex. The wave vector can be defined as $\boldsymbol{k} = (\alpha_r, \beta_r)$, and the amplification vector $(-\alpha_i, -\beta_i)$ denotes the spatial growth in the streamwise direction $x$ and the transverse direction $z$ respectively.

Although both approaches are equivalent using Gaster's transformation (Gaster, 1962), the discussion will be restricted to the spatial approach which is more relevant for boundary-layer flows.
For two-dimensional incompressible flows, Squire's theorem (Squire, 1933) restricts the analysis to two-dimensional disturbances ($\beta = 0$). If there is an unstable three-dimensional mode ($\beta \neq 0$) at a given Reynolds number, this theorem states that there is an unstable two-dimensional mode at a lower Reynolds number.
In this simplified case where $\beta = 0$, combining the equations to eliminate the chordwise and transverse velocity disturbances leads to the Orr-Sommerfeld equation. For given values of $\omega$ and Reynolds number $Re_L$, the stability of the flow is given by the sign of the imaginary part $\alpha_i$ of the chordwise wavenumber. If $\alpha_i > 0$ for all the eigenvalues, then the flow is stable. On the other hand, if one $\alpha_i$ is negative, then the flow is unstable. The isocontour curve where $\alpha_i = 0$ delimits the unstable domain and is called the neutral curve. Such neutral curve is shown in fig. 1.4 for a Blasius boundary layer as a function of the reduced frequency $F = 10^6\omega/Re_{\delta_1}$ and the Reynolds number $Re_{\delta_1}$ based on the boundary layer thickness $\delta_1$. An important result is that the flow is stable for Reynolds numbers below $Re_{\delta_1} = 520$. The inside of the neutral curve represents the unstable region, *i.e.* the frequencies and Reynolds numbers for which Tollmien-Schlichting waves arise in the boundary layer.

The amplitude $A$ of the disturbances is linked to the spatial amplification coefficient $\alpha_i$ through the relation

$$\frac{1}{A}\frac{\mathrm{d}A}{\mathrm{d}x} = -\alpha_i. \tag{1.2}$$

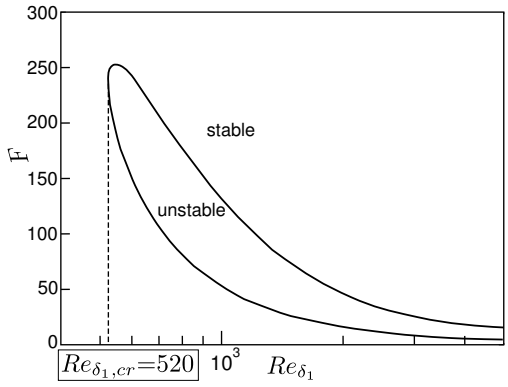


Figure 1.4: Neutral curve for the Blasius boundary layer.

Considering a disturbance propagating at a given frequency $f = \omega/2\pi$ which starts to be amplified at a location $x_0$ with an amplitude $A_0$, the total growth rate can be defined as

$$\ln(A/A_0) = \int_{x_0}^{x} -\alpha_i(\xi, f)\,\mathrm{d}\xi. \tag{1.3}$$

Computing this total amplification rate for a series of unstable frequencies leads to the definition of the $N$ factor as the envelope over all frequencies,

$$N(x) = \max_f \left(\ln(A/A_0)\right). \tag{1.4}$$

Figure 1.5 shows the growth rates for various frequencies and the $N$ factor envelope for the Blasius boundary layer. Van Ingen (1956) and Smith and Gamberoni (1956) developed the $e^N$ method for low speed flows. In this method, transition occurs when the $N$ factor reaches a predefined value, typically between 7–10, which means that the locally most unstable wave is amplified by a factor $e^7$–$e^{10}$. For two-dimensional low speed flows, Mack (1977) linked the critical $N$ factor to the external level of turbulence $Tu$ through the relation

$$N_T = -8.43 - 2.4\ln(Tu) \quad \text{for } 10^{-3} < Tu < 10^{-2}. \tag{1.5}$$

The method has then been extended to compressible and three-dimensional flows, as detailed *e.g.* in Arnal *et al.* (2008a). A brief overview is given in the following.
For two-dimensional compressible flows, Squire's theorem does not hold and the most unstable disturbances are oblique waves (also referred to as three-dimensional waves). The amplification is still assumed to occur only in the streamwise direction so that $\beta_i = 0$, but the real part $\beta_r$ has to be determined. Two methods can be considered:

- the *envelope strategy*: for a given location $x$ and a fixed frequency $f$, $\beta_r$ is determined to follow the maximum amplification rate. The $N$ factor is computed on the basis of this most unstable wavenumber direction $\beta_{r_{\max}}$,

$$N(x) = \max_f \int_{x_0}^{x} -\alpha_i(\xi, f, \beta_{r_{\max}})\,\mathrm{d}\xi. \tag{1.6}$$

- the *fixed $\beta$ strategy*: the total amplification rate is computed for fixed values of $f$ and $\beta$ and the maximisation is done with respect to both parameters (which is also called an Envelop of the Envelops method, denoted EoE),

$$N(x) = \max_{f,\beta_r} \int_{x_0}^{x} -\alpha_i(\xi, f, \beta_r)\,\mathrm{d}\xi. \tag{1.7}$$

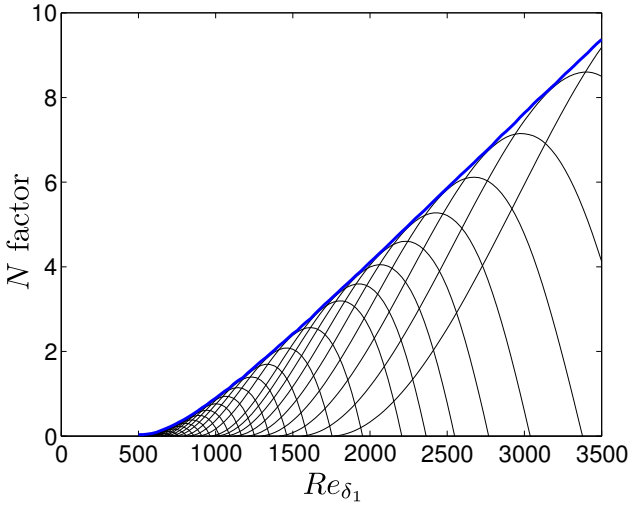


Figure 1.5: Total amplification rate for various frequencies (——) and $N$ factor envelope (——) for the Blasius boundary layer.

For three-dimensional mean flows, transition is triggered either by TS waves (two-dimensional disturbances, see section 1.2.1.1) or CF instabilities (three-dimensional disturbances, see section 1.2.1.2). The favourable pressure gradient that stabilises TS waves also destabilises CF vortices. On a swept-wing, the boundary layer is thus likely to first develop crossflow instabilities when the flow is accelerated (upstream of $X_M$ in fig. 1.6, where the crossflow velocity profile is unstable) and then sustain TS waves in the region where the flow is decelerated (downstream of $X_M$).

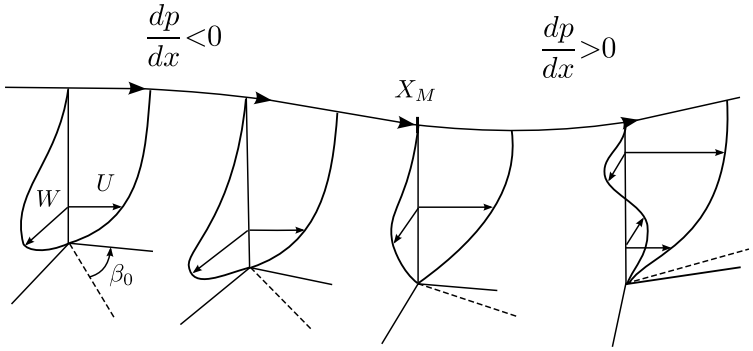


Figure 1.6: Laminar boundary-layer development on a swept wing (Arnal *et al.*, 2008a). The location of the inviscid streamline inflection point is denoted $X_M$ and $\beta_0$ is the angle between the wall and potential streamlines.

The assumption that the amplification only takes place in the chordwise direction (*i.e.* $\beta_i = 0$) is not necessarily verified. Hence $\beta_i$ has to be determined to account for the amplification in the spanwise direction (see Arnal, 1993, for a review on the possible solutions to this problem). Once $\beta_i$ is prescribed, several methods can be identified for computing the $N$ factor. The first one is the previous envelope strategy. Other methods are based upon a constant parameter, where the $N$ factor is determined using an EoE method. Finally, two $N$ factors can be computed separately for the TS and CF instabilities: this is the $N_{\mathrm{CF}}-N_{\mathrm{TS}}$ method, where transition occurs for particular combinations of these two parameters.

#### 1.2.2.2 Non-local approach: parabolised stability equations (PSE)

In order to take non-parallel effects into account, Simen (1992) and Bertolotti *et al.* (1992); Herbert (1993) proposed a new formulation for the stability analysis, known as *parabolised stability equations* (PSE). This formulation covers cases where the flow cannot be considered parallel, such as boundary layers or jets. The idea of the PSE is that quantities that were considered local (*i.e.* independent of the chordwise direction $x$) in the local approach are now slowly-varying functions of $x$. The chordwise wavenumber $\alpha$, which denotes the streamwise dependence in the local approach, now only represents the dominant part of this dependence.
The disturbances $\boldsymbol{q}'$ are decomposed into a slowly varying shape function $\boldsymbol{q}$ and a fast oscillatory phase function $\Theta$ according to

$$\boldsymbol{q}'(x,y,z,t) = \boldsymbol{q}(x,y)\exp(i\Theta(x,z,t)), \tag{1.8a}$$

$$\Theta(x,z,t) = \int_{x_0}^{x} \alpha(\xi)\,\mathrm{d}\xi + \beta z - \omega t. \tag{1.8b}$$

After introducing this decomposition into the linearised Navier-Stokes equations, the shape function and the chordwise wavenumber $\alpha$ have to be determined. The resulting partial differential equations can be solved using a marching technique to compute the shape function $\boldsymbol{q}$ for a given $\alpha$.
The decomposition in eq. (1.8a) causes an ambiguity since both the shape function $\boldsymbol{q}$ and the phase function $\Theta$ depend on the chordwise coordinate $x$. The aim is to determine the chordwise wavenumber $\alpha$ to ensure a slow variation of the shape function in the chordwise direction. The local approach leads to an eigenvalue problem where the dispersion relation is used to determine the eigenvalue $\alpha$. In the parabolised stability equations, $\alpha$ is calculated through another relation which represents a normalisation on the shape function.
From the normal-mode decomposition (eq. (1.1)) used in the local stability theory, the chordwise wavenumber can immediately be obtained according to

$$\alpha(x) = -i\frac{\partial}{\partial x}(\ln(\boldsymbol{q}')) = -i\frac{1}{\boldsymbol{q}'}\frac{\partial \boldsymbol{q}'}{\partial x}. \tag{1.9}$$

Similarly in the non-local framework, starting from eq. (1.8a), a wavenumber $\tilde{\alpha}$ can be defined as

$$\tilde{\alpha}(x,y) = -i\frac{\partial}{\partial x}(\ln(\boldsymbol{q}')) = \alpha(x) - i\frac{1}{\boldsymbol{q}}\frac{\partial \boldsymbol{q}}{\partial x}. \tag{1.10}$$

From eq. (1.10), the total disturbance variation in the chordwise direction is decomposed in two oscillatory parts: one is absorbed by the phase function through $\alpha$ while the other is absorbed by the shape function through the term $i/\boldsymbol{q}\,\partial\boldsymbol{q}/\partial x$.
Equation (1.9) is independent of the wall-normal coordinate $y$, which is not the case in eq. (1.10). Following Airiau (1994), a quantity independent of $y$, equivalent to the chordwise wavenumber of the local approach, can be obtained from eq. (1.10) by multiplying the equation by[1] $\boldsymbol{q}^H\boldsymbol{q}$, integrating over $y$ and dividing by the integral of $\boldsymbol{q}^H\boldsymbol{q}$,

$$\frac{\int_0^\infty \tilde{\alpha}\boldsymbol{q}^H\boldsymbol{q}\,\mathrm{d}y}{\int_0^\infty \boldsymbol{q}^H\boldsymbol{q}\,\mathrm{d}y} = \alpha(x) - i\frac{\int_0^\infty \boldsymbol{q}^H(\partial\boldsymbol{q}/\partial x)\,\mathrm{d}y}{\int_0^\infty \boldsymbol{q}^H\boldsymbol{q}\,\mathrm{d}y}. \tag{1.11}$$

The resulting normalisation condition,

$$\int_0^\infty \boldsymbol{q}^H\frac{\partial \boldsymbol{q}}{\partial x}\,\mathrm{d}y = 0, \tag{1.12}$$

[1] The superscript $H$ denotes complex conjugate transpose.

ensures that both the growth and periodic variation of the disturbance are mainly absorbed by the phase function. It is important to note that this condition depends on the choice of the disturbance amplitude used for determining the amplification rate. Equation (1.11) can be written as

$$\alpha^* = \alpha(x) - i\frac{\mathcal{N}}{A^2}, \tag{1.13}$$

where $\alpha^*$ is the desired chordwise wavenumber, $\mathcal{N}$ is the normalisation condition and $A$ the associated disturbance amplitude. Airiau (1994) gives a review of possible measures of disturbance amplitudes and their associated normalisation conditions.

### 1.2.3 Görtler vortices

As mentioned in section 1.1, the transient growth prior to a Görtler instability will be investigated in chapter 3. The following presents a review on the studies of Görtler vortices.
Streamwise-oriented periodic counter-rotating vortices known as *Görtler vortices* are present in boundary layers over concave walls. For such configurations, the flow is subject to a centrifugal instability which destabilises the laminar boundary layer and leads to the resulting spatially-growing spanwise-periodic longitudinal vortices first observed by Görtler (1941). The amplitude of the vortices increases although their wavelength remains fairly constant in the spanwise direction. The inviscid mechanism, first pointed out by Rayleigh (1916), arises from the disequilibrium between the centrifugal force term and the restoring normal pressure gradient and it has been proven active in both two- and three-dimensional boundary-layer flows. Practical occurrence of this phenomenon can be found in both nature and technical applications, for example over the concave part of a laminar flow wing or on the wall of a supersonic nozzle, and it is known, under some conditions, to lead the flow through transition to turbulence. Some experiments have shown that transition to turbulence in the presence of Görtler vortices can be due to a secondary instability originating from the distortion of the steady velocity profile. It has also been demonstrated that the spanwise modulations of the base flow caused by Görtler vortices can destabilise Tollmien-Schlichting waves. The Görtler centrifugally-driven instability mode bears many similarities with the Taylor mode associated with the instability of a flow between coaxial cylinders. The difference comes from the spatial evolution along the streamwise distance of the Görtler vortices as the boundary layer develops over a wall with non-constant curvature, which is not the case for Taylor vortices. This aspect has significant implications for the study of Görtler vortices.

#### 1.2.3.1 Parallel flow approximation

A review on the topic of Görtler vortices is provided *e.g.* by Saric (1994): studies of boundary layers over curved walls first began with the work of Görtler (1941) building upon Taylor's linear stability analysis for centrifugal instabilities in Couette flow (1923). He considered the stability of a parallel Blasius boundary layer developing over a curved wall of asymptotically large radius of curvature. Solutions to this problem were provided by Görtler and later by Hämmerlin (1955) and Smith (1955), but they noted differences in the computed neutral curves at this early stage. The solutions of the disturbance equations were found in the form of counter-rotating, streamwise-oriented vortices. Herbert (1976) extended Görtler's formulation to consider finite variable radius of curvature and pointed out the dependence of the neutral curve to that curvature at low spanwise wavenumbers. The vast majority of these early studies addressed the problem of determining the linear stability of external two-dimensional boundary-layer flows over curved surfaces. They all took place within the frame of the parallel-flow approximation, assuming a base flow independent of the streamwise

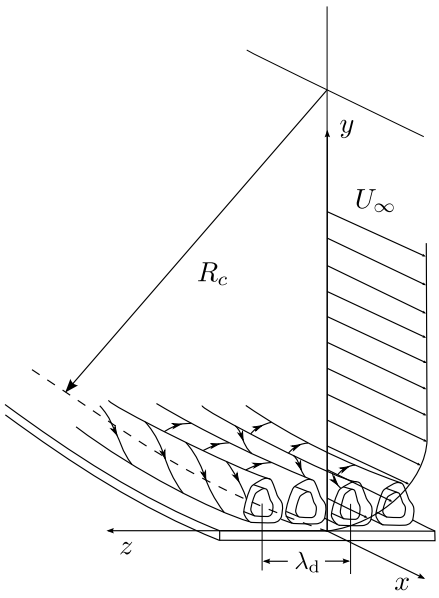


Figure 1.7: Development of Görter vortices in a boundary layer over a concave surface with a radius of curvature $R_c$ (Saric, 1994).

coordinate, hence neglecting the boundary-layer growth. Under this approximation, the partial differential linear stability equations are reduced to an ordinary differential system for easier solving using a separation-of-variables method (normal mode solutions). However, for the Görtler problem, the parallel-flow approximation is no longer valid as opposed to the study of the Taylor instability. Hall (1982) argued that much of the conclusions of these early studies were fundamentally flawed. He proved that the parallel-flow approximation is only justifiable in the limit of a large spanwise wavenumber $\beta >> 1$. Hence the parallel-flow approximation was the cause of many inconsistencies in the early studies. In the large spanwise wavenumber regime where it has been proven valid, this approximation is also unnecessary as an asymptotic solution can be analytically derived.
Hall (1982) developed a WKB expansion in wall-normal direction valid for simultaneously large Görtler numbers and large spanwise wavenumbers. He then obtained an analytic expression for the upper branch of the neutral curve that was in agreement with previous numerical solutions determined for large spanwise wavenumber $\beta$. Experiments have shown that, once established, Görtler vortices remains of constant wavelength. With the development and growth of the boundary layer, the non-dimensional wavenumber increases so that the large wavenumber limit is ultimately appropriate far enough downstream.

#### 1.2.3.2 Experimental studies

It is well known that concave curvature lowers the transition Reynolds number, see for example the work of Liepmann (1943, 1945). Early experiments (Gregory and Walker, 1950) aimed at confirming the existence of Görtler vortices in a laminar boundary layer over a concave wall. Tani et al. (1962) were the first to measure a spanwise velocity component in the boundary layer consistent with the presence of counter-rotating pairs of vortices. In particular, they observed that the vortices physical wavelength remained constant in the streamwise direction once the vortices were established, which has been later confirmed (Finnis and Brown, 1997).
Later experimental work focused on measuring the distributions of the velocity perturbations and computing the position of the neutral curve, in particular with the work of Bippes and Görtler (1972)

who generated different vortex structures and monitored whether these structures were amplified or damped. He found that visualisations of the Görtler vortices were difficult when confronted to low free-stream turbulence, hence the necessity to trigger the formation of the streamwise rolls (either with a turbulence screen ahead of the airfoil, or with small heating wire along the span). This difficulty is clearly linked with the strong dependence of the problem to initial conditions. Despite this strong influence of the inlet conditions, the experiments confirmed the most amplified wavelengths obtained with linear theory, a result later highlighted by Mangalam *et al.* (1985).

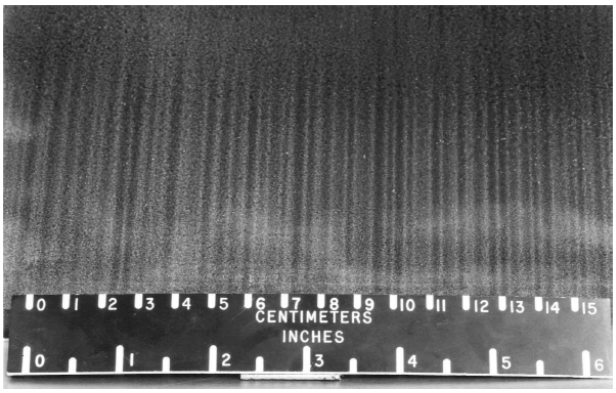


Figure 1.8: Flow visualisation of Görtler vortices using sublimating chemicals (Mangalam *et al.*, 1985). The Mach number is $M_\infty = 0.05$ and the chord Reynolds number is $Re_c = 2.24 \times 10^6$.

#### 1.2.3.3 Quasi-parallel flow approximation and normal mode solutions

Vortices present in a flow over a wall with small curvature grow weakly in the streamwise direction. Hence, there is no order $\mathcal{O}(1)$ streamwise variation of the perturbation due to a travelling wave and it is not possible to separate the weak growth of the boundary layer from the weak growth of the disturbance. The classical linear stability theory is inappropriate and the equations for the Görtler problem have to be rederived to include the non-parallel effect of the boundary layer growth.
A set of non-separable partial differential equations for the linear non-parallel stability problem of the Görtler vortices was first derived by Floryan and Saric (1982) who performed a local stability analysis, implicitly ignoring the streamwise growth of the boundary layer. An incompressible flow with weak non-parallel effect is considered and the stability equations are classically obtained by superposing small, steady, spanwise periodic disturbances onto the base flow. An important feature of steady streamwise vortices within a shear layer is the different scaling used for the streamwise disturbance velocity which is considered larger by an order $\mathcal{O}(\sqrt{Re})$ than the normal and spanwise disturbance velocities. The equations are written in curvilinear coordinates, and the metric coefficients are expanded in terms of the inverse of the Reynolds number and small curvature scale. Terms of higher order than the first in curvature and Reynolds number are disregarded to obtain the parabolic system of the disturbance equation. These equations constitute the zeroth-order statement of the Görtler problem.
From there, Floryan and Saric (1982) replaced partial derivatives of the vortices with respect to the streamwise coordinate by local spatial growth rates in order to reduce the system to a set of ordinary differential equations. When the growth rate vanishes, the solution can be seen as a local Taylor-series solution of the full partial differential equation. This approach is known as the *locally non-parallel stability method*. However, some intrinsic properties of the non-parallel nature of the base flow are ignored using this approach.

#### 1.2.3.4 Marching solutions

Hall dismissed the locally non-parallel stability method, as the equations for the perturbations are non-separable. He used a marching technique where an initial disturbance is imposed at a given location and its development is followed as the equations are marched downstream. Hall (1982) showed that the separation-of-variables solution is only valid for spanwise wavenumber $\beta >> 1$ and he argued (Hall, 1983) that the numerical integration of the parabolic equations is the only appropriate method for analysing the Görtler instability for $\beta = \mathcal{O}(1)$. Since there is no streamwise derivative of the pressure, the disturbance pressure and spanwise velocities are eliminated by cross-differentiation, leading to coupled second- and fourth-order equations in the streamwise and normal disturbance velocities respectively.
Hall also pointed out that the existence of a neutral point strongly depends on the location and shape of the initial conditions (Hall, 1983). Hence, the concept of a unique neutral curve is not readily accessible for the Görtler problem as opposed to usual parallel flow stability problems because of the dependence to initial conditions and to their inlet location. For large spanwise wavenumbers however, the different neutral curves merge into the asymptotic and parallel-flow neutral curves.

#### 1.2.3.5 Comparison between the normal-mode approach and the marching technique

Day *et al.* (1990) and later Goulpié *et al.* (1996) have made detailed comparisons between the normal-mode approach, employed in particular by Floryan and Saric, and the approach consisting of marching the equations downstream developed by Hall. A first difficulty to notice is the use of different definition for the growth rate of Görtler vortices: Hall (1983) used an integral energy while the normal-mode analysis uses the amplitude of the streamwise component of the perturbation velocity.
The results obtained with the locally non-parallel method can be interpreted as the limit the marching solutions asymptotically tend to some distance away from the leading edge. Differences are found in the determination of the first neutral point, before the agreement between marching and normal-mode solutions is obtained at some distance from the leading edge. If the initial conditions are taken as solutions of the local problem, a good agreement is obtained between both methods when comparing neutral curves (the small differences observed do not impact the computation of the integrated amplification). However, the use of particular initial conditions such as the initial disturbances employed by Hall can lead to wide discrepancies in the determination of the neutral stability, a result also emphasised by Kalburgi *et al.* (1988a). Bottaro and Luchini (1999) recently came back to the local stability theory for the Görtler problem by comparing local solutions computed through a WKB expansion (in terms of the inverse of the Görtler number) of various order (including, at leading order, previous local theories, as *e.g.* the one of Görtler) with the solutions obtained with the marching technique. They found good agreement between both methods far enough from the leading edge when the initial conditions are prescribed.
Kalburgi *et al.* (1988b) also compared solutions obtained using the downstream integration technique with measurements of the Görtler instability on an airfoil. Their observations of a double peak of streamwise velocity perturbation highlight the formation of a second pair of vortices when going from a concave to a convex surface, a result numerically observed later by Saric and Benmalek (1991) and Hennequin (1993). The initial pair of vortices is lifted off and vanishes while a second pair of vortices is formed at the wall. Physically, the decrease in the concave curvature decreases the amplitude of the normal and spanwise velocities until they eventually change sign, while the streamwise velocity keeps on increasing.

#### 1.2.3.6 Further linear solutions

- *Walls with variable curvature:*

Floryan (1986) and Jallade (1990) studied the effect of a varying curvature and showed the stabilising effect of a convex curvature and the destabilising effect of a concave one. However, neither the normal-mode solutions nor the asymptotic approach at large wavenumbers $\beta$ can account for a continuous change from a concave to a convex curvature. No Görtler instability is therefore found over convex or flat surfaces downstream a concave wall (no discrete spectrum of eigenvalue exist) despite experiments showing the presence of vortices.
Saric and Benmalek (1991) considered the development of Görtler vortices over wavy walls by means of marching technique. They showed the strong stabilising effect of convex surfaces. A wavy wall is unlikely to cause a strong instability in the boundary layer because of this overall stabilising effect of convex regions. When going from a concave to a convex surface, a new pair of counter-rotating vortices forms at the wall which rotates in the opposite way, while the initial vortices are lifted off and vanish.
The interest in flows over variable curvature comes from both practical applications—where the wall may be unintentionally wavy—and the discussion over the Görtler-Witting mechanism (Lessen and Koh, 1985). This latter mechanism suggests that Tollmien-Schlichting waves of large amplitude might locally induce concave surfaces and lead to the formation of Görtler vortices. However, the work of Saric and Benmalek suggests that the Görtler-Witting mechanism is not an important instability as the maximum source term for the formation of Görtler vortices is located at the wall.

- *Compressibility effects:*

The growth of Görtler vortices in a compressible boundary layer under the parallel-flow approximation was considered notably by Hämmerlin (1961), Aihara (1961), Kobayashi and Kohama (1977), El Hady and Verma (1983), and Jallade (1990). They used the separation-of-variables method and no large spanwise wavenumber asymptotic limit. Conversely, Hall and Malik (1989) studied the impact of compressibility within the large wavenumber limit. Compressibility is found to have an overall stabilising effect on the Görtler instability, although not as important as for Tollmien-Schlichting waves. A difference from the incompressible case is the presence, at hypersonic speeds, of a temperature adjustment layer (*i.e.* a zone where the temperature quickly decreases to the free-stream value) which changes the location of the most unstable vortices (Hall and Fu, 1989).

- *Three-dimensional boundary layers:*

In most practical situations of interest, the basic flow is three-dimensional, as for example for swept-wing configurations, and previous analyses become inadequate. Hall (1985) considered the flow over an infinitely long swept cylinder using asymptotic analysis. He showed that Görtler vortices do not play a role at large sweep angles, or more precisely when the ratio of the size of the crossflow to the size of the chordwise flow is of order $\mathcal{O}(Re^{-1/2})$ (where $Re$ denotes the Reynolds number of the base flow). For such values, the Görtler instability disappears when a weak crossflow is introduced in the base flow, which suggests that there is small risk of Görtler vortices appearing in most swept-wing flow problems as a cause of transition. Instead, crossflow vortices naturally arise and are found to be the only possible unstable structures in three-dimensional boundary layers. Bassom and Hall (1991) later took over this analysis to tackle the problem of the receptivity in the case of three-dimensional flows.

#### 1.2.3.7 Receptivity

Bassom and Seddougui (1995) reviewed the receptivity problem to surface roughness and free-stream disturbances for Görtler vortices. Denier *et al.* (1991) found that distributed surface roughness with a spanwise wavelength comparable to the boundary-layer thickness are an efficient way of exciting Görtler vortices. On the other hand, isolated roughness elements would only be relevant when considering very small free-stream disturbances. Bertolotti (1993) also found streamwise-aligned roughness elements to efficiently trigger Görtler vortices. Schrader *et al.* (2011) showed that the boundary layer is receptive to wall roughness near the leading edge, while the receptivity decreases further downstream. The receptivity is found to decrease with increasing radius of curvature. They also considered streamwise elongated roughness elements and found enhanced transient disturbances that provide energy to the Görtler rolls.
Hall (1990) considered the receptivity to free-stream vortical disturbances. He showed that the boundary-layer is more receptive to free-stream disturbances near the leading edge. Luchini and Bottaro (1998) computed Green's functions from a backward-in-time integration of the adjoint parabolic system. When multiplied by a given external disturbance, these functions yield the downstream amplitude of the most amplified Görtler vortices. They considered both free-stream disturbances and wall roughness and computed the most amplified initial conditions. Cossu *et al.* (2000) computed the maximum spatial growth of Görtler vortices and showed that the receptivity of the boundary layer changes with the location of the inlet condition. This result will be further developed in section 3.2.1. Schrader *et al.* (2011) also showed that free-stream vortical modes with zero or low frequency, large spanwise wavelength and small wall-normal wavelength can penetrate the boundary layer and excite longitudinal streaks through the lift-up effect. These streaks then initiate steady or slowly travelling Görtler vortices.

### 1.2.4 Attachment line phenomena

For simple geometries, such as symmetrical bodies, the attachment line can be viewed as a particular streamline which divides the flow into one branch following the upper surface and one branch following the lower surface. More precisely, it is the spanwise line along which the static pressure is maximum (Arnal *et al.*, 2008b). The attachment line flow on a swept cylinder of infinite span is represented in fig. 1.9. The free-stream velocity $Q_\infty$ has a streamwise component $U_\infty = Q_\infty \cos(\phi)$ normal to the leading edge and a spanwise component $W_\infty = Q_\infty \sin(\phi)$ parallel to the leading edge. For a swept body of infinite span as this one, the boundary layer properties are constant along the attachment line.

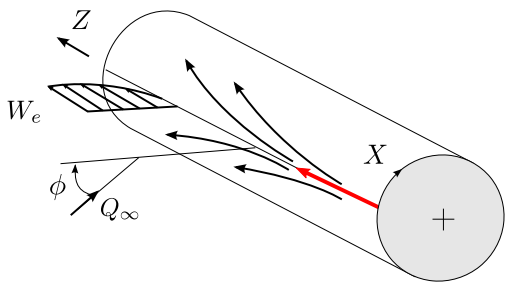


Figure 1.9: Attachment line flow on a swept cylinder.

Along the attachment line, the free-stream velocity components $U_e$ and $W_e$ can be defined as

$$U_e = kX \quad \text{and} \quad W_e = W_\infty = \text{constant}, \tag{1.14}$$

where $k$ is the free-stream velocity gradient in the direction $X$. The attachment line flow can be characterised by the Reynolds number $\overline{R}$,

$$\overline{R} = \frac{W_e \eta}{\nu_e} \quad \text{with } \eta = (\nu_e/k)^{1/2}, \tag{1.15}$$

where $\nu_e$ is the kinematic viscosity.

Two types of attachment-line phenomena can be identified, namely *natural transition* and *leading-edge contamination*.
Natural transition occurs when there is no source of large disturbances at the beginning of the attachment line. A laminar boundary layer starts developing in the spanwise direction $Z$ which can become turbulent further downstream. Transition comes from the amplification of small disturbances in the attachment-line flow leading to viscous instabilities, with mechanisms similar to those observed in a flat plate boundary layer.
These similarities lead to the development of a linearised stability theory to study the growth of the disturbances. A special class of disturbances has first been introduced for low speed flows by Görtler (1955) and Hämmerlin (1955) called the Görtler-Hämmerlin disturbances. The chordwise disturbance velocity is taken as a linear function of the chordwise coordinate $X$ (similarly to the base flow) while the other disturbances are independent of $X$. After introducing these perturbations, the linearised Navier-Stokes equations lead to an eigenvalue problem, which is obtained without resorting to the parallel-flow approximation. Hall *et al.* (1984) first solved the temporal one-dimensional eigenvalue problem, while Theofilis (1995) solved the corresponding spatial eigenvalue problem. They found a critical Reynolds number $\overline{R}_{cr} = 582$ for the Görtler-Hämmerlin instabilities (where $\overline{R}_{cr} = 662$ for the TS waves). This value is in agreement with low speed experiments (Poll, 1978; Bippes, 1990) as well as DNS performed under favourable conditions for linear growth (Hall and Malik, 1986, Theofilis, 1998). The more recent biglobal approach (Lin and Malik, 1996; Theofilis, 2003) starts with no assumption on the form of the disturbances, which requires to solve a generalized eigenvalue problem. This approach shows the existence of additional modes, which can be of importance when considering transient growth.

On the other hand, leading-edge contamination is likely to occur when the swept body is attached to a solid wall. In this case, the leading edge is contaminated by the large turbulent structures coming from the wall. Transition occurs due to the convection of turbulent spots along the attachment line. For instance, the attachment line from the root to the wing tip of an aircraft wing is very sensitive to the contamination by the turbulent flow that arises at the junction between the wing and the fuselage.
For subsonic and transonic flows, a criterion based on the value of $\overline{R}$ has been developed (Pfenninger, 1965; Poll, 1978). If $\overline{R}$ is lower than 250, the turbulent spots are damped as they are convected along the attachment line. When $\overline{R} > 250$, the spots are self-sustaining and grow until the leading-edge region becomes fully turbulent. This value of $\overline{R}_{cr} = 250$ is much lower than the value reported by linear stability analysis using the Görtler-Hämmerlin assumption, which raises the question of possible subcritical instabilities.
The high external disturbances level makes attachment-line flow a potential candidate for non-modal growth. Large temporal transient growth of disturbance energy has been highlighted by Obrist and Schmid (2003) using a non-modal stability analysis and by Guégan *et al.* (2006, 2007) using

an iterative direct/adjoint approach. In the spatial framework, Guégan *et al.* (2008) found large energy amplification due to the lift-up mechanism, with spanwise counter-rotating vortices evolving into spanwise streaks. The disturbance characteristics are found to be similar to that encountered in Blasius boundary layers.
In relation to the existence of subcritical instabilities, Bertolotti (1999) first showed the connection between attachment-line instabilities and stationary crossflow vortices using a PSE formulation. These findings are coherent with results of direct numerical simulations (Spalart, 1988) which show solutions off the attachment-line that strongly resemble crossflow vortices. Mack *et al.* (2008) considered a compressible swept leading-edge flow around a parabolic body and confirmed the connection between the two types of instabilities. Mack and Schmid (2011) also computed the neutral curve for this attachment-line flow and identified both global boundary-layer and acoustic modes. They found these global eigenmodes to be non-orthogonal, which highlights the potential role of transient growth in the transition of attachment-line flows.

## 1.3 Non-normal operators and algebraic growth

### 1.3.1 Algebraic growth phenomenon

The linear stability theory as described in section 1.2.2 addresses the problem of finding the minimum critical parameter (for example the Reynolds or Rayleigh number) above which a specific initial condition of infinitesimal amplitude grows exponentially. This is done by first linearising around the laminar base flow and then looking at the spectrum of the operator of the linearised problem. If one eigenvalue has a positive imaginary part, exponential growth is expected and the smallest critical parameter for which this eigenvalue crosses into the unstable domain is the minimum critical parameter. For some flows, predictions based on eigenvalue analysis present a good agreement with experiments. This is the case for Rayleigh-Bénard convection and Taylor-Couette flow, and more generally for flows where instabilities are caused by thermal or centrifugal disequilibrium. However, there are flows for which linear stability fails to reproduce experimental observations. For a plane Poiseuille flow, eigenvalue analysis predicts a critical Reynolds number of 5772, when transition to turbulence can be observed at Reynolds number of about 1000. Many other shear flows exhibit similar discrepancies between the linear stability results and experiments. For Couette flow, which is unconditionally stable according to linear stability, experiments show a critical Reynolds number under which transition can be observed. To understand the significant discrepancies between the linear stability results and experiments, the steps involved in the eigenvalue analysis have to be investigated.
For many years, these anomalies have been attributed to the linearisation, with much effort devoted to take non-linear terms into account. However, looking at the Reynolds-Orr equation for the energy reveals that non-linear terms of the Navier-Stokes equations conserve the energy (see Waleffe, 1995; Henningson, 1996). This observation indicates that a linear process which does not rely on an unstable eigenvalue is responsible for the amplification of the perturbation.
Perturbation amplification is indeed possible even if all the eigenvalues of a linear system are stable if the eigenfunctions are not orthogonal to one another. Operators which exhibit a set of non-orthogonal eigenfunctions are referred to as *non-normal* operators (Trefethen *et al.*, 1993; Trefethen, 1997). Schmid and Henningson (2001) studied the evolution of a perturbation in a viscous fluid as an initial value problem. They showed that the superposition of two exponentially decaying disturbances can generate algebraic—or *transient*—growth in time. While each eigenvector individually decreases exponentially over time according to the eigenvalues behaviour, their

combination increases in length before decaying exponentially according to the largest eigenvalue. This is illustrated in fig. 1.10 and shows that transient amplification of disturbances over short times comes from the non-orthogonality of the eigenfunction basis.

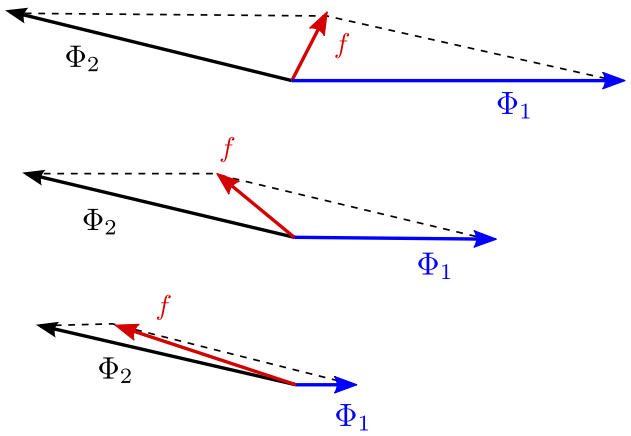


Figure 1.10: Illustration of transient growth due to the combination of non-orthogonal eigenvectors, from Schmid and Henningson (2001). The vector $f$ is defined as the sum of the eigenvectors $\Phi_1 + \Phi_2$: both $\Phi_1$ and $\Phi_2$ decrease, but $f$ strongly increases in length.

### 1.3.2 Stability of non-normal operators

Considering the Navier-Stokes equations linearised about the base flow, the initial value problem can be written as

$$\frac{\mathrm{d}}{\mathrm{d}t}\boldsymbol{q} = \mathcal{L}\boldsymbol{q}. \tag{1.16}$$

The solution can be written as

$$\boldsymbol{q} = \exp(t\mathcal{L})\boldsymbol{q}_0, \tag{1.17}$$

with $q_0$ the initial condition propagated in time by the operator exponential. Schmid (2001) determined a lower and upper bound of the operator exponential norm. As the energy cannot decay at a faster rate than that given by the least stable eigenvalue $\lambda_{\max}$, the lower bound is given by the least stable mode. The upper bound is obtained by diagonalising the operator exponential and using the triangle inequality to split the norm,

$$\|\exp(t\mathcal{L})\| = \|\exp(t\mathcal{S}\Lambda\mathcal{S}^{-1})\| \leqslant \|\mathcal{S}\|\|\mathcal{S}^{-1}\|\exp(t\lambda_{\max}), \tag{1.18}$$

where $\Lambda$ represents the diagonal operator of eigenvalues and $\mathcal{S}$ is the matrix of the eigenvectors. The term $\|\mathcal{S}\|\|\mathcal{S}^{-1}\| = \mathcal{K}(\mathcal{S})$ is referred to as the *condition number* of $\mathcal{S}$ and is equal or larger to 1. If the condition number of $\mathcal{S}$ is equal to 1, the operator $\mathcal{L}$ is normal and the lower and upper bounds coincide so that the energy amplification is governed by the least stable mode. If the condition number of $\mathcal{S}$ is larger than 1, the least stable eigenvalue only governs the energy amplification at large times.

To describe the dynamics over short times, Schmid and Henningson (2001) as well as Trefethen and Embree (2005) expanded the energy growth rate about $t = 0^+$,

$$\frac{1}{E}\frac{\mathrm{d}E}{\mathrm{d}t}\bigg|_{t=0^+} = \frac{\langle \boldsymbol{q}_0, (\mathcal{L}+\mathcal{L}^+)\boldsymbol{q}_0\rangle}{\langle \boldsymbol{q}_0, \boldsymbol{q}_0\rangle} = \lambda_{\max}(\mathcal{L}+\mathcal{L}^+), \tag{1.19}$$

where $\mathcal{L}^+$ is the adjoint operator defined according to the given inner product $\langle a, b\rangle$. The quantity $\lambda_{\max}(\mathcal{L}+\mathcal{L}^+)$ is known as the *numerical abscissa*. The sign of the numerical abscissa determines whether the energy will grow or decay (Schmid, 2007). It can be generalised by considering the *numerical range* (also called *field of values*), which is the set in the complex plane of all Rayleigh quotients of $\mathcal{L}$,

$$\mathcal{F}(\mathcal{L}) = \left\{ z \in \mathbb{C} : z = \frac{\langle \boldsymbol{q}, \mathcal{L}\boldsymbol{q}\rangle}{\langle \boldsymbol{q}, \boldsymbol{q}\rangle} \right\}. \tag{1.20}$$

The numerical abscissa is the Rayleigh quotient of $\mathcal{L}+\mathcal{L}^+$ and coincides with the maximum real part of the numerical range. The maximum energy growth rate over very short times ($t = 0^+$) is given by the largest eigenvalue of the normal operator $\mathcal{L}+\mathcal{L}^+$, which corresponds to the maximum protrusion of the numerical range into the unstable domain.

To study the potential for transient growth for intermediate times, the notion of spectra for operators can be extended based on the resolvent norm of the linear operator. The $\epsilon$-pseudospectrum is defined to measure the sensitivity of the eigenvalues of a non-normal operator to a perturbation (Trefethen, 1991, 1997). A complex $z$ is in the spectrum of the operator $\mathcal{A}$ if there is no bounded inverse of $zI - \mathcal{A}$ (where $I$ denotes the identity). This definition can be extended by measuring if $(zI - \mathcal{A})^{-1}$, the resolvent of $\mathcal{A}$ at $z$, is small or large instead of just checking for its existence. The $\epsilon$-pseudospectrum can be defined as the set in the complex plane parametrised by $\epsilon$ where the resolvent norm $\|(zI - \mathcal{A})^{-1}\|$ is larger than $1/\epsilon$,

$$\Lambda_\epsilon = \left\{ z \in \mathbb{C} : \|(zI - \mathcal{A})^{-1}\| \geqslant \epsilon^{-1} \right\}. \tag{1.21}$$

The 0-pseudospectrum is the spectrum of $\mathcal{A}$ and, for $\epsilon > 0$, $\Lambda_\epsilon$ is the larger set of the complex plane bounded by the $\epsilon^{-1}$ level curves, or similarly curves of the resolvent norm. Measuring how far the contours of the resolvent norm extend into the unstable domain indicates a lower bound for the maximum attainable transient growth in time. The Kreiss constant $\kappa$ can be used to determine precisely this lower bound, *i.e.* $\max_{t>0} G(t) \geq \kappa^2$ (Trefethen and Embree, 2005).

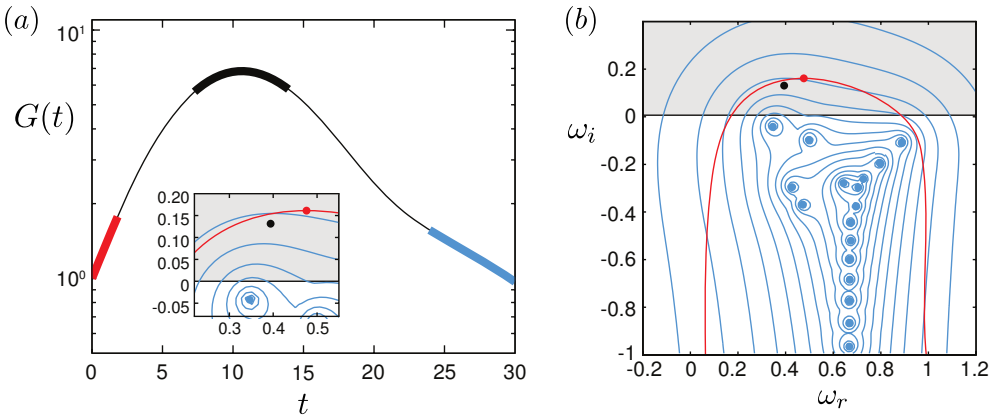


Figure 1.11: Transient growth of perturbation energy for two-dimensional plane Poiseuille flow at Reynolds number $Re = 1000$ and $\alpha = 1$, from Schmid (2007). (*a*) shows energy growth over time and illustrates the significance of the various spectral variables featured in (*b*) on the temporal evolution of the energy growth. (*b*) displays contour plots of the resolvent norm (blue lines). The eigenvalues $\omega$ (blue dots) are confined to the stable domain. The red line denotes the boundary of the numerical range and the red dot represents the numerical abscissa. The black dot indicates the location in the complex plane that results in the Kreiss constant.

The $\epsilon$-pseudospectrum of $\mathcal{A}$ can equally be viewed as the spectrum of the perturbed operator $\mathcal{A}+\mathcal{E}$, with $\mathcal{E}$ a random disturbance of norm $\epsilon$. For well-conditioned eigenvalue problems,

small perturbations of the operator are supposed to have a small effect on the spectrum. In that sense, pseudospectra provide a measure of the sensitivity of the eigenvalues, with highly sensitive eigenvalues being characteristic of non-normal operators.
In order to compute pseudospectra, another definition can be used:

$$\Lambda_\epsilon = \{z \in \mathbb{C} : \sigma_{\min}(zI - \mathcal{A}) \leqslant \epsilon\}, \tag{1.22}$$

where $\sigma_{\min}(zI - \mathcal{A})$ denotes the smallest singular value of $zI - \mathcal{A}$. This means that pseudospectra are the sets in the complex plane bounded by contour curves of $\sigma_{\min}(zI - \mathcal{A})$ (Trefethen, 1999). Computing pseudospectra can be done by evaluating the minimum singular value on a grid in the complex plane and generating contour lines of this quantity.

These sets of variables are illustrated in fig. 1.11 for two-dimensional plane Poiseuille flow (Schmid, 2007). The eigenvalues are displayed as blue dots and are all confined in the stable domain, predicting asymptotic decay given by the least stable eigenvalue. The red line indicates the boundary of the numerical range which extends into the unstable domain, indicating that transient energy growth is to be expected over small times. The numerical abscissa is represented by the red dot, measuring the maximum protrusion of the numerical range into the unstable domain. This numerical abscissa gives the slope of the initial maximum energy growth $G(t)$. A lower estimate for the peak of energy amplification is given by the square of the Kreiss constant, indicated by a black dot.

## 1.4 Transient growth in shear flows

### 1.4.1 Experimental studies and temporal transient growth

Ellingsen and Palm (1975) introduced a low-amplitude longitudinal vortex in a two-dimensional boundary layer and showed that streamwise velocity fluctuations could be created that grow linearly with time. This leads to the formation of elongated structures in the boundary layer consisting of spanwise-alternating low and high velocity streaks. The physical mechanism responsible for the formation of these streaks has been explained by Landahl (1980) and is referred to as the *lift-up* effect. The interaction between a longitudinal vortex and the shear layer lifts up low-velocity fluid particles from the wall and push down high-velocity fluid toward the wall. These fluid particles initially retain their horizontal momentum while being displaced in the wall-normal direction, leading to the formation of streamwise velocity fluctuations, also known as *Klebanoff modes* (Kendall, 1985). This physical interpretation is illustrated in fig. 1.12.

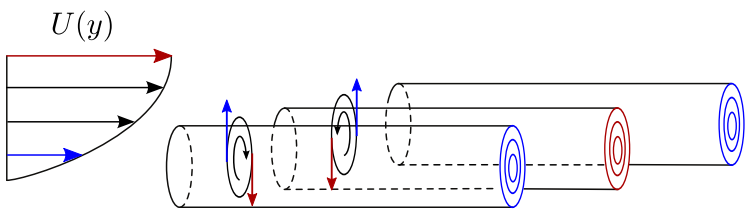


Figure 1.12: Illustration of the lift-up effect: the interaction between the shear flow and a longitudinal vortex leads to the formation of alternating low (blue lines) and high (red lines) velocity streaks.

Butler and Farrell (1992) also highlighted another physical mechanism responsible for non-modal growth in shear flows, which they called the Reynolds stress mechanism and is also known as the

*Orr mechanism* (Orr, 1907). A disturbance can extract energy from the mean shear by transporting momentum down the mean momentum gradient through the action of the perturbation Reynolds stress. This means that structures that are tilted against the shear will rise to an upright position while borrowing energy from the mean flow. This is done via the Reynolds stress production term $\int -\overline{uv}U_y \, \mathrm{d}y$, where $\overline{uv}$ represents the average along the normal direction $y$ of the product of the streamwise and crossflow velocities, and $U_y$ denotes the mean flow shear. Eventually, the disturbances start to lose their energy to the mean flow while they are tilted to align with the base flow vorticity, as depicted in fig. 1.13. Akervik *et al.* (2008) found this mechanism to optimally excite TS waves. However, in Blasius boundary layers, this mechanism is weak compared with the lift-up effect.

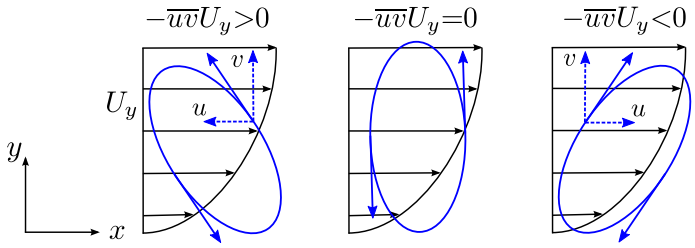


Figure 1.13: Illustration of the Orr mechanism.

Hultgren and Gustavsson (1981) showed that streamwise disturbances could also be amplified in viscous fluids where they eventually decay because of viscous dissipation. The combination of the lift-up mechanism with the viscous damping produces what has then been labelled transient growth. Numerous experiments on boundary layers subjected to free-stream turbulence emphasised the role of streaks to trigger transition, *e.g.* Klebanoff *et al.* (1962); Klebanoff (1971); Gulyaev *et al.* (1989). Experiments by Matsubara and Alfredsson (2001) (see fig. 1.14) showed that streaks develop a streamwise waviness of relatively short wavelength in the case of low turbulence level ((*a*) and (*b*)), leading to the formation of turbulent spots. For the high turbulence cases ((*c*) and (*d*)), streaks also exhibit a wavy type of motion, albeit of larger spanwise scale, before breaking down to turbulence. In these cases however, turbulent spots cannot be as easily identified.

Transient growth has been extensively studied in the temporal framework within the parallel-flow approximation. Most notably are the studies of incompressible flows by Hultgren and Gustavsson (1981); Gustavsson (1991); Butler and Farrell (1992); Reddy and Henningson (1993) and Henningson *et al.* (1993). The parallel-flow approximation employed in these papers allows an explicit computation of the maximum transient growth and the associated initial perturbations, as detailed in section 2.2.2. Many studies in meteorology also focused on the transient growth phenomenon. In particular, Farrell (1988) coined the term *optimal perturbations* to refer to the initial flow disturbances that produce the maximum gain, where the gain is defined as the ratio between disturbance kinetic energies at the final and initial times. The associated transient growth is then called *optimal growth*.

### 1.4.2 Spatial optimal growth in two-dimensional boundary layers

The problem of computing the spatial optimal growth within the scope of the linearised Navier-Stokes equations is radically different and constitutes an ill-posed initial value problem. The problem comes from the presence of modes with an arbitrary large negative imaginary part of the streamwise wavenumber, which take the form of branches of the continuous spectrum for

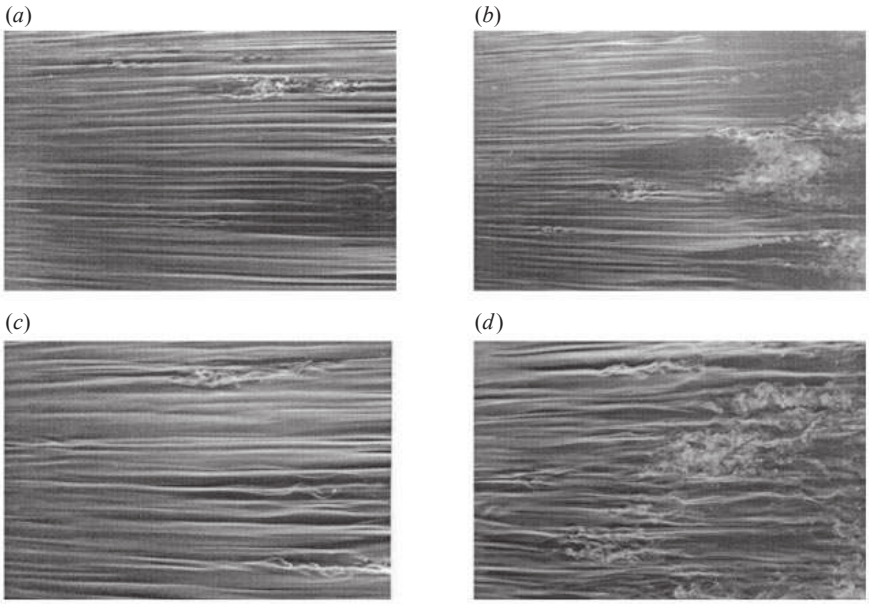


Figure 1.14: Smoke visualisation of streaks in boundary layers subjected to free-stream turbulence, from Matsubara and Alfredsson (2001). The flow direction is from left to right. Turbulence level is 1.5% ((*a*) with $U_\infty = 6\,\mathrm{m\,s^{-1}}$, and (*b*) with $U_\infty = 8\,\mathrm{m\,s^{-1}}$) and 6.6% ((*c*) with $U_\infty = 2\,\mathrm{m\,s^{-1}}$, and (*d*) with $U_\infty = 3\,\mathrm{m\,s^{-1}}$). The streamwise extent of pictures is $220\mathrm{mm} < x < 700\mathrm{mm}$.

boundary-layer flows. Tumin and Reshotko (2001) showed that these modes are associated with the flow response upstream of the disturbance source. They selected the downstream eigenmodes and applied the temporal analysis method for a parallel boundary-layer flow. They found that the maximum transient growth is associated with steady streamwise vortices.

Andersson *et al.* (1999) and Luchini (2000) first included non-parallel effects in the study of spatial optimal growth in the Blasius boundary layer. They considered the linearised boundary-layer equations instead of the Navier-Stokes equations. They used two reference lengths, namely the length of the plate $L$ in the streamwise direction, and a boundary-layer scale $\delta = \sqrt{\nu L/U_\infty}$ in the normal direction, where $\nu$ is the kinematic viscosity and $U_\infty$ is the free-stream velocity. This leads to a parabolic system, where an initial condition can be marched downstream. The optimisation problem is solved using iterations of the direct/adjoint system, as detailed in section 2.2.3. As Tumin and Reshotko (2001), Andersson *et al.* (1999) and Luchini (2000) found that the optimal perturbation consisted of stationary streamwise vortices leading to the formation of streamwise streaks, as illustrated in figs. 1.15 and 1.16. For an incompressible flat plate, the maximum transient growth is found in the steady case (frequency $\omega = 0$) and for a dimensionless spanwise wavenumber[2] $\beta = \beta_\mathrm{d}\delta = 0.45$ (Biau, 2006). Tumin and Ashpis (2003) considered the influence of the pressure gradient on transient growth. They found that an unfavourable pressure gradient increases the non-modal growth while a favourable pressure gradient has a stabilising effect.

Hanifi *et al.* (1996) extended the study to two-dimensional compressible boundary layers within the temporal framework. Their results were similar to the incompressible case, with streamwise vortices giving rise to streaks through the lift-up effect. They also showed that only discrete modes close to the origin of the $\omega$ phase plane were responsible for transient growth. Tumin and Reshotko (2001) studied the spatial optimal growth in compressible boundary layers within the parallel-flow

[2]The subscript d refers to dimensioned quantities.

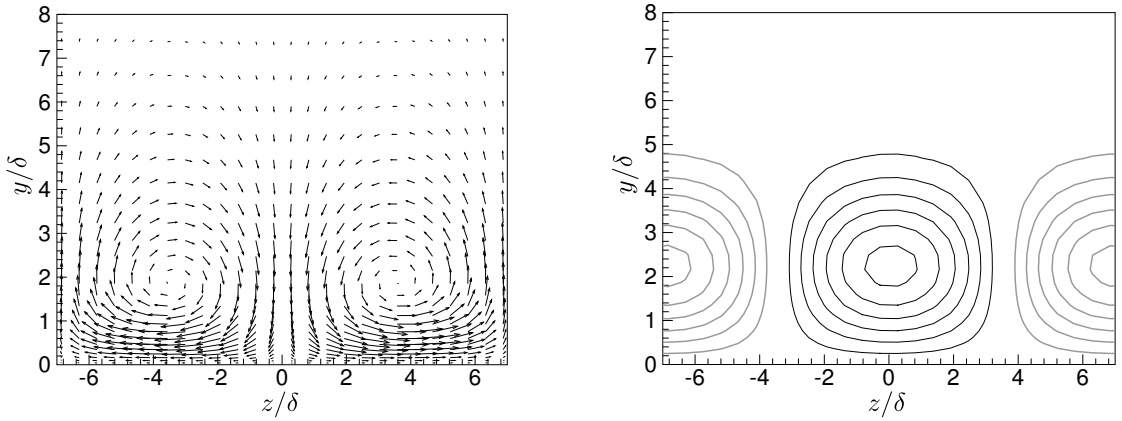


(a) Initial optimal perturbation at $x_{\text{in}} = 0$. (b) Resulting disturbance at $x_{\text{out}} = 1$.

Figure 1.15: Vector representation of the optimal perturbation and downstream contours of positive (black) and negative (gray) streamwise disturbance velocity, in projection onto the crossflow plane ($z$,$y$) for an incompressible Blasius boundary layer with $\beta = 0.45$ and $\omega = 0$.

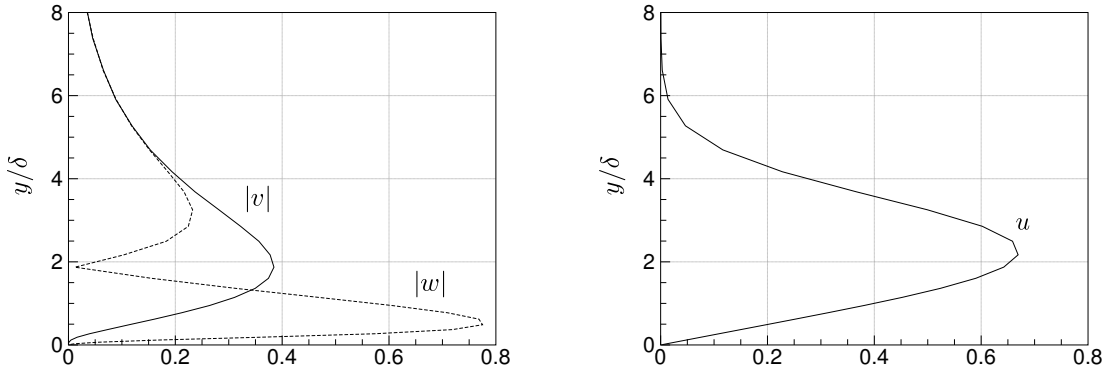


(a) Initial optimal perturbation at $x_{\text{in}} = 0$, $u = 0$ (b) Resulting disturbance at $x_{\text{out}} = 1$, $v = w = 0$.

Figure 1.16: Optimal perturbation and outlet disturbance velocity profiles for an incompressible Blasius boundary layer with $\beta = 0.45$ and $\omega = 0$.

approximation. They later took non-parallel effects into account (Tumin and Reshotko, 2003). They confirmed the formation in the boundary layer of velocity streaks as well as temperature streaks. They also found that the wall temperature significantly affects the structure and amplitude of the streaks. Vermeersch (2009) also studied spatial optimal growth in compressible boundary layers. Cooling the wall so that $T_{\text{wall}}/T_{\text{adiabatic}} = 0.25$ is found to increase the amplification of the perturbations: at $\beta = 0.45$, the gain is multiplied by 8 compared to the adiabatic case. The opposite evolution is observed for Tollmien-Schlichting waves, where heating has a destabilising effect.

### 1.4.3 Optimal growth of Görtler vortices

Cossu *et al.* (2000) first employed an optimal approach to compute the maximum spatial growth rate of Görtler vortices over a concave wall. Their method is based on the computation of a discrete approximation of the spatial propagator which relates the downstream response to the perturbation at the inlet. In particular, the similarities of the inlet optimal perturbations and their resulting responses between the Görtler problem and the case of a flat plate (corresponding to a Görtler

number set to zero) studied by Andersson *et al.* (1999) and Luchini (2000) are emphasised.
Recent computations by means of direct numerical simulation (DNS) by Schrader *et al.* (2011) compared the generation of Görtler vortices by localised roughness and vortical modes. The latter are more efficient as the boundary layer is found to be most receptive to zero- and low-frequency free-stream vortices that excite steady or slowly travelling Görtler vortices. The connection between transient growth and exponential amplification is also pointed out, with rapid non-modal growth near the leading edge and the evolution of boundary layer streaks into Görtler vortices (a specific feature of curved walls for two-dimensional flows).

### 1.4.4 Three-dimensional boundary layers

Breuer and Kuraishi (1994) first studied temporal non-modal growth in three-dimensional boundary layers. They showed that this type of boundary-layer flows could also sustain significant transient growth and studied the effects of the Hartree parameter, Reynolds number, spanwise wavenumber and sweep angle. Their work considers the growth of individual Fourier modes where the normal vorticity is set to zero, which constitutes near-optimal initial conditions. Corbett and Bottaro (2001) later studied the optimal growth in three-dimensional Falkner-Skan-Cooke boundary layers in the temporal framework. Modal and non-modal amplifications are observed for similar disturbances structures, contrary to the two-dimensional case where Tollmien-Schlichting waves bear no resemblance to the Klebanoff modes (Corbett and Bottaro, 2000). They found that optimal perturbations initially take the form of vortices which are almost aligned with the external streamline. These vortices later evolve into streaks further downstream. Corbett and Bottaro (2001) also compared the algebraically growing disturbances with the most unstable crossflow eigenmode. From the similarities they observed, they concluded that transient growth in swept-wing flow might complement exponential amplification by providing an initial amplitude for modal disturbances. This constitutes what they called a preferential receptivity path for exciting modal CF disturbances.

However, the temporal analysis does not allow the study of the downstream development of disturbances as they evolve from sub-critical conditions (*i.e.* experiencing transient growth) to super-critical conditions (*i.e.* undergoing exponential amplification). Pralits *et al.* (2007) described two different approaches to compute spatial optimal disturbances in quasi three-dimensional flows, namely a *single-mode approach* and a *PSE approach*.
The single-mode approach builds on the work of Corbett and Bottaro (2001) and the existence of one dominating mode. Pralits *et al.* (2007) noted that the gain obtained from the optimal perturbation evolves with an exponential behaviour after a short region of non-modal growth. This means that the gain for large times can be computed based on a modal analysis. The modal growth is then shifted to account for the initial non-modal growth. This approach can be extended to the spatial framework using the multiple scales analysis. The optimal initial condition and the associated initial amplification of the dominating mode are given by the eigenvectors of the adjoint stability problem (Hill, 1995). However, this approach only captures the final amplification of the disturbances and the initial phase of transient growth is not described. The application to sub-critical regions (*i.e.* stable regions regarding modal amplification, hence without a dominating mode) represents another inconvenient.

The second approach (Byström, 2007) is based on the parabolised stability equations. A set of parabolic equations is obtained using a scaling proposed by Levin and Henningson (2003) that accounts for the algebraic growth of disturbances. In three-dimensional flows, disturbances tend to be aligned with the external streamline. This means that the streamwise wavenumber is set

to zero, reducing the problem to a two-dimensional flow in the streamwise direction. Byström (2007) formulated the equations in a non-orthogonal coordinate system where the first axis is aligned with the external streamline. However, the disturbances are not perfectly aligned with this external streamline, which is equivalent to neglecting a non-zero streamwise wavenumber. Upon integrating over long distances, this can lead to cumulated errors in the calculated gain. The correct propagation direction of the disturbances has to be determined to correctly align the coordinate system. This disturbance path is referred to as the *streakline* and chosen to follow the maximum of streamwise disturbance velocity.
This streakline is determined iteratively: the external streamline constitutes a first approximation as the integration path, and the optimal perturbation is computed using a direct/adjoint optimisation. The new streakline can be computed from the spatial development of the initial disturbance, and the procedure is repeated until the streakline is fixed. In the small upstream part over the first locations, the streakline is not well defined as the streamwise velocity does not yet transport the major part of the energy (*i.e.* the streak is not completely developed). Different definitions of the streakline have been considered by Byström (2007) which give similar results.

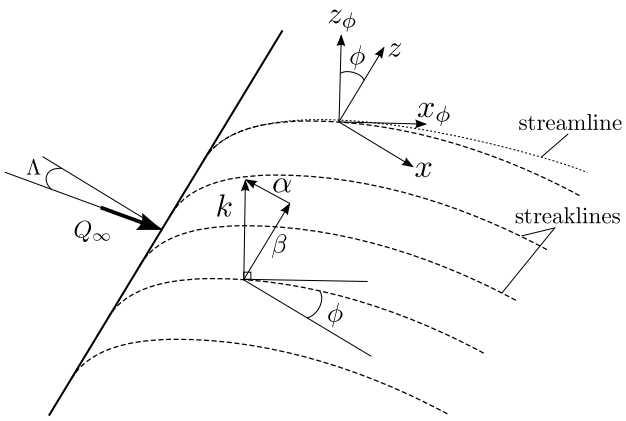


Figure 1.17: Flow over an infinite flat plate subject to a pressure gradient, with a sweep angle $\Lambda$ and an upcoming flow $Q_\infty$. The wing-based coordinate system $(x,z)$ and the orthogonal coordinate system aligned with the streakline $(x_\phi,z_\phi)$ are illustrated. Calculation from Byström (2007) were performed in the non-orthogonal coordinate system $(x_\phi,z)$. The wave vector $\boldsymbol{k} = (\alpha,\beta)^T$ is also represented. The streaklines are not perfectly aligned with the external streamline.

Optimal perturbations for a boundary-layer flow over a flat plate with a sweep angle and subject to a pressure gradient are found to take the form of counter-rotating vortices in projection onto the crossflow plane, as can be seen in fig. 1.18. For a sweep angle $\Lambda = 45°$ optimal spanwise wavenumbers are $\beta = 0.54$ in the accelerated flow (with a Hartree parameter $\beta_H = 0.1$) and $\beta = 0.57$ in the retarded flow ($\beta_H = -0.05$) for a Reynolds number $Re = 10^6$. Contrary to optimal perturbations in two-dimensional boundary layers, the vortices are not symmetrical about the wall-normal axis but are tilted against the mean crossflow shear, with the direction of the tilting changing while evolving downstream. The tilting is also opposite for accelerated and retarded flow (as the crossflow component of the Falkner-Skan-Cooke solution changes for favourable or adverse pressure gradient). The physical mechanisms responsible for transient growth in three-dimensional boundary layers consists in a combination of the lift-up effect and the Orr-mechanism (see section 1.4.1).

Byström (2007) also studied the spatial development of disturbances with non-modal growth followed by exponential amplification. Optimal perturbations are shown to evolve into crossflow modes, which leads to the conclusions that the same physical mechanism is responsible for non-modal and

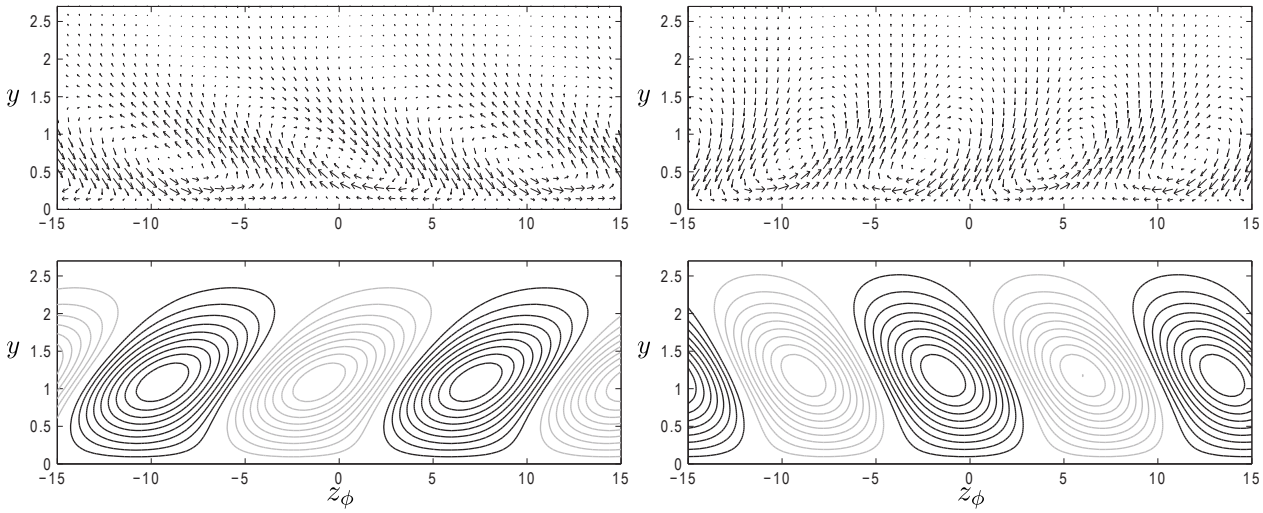


(a) Favorable pressure gradient, $\beta_H = 0.1$.

(b) Adverse pressure gradient, $\beta_H = -0.05$.

Figure 1.18: Vector representation of optimal perturbations and downstream contours of positive (black) and negative (gray) streamwise disturbance velocity, in projection onto the crossflow plane ($z_\phi$,$y$). From Byström (2007).

exponential growth and that non-modal growth gives an initial amplitude to the crossflow instability.

Tempelmann *et al.* (2010) used a similar approach to study the spatial optimal growth in a Falkner-Skan-Cooke boundary layer over a flat plate. The equations are formulated in a Cartesian coordinate system aligned with the plate (see fig. 1.17). Hence, the streamwise wavenumber is no longer set to zero and has to be determined. In order to do so, Tempelmann *et al.* used the PSE decomposition eq. (1.8a). However, contrary to the PSE formulation, the amplification of the perturbation is chosen to be completely absorbed in the shape function (hence the imaginary part of the chordwise wavenumber is set to zero). The real part of the chordwise wavenumber is then determined based on the line of constant phase of the maximum of streamwise disturbance velocity. It is important to note that this method is restricted to the study of disturbances whose lines of constant phase are closely aligned with the external streamline. Therefore, the amplification of Tollmien-Schlichting waves in two-dimensional boundary layers cannot be recovered. It should also be noted that the method is limited to flows which exhibit moderate exponential growth.
Tempelmann *et al.* (2010) performed a parametric study to investigate the effects of the pressure gradient, sweep angle and inlet location for the optimal perturbation. In particular, non-modal growth is found to be more important at small sweep angles. They also determined optimal growth for non-stationary disturbances, optimising the initial disturbance with respect to the spanwise wavenumber, frequency and inlet position. These results will be detailed and used for comparison in (ref chapitre 3D).
Tempelmann *et al.* (2012) later extended the modified PSE to account for compressibility and curvature effects. They studied boundary-layer flows over swept flat plates with both adiabatic and cooled walls as well as flows over swept curved walls with convex and concave curvature. As in two-dimensional boundary layers, cooling the wall strongly increases non-modal growth while stabilising crossflow modes. Concave curvature is found to destabilise modal and non-modal disturbances, with a more pronounced impact on the former.

Different instability mechanisms can be found in two- and three-dimensional boundary layers. Modal stability analysis, both local and non-local, describes the asymptotic behaviour of the flow according to the least stable mode. Transition prediction methods such as the $e^N$ method are based on this modal analysis. However, when the external disturbance level is sufficient, transient growth starts playing a role in the transition process. This phenomenon comes from interactions between non-orthogonal modes. A possible scenario that will be of importance for the rest of this work consists of an initial phase of transient growth prior to modal amplification. In particular, the relation between Klebanoff modes and Görtler vortices will be investigated. The problem of determining the neutral curve for the Görtler problem has been highlighted and will be tackled by taking non-modal growth into account. In three-dimensional boundary layers, the connection between transient growth and crossflow modes will also be studied.
In addition, the mechanisms involved in transient growth for two- and three-dimensional boundary layers have been detailed. In particular, the concept of optimal perturbations—*i.e.* the worst case scenario with respect to the transition—has been introduced. The next chapter will focus on the determination of such optimal initial disturbances.

Chapter 2

# Determination of optimal perturbations

This chapter presents the method for computing optimal perturbations, *i.e.* initial disturbances associated with maximum energy growth in the boundary layer. The Navier-Stokes equations are first linearised about the mean flow and made dimensionless to obtain the parabolised equations for the disturbances. The determination of the optimal perturbation is detailed in the simplified case of a parallel flow where the gain and optimal perturbation are readily accessible through a singular-value decomposition. Then, the general case of a non-parallel flow is considered and the iterative direct/adjoint method for computing the optimal perturbation is presented. The derivation of the continuous adjoint equations via a Lagrange formulation is detailed, before moving to the determination of their discrete counterpart for numerical purposes. Finally, discretisation in the chordwise and wall-normal directions is presented along with the numerical schemes used to solve the direct and adjoint problems.

## Contents

## 2.1 Equations for small disturbances

Transition in boundary layers occurs from the amplification of small disturbances, either of modal or non-modal nature. The Navier-Stokes equations are the starting point for the study of these disturbances. The flow is decomposed into a mean flow $\boldsymbol{Q} = (U, V, W, P)^T$ and small disturbances $\boldsymbol{q'} = (u', v', w', p')^T$. Subtracting the equations for the mean flow and neglecting the quadratic terms of the disturbances then leads to the equations for the small disturbances. For an incompressible flow, these equations can be formulated as

$$\begin{aligned} \nabla \cdot \boldsymbol{u'} &= 0, \\ \frac{\partial \boldsymbol{u'}}{\partial t} + (\boldsymbol{u'} \cdot \nabla)\boldsymbol{U} &= -\frac{1}{\rho}\nabla p' + \nu \nabla^2 \boldsymbol{u'}. \end{aligned} \tag{2.1}$$

In eq. (2.1), $\boldsymbol{U} = (U, V, W)^T$ represents the mean velocity vector and $\boldsymbol{u'} = (u', v', w')^T$ the associated disturbances ; $p'$ is the pressure disturbance, $\rho$ the density and $\nu$ the kinematic viscosity.
These equations can be written in a non-dimensioned form to compare the relative order of the terms and identify dominating phenomena. Characteristic length scales are thus defined to obtain dimensionless variables.
Boundary-layer scaling originates from Prandtl (1904) who first used two different length scales, namely a reference length $L$ in the chordwise direction (*e.g.* the chord) and a boundary-layer length scale $\delta$ in the wall-normal direction.
Hence, the chordwise direction $x$ is made dimensionless with respect to $L$, while the normal and spanwise directions $y$ and $z$ are rescaled by $\delta = Re_L^{-1/2} L$, where $Re_L$ is the Reynolds number based on the reference length $L$. The base-flow velocity $U$ and the associated disturbance $u'$ are scaled with the external velocity $U_\infty$. The continuity equation for the mean flow (and respectively for the disturbances) then implies that $V$ and $W$ (respectively $v'$ and $w'$) are scaled with $U_\infty/\sqrt{Re_L}$. The pressure perturbation $p'$ is scaled with $\rho_\infty U_\infty^2/Re_L$. Diffusion terms in the chordwise direction (*i.e.* terms $\partial_{xx}$) can be neglected. The chordwise pressure gradient also has to be neglected in order to obtain parabolic equations.

| $x$ | $y$ | $U$, $u'$ | $V$, $v'$, $w'$ | $P$, $p'$ | $\omega$ |
|---|---|---|---|---|---|
| $L$ | $\delta = \frac{L}{\sqrt{Re_L}}$ | $U_\infty$ | $\frac{U_\infty}{\sqrt{Re_L}}$ | $\frac{\rho_\infty U_\infty^2}{Re_L}$ | $\frac{U_\infty}{L}$ |

Table 2.1: Boundary-layer scaling for a two-dimensional incompressible base-flow.

Linearising the incompressible Navier-Stokes equations around a two-dimensional mean flow $(U(x,y), V(x,y), 0)$ for three-dimensional disturbances $\boldsymbol{q'}(x,y,z,t)$ leads to

$$\begin{aligned} &u'_x + v'_y + w'_z = 0, \\ &u'_t + U u'_x + V u'_y + u' U_x + v' U_y = u'_{yy} + u'_{zz}, \\ &v'_t + U v'_x + V u'_y + u' V_x + v' V_y = -p'_y + v'_{yy} + v'_{zz}, \\ &w'_t + U w'_x + V w'_y = -p'_z + w'_{yy} + w'_{zz}. \end{aligned} \tag{2.2}$$

Coefficients in eq. (2.2) are independent of the spanwise direction $z$. Perturbations can be written as

$$\boldsymbol{q'}(x,y,z,t) = \boldsymbol{q}(x,y) e^{i(\beta z - \omega t)}. \tag{2.3}$$

Introducing eq. (2.3) into eq. (2.2) yields

$$u_x + v_y + i\beta w = 0, \tag{2.4a}$$
$$-i\omega u + Uu_x + Vu_y + uU_x + vU_y = u_{yy} - \beta^2 u, \tag{2.4b}$$
$$-i\omega v + Uv_x + Vv_y + uV_x + vV_y + p_y = v_{yy} - \beta^2 v, \tag{2.4c}$$
$$-i\omega w + Uw_x + Vw_y + i\beta p = w_{yy} - \beta^2 w. \tag{2.4d}$$

We are interested in solution to eq. (2.2) satisfying a no-slip condition at the wall and vanishing at infinity in the wall-normal direction. In practice, the wall-normal direction is bounded to $[0, y_{\max}]$, where $y_{\max}$ is located sufficiently outside the boundary layer (usually defined as $y_{\max} = 6\delta_{99}$, where $\delta_{99}$ denotes the edge of the boundary layer). Boundary conditions are thus introduced at $y = 0$ and $y = y_{\max}$ according to

$$u = v = w = 0 \quad \text{at } y = 0, \tag{2.5a}$$
$$u = w = p = 0 \quad \text{at } y = y_{\max}. \tag{2.5b}$$

As eq. (2.4) are parabolic in the chordwise direction, this constitutes an initial-value problem which can be solved using a marching technique to obtain the downstream development of a given initial disturbance. Equation (2.4) can also be written in a compact form

$$\mathcal{L}\boldsymbol{q} = 0, \tag{2.6}$$

where $\mathcal{L}$ is a linear operator which can be expanded in the form

$$\mathcal{L} = \mathcal{A} + \mathcal{B}\frac{\partial}{\partial y} + \mathcal{C}\frac{\partial^2}{\partial y^2} + \mathcal{D}\frac{\partial}{\partial x}. \tag{2.7}$$

## 2.2 Optimal perturbations and maximum gain

### 2.2.1 Input-output analysis

Adopting an input-output point of view, the initial value problem of eq. (2.6) can be modelled as

$$\boldsymbol{q}_{\text{out}} = \mathcal{P}\boldsymbol{q}_{\text{in}}, \tag{2.8}$$

for some output $\boldsymbol{q}_{\text{out}}$ at a location $x_{\text{out}}$ and initial disturbance $\boldsymbol{q}_{\text{in}}$ at $x_{\text{in}}$ ; $\mathcal{P}$ is a linear operator called the *spatial propagator*.

The linearised boundary layer can be viewed as an amplifier of velocity disturbances applied at its input. The question then arises of the maximum gain—*i.e.* maximum ratio of output to input energy—which can be attained. The corresponding initial input then constitutes the optimal perturbation. Luchini (2000) details the determination of the gain and corresponding optimal perturbation from the spatial propagator.

The initial perturbation is optimised over all initial inputs to give the maximum spatial transient growth,

$$G_{\max} = \max_{\boldsymbol{q}_{\text{in}}} \frac{\|\boldsymbol{q}_{\text{out}}\|^2}{\|\boldsymbol{q}_{\text{in}}\|^2}, \tag{2.9}$$

where $\|\boldsymbol{q}\|$ denotes the norm associated with the scalar product $(\boldsymbol{q}, \boldsymbol{q})$, while the measure of the disturbances energy is given by $E(\boldsymbol{q}) = \|\boldsymbol{q}\|^2$. This scalar product can be defined as $(\boldsymbol{q}, \boldsymbol{q}) = \boldsymbol{q}^* \cdot M \cdot \boldsymbol{q}$,

where $M$ is a given weight matrix[1]. Note that different norms can be defined to measure the disturbance energy, as detailed in section 2.3. In the following, $M$ is chosen as the unit matrix.
Considering a finite dimension problem and using the matrix representation of the spatial propagator, eq. (2.9) can be written as

$$G_{\max} = \max_{\boldsymbol{q}_{\text{in}}} \frac{\boldsymbol{q}_{\text{in}}^* \cdot \mathcal{P}^H \cdot \mathcal{P} \cdot \boldsymbol{q}_{\text{in}}}{\boldsymbol{q}_{\text{in}}^* \cdot \boldsymbol{q}_{\text{in}}}, \tag{2.10}$$

which represents the Rayleigh quotient generated by the self-adjoint operator $\mathcal{P}^H \cdot \mathcal{P}$. As known from matrix algebra, the maximum gain $G_{\max}$ corresponds to the largest eigenvalue of the generalised eigenvalue problem

$$\mathcal{P}^H \cdot \mathcal{P} \cdot \boldsymbol{q}_{\text{in}} = G \boldsymbol{q}_{\text{in}}, \tag{2.11}$$

and the optimal perturbation is the corresponding eigenfunction. The singular value decomposition of $\mathcal{P}$ corresponds to the eigenvalue problem of $\mathcal{P}^H \mathcal{P}$. Thus the maximum gain can equivalently be seen as the square of the largest singular value of the propagator, and the optimal perturbation is the corresponding left singular vector. The determination of the optimal perturbation can be done by power iterations of the form

$$\boldsymbol{q}_{\text{in}}^{(n+1)} = \mathcal{P}^H \cdot \mathcal{P} \cdot \boldsymbol{q}_{\text{in}}^{(n)}, \tag{2.12}$$

which converges to the initial perturbation maximising the gain. When $n$ is large enough, $\boldsymbol{q}_{\text{in}}^{(n+1)}$ is proportional to $\boldsymbol{q}_{\text{in}}^{(n)}$ and the proportionality ratio gives the maximum gain, as can be inferred from eq. (2.11).
As the problem is linear, the definition of the maximum gain can be modified to add a constraint of unit energy:

$$G_{\max} = \max_{\|\boldsymbol{q}_{\text{in}}\|=1} \|\boldsymbol{q}_{\text{out}}\|^2. \tag{2.13}$$

which can be seen as a normalisation condition.
Finally, different expressions for the input/output energy norms can be used, which leads to the following generalisation for the gain

$$G_{\max} = \max_{\boldsymbol{q}_{\text{in}}} \frac{\boldsymbol{q}_{\text{in}}^* \cdot \mathcal{P}^H \cdot Q_{\text{out}} \cdot \mathcal{P} \cdot \boldsymbol{q}_{\text{in}}}{\boldsymbol{q}_{\text{in}}^* \cdot Q_{\text{in}} \cdot \boldsymbol{q}_{\text{in}}}, \tag{2.14}$$

where $E_{\text{in}} = \boldsymbol{q}^* \cdot Q_{\text{in}} \cdot \boldsymbol{q}$ and $E_{\text{out}} = \boldsymbol{q}^* \cdot Q_{\text{out}} \cdot \boldsymbol{q}$.

From this analysis, two different methods can be identified for solving an optimal perturbation problem:

- The spatial propagator is explicitly constructed, and the optimal perturbation is determined through a singular value decomposition as presented above. This is possible under the parallel-flow approximation, as detailed in section 2.2.2.
- The spatial propagator is not known: the parabolic equations for the disturbances are integrated downstream, meaning that the effect of the propagator is determined without its explicit construction. Backward integrations using the adjoint equations allow for power iterations to determine the optimal perturbations. This is a more general method employed for non-parallel flows, as detailed in section 2.2.3.

[1]The superscript * denotes complex conjugate ; a dot product refers to index contraction.

### 2.2.2 Explicit propagator: the parallel-flow approximation

This section uses the parallel-flow approximation, which neglects the growth of the boundary layer. Although this approximation is too restrictive, it allows for an explicit computation of the spatial propagator and simplifies the determination of the optimal perturbation. As the coefficients in the equations for the disturbances do not depend on the chordwise coordinate $x$, perturbations may be written as a sum of normal modes

$$\begin{aligned} \boldsymbol{q}'(x,y,z,t) &= \boldsymbol{q}(x,y)e^{i(\beta z-\omega t)}, \\ \boldsymbol{q}(x,y) &= \sum_k \hat{\boldsymbol{q}}_k(y)e^{i\alpha_k x}. \end{aligned} \tag{2.15}$$

Equation (2.15) means that perturbations are composed of waves of the same spanwise wavelength $2\pi/\beta$ and same angular frequency $\omega$, with a chordwise wavenumber $\alpha_k$ and the associated amplitude $\tilde{\boldsymbol{q}}_k(y)$. Introducing these perturbations in the parabolised Navier-Stokes equations leads to the dispersion relation

$$\forall k, \quad \mathcal{A}(y,\beta,\omega)\ \hat{\boldsymbol{q}}_k(y) = \mathcal{B}(y,\beta,\omega)\ \alpha_k\ \hat{\boldsymbol{q}}_k(y), \tag{2.16}$$

which gives the eigenmodes $\alpha_k$. This approach is identical to the one described in section 1.2.2.1, except that the whole spectrum is now computed instead of focusing only on the least stable mode. The perturbations can now be decomposed onto the base formed by the eigenvectors according to

$$\begin{aligned} &\boldsymbol{q}(x,y) = \sum_k \kappa_k(x)\hat{\boldsymbol{q}}_k(y), \\ &\text{where} \quad \kappa_k(x) = \kappa_k(0)e^{i\alpha_k x}. \end{aligned} \tag{2.17}$$

Using the vector $K$ of the disturbance coordinates in the base of the eigenvectors, this yields

$$K(x) = e^{i\Lambda x}K(0), \tag{2.18}$$

with $\Lambda$ the diagonal matrix of the eigenvalues $\alpha_k$. We define the matrix $\Theta$ of the scalar product of the eigenfunctions

$$\Theta_{kl} = <\hat{\boldsymbol{q}}_k, \hat{\boldsymbol{q}}_l> = \int_0^\infty \hat{\boldsymbol{q}}_k^H M \hat{\boldsymbol{q}}_l \,\mathrm{d}y, \tag{2.19}$$

which is definite positive, so there exists a Choleski decomposition $\Theta = \mathcal{F}^H\mathcal{F}$ where $\mathcal{F}$ is a triangular matrix. The maximum gain can be rewritten in terms of the $L_2$ norm which, using the change of variable $V = \mathcal{F}\boldsymbol{q}$, leads to the Rayleigh quotient:

$$\begin{aligned} G_{\max} &= \max_{\boldsymbol{q}_{\text{in}}} \frac{\|\boldsymbol{q}_{\text{out}}\|^2}{\|\boldsymbol{q}_{\text{in}}\|^2} = \frac{K^H\cdot\Theta_{\text{out}}\cdot K}{K_0^H\cdot\Theta_{\text{in}}\cdot K_0} \\ &= \frac{K_0^H\cdot\mathcal{P}^H\cdot\mathcal{F}_{\text{out}}^H\cdot\mathcal{F}_{\text{out}}\cdot\mathcal{P}\cdot K_0}{K_0^H\cdot\mathcal{F}_{\text{in}}^H\cdot\mathcal{F}_{\text{in}}\cdot K_0} \\ &= \frac{\|\mathcal{F}_{\text{out}}\cdot\mathcal{P}\cdot K_0\|^2}{\|\mathcal{F}_{\text{in}}\cdot K_0\|^2} \\ &= \frac{\|\mathcal{F}_{\text{out}}\cdot\mathcal{P}\cdot\mathcal{F}_{\text{in}}^{-1}V_0\|_2^2}{\|V_0\|_2^2}. \end{aligned} \tag{2.20}$$

The maximum gain is thus the square of the largest singular value of $\mathcal{M} = \mathcal{F}_{\text{out}}\mathcal{P}\mathcal{F}_{\text{in}}^{-1}$. The optimal perturbation $V_{\text{in}}$ is the corresponding singular vector, which can be obtained through power iterations of the form $V^{(n+1)} = \mathcal{M}^H\mathcal{M}\cdot V^{(n)}$. The proportionality coefficient between $V^{(n+1)}$ and $V^{(n)}$

for large $n$ gives the maximum gain.

However, when considering an evolving base flow, the eigenfunctions can no longer be considered local as they depend on the chordwise coordinate $x$. A numerical approximation of the spatial propagator can no longer be assigned in matrix form. A possibility is to calculate a numerical approximation of the propagator by expanding the initial condition in a set of linearly independent base functions. Numerical solutions of the downstream response of each of the base functions can be determined by solving the parabolic system of equations to construct a matrix approximation of the propagator (Cossu *et al.*, 2000). A much more effective method is the use of iterative solutions of the direct and adjoint equations, which is detailed in the next section.

### 2.2.3 Optimal perturbations via the adjoint equations

The backward integration (*i.e.* marching upstream) of the adjoint equations takes approximately the same computational time as the downstream integration of the direct equations. This makes the use of an iterative algorithm of the form of eq. (2.12) an attractive alternative to the explicit computation of the propagator. The product $\mathcal{P}\cdot\boldsymbol{q}_{\text{in}}^{(n)}$ can be easily obtained by solving the parabolic system of equations, propagating a given initial condition $\boldsymbol{q}_{\text{in}}^{(n)}$ downstream. Further multiplication by $\mathcal{P}^H$ represents the result of the backward computation using the adjoint equations, propagating the product $\mathcal{P}\cdot\boldsymbol{q}_{\text{in}}^{(n)}$ upstream from $x = x_{\text{out}}$ to $x = x_{\text{in}}$.

Considering an inner product between two vectors $\boldsymbol{a}$ and $\boldsymbol{b}$, the adjoint $\mathcal{L}^+$ of a given linear operator $\mathcal{L}$ is defined as

$$\langle \boldsymbol{a}, \mathcal{L}\boldsymbol{b}\rangle = \langle \mathcal{L}^+\boldsymbol{a}, \boldsymbol{b}\rangle. \tag{2.21}$$

In order to measure the disturbance energy, the energy norm can be defined as

$$\|\boldsymbol{q}\|^2 = (\boldsymbol{q}, M\boldsymbol{q}), \tag{2.22}$$

for some weight matrix $M$, according to the inner product

$$(\boldsymbol{a}, \boldsymbol{b}) = \int_0^\infty \boldsymbol{a}^H\boldsymbol{b}\,\mathrm{d}y. \tag{2.23}$$

Equation (2.22) gives a local measure of the energy at a specific location $x$. A global measure of the disturbance energy may thus be given by integrating along the spatial domain according to

$$\langle \boldsymbol{q}, M\boldsymbol{q}\rangle = \int_{x_{\text{in}}}^{x_{\text{out}}}\int_0^{y_{\max}} \boldsymbol{q}^H M\boldsymbol{q}\,\mathrm{d}y\,\mathrm{d}x. \tag{2.24}$$

The adjoint equations may be obtained by integrations by parts on the governing equations, as detailed in appendix A.1. However, another method can be used to obtain the adjoint equations when considering the Lagrangian formulation of the optimal growth problem.

The problem of computing the optimal perturbation is a constrained optimisation problem, where the objective is to maximise the energy amplification at a given outlet location while verifying the parabolised boundary layer equations. A suitable objective function can thus be defined as

$$J(\boldsymbol{q}) = \frac{\|\boldsymbol{q}_{\text{out}}\|^2}{\|\boldsymbol{q}_{\text{in}}\|^2}, \tag{2.25}$$

where the disturbance energies are measured at the outlet and inlet locations $x_{\text{out}}$ and $x_{\text{in}}$ respectively. The idea is to enforce the constraints of the state equation via Lagrange multipliers $\boldsymbol{p}$, also called adjoint variables (see appendix A.2). A supplementary condition of unit energy ($E_{\text{in}} = 1$) can be added as the problem is linear. The appropriate Lagrangian function can be formulated as

$$\mathscr{L}(\boldsymbol{q}, \boldsymbol{p}, \lambda_0) = J(\boldsymbol{q}) - \langle \boldsymbol{p}, \mathcal{L}\boldsymbol{q} \rangle - \lambda_0 \left( \int_0^\infty \boldsymbol{q}_{\text{in}}^T M_{\text{in}} \boldsymbol{q}_{\text{in}} \, \mathrm{d}y - E_{\text{in}} \right), \tag{2.26}$$

where the adjoint variable $\boldsymbol{p}$ ensures the Navier-Stokes equations (eq. (2.6)). The Lagrange multiplier $\lambda_0$ ensures that the unit initial energy condition is respected, although in practice the initial disturbance is scaled to obtain a unit energy. The adjoint system can be retrieved by setting to zero the gradient of the Lagrangian with respect to $\boldsymbol{q}$ for all variations $\delta\boldsymbol{q}$:

$$\left\langle \frac{\partial \mathscr{L}}{\partial \boldsymbol{q}}, \delta\boldsymbol{q} \right\rangle = 0 \;\Rightarrow\; -\langle \mathcal{L}^+ \boldsymbol{p}, \delta\boldsymbol{q} \rangle + \text{boundary terms} + \left\langle \frac{\partial \mathscr{L}}{\partial \boldsymbol{q}_{\text{in}}}, \delta\boldsymbol{q}_{\text{in}} \right\rangle - \left\langle \frac{\partial \mathscr{L}}{\partial \boldsymbol{q}_{\text{out}}}, \delta\boldsymbol{q}_{\text{out}} \right\rangle, \tag{2.27}$$

which gives, by setting to zero the first inner product, the adjoint system

$$-\langle \mathcal{L}^+ \boldsymbol{p}, \delta\boldsymbol{q} \rangle = 0 \;\forall \delta\boldsymbol{q} \;\Rightarrow\; \mathcal{L}^+ \boldsymbol{p} = 0. \tag{2.28}$$

As the direct problem (eq. (2.6)), the adjoint system is parabolic, propagating an initial disturbance upstream from $x_{\text{out}}$ to $x_{\text{in}}$. In eq. (2.27), the last two inner products correspond to variations with respect to the initial disturbances at $x_{\text{in}}$ and output disturbance at $x_{\text{out}}$. The boundary terms read (see appendix A.1)

$$\int_{x_{\text{in}}}^{x_{\text{out}}} \left[ \boldsymbol{q}^H \mathcal{B}^H \boldsymbol{p} + \frac{\partial \boldsymbol{q}^H}{\partial y} \mathcal{C}^H \boldsymbol{p} - \boldsymbol{q}^H \frac{\partial}{\partial y} (\mathcal{C}^H \boldsymbol{p}) \right]_0^{y_{\max}} \mathrm{d}x + \int_0^{y_{\max}} \left[ \boldsymbol{q}^H \mathcal{D}^H \boldsymbol{p} \right]_{x_{\text{in}}}^{x_{\text{out}}} \mathrm{d}y, \tag{2.29}$$

where the first integral gives the boundary conditions verified by the adjoint variables $\boldsymbol{p} = (p_1, p_2, p_3, p_4)^T$. Upon enforcing eq. (2.5) in the wall-normal direction, setting the first integral in eq. (2.29) to zero yields

$$p_2 = p_3 = p_4 = 0 \quad \text{at } y = 0, \tag{2.30a}$$

$$p_1 + 2V p_3 + p_{3,y} = p_2 = p_4 = 0 \quad \text{at } y = y_{\max}. \tag{2.30b}$$

The components of $\boldsymbol{p}$ can be interpreted as velocity- and pressure-like adjoint variables, denoting $\boldsymbol{p} = (p^+, u^+, v^+, w^+)^T$, which leads to

$$u^+ = v^+ = w^+ = 0 \quad \text{at } y = 0, \tag{2.31a}$$

$$p^+ = u^+ = w^+ = 0 \quad \text{at } y = y_{\max}. \tag{2.31b}$$

The second integral in eq. (2.29) contributes to the optimality conditions. Together with the last two inner products of eq. (2.27)—which hold the contribution of the variation of the cost function with respect to $\boldsymbol{q}_{\text{in}}$ and $\boldsymbol{q}_{\text{out}}$—they link the output of the direct system to the initial condition for the adjoint system, and conversely the output of the adjoint system to the initial condition for the direct equations.

We can now determine the optimal perturbation with the following iterative algorithm:

1. An arbitrary initial disturbance $\boldsymbol{q}_{\text{in}}^{(0)}$ is chosen which satisfies the boundary conditions eq. (2.5).

2. The direct system is solved at the $n$-th iteration, propagating $\boldsymbol{q}_{\text{in}}^{(n)}$ from $x_{\text{in}}$ to $x_{\text{out}}$. From the downstream development of the perturbation, the objective function $J^{(n)}$ can be computed and compared to $J^{(n-1)}$ to check if the optimisation can be considered converged.

3. The initial condition for the adjoint system at $x_{\text{out}}$ is obtained from eq. (2.27).

4. The adjoint system eq. (2.28) is solved, marching upstream from $x_{\text{out}}$ to $x_{\text{in}}$.

5. The new initial disturbance $\boldsymbol{q}_{\text{in}}^{(n+1)}$ is chosen according to the optimality condition from eq. (2.27), and the procedure is repeated until the energy growth is converged.

## 2.3 Choice of an appropriate norm

Solving the optimisation problem gives the optimal perturbation, *i.e.* the initial disturbance that gives rise to the less favourable instabilities in the boundary layer in terms of transition to turbulence. The optimal perturbation has to maximise the energy of the disturbances propagating in the boundary layer. The choice of the measure of this energy is not unique.
Considering spatial optimal growth in two-dimensional incompressible boundary layers, the kinetic energy seems a natural choice. Andersson *et al.* (1999) used the complete kinetic energy defined by three disturbance velocity components. For large Reynolds numbers, they noted that the maximum spatial gain curves become Reynolds number independent.

$$E = \int_0^\infty u^2 + Re_L^{-1}(v^2 + w^2)\,\mathrm{d}y. \tag{2.32}$$

Luchini (2000) used different measures of the energy at the inlet and outlet location based on the physical lift-up mechanism leading to the formation of streaks. The inlet energy uses the normal and spanwise velocities $v$ and $w$ while the outlet energy is based on the chordwise velocity $u$. Both approaches give similar results in the large Reynolds number limit ($Re_L > 10^4$ in practice). In eq. (2.32), the term of order $\mathcal{O}(Re_L^{-1})$ is thus neglected when measuring the energy at the outlet, while the assumption $u = 0$ is made at the inlet. The expression of the maximum gain is then reduced to

$$G_{\max} = Re_L \max_{\boldsymbol{q}_{\text{in}} \neq 0} \frac{\int_0^\infty u^2\,\mathrm{d}y\ |_{x=x_{\text{out}}}}{\int_0^\infty v^2 + w^2\,\mathrm{d}y\ |_{x=x_{\text{in}}}}. \tag{2.33}$$

The choice of a norm is more delicate when considering compressible flows, as the kinetic energy alone is not sufficient to render the effects of temperature and density variations due to compressibility. Hanifi *et al.* (1996) rederived the norm formulated by Mack (1969) by integrating the momentum equations under the parallel-flow approximation (see also Vermeersch, 2009). Since pressure work is conservative, they chose a norm that eliminates the contribution of pressure-related energy from the total disturbance energy. This leads to the expression

$$E = \int_0^\infty \left[\rho\left(u^2 + \frac{1}{Re_L}\left(v^2 + w^2\right)\right) + \frac{P\theta^2}{(\gamma - 1)\,T^2 M^2}\right]\mathrm{d}y, \tag{2.34}$$

where $(u, v, w)$ are the velocity disturbances and $\theta$ denotes the variation of temperature $T$. The mean flow density is $\rho$, the specific heat ratio is denoted $\gamma$ and the Mach number is $M$. Again, the outlet energy is the energy of the streaks characterised by the chordwise velocity disturbance $u$

so the term of order $\mathcal{O}(Re_L^{-1})$ can be neglected according to Luchini (2000). Considering disturbances $\boldsymbol{q} = (u, v, w, \theta, p)^T$ in a two-dimensional compressible flow, the outlet energy can be written

$$\begin{cases} E_{\text{out}} = \int_0^\infty \left[\boldsymbol{q}_{\text{out}}^T M_{\text{out}} \boldsymbol{q}_{\text{out}}\right] \mathrm{d}y \\ M_{\text{out}} = \text{diag}\left(\rho, 0, 0, \frac{P}{(\gamma-1)T^2M^2}, 0\right). \end{cases} \tag{2.35}$$

For the inlet energy, the gain is maximum for $u = \theta = 0$, which leads to

$$\begin{cases} E_{\text{in}} = \frac{1}{Re_L} \int_0^\infty \left[\boldsymbol{q}_{\text{in}}^T M_{\text{in}} \boldsymbol{q}_{\text{in}}\right] \mathrm{d}y \\ M_{\text{in}} = \text{diag}\left(0, \rho, \rho, 0, 0\right), \end{cases} \tag{2.36}$$

and the expression of the maximum gain reads

$$G_{\max} = Re_L \max_{\boldsymbol{q}_{\text{in}} \neq 0} \frac{\int_0^\infty \left[\boldsymbol{q}_{\text{out}}^T M_{\text{out}} \boldsymbol{q}_{\text{out}}\right] \mathrm{d}y}{\int_0^\infty \left[\boldsymbol{q}_{\text{in}}^T M_{\text{in}} \boldsymbol{q}_{\text{in}}\right] \mathrm{d}y}. \tag{2.37}$$

From eqs. (2.33) and (2.37), the Reynolds number appears as a scale parameter in the definition of the maximum gain for two-dimensional flows.
Zuccher and Tumin (2005) studied the influence of the different norms in the computation of the maximum gain for compressible flows. They compared the complete norm eq. (2.34) and the reduced norm where the terms of order $\mathcal{O}(Re_L^{-1})$ are neglected in the computation of the outlet energy. For a Reynolds number $Re_L \approx 10^3$, the reduced norm underestimates the gain, with larger differences at high Mach numbers. For $Re_L > 10^4$ the results are similar as highlighted for incompressible flows. However, the reduced norm might be insufficient when the transition is close to the stagnation point (*e.g.* on a sphere, or in the case of the "Blunt Body paradox", which refers to the early transition on spherical surfaces at supersonic and hypersonic speeds). In these cases, the streaks are not fully developed and normal and spanwise velocity disturbances cannot be neglected.

## 2.4 Numerical approach

### 2.4.1 Computation of the base flow

The base flow is computed using the Onera three-dimensional boundary-layer solver *3C3D* (Perraud *et al.*, 2011). The boundary-layer equations are solved using a finite-difference method along a local Cartesian coordinate system. Various boundary conditions can be enforced, particularly at the wall. The inputs for the code are the geometry of the body and the external velocity profiles.
Considering an airflow over a flat plate, the boundary-layer thickness is set to zero at the origin. Initial conditions are given by a Blasius velocity profile or equivalently by a Falkner-Skan self-similar solution at a stagnation point. The ideal gas hypothesis is employed with $\gamma = 1.4$. When compressibility effects are involved, the Prandtl number is considered constant with $Pr = 0.7$, and the dynamic viscosity $\mu$ depends on the temperature according to Sutherland's law. Both an adiabatic wall ($\partial T/\partial y|_{y=0} = 0$) or a fixed wall temperature $T_{\text{wall}}$ can be considered.

### 2.4.2 Continuous and discrete adjoint formulations

The formulation of the adjoint equations presented in section 2.2.3 is a continuous formulation. The adjoint equations are derived directly from the continuous analytical system of partial differential equations for the small disturbances. The adjoint system is then discretised to obtain a discrete

scheme to be used numerically. Conversely, a discrete approach can be used where the discrete governing equations are used to derive discrete adjoint equations. Although both methods lead to discrete adjoint equations, as illustrated in fig. 2.1, these equations and the associated adjoint variables usually differ. The same equations can be recovered by both methods in some cases, *e.g.* using the discontinuous Galerkin method (Pascal, 2013).

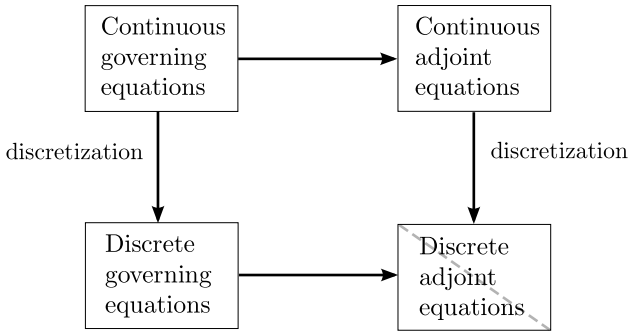


Figure 2.1: Continuous and discrete approaches leading to the formulation of the discrete adjoint equations.

The reason for using the continuous approach is that it clarifies the boundary conditions for the adjoint variables in the wall-normal coordinate (see for instance eq. (2.31)). However, from a numerical point of view, the discrete governing equations are implemented and the discrete adjoint equations are derived directly from the discrete direct system, as detailed in the following.

Equation (2.4) can be written in a conservative form using the continuity equations for the base flow and disturbances,

$$\begin{aligned}
&u_x + v_y + i\beta w = 0,\\
&(2Uu)_x = (-V_y + i\omega - \beta^2)u - U_y v - i\beta U w - V u_y - U v_y + u_{yy},\\
&(Vu)_x + (Uv)_x = (-2V_y + i\omega - \beta^2)v - i\beta V w - 2V v_y - p_y + v_{yy},\\
&(Uw)_x = (-V_y + i\omega - \beta^2)w - i\beta p - V w_y + w_{yy}.
\end{aligned} \tag{2.38}$$

Denoting $\mathbb{Q}$ the discretised vector of the state variables $\boldsymbol{q}$, and $\mathbb{P}$ the discretised vector of the adjoint variables $\boldsymbol{p}$, these equations can be written in matrix form as

$$\begin{aligned}
&(H_1 \cdot \mathbb{Q})_x = H_2 \cdot \mathbb{Q},\\
&\text{with} \quad H_2 = B_0 + B_1 \cdot D_y + B_2 \cdot D_{yy}.
\end{aligned} \tag{2.39}$$

In eq. (2.39), $D_y$ and $D_{yy}$ are differentiation matrices in the wall-normal direction that are detailed in section 2.4.3. The discretisation of the chordwise derivative is described in section 2.4.4. The corresponding discrete adjoint equations[2] and optimality conditions then read

$$-H_1^T \cdot \mathbb{P}_x = H_2^T \cdot \mathbb{P}\ , \tag{2.40a}$$

$$H_{1_{\text{out}}}^T \cdot \mathbb{P}_{\text{out}} = 2Q_{\text{out}} \cdot \mathbb{Q}_{\text{out}}\ , \tag{2.40b}$$

$$\mathbb{Q}_{\text{in}} = Q_{\text{in}}^{-1} \cdot H_{1_{\text{in}}}^T \cdot \mathbb{P}_{\text{in}}\ , \tag{2.40c}$$

[2]More precisely, eq. (2.40a) can be considered as the *half-discretised* adjoint equations, since they are derived from the discrete direct equations in the $y$-direction only. The chordwise discretisation is done afterwards using the numerical scheme described in section 2.4.4.

where, in eqs. (2.40b) and (2.40c), matrices $Q_{\text{in}}$ and $Q_{\text{out}}$ contain the integration weights as detailed in section 2.4.3 and are used in the definition of the energy $E = \mathbb{Q}^T \cdot Q \cdot \mathbb{Q}$. The minus sign in the adjoint equation eq. (2.40a) means that disturbances are propagated upstream from $x_{\text{out}}$ to $x_{\text{in}}$.

The initial condition for the adjoint problem, which links the output of the direct problem $\mathbb{Q}_{\text{out}}$ to the input for the adjoint equation $\mathbb{P}_{\text{out}}$, is given by eq. (2.40b). Note that, when compressibility effects are taken into account ($\boldsymbol{q} = (u, v, w, \theta, p)^T$), one of the five adjoint variables is not prescribed as $H_{1_{\text{out}}}$ is singular. The last component of $\mathbb{P}$ can be set to zero (Zuccher *et al.*, 2006) and a non-singular matrix can be obtained by eliminating the last row and column of $H_{1_{\text{out}}}$.

The initial disturbance is given by eq. (2.40c), where $Q_{\text{in}}$ is singular (diagonal matrix with zeros on the diagonal) so its inverse has to be formulated explicitly as

$$(Q_{\text{in}}^{-1})_{i,j} = \begin{cases} \frac{1}{(Q_{\text{in}})_{i,j}} & \text{if} \quad (Q_{\text{in}})_{i,j} \neq 0, \\ 0 & \text{otherwise.} \end{cases} \tag{2.41}$$

### 2.4.3 Discretisation in the wall-normal direction

At each chordwise location $x$, the parabolised equations are solved in the wall-normal direction $y$ using a spectral collocation method. The solution is found as a linear combination of global functions, *i.e.* functions that span over the whole wall-normal domain. The results are more precise compared to local approximations of finite differences, although the operators are more difficult to inverse.

The operator matrices are computed on the $N_y$ Chebyshev-Gauss-Lobatto collocation points

$$\xi_i = \cos\left(\frac{\pi i}{N_y}\right); \quad i = 0, ..., N_y. \tag{2.42}$$

The Chebyshev interval $-1 \leq \xi_i \leq 1$ is then transformed into the physical domain $0 \leq y_i \leq Y_\infty$ according to

$$y_i = \frac{Y_\infty \Upsilon}{2} \frac{1 - \xi_i}{1 + \Upsilon - \xi_i}, \tag{2.43}$$

where $\Upsilon$ is used to refine the number of points close to the wall and boundary-layer edge ($y = 0$ and $y = y_{\max}$ respectively). Boundary conditions at $y_{\max}$ are implicitly enforced in the differentiation matrices, as detailed in appendix B.3. Let $\mathbb{U}$ be the discretised vector of the quantity $u(\bar{x}, y)$ at a fixed chordwise location $\bar{x}$, then the wall-normal derivative of $u$ can be expressed on the collocation points as

$$\frac{\partial u}{\partial y} \approx D_y \cdot \mathbb{U}. \tag{2.44}$$

More details can be found in appendix B concerning the spectral collocation method for differentiation in the wall-normal direction.

Integration in the wall-normal direction is done by using the Clenshaw-Curtis method (see Waldvogel, 2006), where the integral is replaced by a finite sum according to

$$\int_{-1}^{1} f(x)\,\mathrm{d}x = \sum_{k=0}^{N_y} w_k f(x_k) + R_N. \tag{2.45}$$

In this equation, $R_N$ is the approximation error and $w_k$ denotes the integration weights. The integral is also computed on the Gauss-Lobatto points $\xi_i$ used for differentiation. For $u$, we get

$$\int_0^{y_{\max}} u(\bar{x}, y)\,\mathrm{d}y \approx W_y \cdot \mathbb{U}, \tag{2.46}$$

where $W_y$ contains the integration weights (see also appendix B.4 for more details).

### 2.4.4 Discretisation in the chordwise direction

The chordwise direction is discretised in $N_x$ points, refined at both ends $x_{\text{in}}$ and $x_{\text{out}}$ according to

$$x^{[n]} = \begin{cases} \left(x_{\text{in}}^h + n\,\frac{(x_{\text{out}}/2)^h - x_{\text{in}}^h}{E(\frac{N_x}{2})-1}\right)^{1/h} & \text{for} \quad n = 0, \cdots, E(N_x/2) - 1\ ; \\ x_{\text{out}} - x^{[N_x - n]} & \text{for} \quad n = E(\frac{N_x}{2}) + 1, \cdots, N_x - 1\ ; \\ x_{\text{out}} & \text{for} \quad n = N_x\ , \end{cases} \tag{2.47}$$

where $0 \leq h \leq 1$ is used to control the refinement close to $x_{\text{in}}$ and $x_{\text{out}}$. When $h = 1$, the discretisation is equidistant ; when $h \to 0$, most of the points are located close to the edges of the mapping.

The parabolic direct (eq. (2.39)) and adjoint (eq. (2.40)) problems are approximated in the streamwise direction $x$ using an implicit finite-difference scheme. The following second-order backward-difference scheme is used

$$\mathbb{Q}^{(n+1)} = \left(a_1 H_1^{(n+1)} - (x^{(n+1)} - x^{(n-1)}) H_2^{(n+1)}\right)^{-1} \left(-a_2 (H_1\mathbb{Q})^{(n)} - a_3 (H_1\mathbb{Q})^{(n-1)}\right), \tag{2.48}$$

where the coefficients $a_1$, $a_2$ and $a_3$ are given by a second-order Taylor development of $(H_1\mathbb{Q})^{(n+1)}$, $(H_1\mathbb{Q})^{(n)}$ and $(H_1\mathbb{Q})^{(n-1)}$:

$$\begin{cases} a_2 &= -\frac{\left(x^{(n+1)} - x^{(n-1)}\right)^2}{\left(x^{(n+1)} - x^{(n)}\right)\left(x^{(n)} - x^{(n-1)}\right)}, \\ a_3 &= \frac{\left(x^{(n+1)} - x^{(n)}\right)}{\left(x^{(n)} - x^{(n-1)}\right)}, \\ a_1 &= -a_2 - a_3. \end{cases} \tag{2.49}$$

Equation (2.48) is used to compute $\mathbb{Q}$ at a location $x^{(n+1)}$. However, it requires the knowledge of the solution at $x^{(n)}$ and $x^{(n-1)}$. For the first step, a first backward-Euler scheme is used

$$\mathbb{Q}^{(1)} = \left(H_1^{(1)} - (x^{(1)} - x^{(0)}) H_2^{(1)}\right)^{-1} (H_1\mathbb{Q})^{(0)}. \tag{2.50}$$

The adjoint equations may be discretised similarly using a second-order backward-difference scheme

$$\begin{aligned} \mathbb{P}^{(N_x-1)} &= \left(H_1^{T(N_x-1)} - (x^{(N_x)} - x^{(N_x-1)}) H_2^{T(N_x-1)}\right)^{-1} (H_1^T)^{(N_x-1)} \mathbb{P}^{(N_x)}, \\ \mathbb{P}^{(n-1)} &= \left(a_1 H_1^{T(n-1)} - (x^{(n+1)} - x^{(n-1)}) H_2^{T(n-1)}\right)^{-1} \left(-a_2 H_1^{T(n-1)} \mathbb{P}^{(n)} - a_3 H_1^{T(n-1)} \mathbb{P}^{(n+1)}\right). \end{aligned} \tag{2.51}$$

The method for computing optimal perturbations and the associated gain has been presented. In the general case of a non-parallel flow, successive iterations of the direct and adjoint equations are used to solve the optimisation problem. The choice of an appropriate norm to measure the disturbance energy has also been discussed for both incompressible and compressible flows. The numerical scheme used to solve the direct/adjoint system has been introduced for a two-dimensional incompressible boundary layer over a flat plate. The next chapter will focus on the introduction of curvature effects in the equations and the spatial development of optimal disturbances on curved surfaces.

# Part II

# Two-dimensional boundary layers over curved surfaces

Chapter 3

# Optimal disturbances on curved surfaces

In this chapter, a set of linear partial differential equations is derived to take curvature effects into account. These equations are used to determine optimal disturbances in boundary layers over curved surfaces. The optimisation problem is solved in a classical way using iterations of the direct/adjoint system. The optimal perturbation attaining the largest growth at the shortest chordwise location is then determined based on the first neutral position. Considering an incompressible boundary layer over a concave wall, a receptivity analysis is presented. The most dangerous inlet location is also determined. The optimal perturbation method proves adequate to compute the neutral curve for the Görtler problem, delimiting a unique envelope for the unstable domain. In the framework of the parallel-flow approximation, the spectrum and pseudospectrum of the operators are determined. This approach reveals the potential for non-modal growth in the early development of Görtler vortices.

## Contents

## 3.1 Mathematical formulation of the problem

### 3.1.1 Governing equations for a two-dimensional compressible flow

We consider the flow over a curved wall with a radius of curvature $R_c$ large compared to the boundary-layer scale $\delta$. As detailed in the previous chapter, different length scales are introduced, namely a reference length $L$ in the chordwise direction and a boundary-layer scale $\delta = {}^{L}/\sqrt{Re_L}$ in the wall-normal direction. The Reynolds number $Re_L = {}^{U_\infty L}/\nu$ is based on $L$ and $\nu$ is the dimensional kinematic viscosity of the fluid. We use a curvilinear orthogonal reference frame where $x = x_\mathrm{d}/L$ is measured along the wall, $y = y_\mathrm{d}/\delta$ is normal to the surface, and $z = z_\mathrm{d}/\delta$ is perpendicular to the $(xy)$-plane.

A two-dimensional compressible flow $\boldsymbol{U} = (U(x,y), V(x,y), 0)^T$ is considered. The non-dimensional conservation equations of mass, momentum and energy in vector notation are given by

$$\begin{aligned}
&\frac{\partial \rho}{\partial t} + \nabla\cdot(\rho\boldsymbol{U}) = 0 \ ; \\
&\rho\left(\frac{\partial \boldsymbol{U}}{\partial t} + (\boldsymbol{U}\cdot\nabla)\boldsymbol{U}\right) = -\frac{1}{\gamma M^2}\nabla p + \frac{c}{Re_L}\nabla(\mu\nabla\cdot\boldsymbol{U}) + \frac{1}{Re_L}\nabla\cdot\left[\mu(\nabla\boldsymbol{U} + \nabla\boldsymbol{U}^T)\right] \ ; \\
&\rho\left(\frac{\partial T}{\partial t} + (\boldsymbol{U}\cdot\nabla)T\right) = \frac{\gamma-1}{\gamma}\left(\frac{\partial p}{\partial t} + (\boldsymbol{U}\cdot\nabla)p\right) + \frac{(\gamma-1)M^2}{Re_L}c\mu(\nabla\cdot\boldsymbol{U})^2 \\
&\qquad\qquad + 2\mu\frac{(\gamma-1)M^2}{Re_L}\left(\nabla\boldsymbol{U} + \nabla\boldsymbol{U}^T\right) + \frac{1}{Re_L Pr}\nabla\cdot(\kappa\nabla T) \ ;
\end{aligned} \tag{3.1}$$

with the state relation

$$P = \rho R T. \tag{3.2}$$

In eq. (3.1), $\lambda$ and $\mu$ are the conductivity and viscosity coefficients, linked by Stokes' hypothesis $c = {}^{\lambda}/_{\mu} = {}^{-2}/_{3}$. The specific heat ratio is denoted $\gamma$, while $\kappa$ is the heat conductivity, $M$ the Mach number and $Pr$ the Prandtl number. The dynamic viscosity is a function of the temperature only via Sutherland's law.

In order to express system (3.1) in a general curvilinear system, we introduce a metric tensor (Bonnet and Luneau, 1989; Copie, 1996; Jallade, 1990). The scale factors can be expressed as

$$h_1 = 1 - \frac{y}{R_c} \ ; \qquad h_2 = h_3 = 1, \tag{3.3}$$

and the metric tensor is written as the diagonal matrix of the square of the scale factors. From eq. (3.3), the gradient of a given function $f$ becomes

$$\nabla f = \left(\frac{1}{h_1}\frac{\partial f}{\partial x}; \frac{\partial f}{\partial y}; \frac{\partial f}{\partial z}\right), \tag{3.4}$$

and the Laplace operator

$$\Delta f = \frac{1}{h_1}\frac{\partial}{\partial x}\left(\frac{1}{h_1}\frac{\partial f}{\partial x}\right) + \frac{1}{h_1}\frac{\partial}{\partial y}\left(h_1\frac{\partial f}{\partial y}\right) + \frac{\partial^2 f}{\partial z^2}. \tag{3.5}$$

The divergence of $\boldsymbol{U}$ can also be re-written as

$$\nabla\cdot\boldsymbol{U} = \frac{1}{h_1}\frac{\partial U}{\partial x} + \frac{\partial V}{\partial y} + \frac{1}{h_1}\frac{\partial h_1}{\partial y}V + \frac{\partial W}{\partial z}. \tag{3.6}$$

Three-dimensional disturbances of the form $\boldsymbol{q}'(x,y,z,t) = \boldsymbol{q}(x,y)\exp(i(\beta z - \omega t))$ are introduced, where $\beta = \beta_\mathrm{d}\delta$ is the dimensionless spanwise wavenumber and $\omega = \omega_\mathrm{d}U_\infty/L$ is the dimensionless angular frequency. As compressibility effects are taken into account, we define $\boldsymbol{q}' = (u', v', w', \theta', p')^T$. The linearised disturbance equations are written in matrix formulation

$$(A \cdot q)_x = (E \cdot q_y)_x + B \cdot q + C \cdot q_y + D \cdot q_{yy}, \tag{3.7}$$

where the coefficients of $A$, $B$, $C$, $D$ and $E$ are detailed in appendix C.2. Upon assuming that the radius of curvature $R_c$ and the reference length $L$ are large compared to the boundary-layer scale $\delta$ used for rescaling $y$, and neglecting the derivative of $h_1$ with respect to the streamwise coordinate $x$, the curvature effect is taken into account through the terms

$$m_{ij} = \frac{1}{h_i h_j}\frac{\partial h_i}{\partial x_j}, \tag{3.8}$$

with $m_{12} = {}^1\!/_{h_1}{}^{\partial h_1}\!/_{\partial y}$ being the only non-zero term in this case.

We introduce the Görtler number which compares the sum of inertial and centrifugal forces to viscous terms,

$$\mathsf{G} = \frac{L}{R_c}\sqrt{Re_L}. \tag{3.9}$$

We can define two small parameters,

$$\varepsilon_\nu = \frac{1}{\sqrt{Re_L}} \quad \text{and} \quad \varepsilon_c = \frac{\delta}{R_c}, \tag{3.10}$$

with $\varepsilon_c$ linked to $m_{12}$ through the relation

$$\varepsilon_c = \left(\frac{-1}{h_1 h_2}\frac{\partial h_1}{\partial y}\right). \tag{3.11}$$

Strictly speaking, this relation is only valid near the wall ($y = 0$), although the generalisation is straightforward considering that streamlines have a smaller radius of curvature compared to the wall. Hence if $\varepsilon_c \ll 1$ at the wall, the relation holds for the whole boundary layer. The Görtler number can then be related to $\varepsilon_c$ and $\varepsilon_\nu$ through the relation

$$\mathsf{G} \sim \frac{\varepsilon_c}{\varepsilon_\nu^2}. \tag{3.12}$$

Taking curvature effects into account adds one term in the wall-normal momentum equation, which can be expressed as $2\mathsf{G}Uu$ (see appendix C).

We have derived a set of linear partial differential equations taking curvature effects into account. The objective is now to use these equations to determine the optimal perturbations taking place on curved surfaces.

### 3.1.2 Maximum energy growth at the shortest chordwise location

Optimal perturbations are the disturbances which experience maximum energy amplification at a specific chordwise position $x_\mathrm{out}$. The optimal perturbation problem consists in maximising the gain defined as the ratio of the outlet perturbation energy at $x_\mathrm{out}$ to the inlet perturbation energy

at $x_{\text{in}}$, $G = E_{\text{out}}/E_{\text{in}}$. To measure the disturbance energy in a compressible flow, we use the norm derived by Mack presented in section 2.3

$$E = \int_0^\infty \left[ \rho \left( u^2 + \frac{1}{Re_L} \left( v^2 + w^2 \right) \right) + \frac{P\theta^2}{(\gamma - 1)\, T^2 M^2} \right] \mathrm{d}y. \tag{3.13}$$

We recall that $P$ is the pressure of the base flow, $T$ its temperature and $\theta$ the associated perturbation. The density, pressure and temperature perturbations are linked through the relation $r = -\rho\theta/T$, with $\rho$ and $r$ the density of the base flow and its disturbance respectively. Throughout the rest of this chapter, this definition of the disturbance energy is used, compressibility effects only playing a role with increasing Mach numbers.

The optimal perturbation is found by using an iterative direct/adjoint method, as presented in chapter 2. An arbitrary initial condition is set at the inlet location $x_{\text{in}}$. The direct problem is then solved, marching the perturbation downstream to the outlet location $x_{\text{out}}$. The resulting perturbation at the outlet is used to compute the gain $G$ which is compared to the value at previous iterations at the optimisation location $x_{\text{out}}$. The initial condition for the adjoint system is then computed and the system is solved marching backward up to $x_{\text{in}}$. The procedure is repeated until variations in the computed values of the gain become negligible. In practice, convergence turns out to be relatively fast with an average of three iterations needed.

The aim of this chapter is to compute optimal perturbations on curved surfaces. The spatial optimal growth of Görtler vortices, which appear on concave walls as presented in section 1.2.3, is of particular interest.
In order to be able to compute a unique neutral curve for the Görtler problem, we define a new criterion for the convergence of the disturbance gain. The neutral curve separates the domain into a stable and an unstable region. The most quickly amplified disturbances then have to be determined. As the gain is optimised for a given outlet location $x_{\text{out}}$, the new criterion for convergence uses the neutral position (i.e. the position where $\mathrm{d}E/\mathrm{d}x$ first vanishes) as a new value for this outlet location. This means that the new criterion searches for the smallest value of $x$ where $\mathrm{d}E/\mathrm{d}x = 0$ and uses this value as the outlet location for the optimisation of the gain. Physically, it ensures that the computed optimal perturbation is the perturbation that will undergo the largest amplification over the shortest distance. From a computational point of view, the outlet location $x_{\text{out}}$ where the gain is maximised is first prescribed large enough to be able to compute the neutral position. This neutral position is then used in the code as the new value for the outlet location $x_{\text{out}}$. The spatial domain changes and the direct/adjoint equations are solved between the inlet location $x_{\text{in}}$ and the new value of the outlet location $x_{\text{out}}$. The procedure is iterated until a fixed value of the neutral position is found. This method ensures that the computed optimal perturbation is the initial disturbance that grows the quickest. In practice, two iterations are needed to compute a converged value for $x_{\text{out}}$.

A new criterion that ensures the computation of the maximum energy at the shortest chordwise location has been developed. In the following, the optimal disturbances over a wall with constant curvature are investigated.

## 3.2 Constant curvature

### 3.2.1 Receptivity

We consider an incompressible base flow over a concave wall with a constant curvature defined through the Görtler number G = 0.025. The base flow is computed using the solver *3C3D* as described in section 2.4.1 As mentioned in section 1.4.3, Cossu *et al.* (2000) first employed an optimal approach to compute the maximum spatial growth of Görtler vortices. Figure 3.1 represents the longitudinal evolution of the gain in a semi-log plot. Optimal perturbations are introduced at $x_{in}$ = 20 and computations are carried out to obtain a maximum energy at several outlet locations, namely $x_{out}$ = 40, 120 and 200. These initial disturbances take the form of streamwise-oriented vortices at the inlet location. The gain curves for the different initial conditions shown in fig. 3.1 are in excellent agreement with the results of Cossu *et al.* (2000). For large values of $x_{out}$ ($x_{out} > 120$), these curves lie on top of each other. If $x_{out}$ is placed sufficiently downstream from $x_{in}$, the gain (and the associated optimal perturbation) becomes independent from the outlet location.

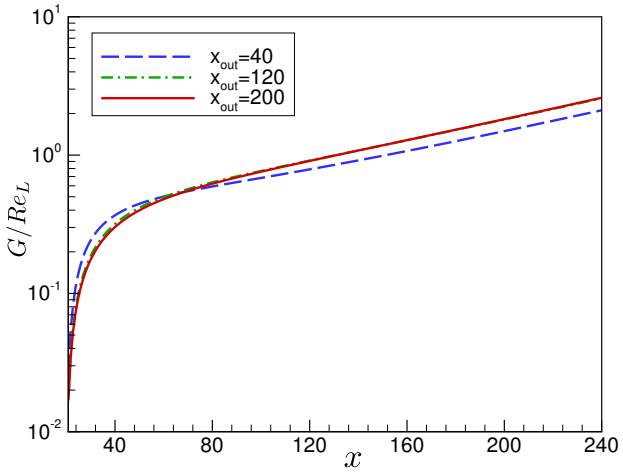


Figure 3.1: Gain curves for different outlet locations $x_{out}$, with a Görtler number G = 0.025 and a spanwise wavenumber $\beta$ = 0.069. Disturbances are introduced at $x_{in}$ = 20.

In order to study the receptivity problem for a flow over a concave wall, the effect of the inlet location is investigated by varying $x_{in}$ for a fixed outlet location $x_{out}$ = 200. Table 3.1 shows the altitude of the maximum of the velocity component $v_{opt}(x_{in})$ of the optimal perturbation at the inlet in terms of the similarity variable $\eta = y/(2\sqrt{x})$. This altitude increases as $x_{in}$ moves upstream ($x_{in}/x_{out}$ tends to 0). The ratio $x_{in}/x_{out}$ ranges from 0.6 to $3.10^{-5}$ as $x_{in}$ is moved towards the leading edge. Cossu *et al.* (2000) computed the same altitude in terms of the dimensional variable $y_d$ scaled with the spanwise wavelength $\lambda_d = 2\pi/\beta_d$ and suggested a possible convergence towards a finite value of $y_d/\lambda_d$ as the ratio $x_{in}/x_{out}$ goes to 0. However, their numerical scheme is limited to values of $x_{in}$ that did not allow to confirm this hypothesis. In this work, smaller values of $x_{in}$ have been tested, and results are displayed in fig. 3.2. Values of $y_d/\lambda_d$ as low as $y_d/\lambda_d = 0.166$ have been found as $x_{in}$ moves towards the leading edge.

These results suggest that the receptivity process is different when the inlet location changes. The optimal perturbations are first receptive to free-stream perturbations as $x_{in}$ is close to the leading edge. As the inlet location moves downstream towards $x_{out}$ and the boundary layer becomes thicker, they become more receptive to perturbations localised within the boundary layer.

| $x_{in}/x_{out}$ | $y_d/\lambda_d$ | $\eta$ |
|---|---|---|
| 0.6 | 0.32 | 1.33 |
| 0.4 | 0.32 | 1.629 |
| 0.2 | 0.283 | 2.039 |
| 0.05 | 0.219 | 3.158 |
| 0.025 | 0.191 | 3.904 |
| $3.10^{-5}$ | 0.166 | 97.932 |

Table 3.1: Location in the boundary layer of the maximum of the normal velocity component $v_{opt}(x_{in})$ for the optimal perturbation at the inlet in terms of the dimensional variable $y_d$, where $y_d$ is scaled with the spanwise wavelength $\lambda_d = 2\pi/\beta_d$ and $\eta = y/(2\sqrt{x})$ (with a Görtler number $\mathsf{G} = 0.025$ and $\beta = 0.069$).

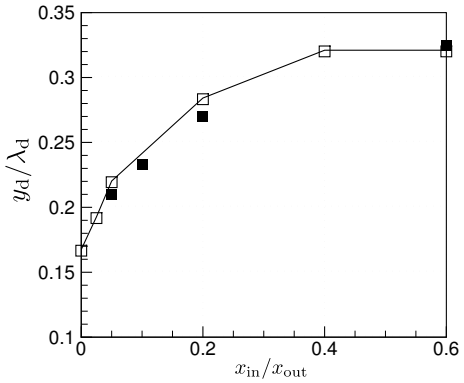


Figure 3.2: Altitude above the wall of the maximum of the normal velocity component $v_{opt}(x_{in})$ of the optimal perturbation (□). The maximum is indicated in terms of the dimensional variable $y_d$ rescaled by the spanwise wavelength $\lambda_d = 2\pi/\beta_d$ for comparison with the results obtained by Cossu *et al.* (2000) (■).

### 3.2.2 Neutral curve for the Görtler problem

In order to compute the neutral curve for the Görtler problem, the disturbance energy is computed according to eq. (3.13). We can define the neutral position as the first chordwise station where the longitudinal derivative of the energy vanishes, *i.e.* $\mathrm{d}E/\mathrm{d}x = 0$. At any location $x$ where this condition is verified, we can define a local Görtler number $\mathsf{G}_x$ and a local spanwise wavenumber $\beta_x$ according to

$$\mathsf{G}_x = \mathsf{G} \times x^{3/2}\,, \tag{3.14}$$

$$\beta_x = \beta \times x^{1/2}\,. \tag{3.15}$$

The neutral curve is the zero-contour curve of growth rate and separates the domain into the unstable region and the stable region. We can now compute this curve in the ($\beta_x$,$\mathsf{G}_x$)-plane by varying the global spanwise wavenumber $\beta$ of the initial disturbance or the Görtler number $\mathsf{G}$.

Hall (1983) pointed out that, for low values of the spanwise wavenumber, the neutral curve is very dependent on the form of the initial disturbance. Therefore, he had to introduce several shapes of initial perturbations, as illustrated in fig. 3.3, and propagate them downstream using a parabolic set of equations. Each set of initial disturbance has to be propagated downstream, which results in a large amount of computations to determine the optimal perturbation. Using the optimal perturbation approach, the dependence on the initial condition is removed as we compute the most amplified perturbation over all possible initial disturbance. The criterion for convergence developed in section 3.1.2 also ensures the computation of the disturbance that undergoes maximum energy amplification at the smallest chordwise location. The resulting neutral curve is thus associated with the fastest growing optimal perturbation and represents the envelope for the unstable domain.

Figure 3.3 displays such neutral curve for a Görtler number $\mathsf{G} = 0.025$ and a disturbance introduced at $x_{in} = 50$ (the influence of the inlet location $x_{in}$ will be investigated in the following). These parameters were used by Hall (1983) along with a set of different initial conditions. The different resulting neutral curves that he obtained (blue dash-dotted lines) illustrate the dependence on the form of the initial disturbance. For large values of the spanwise wavenumber, the neutral curves tend towards the same asymptote that can be determined using the parallel-flow approximation.

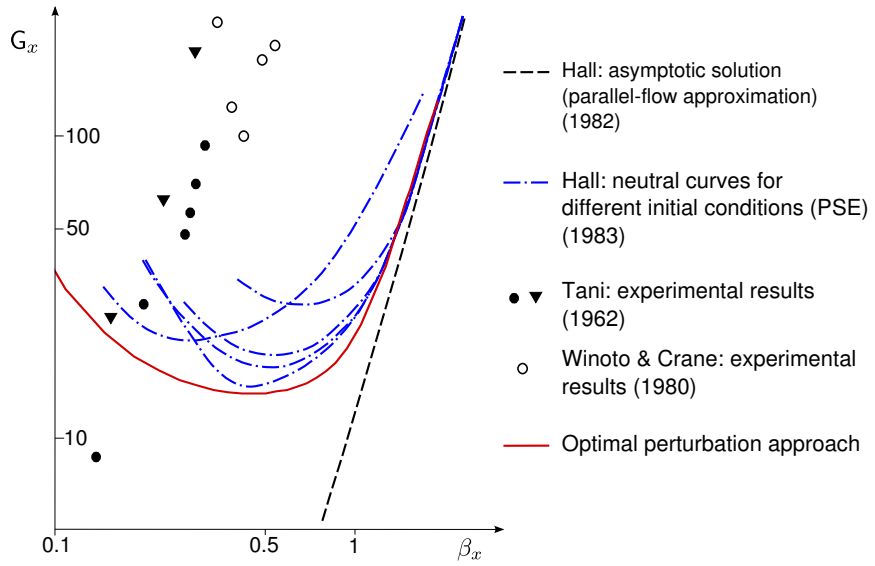


Figure 3.3: Comparison between neutral curves computed by Hall (1983) for different initial conditions imposed at $x_{\text{in}} = 50$ (- · - · -), the two-terms asymptotic neutral curve developed by Hall (1982) (- - -), the experimental observations of Tani (1962) (• and ▼) and Winoto & Crane (1980) (∘), and the neutral curve corresponding to the optimal perturbation introduced at $x_{\text{in}} = 50$ (——).

Hall (1982) developed a formal asymptotic solution of the linear partial differential equations in the large spanwise wavenumber limit, assuming the wavelength of the vortices small compared with the boundary-layer thickness. For large values of the wavenumber, the asymptotic agreement of the results is clearly visible in fig. 3.3.
The neutral curve computed with the optimal perturbation approach (red solid line), by varying the spanwise wavenumber $\beta$ of the initial disturbance, includes all the curves computed by propagating different initial conditions (blue dash-dotted lines). Again, this curve is associated with the fastest most amplified perturbation, optimised over all possible inputs. Various experimental points are also displayed in fig. 3.3, which correspond to flow conditions where Görtler rolls were observed. All these points, except one, are also included in the unstable domain defined by the optimal neutral curve. We emphasise here the interest of the optimal perturbation approach: the optimisation over every possible initial disturbance allows for the computation of a global neutral curve without having to test for various initial conditions. The resulting neutral curve defines a unique envelope for the unstable domain. The concept of neutral curve that had been discarded for the Görtler problem because of the dependence on the shape of the initial disturbance can thus be restored through the optimal approach.

The optimal neutral curve in fig. 3.3 features a minimum at $(0.45; 14.5)$ in the $(\beta_x, \mathsf{G}_x)$-plane. This is the most unstable point and corresponds to a global spanwise wavenumber $\beta = 0.055$ at a global Görtler number $\mathsf{G} = 0.025$ (as the neutral point is found at $x = 69$). Figure 3.4a displays the optimal initial perturbation applied at $x_{\text{in}} = 50$ that corresponds to that most unstable point, with a streamwise velocity perturbation $u = 0$ at the inlet. In this figure, initial velocity components are normalised to obtain a unit initial energy and are plotted against the similarity variable $\eta = y/2\sqrt{x}$. Figure 3.4b displays the resulting streamwise velocity component of the perturbation at $x = 240$. The perturbation has been propagated downstream of the optimisation location $x_{\text{out}}$, where $v$ and $w$ are negligible. Let us recall that $v$ and $w$ are of order $\mathcal{O}(Re_L^{-1/2})$ while $u$ is of order $\mathcal{O}(1)$. The

edge of the boundary layer is located at $\eta = 2.8$. The wall-normal and transverse velocity profiles of the optimal perturbation stretch out into the free-stream, suggesting that the boundary layer is receptive to free-stream disturbances. The resulting streamwise disturbance velocity component is fully comprised within the boundary layer.

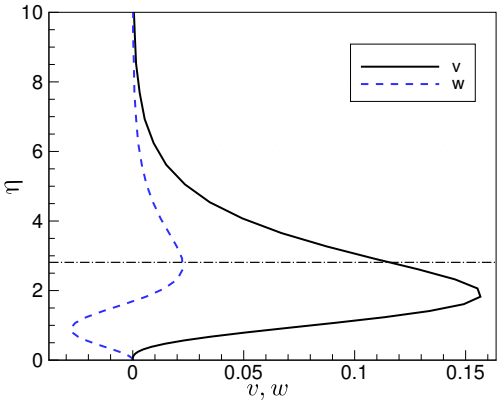


(a) Initial spanwise and normal velocity components of the perturbation introduced at $x_{\text{in}} = 50$, with $u = 0$.

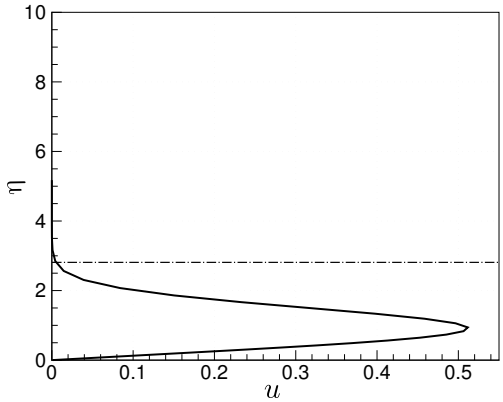


(b) Streamwise velocity component of the perturbation at $x = 240$.

Figure 3.4: Optimal perturbation applied at $x_{\text{in}} = 50$ that leads to the most unstable point on the neutral curve (fig. 3.4a), and the resulting disturbance at $x = 240$ (fig. 3.4b). The dash-dotted line indicates the edge of the boundary layer.

The same perturbation components are displayed in fig. 3.5 in the $\eta - z$ plane. The transverse velocity field $(w_{\text{opt}}(x_{\text{in}}), v_{\text{opt}}(x_{\text{in}}))$ of the optimal perturbation that maximises the gain at $x_{\text{out}} = 200$ is displayed in fig. 3.5a, where the inlet location is $x_{\text{in}} = 50$. The magnitude of the $u$-velocity component of the resulting disturbance at $x = 240$ is plotted in fig. 3.5b, where grey lines indicate negative values. The optimal perturbation consists of counter-rotating streamwise vortices. This initial disturbance then evolves downstream into alternating regions of high and low streamwise velocity. These streaks arise from the lift-up effect, which is known to play a role in the formation of Görtler vortices (Saric and Benmalek, 1991) as it does in the formation of Klebanoff modes (Landahl, 1980).

Figure 3.6 illustrates the streamwise evolution of the growth rate $\sigma = (\mathrm{d}E/\mathrm{d}x)/E$ and of the gain $G$ scaled with the Reynolds number $Re_L$ for the optimal perturbation plotted in fig. 3.4. The energy decreases over the first stations as disturbances are damped over the beginning of the wall. As vortices start developing over the concave surface the energy increases, which can also be observed on the evolution of the disturbances gain.

The most dangerous location for introducing disturbances can be determined by varying the inlet location $x_{\text{in}}$ for a given outlet location $x_{\text{out}}$ and computing the optimal neutral curve. Figure 3.7 shows these neutral curves computed for various inlet locations, with a Görtler number $\mathsf{G} = 0.025$. As the optimal perturbation is introduced closer to the leading edge, the neutral curves tend to converge on top of each other. As $x_{\text{in}}$ moves upstream towards the leading edge, the boundary layer thus becomes more likely to be destabilised for lower values of $\mathsf{G}_x$. This means that if the concave part of the surface is located close to the leading edge, the boundary layer will be more prone to be destabilised by Görtler vortices. The most unstable point is lowered to a local Görtler number $\mathsf{G}_x = 7.72$ at $\beta_x = 0.4$ for a disturbance introduced at $x_{\text{in}} = 10$.

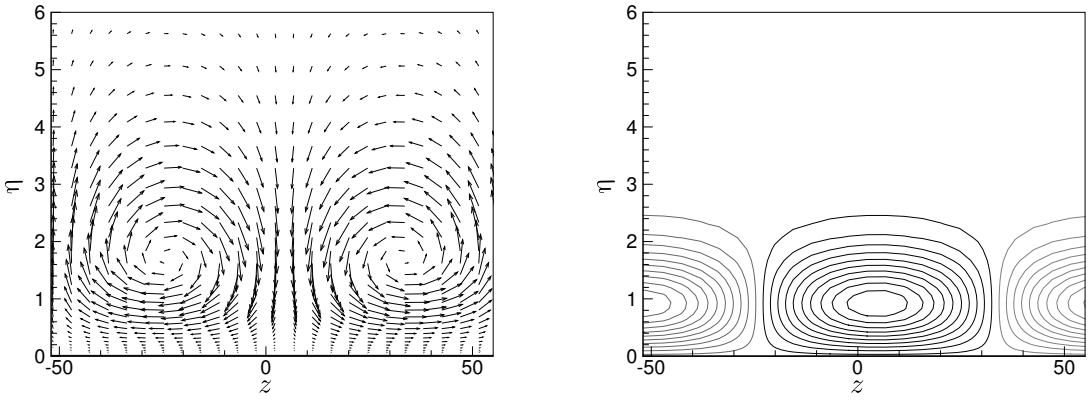


(a) $x = 50$ (b) $x = 240$

Figure 3.5: $(w_{\text{opt}}(x_{\text{in}}), v_{\text{opt}}(x_{\text{in}}))$ velocity field for the optimal initial perturbation applied at $x_{\text{in}} = 50$ which leads to the most unstable point on the neutral curve (fig. 3.5a) and magnitude of the resulting $u$-velocity component for the corresponding perturbation at $x = 240$ in the $\eta - z$ plane (fig. 3.5b, where grey lines correspond to negative values).

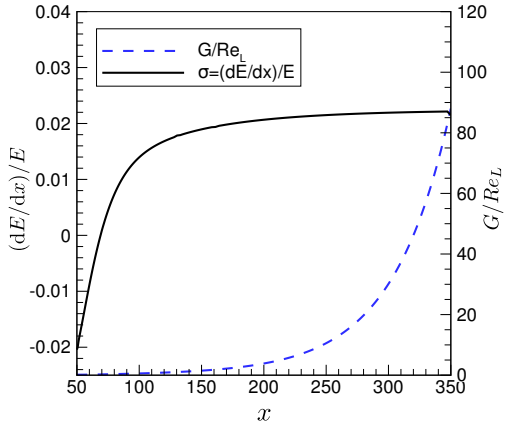


Figure 3.6: Streamwise evolution of the growth rate $\sigma = (\mathrm{d}E/\mathrm{d}x)/E$ and gain $G/Re_L$, with $x_{\text{in}} = 50$, $x_{\text{out}} = 200$ and $\mathsf{G} = 0.025$. The neutral position where $\mathrm{d}E/\mathrm{d}x = 0$ is $x = 69$.

### 3.2.3 Compressibility effects

Having written the equations governing a compressible flow over a curved surface, we now investigate compressibility effects on the spatial growth of Görtler vortices. We compute the neutral curves for a compressible boundary layer over a wall with constant curvature. The stagnation temperature is fixed to $T_i = 311\,\mathrm{K}$, and different Mach numbers are tested, ranging from $M = 0$ to 4. The corresponding neutral curves are plotted in fig. 3.8, with a Görtler number $\mathsf{G} = 0.025$, $x_{\text{in}} = 50$ and $x_{\text{out}} = 200$. As the Mach number increases, and for a fixed local spanwise wavenumber $\beta_x \geqslant 0.4$, the local Görtler number, and equivalently the associated neutral curve, moves upward, increasing the region of stability. The boundary layer is thus less likely to be destabilised because of vortices forming on the concave part of the wall. Görtler vortices that were found to be amplified for low speeds are going to be damped at higher Mach numbers. Hall and Malik (1989) also emphasised this stabilising effect of compressibility.

The velocity field for the optimal perturbation introduced at $x_{\text{in}} = 50$ and optimised at $x_{\text{out}} = 200$ for a Mach number $M = 3$, with $\beta = 0.055$ and $\mathsf{G} = 0.025$ is displayed in fig. 3.9a. The $u$-velocity component of the disturbance propagated downstream at $x = 240$ is plotted in fig. 3.9b. These

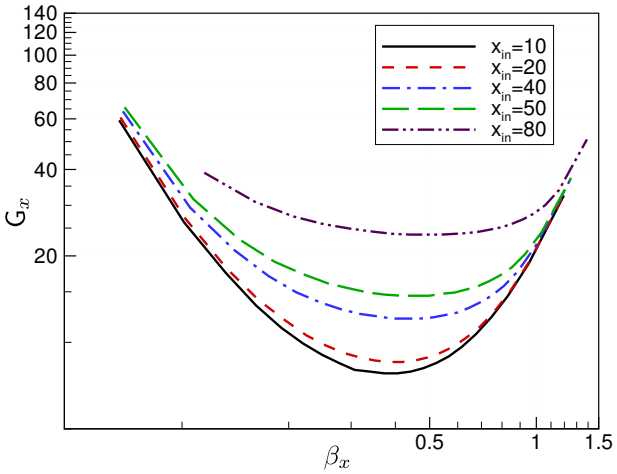


Figure 3.7: Neutral curves for different inlet locations $x_{\text{in}}$, with the optimisation location fixed at $x_{\text{out}} = 200$ and a Görtler number $\mathsf{G} = 0.025$.

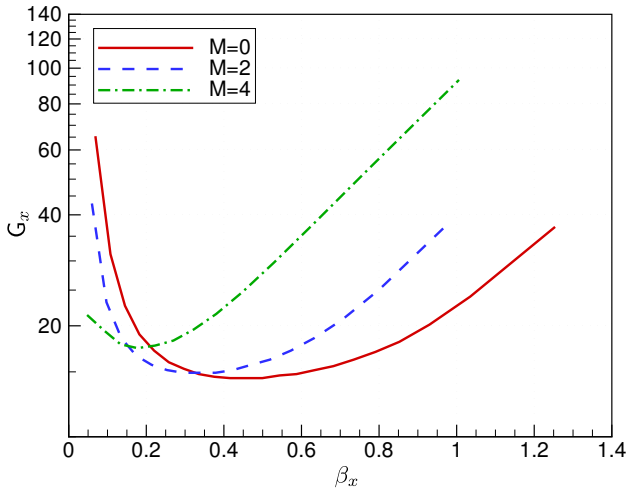


Figure 3.8: Neutral curves for different Mach numbers, with $x_{\text{in}} = 50$, $x_{\text{out}} = 200$ and $\mathsf{G} = 0.025$.

results can be compared with those obtained for an incompressible flow, where the same quantities are plotted in fig. 3.5. Comparison shows that compressibility effect leads to the formation of streaks that are stretched towards the outer edge of the boundary layer. The maximum of the $u$-velocity component is displaced from $\eta = 0.95$ in the incompressible case to $\eta = 2.8$ when the Mach number is set to $M = 3$. This behaviour is also observed when studying the formation of Klebanoff modes on a flat plate for compressible flows (Vermeersch, 2009).

## 3.3 Spectral analysis

We now adopt the hypothesis of a parallel-flow, neglecting the boundary-layer growth, in order to determine the influence of curvature on the spectrum of the operators. This approach allows us to come back to the definition of transient growth, which is due to possible interactions between non-orthogonal modes. Spectra and pseudospectra are computed to investigate the effect of the Görtler number on the eigenvalues.

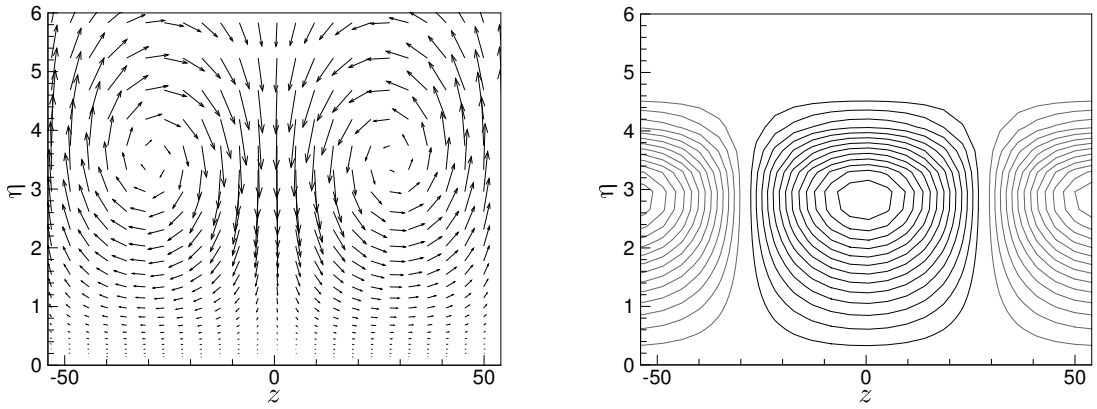


(a) $x = 50$ (b) $x = 240$

Figure 3.9: $(w_{\text{opt}}(x_{\text{in}}), v_{\text{opt}}(x_{\text{in}}))$ velocity field for the optimal initial perturbation applied at $x_{\text{in}} = 50$ and optimised at $x_{\text{out}} = 200$, and magnitude of the resulting $u$-velocity component for the corresponding perturbation propagated at $x = 240$ in the $\eta - z$ plane (fig. 3.9b, where grey lines correspond to negative values). The Mach number is set to $M = 3$, with $\beta = 0.055$ and $\mathsf{G} = 0.025$. To be compared with the incompressible case displayed in fig. 3.5.

As detailed in section 2.2.2, disturbances are now decomposed as a sum of modes,

$$\begin{aligned} \boldsymbol{q}'(x,y,z,t) &= \boldsymbol{q}(x,y)e^{i(\beta z-\omega t)}, \\ \boldsymbol{q}(x,y) &= \sum_k \hat{\boldsymbol{q}}_k(y)e^{i\alpha_k x}. \end{aligned} \tag{3.16}$$

Equation (3.16) shows that the whole spectrum is considered and that all the eigenvalues (especially from the continuous branch) contribute to the computation of the gain. The introduction of the perturbations into the linearised Navier-Stokes equations leads to a general eigenvalue problem,

$$\forall k, \quad \mathcal{A}(y,\beta,\omega)\ \hat{\boldsymbol{q}}_k(y) = \mathcal{B}(y,\beta,\omega)\ \alpha_k\ \hat{\boldsymbol{q}}_k(y), \tag{3.17}$$

which gives the eigenvalues $\alpha_k$. The whole discrete spectrum of the operator is computed for different values of $N_y$ (number of collocation points in the normal direction) to ensure the convergence of the eigenvalues and isolate discrete modes from the continuous branch. Figure 3.10 shows the discrete spectrum for a Görtler number $\mathsf{G} = 4$ based on the inlet location, a spanwise wavenumber $\beta = 0.22$ and two values of $N_y$. The least stable mode evolves towards larger negative values when moving along the streamwise coordinate. This characterises the expected exponential growth of the disturbance when moving downstream. Values of the dimensionless imaginary part of the least stable span from $\alpha_i = -0.15$ at $x = 0.1$ to $\alpha_i = -0.56$ at $x = 20$, with a corresponding $\alpha_r = 0$. Figure 3.10b also reveals a second unstable mode, with a lower amplification $\alpha_i = -0.16$ and $\alpha_r = 0$ at $x = 20$.

The pseudospectrum for the generalised eigenvalue problem (eq. (3.17)) can be determined by computing the boundaries of the resolvent norm (see section 1.3.2). We use the following expression to define the pseudospectrum (Dorsselaer, 1996; Trefethen, 1997),

$$\Lambda_\epsilon(\mathcal{A},\mathcal{B}) = \{z \in \mathbb{C} : \sigma_{\min}(z\mathcal{B} - \mathcal{A}) \leqslant \epsilon\}. \tag{3.18}$$

Computing the smallest singular value $\sigma_{\min}$ defined by eq. (3.18) at $x = 20$ on a $100 \times 100$ grid gives the contours displayed in fig. 3.11, where the eigenvalues plotted in fig. 3.10b have been superimposed. The pseudospectrum provides a measure of the sensitivity of the eigenvalues to a perturbation. The sensitivity is given by the inverse of the singular value $\sigma_{\min}$. Figure 3.11 shows

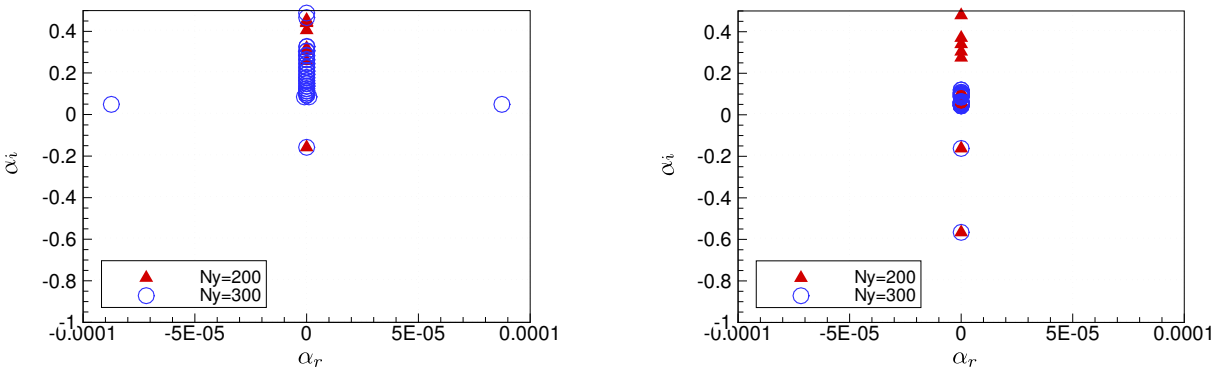


(a) $x = 0.1$ (b) $x = 20$

Figure 3.10: Evolution of the discrete spectrum from $x = 0.1$ (fig. 3.10a) to $x = 20$ (fig. 3.10b) for different values of $N_y$. The Görtler number is $\mathsf{G} = 4$ and the spanwise wavenumber is $\beta = 0.22$.

that the degree of non-normality is pronounced in the upper continuous branch of the spectrum, with sensitivities of order $10^6$. The interactions between modes can therefore be accounted for by considering part of the upper branch when computing the optimal perturbations, which is done in the following. The unstable modes do not contribute to these interactions.

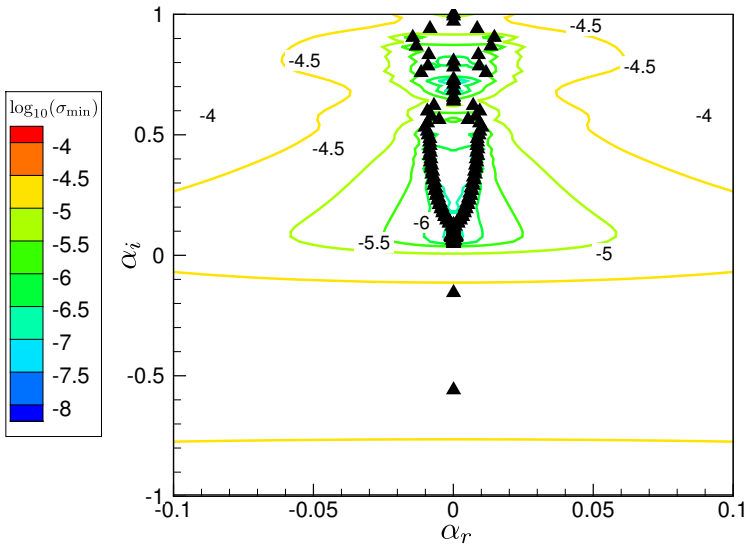


Figure 3.11: Spectrum (with $N_y = 300$) and pseudospectrum (iso-contours of $\log_{10}(\sigma_{\min})$) at $x = 20$, with $\mathsf{G} = 4$ and $\beta = 0.22$.

Computations of the pseudospectrum for various Görtler numbers have been carried out, and results are displayed in fig. 3.12. The smallest singular value decreases, with a minimum value of $\sigma_{\min} = 1.8 \times 10^{-7}$ at $\mathsf{G} = 2$ (see fig. 3.12a) to a minimum value of $\sigma_{\min} = 7 \times 10^{-9}$ at $\mathsf{G} = 25$ (see fig. 3.12b). Plotting the contours of the smallest singular value also reveals that the region of non-normality extends when increasing the Görtler number. These results show that the potential for non-normal interactions between modes—and in turn for transient growth—is more noticeable at high Görtler numbers.

Figure 3.13 shows the $N$ factor computed using the modes highlighted in fig. 3.11. Selecting the most non-normal modes on the basis of the pseudospectrum can be referred to as a multimodal

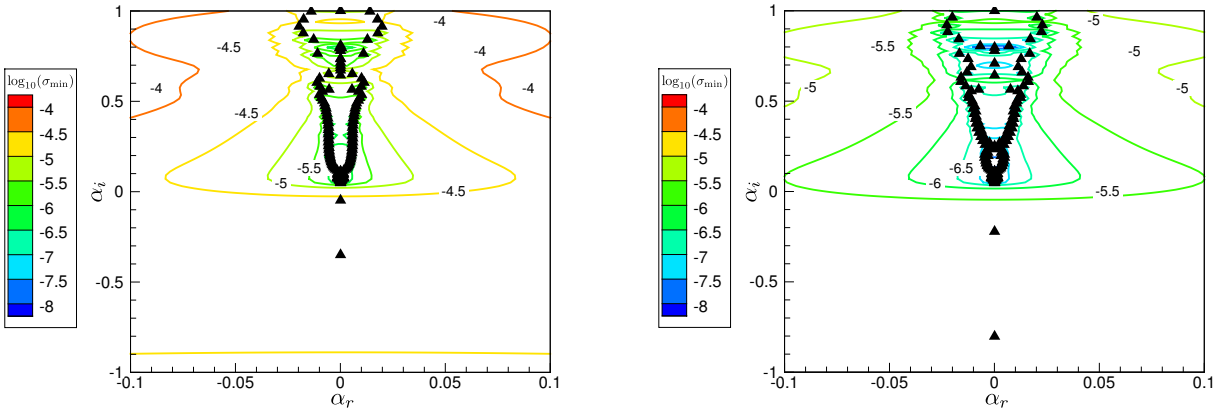


(a) G = 2 (b) G = 25

Figure 3.12: Spectra (with $N_y = 300$) and pseudospectra (iso-contours of $\log_{10}(\sigma_{\min})$) for different Görtler numbers at $x = 20$, with $\beta = 0.22$.

approach. In this approach, the determination of the gain is reduced to the computation of a Rayleigh quotient, as detailed in section 2.2.2. The $N$ factor is based on the maximum of longitudinal disturbance velocity $u$ inside the boundary layer,

$$\begin{aligned} A(x) &= |u(x, y_{\max})|\,; \\ N &= \ln(A(x)/A_0)\,; \end{aligned} \tag{3.19}$$

where $y_{\max}$ is the wall-normal coordinate at each chordwise location $x$ where $|u(x, y)|$ is maximum, while $A_0$ is the initial amplitude of the disturbance at $x_{\text{in}}$, $A_0 = A(x_{\text{in}})$. In fig. 3.13, we compare the mutimodal approach to the optimal approach where the boundary layer is artificially set to a parallel-flow. Both curves coincide, which validates the multimodal approach and ensures that enough modes are taken into account when computing the optimal perturbation.

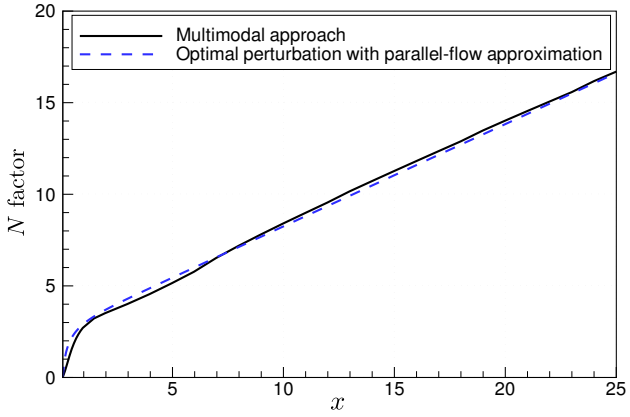


Figure 3.13: Validation of the multimodal approach: comparison with the $N$ factor curve computed using the optimal perturbation approach with a parallel boundary layer. The Görtler number is set to G = 4 and the spanwise wavenumber is $\beta = 0.22$.

Having validated the multimodal approach, we now want to quantify the effect of the parallel-flow approximation. Figure 3.14 displays several $N$ factor curves for both parallel and non-parallel flows. Computation of the $N$ factor for the local analysis is done by following the evolution of the least

stable mode along the streamwise direction. It uses a Newton-Raphson shooting algorithm, where the initial condition is an approximate value of the least stable mode based on the full spectrum. Figure 3.14 shows that the parallel-flow approximation leads to an overestimation of the $N$ factor (Tumin and Reshotko (2001) also noted a similar trend for a compressible boundary layer over a flat plate). Parallel-flows (dashed lines), both with the local analysis and the multimodal approach, exhibit larger values than their non-parallel counterparts (solid lines).

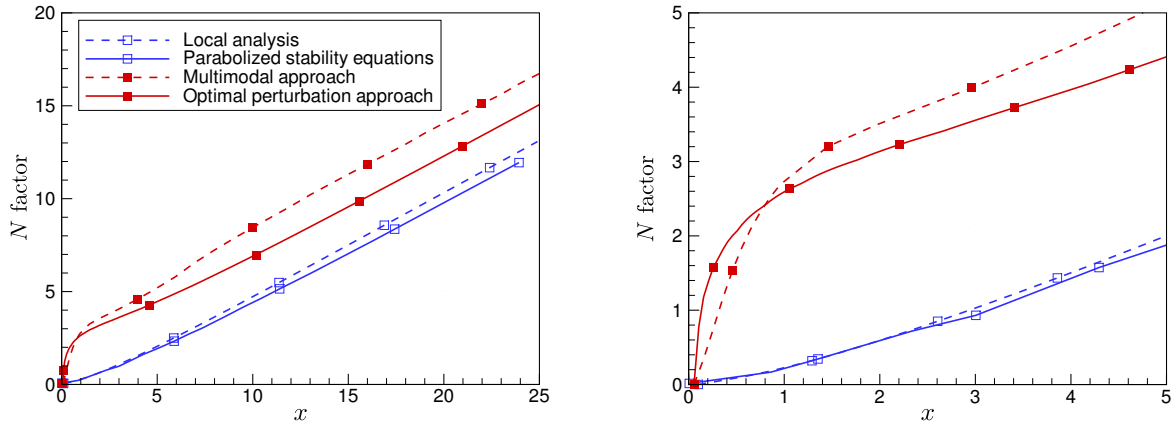


(a) (b) Zoom on the first streamwise locations

Figure 3.14: Comparison of $N$ factor curves computed using the least stable mode only (- - ⊟ - -), the parabolised stability equations (——⊟——), the multimodal approach (- - ■ - -) and the optimal perturbation approach (——■——).

Figure 3.14 also highlights an initial increase of the $N$ factor over the first stations when non-modal interactions are taken into account (filled symbols). Selecting only the least stable mode ($\alpha_i = -0.55$ in fig. 3.11) is insufficient to compute the correct initial growth of the $N$ factor. Taking the most non-normal modes into account based on the pseudospectrum leads to an accurate determination of this region using the multimodal approach. This initial increase corresponds to a phase of transient growth before recovering the amplification of the Görtler instabilities. This initial growth is captured with the optimal approach, which also includes non-parallel effects. Comparing the multimodal approach to the local analysis reveals a difference in $N$ factor of around 4. The same result appears when comparing the PSE and the optimal approach, with a difference in $N$ factor of around 3.5. These differences highlight the need to take transient growth into account when computing disturbances amplification, especially when using transition prediction methods such as the $e^N$ method. This aspect is further developed in the next chapter which considers surface waviness.

Optimal disturbances developing over concave walls have been determined. The receptivity analysis shows a shift in the receptivity process, with disturbances localised closer to the wall as the inlet location moves downstream towards the outlet location. A parametric study of the initial location also reveals that the boundary layer is more prone to be destabilised as disturbances are introduced closer to the leading edge. Computing the neutral curve associated with the fastest growing optimal perturbation defines the envelope of the unstable domain. Such perturbation is determined with a new criterion, in which the outlet location where the gain is maximised is iteratively set to the first neutral position. This approach restores the concept of a unique neutral curve for the Görtler problem.
A parallel-flow approximation has been adopted to investigate the potential for non-normal modes interactions. Computing the $N$ factor reveals an initial phase of transient growth that is not taken into account by classic theories. This initial growth proves to be non-negligible, in particular within the scope of predicting transition locations based on the $N$ factor. This aspect is further investigated in the next chapter, where surface waviness and practical transition prediction methods are considered.

Chapter 4

# Application to surface waviness

Transition prediction for compressible boundary-layer flows over wavy surfaces is investigated in this chapter. This is done by computing the fastest growing optimal disturbance, as detailed in the previous chapter. First a concave/convex wall following a flat plate is investigated. The evolution from Klebanoff modes developing on the flat plate region to Görtler vortices amplified over the concave region is particularly considered. Surfaces with multiple oscillations are then studied for both incompressible and compressible flows. Non-modal amplification of Görtler vortices is computed using the optimal initial disturbance and compared to modal amplification. Finally, a periodic curvature superimposed over a constant concave curvature is considered, that is representative of curved surfaces featuring unintentional waviness.

## Contents

## 4.1 Concave/convex surface

### 4.1.1 Destabilising/stabilising effect

Efforts to increase laminar flow past a surface are still ongoing as an attempt to reduce friction drag. Laminar flow performances strongly depends on the accurate prediction of laminar-turbulent transition location. This location is affected by wall imperfections inherent to real surfaces which may be unintentionally wavy (Wie and Malik, 1998). Linear stability theory combined with the $e^N$ method (see section 1.2.2.1) is considered a standard tool for transition prediction. Models representing the $N$ factor increase $\Delta N$ in terms of characteristics of the wall imperfections are developed (Crouch *et al.*, 2006; Perraud and Arnal, 2013). Transition location is then determined based on $N$ factor curves computed without surface imperfection with the $\Delta N$ correction. The following focuses on the initial phase of transient growth arising prior to the development of Görtler vortices on wavy walls.

The flow over a curved wall with periodic curvature that can be both convex and concave is first investigated. This problem was first studied by Saric and Benmalek (1991), and later by Hennequin (1993), using parabolised stability equations as local analysis cannot address this problem. The reference length is set to $L = 1\,\mathrm{m}$ and the curvature is given by

$$\begin{cases} \dfrac{1}{R_c} = 0 \text{ for } x < 0.3\,\mathrm{m}\,; \\ \dfrac{1}{R_c} = 4\sin\left(\dfrac{2\pi(x-0.3)}{0.7}\right) \text{ for } x \geqslant 0.3\,\mathrm{m}. \end{cases} \tag{4.1}$$

After the first part of the wall that consists of a flat plate with zero curvature, the wall is first concave with a minimum radius of curvature of $0.25\,\mathrm{m}$ at $x = 0.475\,\mathrm{m}$. The surface then becomes convex after the inflection point at $x = 0.65\,\mathrm{m}$. Figure 4.1 displays the radius of curvature $R_c$ along with a representation of the geometry (where $y$ is scaled with $\delta = L/\sqrt{Re_L}$). The unit Reynolds number is chosen as $Re_u = 1.5 \times 10^6\,\mathrm{m}^{-1}$ with the incoming velocity $U_\infty = 11.3\,\mathrm{m\,s}^{-1}$, and the spanwise wavelength of the vortices is set to $\lambda_\mathrm{d} = 3 \times 10^{-3}\,\mathrm{m}$.

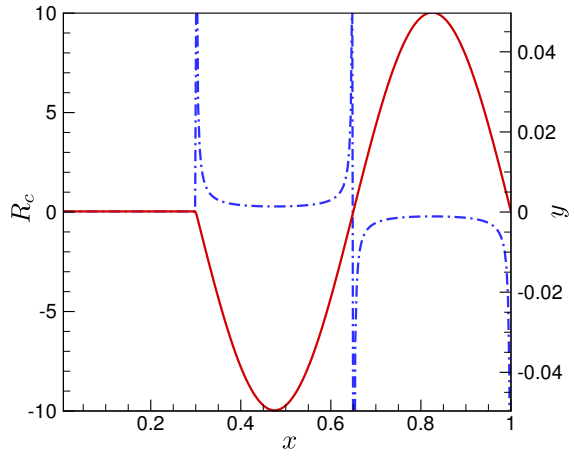


Figure 4.1: Radius of curvature (- · - · -) and geometry (——) for the concave-convex wall.

Computations are carried out using the optimal perturbation approach. Figure 4.2 shows the evolution of the energy along the chordwise location, with $x_\mathrm{out} = 1$. Disturbances introduced at

the leading edge are first damped over the flat plate part. Over the concave part of the wall ($0.3 \leqslant x \leqslant 0.65$), the perturbations are strongly amplified, before being damped again after the inflection point. This illustrates the deep destabilising effect of a concave curvature, and conversely the stabilising effect of a convex wall.

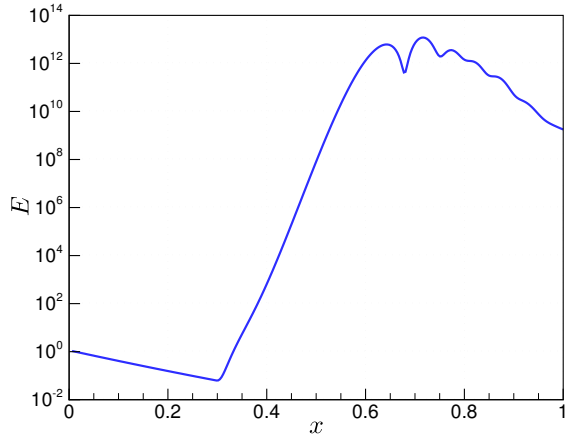


Figure 4.2: Evolution of the energy along the chordwise location. Disturbances are amplified over the concave part of the surface ($0.3 \leqslant x \leqslant 0.65$), then damped after the inflection point.

Vortices form over the concave part, and initially grow stronger while moving towards the wall. Next, as the disturbances evolve downstream, they move away from the wall and become weaker. Over the convex part, a new pair of counter-rotating vortices forms at the wall, as illustrated in fig. 4.3, that rotates in the opposite way. The upper vortices are damped and replaced by the newly formed ones. This result is already mentioned in previous publications, in particular by Saric and Benmalek (1991) who detailed the stabilising effect of a convex curvature. The creation of an additional pair of vortices rotating in the opposite direction compared to the primary instability is also noted. This latter feature has been highlighted by Kalburgi *et al.* (1988b) and will be further detailed in the next section. It also appears in fig. 4.2, where the evolution of the energy is characterised by secondary peaks over the convex surface.

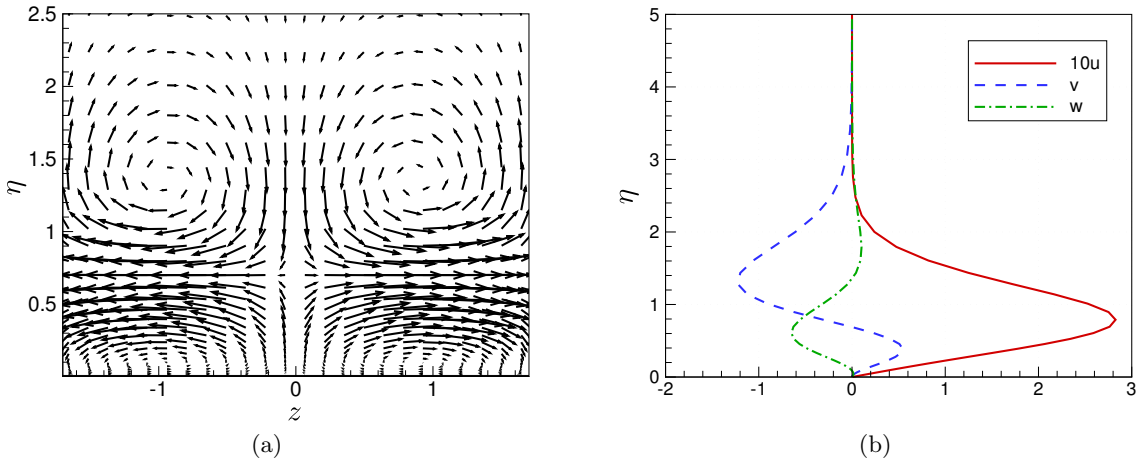


Figure 4.3: Velocity field in the $\eta - z$ plane (where $\eta = y/(2\sqrt{x})$) and velocity profiles of the disturbance components at $x = 0.675$ (convex part).

### 4.1.2 From Klebanoff rolls to Görtler vortices

Transient growth on a flat plate is characterised by streamwise rolls called Klebanoff modes. As detailed in section 1.4.2, the optimal spanwise wavenumber can be determined when computing the optimal perturbation. Transition from a flat plate to a concave surface raises the question of the evolution from Klebanoff modes to Görtler vortices.
The curvature is still defined according to eq. (4.1). This geometry allows the development of Klebanoff rolls over the flat plate part, before the amplification of Görtler vortices over the concave part, that are later damped when the curvature becomes convex. A parametric study on the spanwise wavenumber $\beta$ is realised to determine the optimal wavelength. The outlet locations $x_{\text{out}}$ varies to study the optimal wavenumber for both Klebanoff and Görtler vortices. The end of the flat plate, where Klebanoff vortices are fully developed, is first considered with $x_{\text{out}} = 0.3$. Then $x_{\text{out}} = 0.65$, which represents the end of the concave region, and $x_{\text{out}} = 1$, which is the end of the convex region, are investigated. In the latter two cases, Görtler vortices are supposed to be present. The dimensional spanwise wavenumber $\beta_{\text{d}}$ is scaled with $\delta$, which represents the boundary-layer reference scale at the outlet location $x_{\text{out}}$.

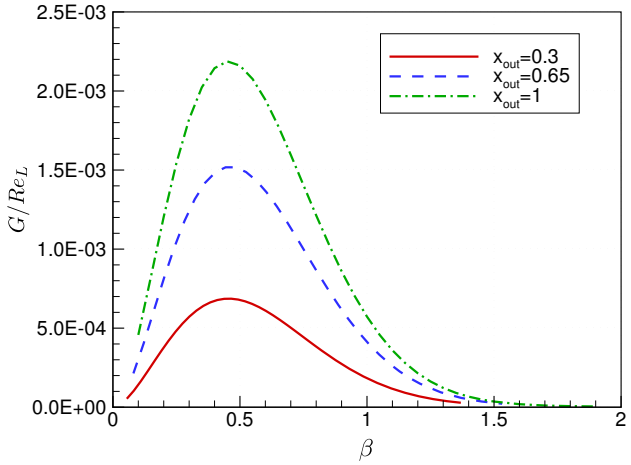


Figure 4.4: Optimal spanwise wavenumber $\beta$ for different outlet locations $x_{\text{out}}$.

Figure 4.4 shows the result of the parametric study for the different outlet locations. The optimal spanwise wavenumber, scaled with the boundary-layer reference length at $x_{\text{out}}$, is the same for the different cases. We find a dimensionless optimal wavenumber $\beta = 0.45$. This wavenumber is known to be related to the largest transient growth of Klebanoff modes in two-dimensional boundary layers (see section 1.4.2). We find the same value for the optimisation over concave and convex surfaces, which means that this wavenumber is also optimal for the Görtler vortices.
Together with comparing the shape functions, this result means that there is a continuous evolution from Klebanof rolls to Görtler vortices, both being optimally excited by similar disturbances. Non-modal instabilities and Görtler rolls share the same characteristics in two-dimensional boundary layers. The difference from a flat plate comes from the centrifugal forces. Over a curved wall, these centrifugal forces maintain the streamwise streaks, which lead to an exponential amplification of the Görtler instabilities.
It is thus reasonable to investigate the transient growth that takes place before the amplification of Görtler vortices. This is done in the next section, which considers curvature with multiple oscillations.

## 4.2 Curvature with multiple oscillations

### 4.2.1 Secondary vortices

Saric and Benmalek (1991) initially solved the Görtler problem by integrating the equations downstream using the parabolised stability equations, *i.e.* marching an initial condition obtained by performing a local linear stability analysis. Following their work, we define the Görtler number to take variable curvature into account,

$$\mathsf{G} = 2\mathsf{G}_0^2 \cos\left(2\pi m \frac{x-1}{x_{\text{out}}-1}\right), \tag{4.2}$$

where $\mathsf{G}_0$ is the Görtler number at the inlet location $x_{\text{in}} = 1$, while the outlet location is fixed to $x_{\text{out}} = 25$. The wall has a maximum concave curvature at the inlet location, the radius of curvature then decreases until the wall becomes convex, as represented in fig. 4.5. The parameter $m$ defines the number of wavelengths, where $m = 0.5$ represents a single oscillation from concave to convex curvature. The wavenumber is $\beta = 0.22$, so the vortices have a spanwise wavelength $\lambda_{\text{d}} = 2.3 \times 10^{-4}$m that matches the dimensionless wavenumber defined by Floryan and Saric (1982).

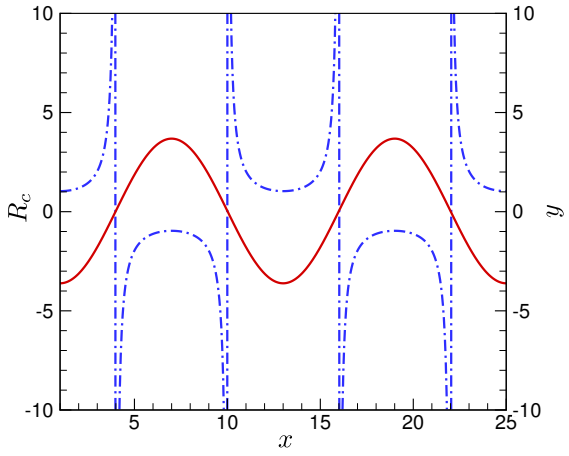


Figure 4.5: Radius of curvature (-·-·-) and geometry (——) for a wall with multiple oscillations ($m = 2$).

Figures 4.6 to 4.10 compare the velocity fields and profiles of the perturbation at various locations. The configuration illustrated in fig. 4.5 ($m = 2$) is considered, with $\mathsf{G}_0 = 2$ and $\beta = 0.22$, while $\eta$ is redefined to match the definition from Saric and Benmalek (1991): $\eta = y/\sqrt{x}$. We focus on locations between $x = 5$ and $x = 10$, that is from the end of the first concave part to the end of the first convex part.

As the perturbation moves downstream along the concave wall, the vortices move towards the wall and become stronger. Further downstream, as the curvature decreases, the vortices become weaker and tend to move away from the wall (fig. 4.6). When curvature becomes convex, a new pair of counter-rotating vortices forms at the wall, that rotates in the opposite direction as the primary instability (fig. 4.7). The initial pair of vortices is gradually lifted off and its amplitude decreases (figs. 4.8 and 4.9) before vanishing (fig. 4.10). This process is then repeated for each oscillation of the wall. As explained in the previous section, this behaviour is typical of flows over curved walls with concave and convex parts and is mentioned in previous publications (see *e.g.* Kalburgi *et al.*, 1988b).

We are therefore able to correctly describe the behaviour of Görtler instabilities. In addition, our calculations also capture the non-modal growth that gives supplementary information on the

dynamic of boundary layers over curved walls. The influence of transient growth is precisely investigated in the following.

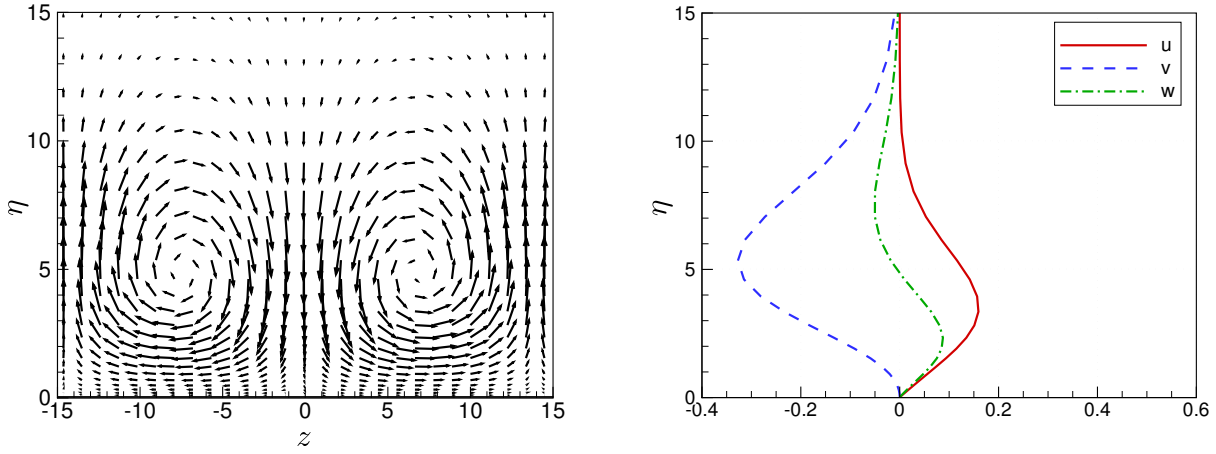


(a) (b)

Figure 4.6: $w - v$ velocity field in the $\eta - z$ plane and velocity profiles of the perturbation components at $x = 5$ (beginning of the convex part).

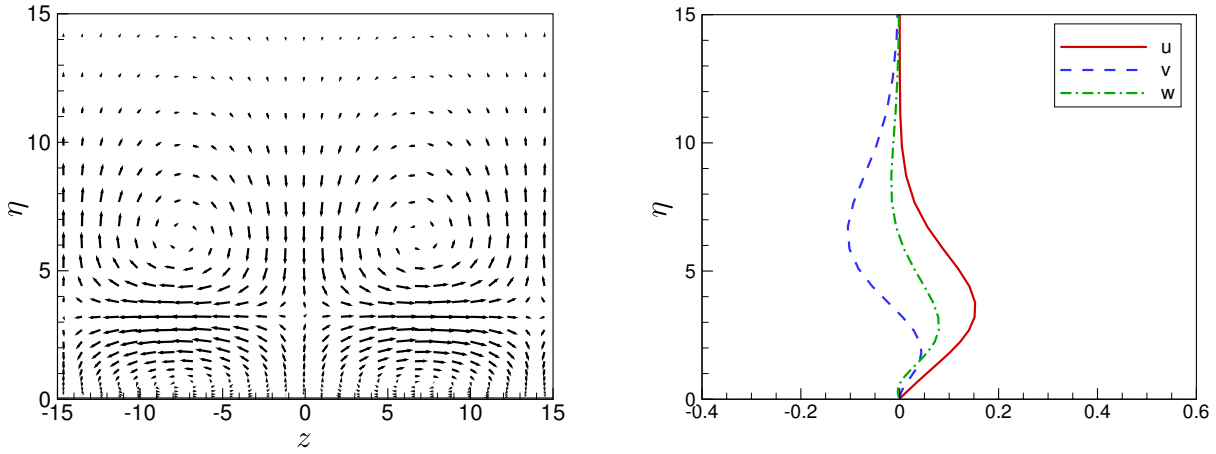


(a) (b)

Figure 4.7: $w - v$ velocity field in the $\eta - z$ plane and velocity profiles of the perturbation components at $x = 5.52$.

### 4.2.2 Initial transient growth

We quantify the amplification of disturbances using the $N$ factor based on the maximum longitudinal velocity $u$ inside the boundary layer. Recalling eq. (3.19), this yields

$$\begin{aligned} A(x) &= |u(x, y_{\max})|\,; \\ N &= \ln(A(x)/A_0)\,. \end{aligned} \tag{4.3}$$

When considering wavy walls, the amplitude—or equivalently the $N$ factor—can be defined in two ways: for only one pair of vortices by following the local maximum of $u$ of the vortices until

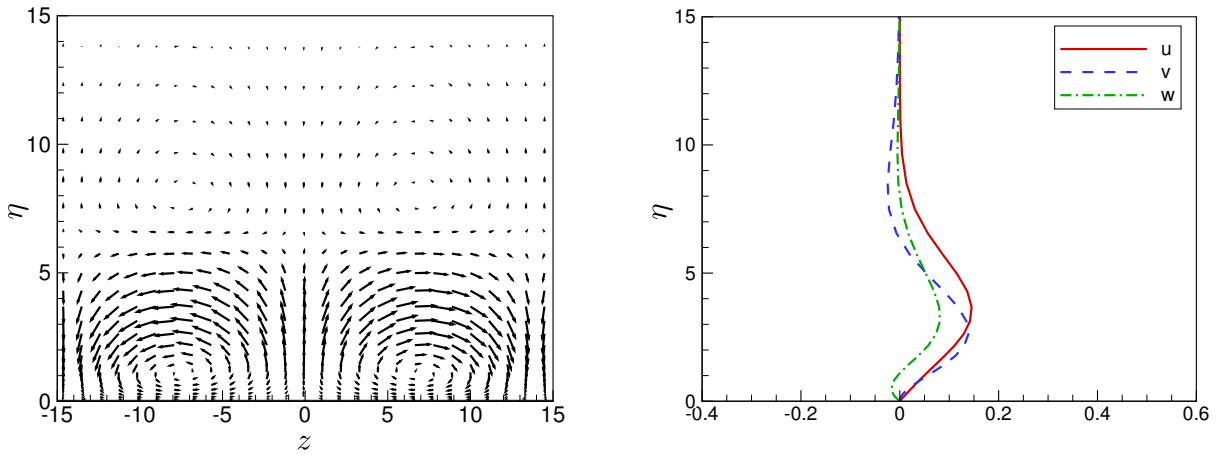


(a) (b)

Figure 4.8: $w - v$ velocity field in the $\eta - z$ plane and velocity profiles of the perturbation components at $x = 5.76$.

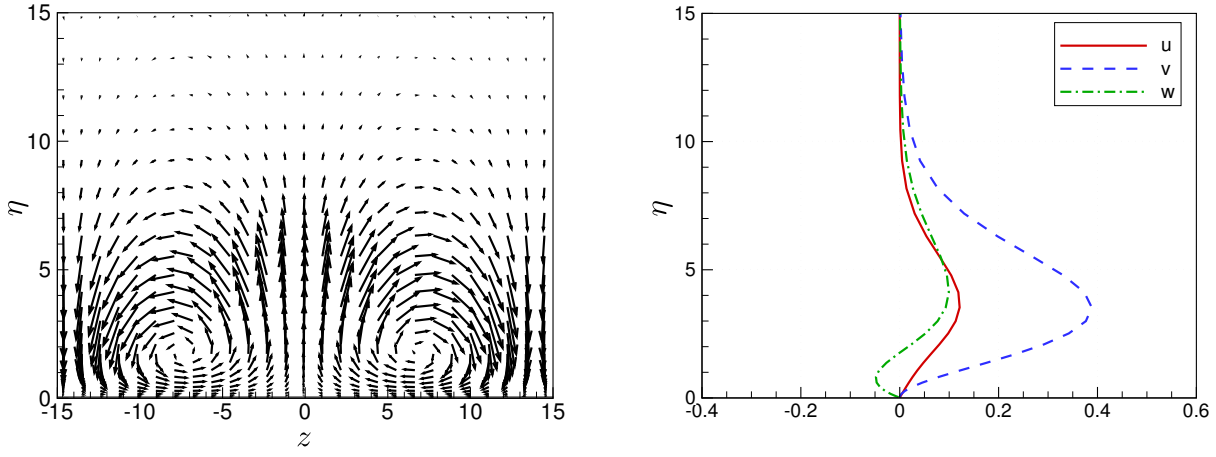


(a) (b)

Figure 4.9: $w - v$ velocity field in the $\eta - z$ plane and velocity profiles of the perturbation components at $x = 6.25$.

it vanishes ; or for all the vortices using the global maximum of $u$. Figure 4.11 compares the two approaches. The $N$ factor associated with all the vortices features a secondary maximum at $x \approx 21$. This maximum is related to the growing pair of counter-rotating vortices that becomes dominant while the first pair decreases. The geometry is also plotted in fig. 4.11 (with $m = 0.5$). When the curvature becomes convex ($y > 0$), the $N$ factor strongly decreases, which illustrates the aforementioned stabilising effect of convex surfaces on disturbances.

Figure 4.12 displays the evolution of the $N$ factor along the chordwise location $x$ for $\mathsf{G}_0 = 2$ and $\beta = 0.22$. We consider both a constant maximum curvature ($m = 0$) and a variable curvature ($m = 0.5$). The results are compared with computations by Saric and Benmalek (1991) using the PSE. Their results are scaled by a factor 0.5 for comparison as they defined the $N$ factor as $N = \ln(A/A_0)$ with $A = \int_y u^2 \, \mathrm{d}y$.

The $N$ factor curve obtained using the optimal approach features an initial phase of transient growth over the first chordwise locations, close to $x_{\text{in}}$. This initial non-modal growth leads to an early amplification of the $N$ factor. At the end of this region, the $N$ factor has reached a non-negligible

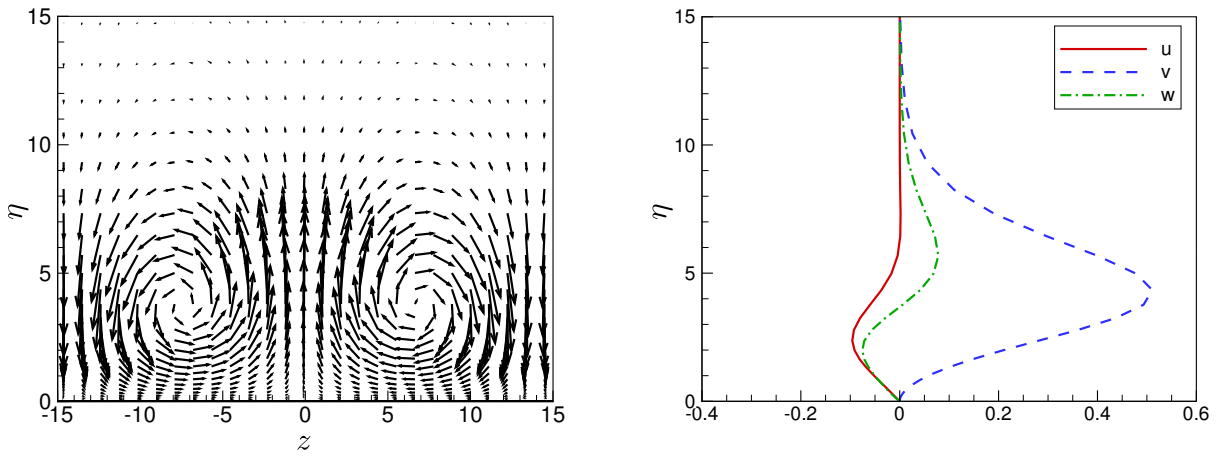


(a) (b)

Figure 4.10: $w - v$ velocity field in the $\eta - z$ plane and velocity profiles of the perturbation components at $x = 10$.

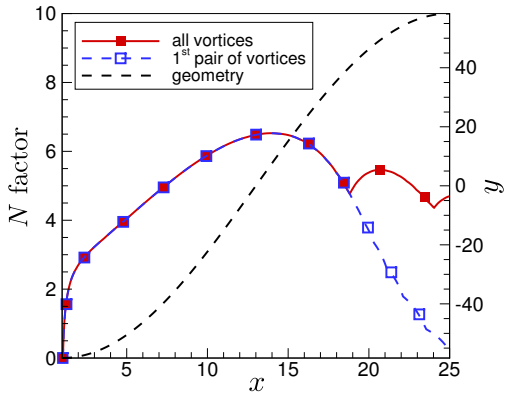


Figure 4.11: $N$ factor for the first pair of vortices only (- -⊟- -) and for all the vortices (—■—): the latter features a second maximum where the second pair of vortices that forms at the wall becomes dominant. The dashed line shows the geometry of the wall ($m = 0.5$).

value of about $N \simeq 3.5$ that is not predicted by linear stability theory. After this zone, the $N$ factor recovers the evolution associated with modal amplification, which is captured by the PSE.

Figure 4.13 illustrates the disturbance growth for a constant and maximum wall curvature and for variable curvatures with different number of oscillations of the wall (parameter $m$). The $N$ factor is here evaluated by taking all vortices into account. As the number of oscillations increases (larger values of $m$) and the length of the initial concave part is reduced, the $N$ factor undergoes a less important initial phase of transient growth. Overall, disturbances growth on a wall with variable curvature is always smaller than on a concave surface with constant curvature. In fig. 4.13, increasing the number of oscillations up to $m = 3$ leads to a difference in $N$ factor of about 10 at the end of the domain ($x = 25$). This shows that convex parts have a globally stabilising effect on the flow. Non-modal growth does not have an impact on the disturbance growth evolution, but provides an initial $\Delta N$ which remains fairly constant while evolving downstream.

Keeping the curvature defined according to eq. (4.2), compressibility effects for a flow over a

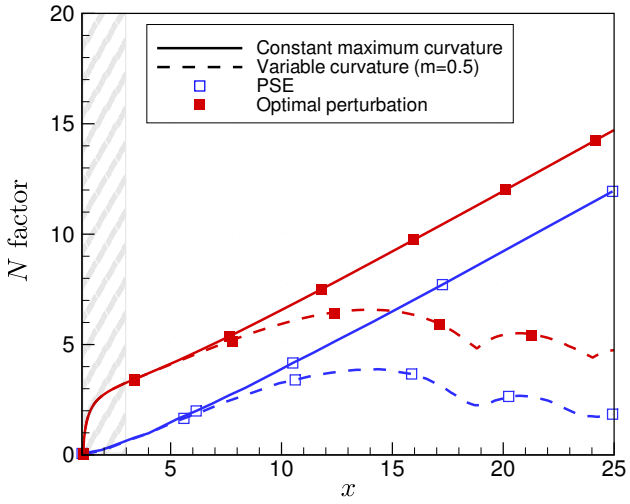


Figure 4.12: $N$ factor curves for constant maximum curvature (——) and $m = 0.5$ (- - -), with $\mathsf{G}_0 = 2$ and $\beta = 0.22$. Comparison between the optimal approach (■) and results obtained by Saric and Benmalek (1991) using the parabolised stability equations (□). The hatched area represents the region where transient growth occurs.

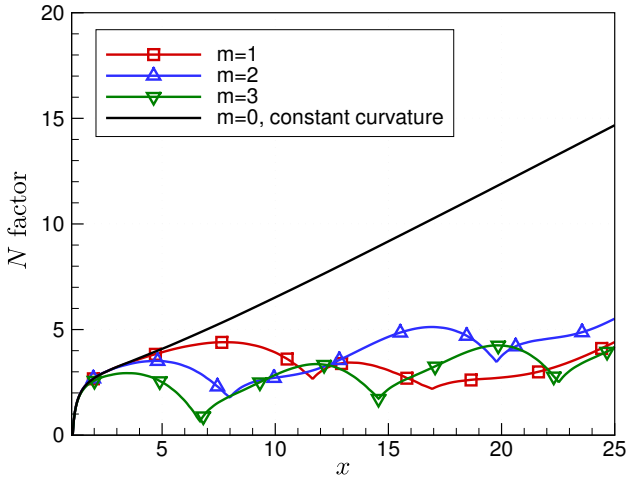


Figure 4.13: $N$ factor along the chordwise locations for different values of $m$, with $\mathsf{G} = 2$ and $\beta = 0.22$.

surface with constant ($m = 0$) and variable ($m = 0.5$) curvature are investigated. The Mach number is successively set to $M = 0,\ 2$ and 4. The evolution of the disturbances growth rate is displayed in fig. 4.14. The $N$ factor of the perturbation decays in both cases when the Mach number increases, which illustrates once more the stabilising effect of compressibility. This effect is double: the initial region of transient growth is spatially reduced and the modal amplification is less important. Although it is reduced to the very first chordwise locations, the initial phase of non-modal growth still provides significant values $\Delta N \approx 2$ that need to be accounted for when predicting transition location. The effect of cooling and heating the wall has also been investigated but no effect on the stability of the flow has been found, with identical values of the $N$ factor.

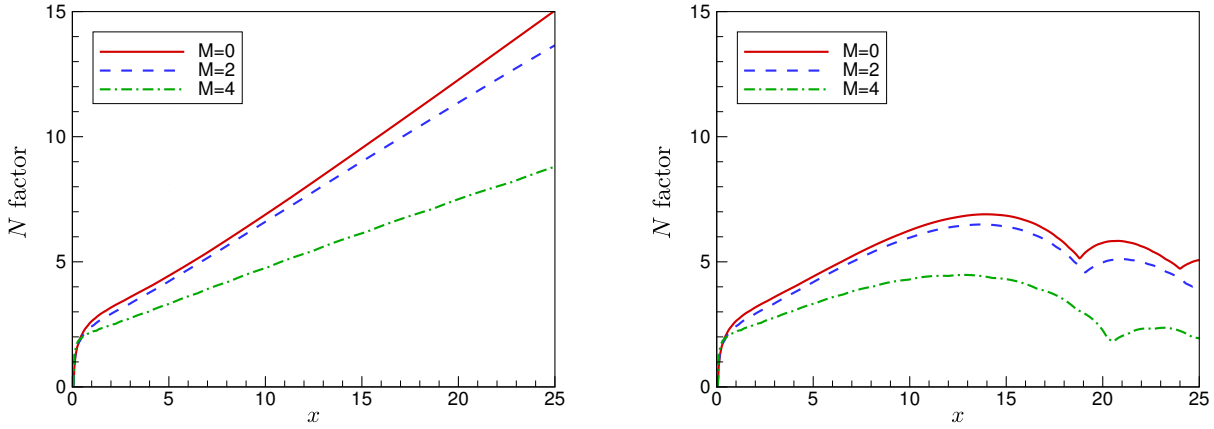


(a) $m = 0$ (b) $m = 0.5$

Figure 4.14: $N$ factor curves for constant (fig. 4.14a) and variable (fig. 4.14b) curvature at different Mach numbers $M = 0,\ 2$ and 4, with $\mathsf{G}_0 = 2$, $\beta = 0.22$.

## 4.3 Periodic curvature superposed on constant curvature

Curved surfaces may themselves exhibit surface imperfections or unintentional waviness. Building on the two previous sections, we now consider the case of periodic curvature superposed on a constant concave curvature. The departure from a constant concave curvature $\kappa_0$ is defined as

$$\kappa = \kappa_0 \left[ 1 + \gamma \sin\left( 2\pi m \frac{x - 1}{x_{\text{out}} - 1} \right) \right], \tag{4.4}$$

where $m$ still represents the number of oscillations of the superposed waviness. The parameter $\kappa_0$ can be linked to the Görtler number at the inlet, $\mathsf{G}_0^2 = \kappa_0 L / Re_\delta$. Figure 4.15 displays periodic waviness superposed to the constant curvature for $\gamma = \pm 0.5$ and $\gamma = \pm 2$. When $|\gamma| < 1$, there is no convex curvature, and the periodic waviness has little effect on the global evolution of the $N$ factor (see fig. 4.15a). Increasing the value of $\gamma$ leads to smaller values of $N$ (see fig. 4.15b). Saric and Benmalek (1991) also highlighted the need for a convex region in order to observe a significant change when superposing periodic waviness on constant curvature. The first chordwise locations still feature an initial phase of transient growth. This non-modal amplification does not depend on the value of $\gamma$.

When we increase the number of oscillations for the superposed waviness (increasing values of $m$), the $N$ factor curves tend to the one of the constant curvature, as illustrated in fig. 4.16. The effect of concave and convex surfaces is reduced due to the larger number of curvature changes. The initial region of non-modal growth is not affected by the increasing values of $m$ and still provides an initial value $\Delta N$.

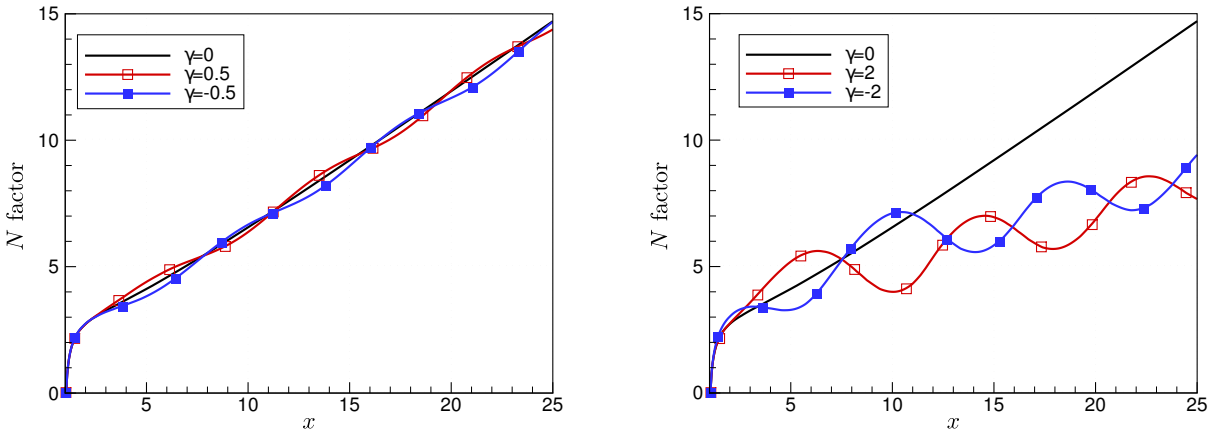


(a) $\gamma = -0.5; 0; 0.5$ (b) $\gamma = -2; 0; 2$

Figure 4.15: $N$ factor curve for a periodic curvature superposed to a constant concave curvature, with $m = 3$, $G_0 = 2$, $\beta = 0.22$ and different values of $\gamma$.

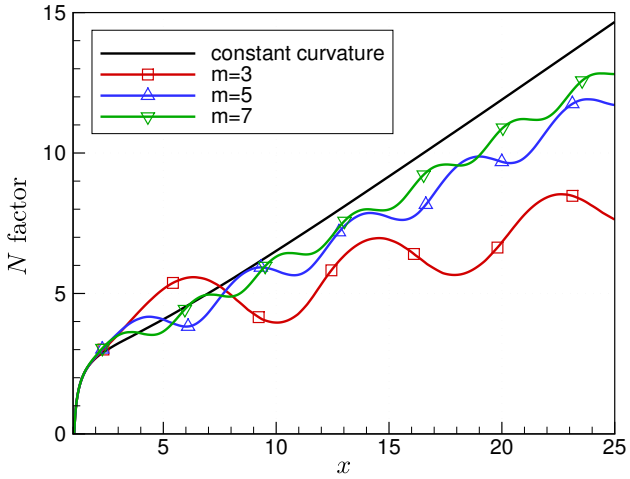


Figure 4.16: $N$ factor curve for a constant departure $\gamma = 2$ and increasing number of oscillations $m$ for the superposed waviness.

We have first considered transition from a flat plate to a concave, then convex, surface. Determining the optimal spanwise wavenumber shows that Klebanoff modes and Görtler vortices are optimally excited by similar structures. They represent the same disturbances, with Görtler instabilities exhibiting an exponential amplification under the action of centrifugal forces. The classical behaviour of Görtler rolls over wavy walls is correctly described by the optimal perturbation approach. In addition, the non-modal growth prior to the modal amplification of Görtler instabilities is also captured. This non-modal growth is further investigated by considering surfaces with multiple oscillations. The region of transient growth over the first chordwise locations provides a significant initial $\Delta N$ value that is not taken into account by classic methods. Compressibility has a stabilising effect on the disturbances amplification. The transient growth region is reduced at large Mach numbers, but still provides an initial $N$ factor value. Overall, non-modal growth is found to play a role before the amplification of Görtler vortices and has to be taken into account for accurate prediction of transition locations. The next part of this work will investigate the role of optimal perturbations as initial inputs to modal amplification in the framework of three-dimensional boundary layers.

# Part III

# Three-dimensional boundary layers

Chapter 5

# Spatial optimal growth in three-dimensional boundary layers

This chapter details the methodology for computing optimal perturbations in three-dimensional boundary layers. The parabolised equations governing the propagation of small disturbances in Falkner-Skan-Cooke boundary layers are first presented. These equations can be solved using a marching technique for a fixed value of the chordwise wavenumber that has to be computed. A new modification of the PSE is thus presented, where the chordwise wavenumber is determined locally to follow the maximum of disturbance energy. As previously, the optimisation problem is solved employing iterations of the direct/adjoint system. Optimal perturbations developing in Falkner-Skan-Cooke boundary layers are then investigated using this method. A parametric study of stationary disturbances in both accelerated and decelerated flows is presented, and the connection between non-modal growth and the exponential amplification of crossflow vortices is particularly considered.

## Contents

## 5.1 Mathematical formulation of the problem

### 5.1.1 Falkner-Skan-Cooke boundary layer

A swept-wing boundary layer is modelled by considering the flow over a flat plate that is infinitely elongated in the spanwise direction, with a given sweep angle and subject to a chordwise pressure gradient. The mean flow is now composed of a streamwise and a crossflow velocity profile. As described in section 1.2.1.2, the disequilibrium between the pressure gradient and the centrifugal forces creates a crossflow velocity profile with an inflection point This inflection point leads to an inviscid instability which in turn gives rise to the crossflow vortices.
Mathematically, the boundary-layers profiles can be described by the similarity solutions called Falkner-Skan-Cooke (FSC) boundary layers (Cooke, 1950). Using the Falkner-Skan (FS) solutions for two-dimensional flows, an additional equation is written for the spanwise profile $W$ (see appendix D.1). A self-similar solution is obtained assuming the following chordwise and spanwise velocity distributions $U_e$ and $W_e$ at the boundary-layer edge,

$$\frac{U_e}{Q_\infty} = \left(\frac{x}{L}\right)^m \qquad \text{and} \qquad \frac{W_e}{Q_\infty} = \sin(\Lambda), \tag{5.1}$$

where $\Lambda$ is the sweep angle and $m = \beta_H/(2-\beta_H)$ where $\beta_H$ is the Hartree parameter characterising the pressure gradient. Having determined the mean velocity profiles $U$, $V$ and $W$, their projections onto the streamwise and crossflow direction are obtained using

$$U_s = U\cos\phi + W\sin\phi \qquad \text{and} \qquad W_s = -U\sin\phi + W\cos\phi, \tag{5.2}$$

where $\phi(x)$ denotes the angle between the streamwise and the chordwise direction at each location $x$, as illustrated in fig. 5.1.

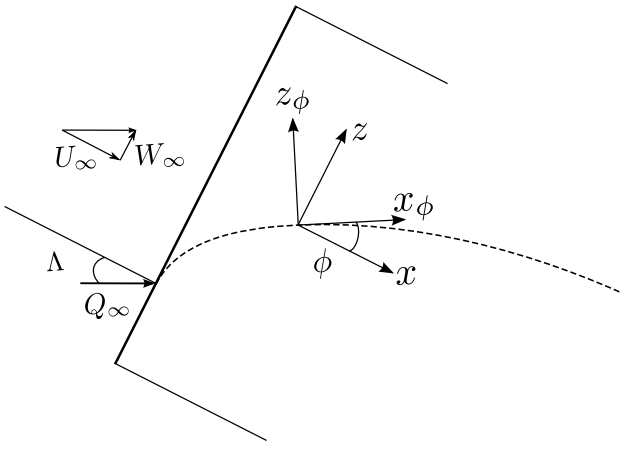


Figure 5.1: Swept flat plate for the development of a FSC boundary layer. The dashed line indicates the external streamline. The coordinates $(x, y, z)$ refer to the chordwise, normal and spanwise directions respectively, while $(x_\phi, y, z_\phi)$ denote the streamwise, normal and crossflow directions respectively. The incoming total velocity $Q_\infty$ is composed of a chordwise velocity $U_\infty$ and a crossflow velocity $W_\infty$. The sweep angle is denoted $\Lambda$ while $\phi(x)$ represents the angle between the chordwise and streamwise direction at each location.

As described in previous sections, the mean flow profiles are computed using the boundary-layer solver *3C3D*. Figure 5.2 shows the velocity profiles, projected onto the streamwise and crossflow directions, for both an accelerated ($\beta_H = 0.1$) and decelerated ($\beta_H = -0.05$) FSC boundary layer at $x/L = 0.01$ and with a sweep angle $\Lambda = 45°$

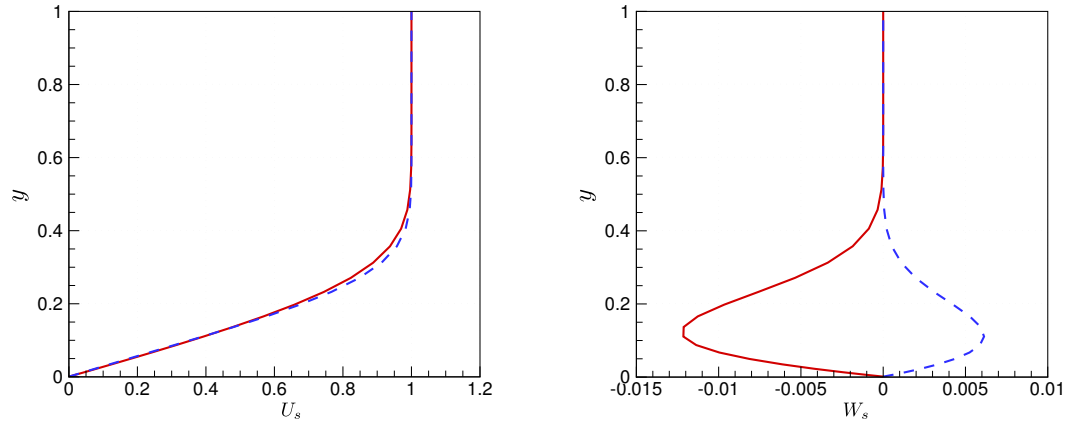


(a) Streamwise velocity profile. (b) Crossflow velocity profile.

Figure 5.2: FSC profiles for an accelerated flow with $\beta_H = 0.1$ (dashed lines) and a decelerated flow with $\beta_H = -0.05$ (solid lines) at $x/L = 0.01$ and with a sweep angle $\Lambda = 45°$. The velocity components are projected onto the streamwise and crossflow directions as illustrated in fig. 5.1.

### 5.1.2 Governing disturbance equations

In order to describe the evolution of disturbances in a three-dimensional boundary layer, we want to obtain a linear and parabolic set of partial differential equations that can be numerically solved using a marching technique. As detailed in section 2.1, we start with the Navier-Stokes equations for an incompressible mean flow $\boldsymbol{Q} = (U, V, W, P)^T$ with small disturbances $\boldsymbol{q'} = (u', v', w', p')^T$ superposed. Neglecting the quadratic terms of the disturbances leads to the linearised Navier-Stokes equations,

$$\begin{aligned} \nabla \cdot \boldsymbol{u'} &= 0, \\ \frac{\partial \boldsymbol{u'}}{\partial t} + (\boldsymbol{u'} \cdot \nabla)\boldsymbol{U} &= -\frac{1}{\rho}\nabla p' + \nu \nabla^2 \boldsymbol{u'}. \end{aligned} \tag{5.3}$$

In these equations, $\boldsymbol{U} = (U, V, W)^T$ represents the mean velocity vector and $\boldsymbol{u'} = (u', v', w')^T$ the associated disturbances ; $p'$ is the pressure disturbance, $\rho$ the density and $\nu$ the kinematic viscosity. In order to describe the evolution of disturbances in three-dimensional boundary-layer flows, we start with the classical PSE approach (see section 1.2.2.2). Disturbances are written in the form

$$\boldsymbol{q'}(x, y, z, t) = \boldsymbol{q}(x, y) \exp(i\Theta(x, z, t)) \,; \tag{5.4a}$$

$$\Theta(x, z, t) = \int_{x_0}^{x} \alpha(\xi)\, \mathrm{d}\xi + \beta z - \omega t \,, \tag{5.4b}$$

where $\boldsymbol{q} = (u, v, w, p)^T$ is the shape function and $\Theta$ is a fast oscillatory phase function. The chordwise and spanwise wavenumbers are denoted $\alpha$ and $\beta$, whereas $\omega$ is the angular frequency. In the PSE method, the chordwise wavenumber is a complex number depending on $x$, while the shape function also depends on $x$. This ambiguity is removed using a normalisation condition of the form

$$\int_0^\infty \boldsymbol{q}^H \frac{\partial \boldsymbol{q}}{\partial x}\, \mathrm{d}y = 0 \tag{5.5}$$

which ensures that the growth and oscillation of the disturbance are captured in the phase function (*i.e.* $\partial \boldsymbol{q}/\partial x \ll i\alpha \boldsymbol{q}$), and thus ensures a slow variation of the shape function in the chordwise direction. Equation (5.5) yields two conditions to determine the real and imaginary parts of the

chordwise wavenumber $\alpha$. However, if this approach is appropriate to study the modal amplification of disturbances, it falls short of capturing the transient behaviour. Parabolised stability equations focus on the exponential growth of a given mode and is thus inappropriate to study the interactions between non-normal modes that constitute non-modal growth. Tempelmann *et al.* (2010) modified the PSE to account for both modal and non-modal growth of disturbances whose lines of constant phase are almost aligned with the external streamline. The chordwise wavenumber is prescribed as a real number based on lines of constant phase. In section 5.2, we review this method and propose a new method for computing the chordwise wavenumber $\alpha$.
In order to obtain a parabolised system, variables in eq. (5.3) are scaled to compare the relative order of the different terms. For two-dimensional flows, the boundary-layer scaling employed to study the spatial non-modal evolution of optimal perturbations has been introduced in section 2.1. The main length scales are the reference scale $L$ in the chordwise direction and a measure of the boundary-layer thickness $\delta = {}^{L}/\sqrt{Re_L}$ in the wall-normal direction. However, the scaling proposed by Andersson *et al.* (1999) or Luchini (2000) has to be modified for three-dimensional flows. The spanwise disturbance velocity component can no longer be considered $\mathcal{O}(Re_\delta^{-1})$ but is of the same order as the chordwise disturbance velocity $u$. We follow the approach of Levin and Henningson (2003) who extended the study of non-modal streaks in Falkner-Skan boundary layers to determine the exponential growth of disturbances. Additionally to the terms coming from the boundary-layer scaling, they included terms that originate from a scaling based on the PSE to account for modal growth. In what follows, we use the boundary-layer and PSE scaling presented in table 5.1.

| | $x$, $z$ | $y$ | $U$, $W$ | $V$ | $u$, $w$ | $v$ | $p$ | $\alpha$ | $\beta$ | $\omega$ |
|---|---|---|---|---|---|---|---|---|---|---|
| Non-modal | $L$ | $\delta$ | $U_\infty$ | $U_\infty\delta/L$ | $U_\infty$ | $U_\infty\delta/L$ | $\rho U_\infty^2\delta^2/L^2$ | $1/\delta$ | $1/\delta$ | $U_\infty/L$ |
| Modal | $\delta$ | $\delta$ | $U_\infty$ | $U_\infty$ | $U_\infty$ | $U_\infty$ | $\rho U_\infty^2$ | $1/\delta$ | $1/\delta$ | $U_\infty/\delta$ |

Table 5.1: Boundary-layer (non-modal) and PSE (modal) scalings for three-dimensional incompressible flows.

Both scalings are applied to the disturbances equations (5.3). Only terms of order higher than $Re_\delta^{-1}$ with respect to both scalings are neglected. This means that the resulting equations are valid for modal and non-modal growth. Considering the boundary-layer scaling, terms $\mathcal{O}(1)$ and $\mathcal{O}(Re_\delta^{-1})$ yield

$$u_x + iRe_\delta\alpha u + v_y + iRe_\delta\beta w = 0, \tag{5.6a}$$

$$(U_x + iRe_\delta\alpha U + iRe_\delta\beta W - i\omega)u + Uu_x + Vu_y + U_y v + \frac{p_x}{Re_\delta^2} + \frac{i\alpha p}{Re_\delta} = u_{yy} - k^2 u, \tag{5.6b}$$

$$(V_y + iRe_\delta\alpha U + iRe_\delta\beta W - i\omega)v + Uv_x + Vv_y + V_x u + p_y = v_{yy} - k^2 v, \tag{5.6c}$$

$$(iRe_\delta\alpha U + iRe_\delta\beta W - i\omega)w + Uw_x + Vw_y + uW_x + vW_y + \frac{i\beta p}{Re_\delta} = w_{yy} - k^2 w, \tag{5.6d}$$

where $k^2 = \alpha^2 + \beta^2$. In these equations, the term $uV_x$ in eq. (5.6c) is $\mathcal{O}(Re_\delta^{-2})$ for the PSE scaling, but is not negligible for the boundary-layer scaling. It is therefore important to take this term into account to describe the transient evolution of disturbances (Bagheri and Hanifi, 2007). Physically, this means that terms that describe non-modal growth are added to the PSE formulation that describes exponential amplification.
As it is, these equations are only quasi-parabolic due to the ellipticity introduced by the chordwise disturbance pressure gradient $p_x$ in eq. (5.6b). For small step sizes $\Delta x$, numerical instabilities appear

in the marching solution (Airiau, 1994). The term $p_x$ is then omitted to relax these instabilities, as suggested for the classical PSE by Li and Malik (1996). Comparisons with DNS show that $p_x$ also has a negligible effect on the results in the case of the modified PSE (Tempelmann *et al.*, 2010).
When studying two-dimensional boundary layers, the parabolised equations are independent of the Reynolds number which is implicitly contained in the scaling employed (see eq. (2.4)). For three-dimensional boundary layers, the Reynolds number arises explicitly in the equations. This means that disturbances will evolve from a subcritical regime (*i.e.* stable with respect to exponential amplification) to a supercritical regime.
System (5.6) can now be solved using a marching technique to propagate a given initial condition. The resulting disturbances have to verify the boundary conditions

$$u = v = w = 0 \quad \text{at } y = 0, \tag{5.7a}$$

$$u = w = p = 0 \quad \text{at } y = y_{\max}. \tag{5.7b}$$

Equations (5.6) can also be expressed in operator form according to

$$\mathcal{L}\boldsymbol{q} = 0, \tag{5.8}$$

where $\mathcal{L}$ is a linear operator that can be expanded in the form

$$\mathcal{L} = \mathcal{A} + \mathcal{B}\frac{\partial}{\partial y} + \mathcal{C}\frac{\partial^2}{\partial y^2} + \mathcal{D}\frac{\partial}{\partial x}. \tag{5.9}$$

Details of the operators $\mathcal{A}$, $\mathcal{B}$, $\mathcal{C}$ and $\mathcal{D}$ are presented in appendix D.2.

## 5.2 Modification of the parabolised stability equations

At this point, we wish to solve for the chordwise wavenumber $\alpha$ and the shape functions $\boldsymbol{q} = (u, v, w, p)^T$ (eq. (5.4a)). The parabolised equations (5.6) can be solved using a marching technique to obtain the shape functions for a given, but still unknown, chordwise wavenumber $\alpha$.
Under the parallel-flow approximation, this wavenumber is given by a dispersion relation. In the PSE, the idea is to use an additional relation called a normalisation condition to determine $\alpha$ (see section 1.2.2.2). In this section, the method proposed by Tempelmann *et al.* (2010) to compute the chordwise wavenumber is reviewed. A new method is then presented that is rooted in the fixed $\beta$ strategy and determines the chordwise wavenumber to follow the maximum of disturbance energy. In both cases, the aim is to compute $\alpha$ to ensure that the periodic variations of the disturbances are captured by the oscillatory function $\Theta$ detailed in eq. (5.4b).

### 5.2.1 Lines of constant phase (Tempelmann *et al.*, 2010)

In the approach employed by Tempelmann *et al.* (2010), the chordwise wavenumber is considered as a real function of the chordwise location. This wavenumber can be determined from the angle $\phi$ between the streakline and the chordwise direction (see fig. 5.3) according to

$$\alpha(x) = -\tan(\phi(x))\beta. \tag{5.10}$$

The angle $\phi$ (or equivalently the wave vector $\boldsymbol{k}$) is not generally known. However, the propagation of the waves is known to be perpendicular to the lines of constant phase. The trajectory of these lines can then be related to $\phi$ through

$$\frac{\partial z}{\partial x} = \tan(\phi(x)). \tag{5.11}$$

The determination of the lines of constant phase can be based on several quantities. The choice of the disturbance velocity component that contains most of the disturbance energy ensures that most of the oscillations in the chordwise direction are captured by $\alpha$. As optimal perturbations take the form of streaks, the quantity $u_\phi$ perpendicular to the wave vector characterises the disturbance energy. The chordwise wavenumber $\alpha$ is then determined iteratively based on the line of constant phase of $A$, defined as

$$A(x) = \max_y(u_\phi(x,y)). \tag{5.12}$$

In the first iteration, the external streamline acts as a guess for the line of constant phase and the direct system is solved. Based on the first solution $u_\phi$, the angle $\phi$ and the chordwise wavenumber $\alpha$ are updated and used to solve the next iteration. This procedure is repeated until the energy growth has converged. It is important to note that this iterative procedure is global, contrary to

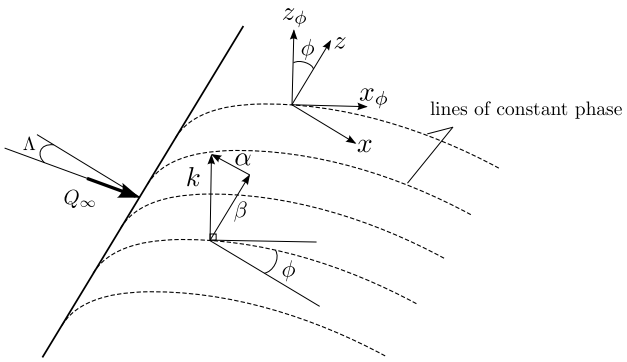


Figure 5.3: Lines of constant phase in a three-dimensional boundary layer. The wave vector $\boldsymbol{k} = (\alpha, \beta)^T$ is represented.

the normalisation condition that takes place in the PSE. This means that the direct equations are first solved on the whole domain to $x_{\text{out}}$. The chordwise wavenumber $\alpha(x)$ is then updated globally. In the PSE, the normalisation condition is ensured iteratively at each station before marching to the next one.
Tempelmann et *al.* noted that the quantity $A(x)$ defined according to eq. (5.12) only correctly describes the streaks after a sufficient distance downstream. Before that, the streak is not fully formed and disturbance velocity components $v$ and $w_\phi$ also contain a significant part of the disturbance energy.

This procedure can also be interpreted in terms of a normalisation condition, in a manner similar to what has been described for the PSE. A real wavenumber can be defined in the local framework according to the scalar relation

$$\tilde{\alpha}(x,y) = \alpha(x) - \Re\left(i\frac{1}{A}\frac{\partial A}{\partial x}\right). \tag{5.13}$$

In this equation, $\Re$ denotes the real part of the complex fraction, and $A(x)$ is a complex amplitude chosen to scale the shape function so that

$$\boldsymbol{q}(x,y) = A(x)\tilde{\boldsymbol{q}}(x,y), \tag{5.14}$$

where $\tilde{\boldsymbol{q}}(x,y)$ is the normalised shape function. Equation (5.13) means that disturbance oscillations are contained in the oscillatory function (through $\alpha$) and in the shape function (through the

term $\mathfrak{R}(i/A\,\partial A/\partial x)$. The complex amplitude can be expanded as $A(x) = |A(x)|\exp(i\vartheta(x))$, which leads to

$$i\frac{1}{A}\frac{\partial A}{\partial x} = i\frac{1}{|A|}\frac{\partial |A|}{\partial x} - \frac{\partial \vartheta}{\partial x}. \tag{5.15}$$

Enforcing that the periodic variations of the disturbances are captured by the exponential part of the disturbances in turn yields the normalisation condition on the phase for the real wavenumber

$$\mathfrak{R}\left(-i\frac{1}{A}\frac{\partial A}{\partial x}\right) = 0 \iff \frac{\partial \vartheta}{\partial x} = 0. \tag{5.16}$$

Going back to eq. (5.4), the disturbances can be written as

$$\boldsymbol{q}'(x,y,z,t) = |A(x)|\exp(i\vartheta(x))\tilde{\boldsymbol{q}}(x,y)\exp(i\Theta(x,z,t)), \tag{5.17}$$

which may be reformulated as

$$\boldsymbol{q}'(x,y,z,t) = |A(x)|\tilde{\boldsymbol{q}}(x,y)\exp(i\Theta'(x,z,t))\,; \tag{5.18a}$$

$$\Theta'(x,z,t) = \vartheta(x_0) + \int_{x_0}^{x}\left(\alpha(\xi) + \frac{\partial \vartheta}{\partial \xi}\right)\mathrm{d}\xi + \beta z - \omega t. \tag{5.18b}$$

The normalisation condition $\partial\vartheta/\partial x = 0$ can be enforced iteratively according to

$$\alpha^{(k+1)} = \alpha^{(k)} + \frac{\partial \vartheta}{\partial x}. \tag{5.19}$$

### 5.2.2 Fixed $\alpha_r$ strategy (present work)

In this work, we choose a different approach to determine the chordwise wavenumber. This new method is similar to the fixed $\beta$ strategy employed in the local stability analysis (see section 1.2.2.1), where the maximum amplification rate is computed for fixed values of the frequency $f$ and wavenumber $\beta$. The maximisation is then done with respect to both parameters to obtain the envelope of $N$ factor.

As previously, $\alpha$ is chosen to be a real function of the chordwise location, $\alpha = \alpha_r(x)$. The parabolised equations (5.6) are solved up to a given location $x_i$. At this location, $\alpha_r$ is determined in order to maximise the local energy at the next station $x_{i+1}$. The chordwise wavenumber at $x_i$ is determined iteratively based on its value at the previous location $x_{i-1}$. The local energy is defined as

$$E(x) = \int_0^{y_{\max}} (u^2 + v^2 + w^2)\,\mathrm{d}y, \tag{5.20}$$

for an incompressible flow, in the wing coordinates system $(x, y, z)$. We use the total disturbance energy to be able to capture the most amplified perturbations over the first locations where the streak is not yet fully formed. The first iteration uses the wavenumber based on the streamline according to

$$\alpha = -\tan(\phi)\beta, \tag{5.21}$$

where $\phi$ denotes the streamline angle defined as $\phi = \arctan(W_e/U_e)$, with $W_e$ and $U_e$ the mean flow velocity components at the boundary-layer edge in the spanwise and chordwise directions respectively.
Hence, we determine the real-valued wavenumber to obtain a maximum local disturbance energy at the next location. This means that we ensure that the chordwise wavenumber captures most of the

oscillations in the chordwise direction.
Contrary to the approach based on lines of constant phase, the wavenumber is determined locally. At each location, $\alpha$ is computed to follow the maximum of disturbance energy before marching to the next location.

It is possible to consider a complex-valued chordwise wavenumber, thus capturing the growth of the disturbances $\boldsymbol{q}'$ in the phase function. This is done by setting

$$\Im(\tilde{\alpha}) = \Im(\alpha) - \frac{1}{|A|}\frac{\partial |A|}{\partial x}, \tag{5.22}$$

where $\Im$ denotes the imaginary part and $A(x) = |A(x)|\exp(i\nu(x))$ is chosen according to eq. (5.12). The imaginary part is determined based on previous iterations. The disturbance growth is then described by the complex chordwise wavenumber, which allows to consider disturbances with large exponential amplification.

## 5.3 Optimisation problem

We are interested in initial disturbances $\boldsymbol{q} = (u, v, w, p)^T$ introduced at $x_{\text{in}}$ that maximise the disturbance energy at a specific outlet location $x_{\text{out}}$. For an incompressible flow, the total disturbance energy is used,

$$E(x) = \int_0^{y_{\max}} (u^2 + v^2 + w^2)\,\mathrm{d}y. \tag{5.23}$$

The optimisation problem is formulated using the Lagrange functional, where the constraints of the parabolised equations are enforced using the Lagrange multipliers $\boldsymbol{p}$ as described in section 2.2.3. The adjoint equations are found by setting to zero the gradient of the Langrangian function with respect to the state variable $\boldsymbol{q}$. Similarly, the optimality conditions are determined by setting to zero the gradient of the Langrangian function with respect to $\boldsymbol{q}_{\text{in}}$ and $\boldsymbol{q}_{\text{out}}$. Details of the adjoint operators and optimality conditions can be found in appendix A.1 and section 2.2.3.

The optimal perturbation is obtained using iterations of the direct/adjoint system according to the iterative algorithm presented in section 2.2.3. The numerical approach is similar to that described in section 2.4.

## 5.4 Optimal perturbations in FSC boundary layers

We can now solve the parabolised equations (5.6) with the chordwise wavenumber determined according to the approach presented in section 5.2.2. This means that we are able to describe the spatial evolution of both modal and non-modal disturbances closely aligned with the external streamline in a non-parallel three-dimensional boundary layer subject to a chordwise pressure gradient.
The correct implementation of the optimization algorithm is verified by reproducing results obtained for a two-dimensional incompressible boundary-layer (Levin and Henningson, 2003; Vermeersch, 2009). The validity of the modified PSE is checked by reproducing results reported by Tempelmann *et al.* (2010) using the method based on lines of constant phase.
In the following, we present a brief parametric study of stationary optimal perturbations in both accelerated and decelerated FSC boundary layers. In two-dimensional boundary layers, stationary disturbances lead to the largest non-modal growth. These disturbances will also play a role in the

applications that will be investigated in chapter 6. The Reynolds number is chosen as $Re_L = 10^6$ and the flow can be either accelerated ($\beta_H = 0.1$) or decelerated ($\beta_H = -0.05$). Comparisons to crossflow modes employing the classical PSE are also made.

### 5.4.1 Stationary optimal disturbances

#### 5.4.1.1 Influence of the outlet location

We start by studying the influence of the outlet location $x_{\text{out}}$ for stationary disturbances introduced at a fixed initial location $x_{\text{in}} = 0.01$. The optimal growth is determined for different values of $x_{\text{out}}$ as well as a range of spanwise wavenumbers $\beta$. The outlet location ranges from $x_{\text{out}} = 0.1$ to $x_{\text{out}} = 1$. Figure 5.4a shows the contours of gain $G/Re_L$ for an accelerated boundary layer with $\beta_H = 0.1$. For the range of $\beta$ and $x_{\text{out}}$ considered here, positive values of the gain are observed over the major part of the domain. The same observation can be made for a decelerated boundary layer, as displayed in fig. 5.4b where $\beta_H = -0.05$.

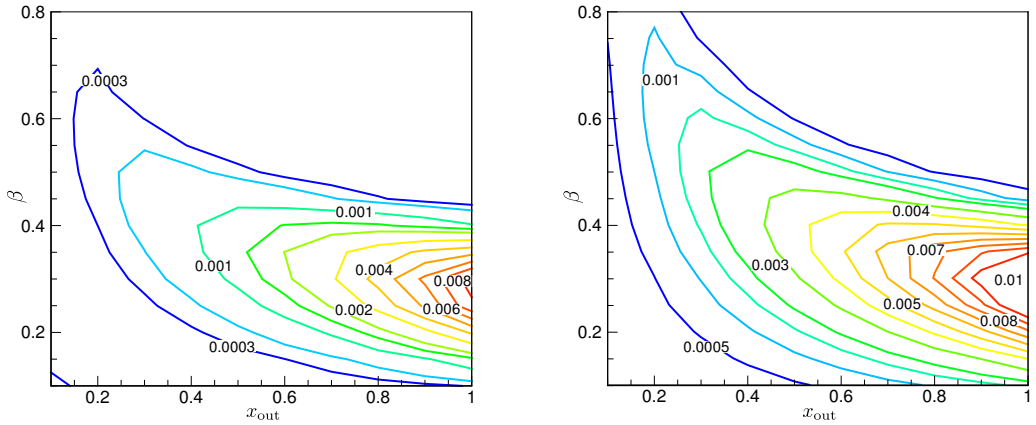


(a) $\beta_H = 0.1$ (b) $\beta_H = -0.05$

Figure 5.4: Contours of gain $G/Re_L$ of stationary disturbances in an accelerated (a) and decelerated (b) boundary layer for different outlet locations $x_{\text{out}}$ and spanwise wavenumbers $\beta$, with $x_{\text{in}} = 0.01$ and $\Lambda = 45°$.

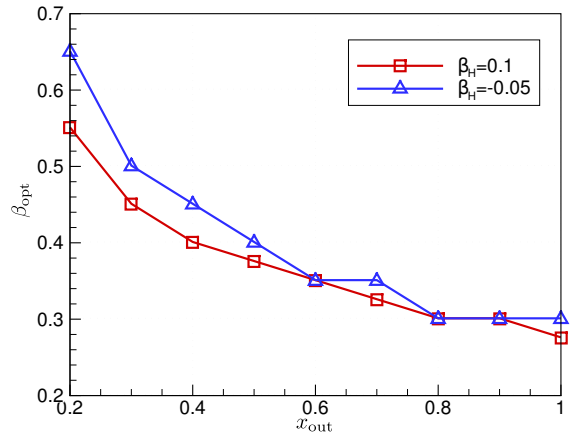


Figure 5.5: Spanwise wavenumber $\beta$ that yields maximum disturbance growth at a given $x_{\text{out}}$. The initial location is $x_{\text{in}} = 0.01$, with a sweep angle $\Lambda = 45°$.

These results are consistent with the findings reported by Tempelmann *et al.* (2010), although the determination of the chordwise wavenumber is done with the new modification of the PSE described in section 5.2.2. The spanwise wavenumber that leads to the maximum disturbance growth can also be determined. Figure 5.5 reveals that this optimal wavenumber decreases for increasing values of the outlet location. When $x_{\text{out}}$ is located close to the leading edge, the spanwise wavenumber takes relatively high values with $\beta_{\text{opt}} = 0.55$ when $\beta_H = 0.1$ and $\beta_{\text{opt}} = 0.65$ when $\beta_H = -0.05$ at $x_{\text{out}} = 0.2$. These values then decrease with increasing values of $x_{\text{out}}$, with $\beta_{\text{opt}}$ close to 0.3 for both accelerated and decelerated flows at $x_{\text{out}} = 1$.

#### 5.4.1.2 Influence of the initial location

The effect of the initial location where disturbances are introduced on the energy amplification is now investigated. So far this inlet location has been fixed to $x_{\text{in}} = 0.01$ and is now set to range from this value up to $x_{\text{in}} = 0.9$. The outlet location where the gain is maximised is fixed to $x_{\text{out}} = 1$. For a Blasius boundary layer, Vermeersch (2009) found an optimal initial location $x_{\text{in}} = 0.35$ that leads to a gain $G/Re_L = 3.5 \cdot 10^{-3}$ at $x_{\text{out}} = 1$.
Figure 5.6 displays the contours of gain $G/Re_L$ maximised at $x_{\text{out}} = 1$ for the different initial locations when the spanwise wavenumber ranges from $\beta = 0.2$ to $\beta = 0.8$. Both accelerated (fig. 5.6a) and decelerated (fig. 5.6b) boundary layers are investigated. Similarly to the two-dimensional case,

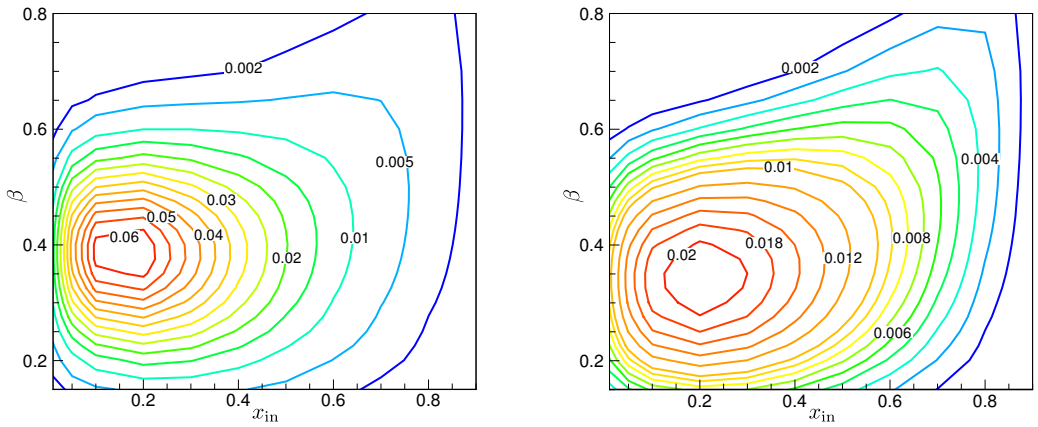


(a) $\beta_H = 0.1$ (b) $\beta_H = -0.05$

Figure 5.6: Contours of gain $G/Re_L$ of stationary disturbances in an accelerated (a) and decelerated (b) boundary layer for different inlet locations $x_{\text{in}}$ and spanwise wavenumbers $\beta$, with $x_{\text{out}} = 1$ and $\Lambda = 45°$.

the optimal initial station is located some distance from the leading edge. In the accelerated case, it can be argued that the optimal location is close to the neutral point (Tempelmann *et al.*, 2010). In the decelerated case, the overall maximum growth is attained for smaller values of $\beta$, with $\beta = 0.35$ for $\beta_H = -0.05$ where $\beta = 0.4$ for $\beta_H = 0.1$.
For large values of the spanwise wavenumber (approximately $\beta \geqslant 0.6$), the initial location that leads to the maximum disturbance energy amplification is shifted close to $x_{\text{out}}$. These wavenumbers correspond to a subcritical region where exponential amplification is absent. Disturbances that are introduced some distance from the leading edge will eventually decay before reaching the outlet location. On the other hand, disturbances that are introduced closer to $x_{\text{out}}$ will still experience non-modal growth at the location where the gain is maximised. For this reason, the optimal initial position is located close to $x_{\text{out}}$ for large values of the spanwise wavenumbers.

It is also important to understand that an optimal perturbation is computed for a given initial location. If the disturbance computed for a given $x_{\text{in}}$ is introduced at a different location $x$, the evolution of the gain will be suboptimal. This property is important when comparing the theoretical evolution of Klebanoff modes to experiments.

#### 5.4.1.3 Dependence on the sweep angle

The optimal growth is determined for accelerated and decelerated boundary layers with three different sweep angles, $\Lambda = 45°$, $\Lambda = 35°$ and $\Lambda = 25°$. The outlet location is chosen as $x_{\text{out}} = 0.13$ where only non-modal growth occurs, and disturbances are introduced at $x_{\text{in}} = 0.01$. Figure 5.7 represents the gain for the different flow configurations as a function of the spanwise wavenumber.

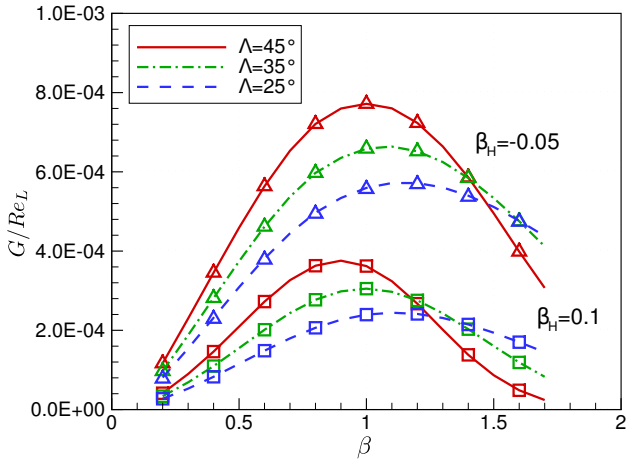


Figure 5.7: Gain curves at $x_{\text{out}} = 0.13$ for $x_{\text{in}} = 0.01$ and $\omega = 0$. Accelerated ($\beta_H = 0.1$, —□—) and decelerated ($\beta_H = -0.05$, —△—) boundary-layer flows with different sweep angles $\Lambda = 45°$ (——), $\Lambda = 35°$ (-·-·-) and $\Lambda = 25°$ (- - -).

The first observation is that decelerated boundary layers exhibit larger transient growths than their accelerated counterparts. This result has first been highlighted by Corbett and Bottaro (2001) in the temporal framework and is in accordance with results obtained for two-dimensional boundary layers. It is important to note that the amplification of crossflow vortices is less important for decelerated flows. However, the larger transient growth observed in decelerated boundary layers means that the initial amplification of modal disturbances might be greater, thus compensating the stabilising effect of the positive pressure gradient.

The maximum growth is also attained for the largest sweep angle ($\Lambda = 45°$) and accordingly for the largest crossflow component.The same observations can be made in the supercritical domain for $x_{\text{out}} = 1$ where exponential amplification takes place. It is visible from fig. 5.8 that the largest growth is attained for $\Lambda = 45°$. However, comparing the modal amplification using the classic PSE and the disturbance amplification using the modified PSE reveals that the initial amplification of crossflow modes due to transient growth is larger for $\Lambda = 25°$ (Tempelmann, 2010a). Non-modal growth is therefore more important for boundary-layer flows with a small sweep angle. In this case, the neutral point for the onset of exponential amplification moves away from the leading edge, resulting in a larger region of non-modal growth. As with the pressure gradient, crossflow vortices are weaker for small sweep angles, but this effect may be compensated with a larger initial non-modal amplification of the corresponding eigenmode.

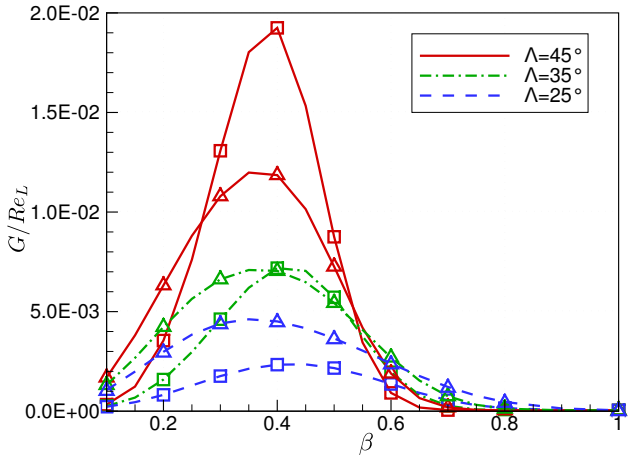


Figure 5.8: Gain curves at $x_{\text{out}} = 1$ for $x_{\text{in}} = 0.01$ and $\omega = 0$. Accelerated ($\beta_H = 0.1$, —□—) and decelerated ($\beta_H = -0.05$, —△—) boundary-layer flows with different sweep angles $\Lambda = 45°$ (——), $\Lambda = 35°$ (-·-·-) and $\Lambda = 25°$ (- - -).

### 5.4.2 Connection to crossflow modes

The connection between optimal initial disturbances and the downstream development of crossflow vortices is investigated. The inlet and outlet locations as well as the spanwise wavenumber are chosen so that both non-modal and modal growth are present in an accelerated boundary layer. Figure 5.9 shows that non-modal growth results in a significant initial amplification of $N$ factor over the first locations, in a manner similar to what has been described in the case of Görtler vortices (chapter 3). The exponential amplification of the crossflow mode is then recovered after the neutral point ($x \geqslant 0.4$). In this figure, the $N$ factor, defined as $N = 0.5\ln(G/Re_L)$, has been scaled by a factor 0.5 to match the definition from the PSE. Comparing the $N$ factor curves for both the optimal perturbation and the PSE shows that non-modal growth gives a larger initial amplitude for the amplification of the crossflow modes.

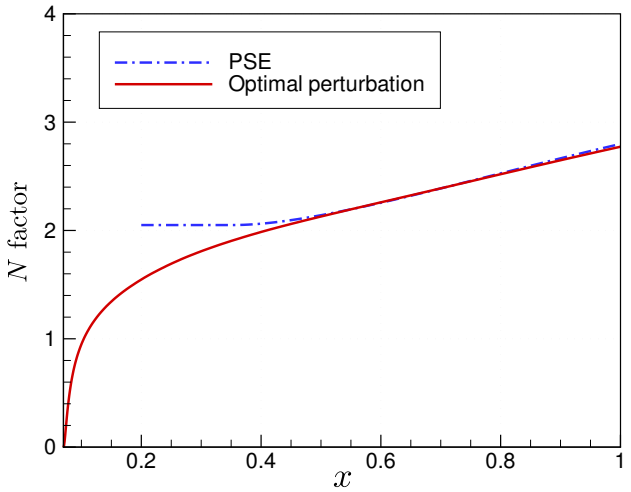


Figure 5.9: $N$ factor curves for the non-modal growth (solid line) and a crossflow mode (dash-dotted line) for $x_{\text{in}} = 0.07$, $x_{\text{out}} = 1$, $\beta_H = 0.1$, $\Lambda = 45°$, $\omega = 0$ and $\beta = 0.38$. The latter curve is shifted to take non-modal growth into account.

To further investigate the connection between crossflow vortices and non-modal growth, we compare the shape functions of the optimal perturbation propagated downstream to the shape function of the corresponding eigenmode in the supercritical domain. Figure 5.10 displays the chordwise disturbance velocity for both the non-modal and modal cases at two different locations. The first location $x = 0.4$ corresponds to the beginning of the exponential amplification of the crossflow mode, while the second location $x = 0.8$ is located further downstream.

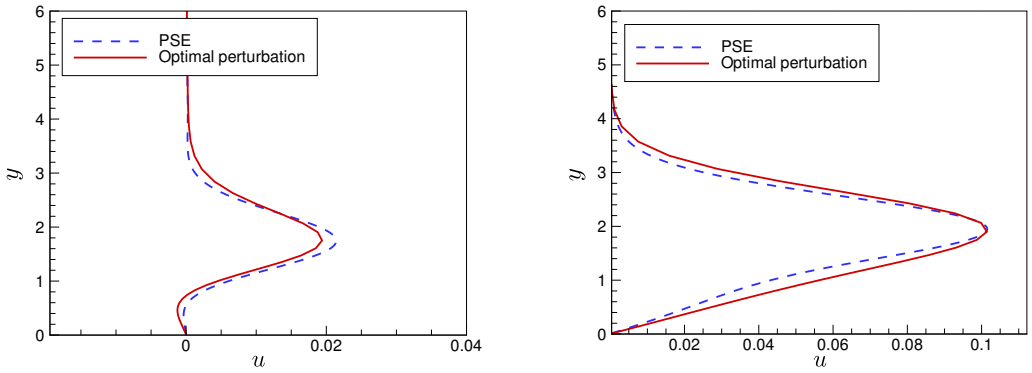


(a) $x = 0.4$ (b) $x = 0.8$

Figure 5.10: Shape function $u$ of the propagated optimal perturbation (solid line) and shape function of the corresponding crossflow mode from the PSE (dashed line) at $x = 0.4$ (beginning of the modal amplification, see fig. 5.9) and $x = 0.8$.

The shape functions display the same characteristics, which means that the downstream development of the optimal perturbation corresponds to the development of the corresponding crossflow mode. This result has been highlighted by Corbett and Bottaro (2001) in the temporal framework. They found that the propagated optimal perturbation strongly resembles the eigenfunction of the most amplified crossflow mode.

This result can be further emphasized from the projection of the shape functions of the optimal perturbation onto a plane perpendicular to the streakline (figs. 5.11 to 5.14). The initial disturbances take the form of tilted vortices that evolve into bent streaks further downstream. Optimal perturbation are initially tilted against the mean crossflow shear. When evolving downstream, the disturbances are first erected and later slightly tilted in the direction of the mean crossflow shear. This behaviour is similar to the Orr mechanism resulting from the action of the perturbation Reynolds stress, as described in section 1.4.1. The wall-normal position of the maximum of $u_\phi$ scales with the boundary-layer reference length $\delta(x_{\text{out}})$, with $y_{\text{d}}/\delta(x_{\text{out}}) = 2.1$ for $\beta_H = 0.1$ and $y_{\text{d}}/\delta(x_{\text{out}}) = 2.4$ for $\beta_H = -0.05$.

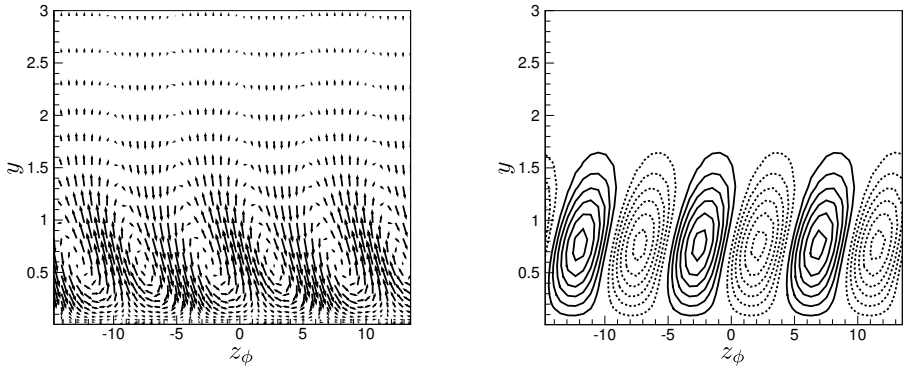


(a) Vectors $v$ and $w_\phi$ (b) Contours of $u_\phi$

Figure 5.11: Optimal perturbation at $x_{\text{in}} = 0.01$ and downstream development at $x_{\text{out}}$ with non-modal growth only ($\beta = 0.82$, $x_{\text{out}} = 0.13$) at $\Lambda = 45°$ and $\beta_H = 0.1$.

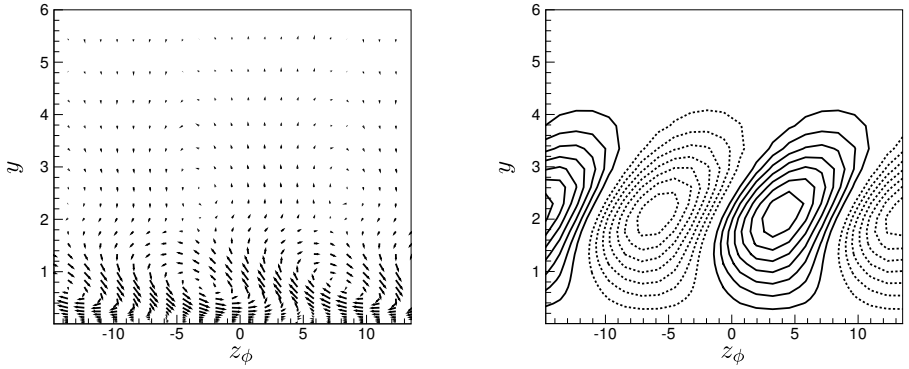


(a) Vectors $v$ and $w_\phi$ (b) Contours of $u_\phi$

Figure 5.12: Optimal perturbation at $x_{\text{in}} = 0.01$ and downstream development at $x_{\text{out}}$ with exponential amplification following non-modal growth ($\beta = 0.38$, $x_{\text{out}} = 1$) at $\Lambda = 45°$ and $\beta_H = 0.1$.

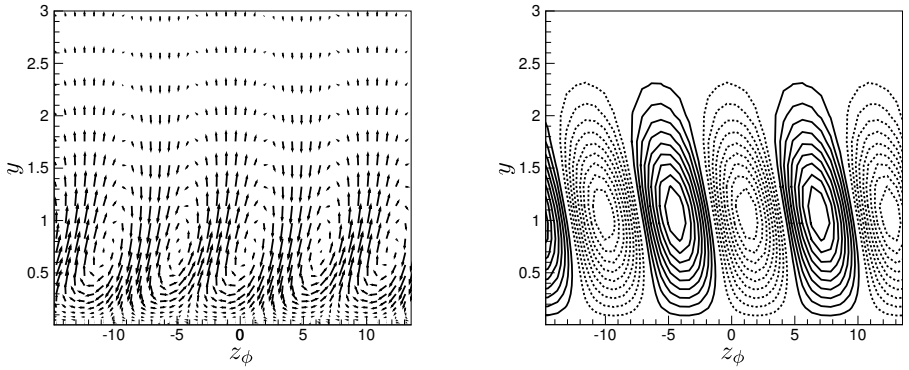


(a) Vectors $v$ and $w_\phi$ (b) Contours of $u_\phi$

Figure 5.13: Optimal perturbation at $x_{\text{in}} = 0.01$ and downstream development at $x_{\text{out}}$ with non-modal growth only ($\beta = 0.66$, $x_{\text{out}} = 0.21$) at $\Lambda = 45°$ and $\beta_H = -0.05$.

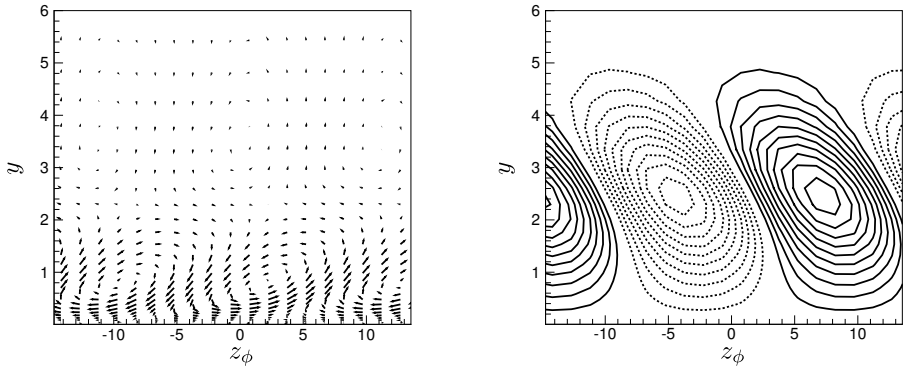


(a) Vectors $v$ and $w_\phi$ (b) Contours of $u_\phi$

Figure 5.14: Optimal perturbation at $x_{\text{in}} = 0.01$ and downstream development at $x_{\text{out}}$ with exponential amplification following non-modal growth ($\beta = 0.33$, $x_{\text{out}} = 1$) at $\Lambda = 45°$ and $\beta_H = -0.05$.

When superposing the mean flow to the optimal disturbance, the well-known structure of co-rotating crossflow vortices is recovered, as illustrated in fig. 5.15.

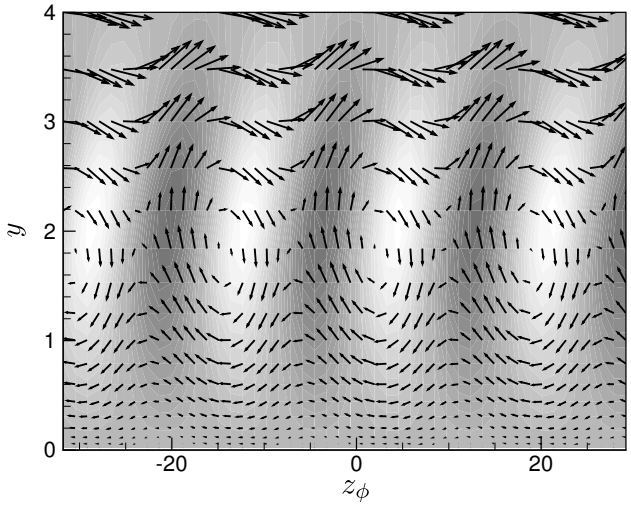


Figure 5.15: Vector representation of the optimal perturbation at $x_{\text{out}} = 1$ superposed to the mean flow, with $x_{\text{in}} = 0.01$, $\beta = 0.38$ and $\Lambda = 45°$. The grey scale indicates the disturbance streaks.

These observations lead to the conclusion that non-modal growth in three-dimensional boundary layers is triggered by a combination of the lift-up effect and the Orr-mechanisms. From the comparison between the shape function of the optimal perturbations and the corresponding eigenfunction, it is argued that non-modal streaks later evolve into crossflow vortices. Projecting the optimal perturbations in the subcritical and supercritical regime further confirms this connection. This shows the potential for initial amplification of crossflow vortices through non-modal growth, which will be investigated in the following chapter on more complex geometries.

We have developed a set of parabolised equations that describes non-modal as well as modal growth in three-dimensional boundary layers. A new modification of the classic PSE is proposed in order to determine the chordwise wavenumber locally based on the maximum of energy disturbance. The optimal perturbation is obtained by means of iterations of the direct and adjoint equations.
Stationary optimal perturbations are then investigated. A parametric study using the new local determination of the chordwise wavenumber confirmed the results obtained by Tempelmann *et al.* (2010). The initial disturbances take the form of streamwise-oriented vortices tilted against the mean crossflow shear. Further downstream, they evolve into streaks that are slightly tilted in the direction of the mean crossflow and almost aligned with the external streamline. The physical mechanism responsible for non-modal growth in three-dimensional boundary layers thus consists in a combination of the lift-up effect and the Orr mechanism. Comparisons with crossflow vortices downstream of the neutral point reveal that the initial disturbances share the same characteristics as the corresponding eigenmode. Non-modal growth provides an initial amplification of crossflow vortices over the first chordwise location that is not taken into account in the classic PSE. The last chapter further investigates this potential for initial amplification of modal instabilities on more complex geometries.

Chapter 6

# Applications to complex geometries

This chapter is the direct application of the numerical tools developed previously for three-dimensional boundary layers. The Onera DTP-B model is first considered. Detailed comparisons are made between the amplification of the different crossflow modes identified on this airfoil using both the classic and modified PSE method. The influence of transient growth on the modal amplification of crossflow is thus further explored on a more realistic configuration. In a second part, the stability of the attachment-line boundary layer is investigated. The practical criterion developed to detect the onset of the leading-edge contamination phenomenon is discussed. To this end, stationary optimal perturbations are computed along the attachment line and the influence of the sweep angle (or equivalently of the leading edge Reynolds number) is studied. In the last section, disturbance growth is computed in the vicinity of the attachment line.

## Contents

## 6.1 Disturbance amplification on a swept wing

In this section, we compute disturbance amplification over a swept wing. Computations in the three-dimensional boundary-layer are carried out using the method presented in the previous chapter. The resulting $N$ factor curves are then compared to the ones obtained using the classic PSE.

### 6.1.1 Baseline description

This investigation is based on the geometry of the DTP B Onera model[1]. This model is characterised by a chord $L = 0.7\,\mathrm{m}$ perpendicular to the leading edge, a maximum thickness of 94 mm and a span of 2.5 m.
This model was used in previous studies attempting to control transition and extend the laminar zone on swept wings, and tested in the Onera F2 subsonic wind tunnel. The stabilizing effect of micron-sized roughness on crossflow-induced transition was investigated both numerically and experimentally. The major stationary disturbances were determined on this geometry in several configurations and will be used in our calculations.

We consider sweep angles between 35° and 45° while the angle of attack in the streamwise direction ranges from 5° to 7°. The free-stream velocity is set to $70\,\mathrm{m\,s^{-1}}$, which corresponds to a chord Reynolds number $Re_c = 3.2 \times 10^6$. Figure 6.1 shows the pressure coefficients $K_p$ on the lower surface for the different angles of attack considered and a sweep angle $\Lambda = 40°$. A negative pressure gradient that is favourable to crossflow instabilities is present on the major part of the wing, from 0% to 70% of the chord. The corresponding values of $\beta_H$ considered in the previous chapter are located close to $x/c = 0.6$ for $\beta_H = 0.1$ and close to $x/c = 0.8$ for $\beta_H = -0.05$.

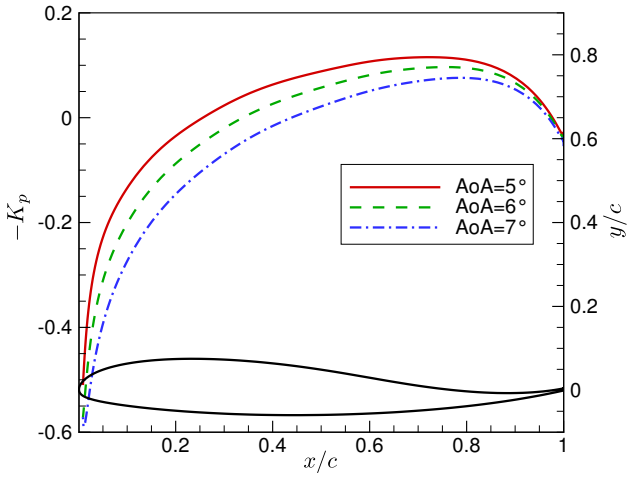


Figure 6.1: Pressure coefficient distributions and geometry of the DTP B model for a sweep angle of 40° and various angles of attack.

The base flow is computed using the boundary layer code *3C3D* as described in previous sections, based on the pressure and velocity distributions over the airfoil. Comparisons are made between $N$ factor curves computed using the classical PSE and the modified PSE that takes both non-modal and modal growth into account.

[1]DTP stands for "Développement Technique Probatoire".

### 6.1.2 Comparisons between modal and non-modal disturbance growth

Figure 6.2 shows different modes computed using both the classic and the modified PSE. A region of transient growth takes place over the very first stations and provide initial values of $N$ factor before recovering a modal amplification, in a manner similar to what has been described in the previous chapter. The first neutral point is located close to the leading edge, around 2% of chord, meaning that the region where transient growth plays a significant role is reduced. The flow is also mainly accelerated and thus shows less potential for transient growth than a decelerated boundary layer, as illustrated in the previous chapter. However, this region still provides an initial increase of $N$ factor over the first locations, as depicted in the following comparisons.

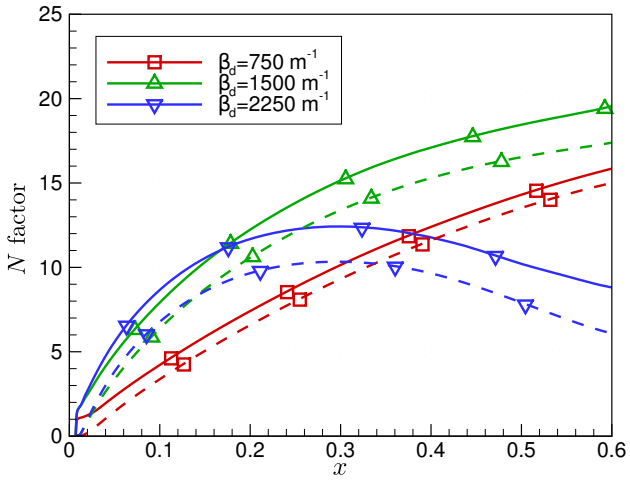


Figure 6.2: $N$ factors of major modes, computed with the classic PSE (- - -) and the modified PSE to account for non-modal growth (——). The sweep angle is $\Lambda = 40°$ and the angle of attack is set to 6°.

It can be seen from fig. 6.2, that the initial amplification $\Delta N$ is more important when the value of the dimensional spanwise wavenumber $\beta_d$ increases. The value $\Delta N = 0.8$ for $\beta_d = 750\,\mathrm{m}^{-1}$ increases to $\Delta N = 1.7$ for $\beta_d = 1500\,\mathrm{m}^{-1}$ and up to $\Delta N = 2.1$ for $\beta_d = 2250\,\mathrm{m}^{-1}$. This observation means that the different crossflow modes are not equally affected by the transient growth. The initial amplitude of the modes increases with the range of spanwise wavenumbers considered in this chapter. The modal amplification of the different crossflow vortices is well recovered past the region of transient growth and the value of $\Delta N$ remains constant.

Figure 6.3 displays $N$ factor curves for the different angles of attack considered here, namely 5° to 7°. The most amplified mode of fig. 6.2 is considered here, that is $\beta_d = 1500\,\mathrm{m}^{-1}$. The value of the initial $\Delta N$ provided by transient growth decreases when the angle of attack increases. This value decreases from $\Delta N = 2.2$ at 5° to $\Delta N = 1.7$ at 6° and $\Delta N = 0.7$ at 7°. This means that, although maximum amplitude for crossflow modes is attained for the largest angle of attack, the maximum initial amplification is obtained for 5°. Transient growth is thus more relevant for smaller angles of attack. This may be due to the lower values of the pressure coefficient, which correspond to a less accelerated base flow that is more favourable to transient amplification.

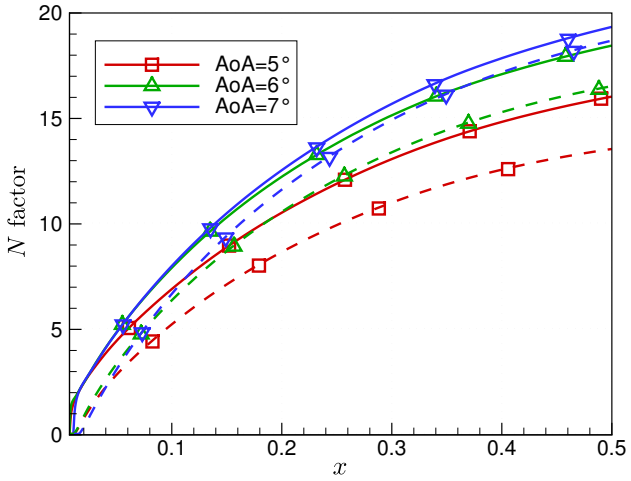


Figure 6.3: $N$ factors for different angles of attack, computed with the classic PSE (- - -) and the modified PSE to account for non-modal growth (——). The sweep angle is $\Lambda = 40°$ and the dimensional spanwise wavenumber is $\beta_d = 1500\,\mathrm{m}^{-1}$.

The influence of the sweep angle can also be evaluated. Computations with values of the sweep angle $\Lambda$=35°, 40° and 45° are displayed in fig. 6.4. Maximum growth is obtained for the largest sweep angle, which corresponds to the largest crossflow component, both with the classic and modified PSE. The value of $\Delta N$ remains fairly constant when increasing the sweep angle, which means that for the dimensional spanwise wavenumber $\beta_d = 1500\,\mathrm{m}^{-1}$ considered here, the sweep angle does not affect the initial amplitude of the crossflow mode that is provided by transient growth. This is because the neutral point for the exponential amplification of crossflow vortices is located very close to the leading edge and its position is not strongly affected by the value of the sweep angle. In this case, disturbance amplification due to transient growth does not significantly change when increasing $\Lambda$.

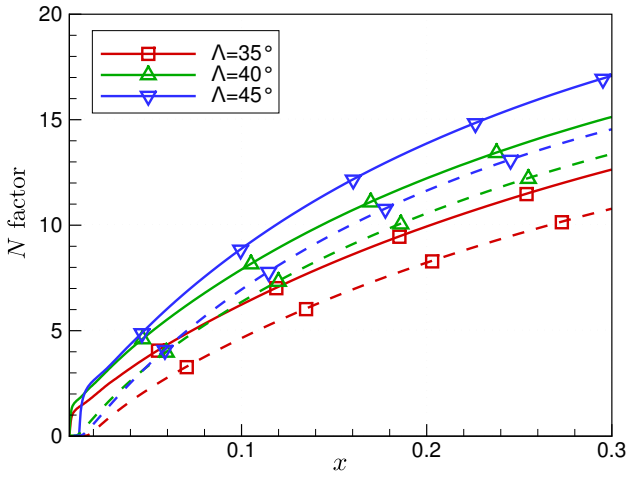


Figure 6.4: $N$ factors for different sweep angles, computed with the classic PSE (- - -) and the modified PSE to account for non-modal growth (——). The angle of attack is set to 6° and the dimensional spanwise wavenumber is $\beta_d = 1500\,\mathrm{m}^{-1}$.

Overall, the phase of transient growth is reduced to the very first chordwise stations before the neutral point. It provides an initial amplitude to crossflow vortices that corresponds to an $N$ factor increase up to $\Delta N \simeq 2$. Transient growth is particularly found important for small angles of attack. The experimental transition location has been measured around 20–30% of chord, which is equivalent to a critical $N$ factor at the transition around 8 to 10. The values of $\Delta N$ are thus significant and might lead to a consequent shift in the transition location if the method used for predicting the transition does not take transient amplification into account.

## 6.2 Attachment line flow

Attachment-line boundary-layer flows occur on yawed blunt bodies such as the leading edge of swept wings. As detailed in section 1.2.4, leading-edge contamination is possible when the attachment-line boundary layer is subject to high levels of external turbulence. This might happen at an airfoil wing-wall junction where large turbulent structures come from the fuselage and impact the boundary layer. Surface imperfections, such as roughness on the attachment line, are also likely to cause leading-edge contamination. In this section, we look at the possible influence of transient growth on this phenomenon. Non-modal growth of disturbances has been previously highlighted in both the temporal (Obrist and Schmid, 2003; Guégan *et al.*, 2006, 2007) and the spatial (Guégan *et al.*, 2008) framework, although restricted to two-dimensional computations. In this section, optimal perturbations are computed along the attachment line and in its vicinity with the method presented in the previous chapter, which allows to determine disturbance growth in three-dimensional boundary layers.

### 6.2.1 Base flow

We are interested in the incompressible flow around a swept cylinder of infinite span, as represented in fig. 1.9. As described in section 1.2.4, the free-stream velocity $Q_\infty$ can be decomposed into a streamwise component $U_\infty = Q_\infty \cos(\Lambda)$ in the direction $X$ normal to the leading edge, and a spanwise component $W_\infty = Q_\infty \sin(\Lambda)$ in the direction $Z$ along the span, where $\Lambda$ is the sweep angle. The free-stream velocity components $U_e$ and $W_e$ can be defined as

$$U_e = kX \quad \text{and} \quad W_e = W_\infty = \text{constant}, \tag{6.1}$$

where $k$ is the free-stream velocity gradient in the direction $X$ that can be expressed, for a circular cylinder of radius $R$, as

$$k = 2\frac{U_\infty}{R}. \tag{6.2}$$

The Reynolds number $\overline{R}$ that characterises the attachment line flow at low speed is defined as

$$\overline{R} = \frac{W_e \eta}{\nu_e} \quad \text{with } \eta = (\nu_e/k)^{1/2}, \tag{6.3}$$

where $\nu_e$ is the kinematic viscosity. The non-dimensional components of the mean flow, invariant in the direction $Z$, are taken to be of the form

$$U = \frac{x}{\overline{R}}\bar{u}(y); \quad V = \frac{1}{\overline{R}}\bar{v}(y); \quad W = \bar{w}(y). \tag{6.4}$$

The velocities $(U, V, W)$ are scaled with the spanwise velocity $W_e$ and the lengths $(x, y, z)$ are scaled with $\eta$. Substituting (6.4) into the Navier-Stokes equations lead to a system of ordinary differential

equations of the Falkner-Skan family with respect to $y = Y/\eta$,

$$\begin{aligned} &\bar{u} + \bar{v}' = 0, \\ &\bar{v}''' + \bar{v}'^2 - \bar{v}\bar{v}'' - 1 = 0, \\ &\bar{w}'' - \bar{v}\bar{w}' = 0, \end{aligned} \tag{6.5}$$

with the boundary conditions

$$\begin{aligned} &\bar{u}(0) = \bar{v}(0) = \bar{w}(0) = 0, \\ &\lim_{y\to\infty} \bar{u}(y) = \lim_{y\to\infty} \bar{w}(y) = 1. \end{aligned} \tag{6.6}$$

This solution is a generalisation of the two-dimensional Hiemenz flow and is obtained as an exact solution of the Navier-Stokes equations. Equations (6.5) and (6.6) are solved to obtain the similarity solutions displayed in fig. 6.5. The physical variables are then expressed from these similarity solutions and made dimensionless with respect to the reference lengths presented in table 5.1.

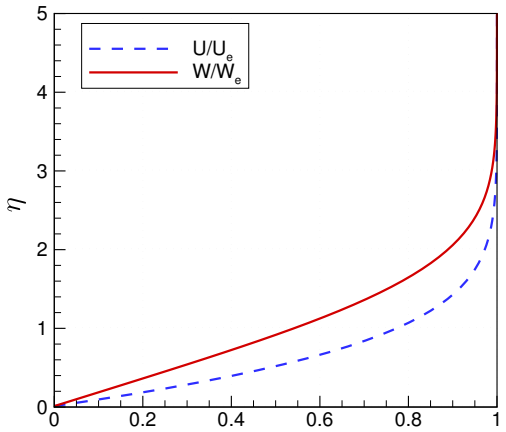


Figure 6.5: Attachment line mean velocity profiles.

In order to be consistent with the scaling employed in our approach, the velocity is made dimensionless with respect to $W_\infty = Q_\infty \sin\Lambda$, so that the Reynolds number is now defined accordingly as

$$Re_L = \frac{Q_\infty \sin(\Lambda) R}{\nu}, \tag{6.7}$$

where $R$ denotes the radius of the cylinder and is chosen as the reference length. The boundary-layer reference length is thus defined as $\delta = \sqrt{\nu R/(Q_\infty \sin\Lambda)}$. It is important to note that the Reynolds number defined in eq. (6.7) is different from the Reynolds number $\overline{R}$ but takes into account both the radius of the cylinder $R$ and the sweep angle $\Lambda$. The influence of the free-stream velocity gradient $k = 2U_\infty/R$ and the sweep angle are thus also expressed in $Re_L$. This Reynolds number is used for scaling and in the measure of the disturbance energy.

### 6.2.2 Optimal perturbations along the attachment line

We are interested in the flow along the attachment line of a swept cylinder as illustrated in fig. 6.6. The boundary layer is developing in the $z$-direction with a constant external velocity $W_e = W_\infty$. Adopting the formalism introduced in chapter 5 in the coordinate system of fig. 6.6, the reference

frame is shifted in the $z$-direction. The chordwise wavenumber is thus fixed and the spanwise wavenumber is chosen as a real function of $z$ and determined to follow the maximum local energy disturbance according to the modified PSE presented in section 5.2.2.

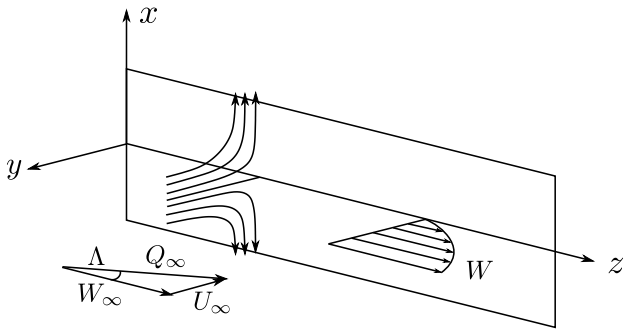


Figure 6.6: Coordinate system $(x, y, z)$ for the flow along the attachment line, with a sweep angle $\Lambda$ and an upcoming flow $Q_\infty$.

The optimal chordwise wavenumber $\alpha_{\text{opt}}$ that leads to the maximum energy growth at the outlet location $z_{\text{out}} = 1$ is first determined along the attachment line ($x = 0$). Figure 6.7 displays gain curves for several Reynolds numbers $\overline{R}$ that correspond to sweep angles[2] from 20° to 60°. The chordwise wavenumber is made dimensionless with respect to $\delta$ as in previous sections. The optimal wavenumber increases when the sweep angle becomes more important, with values ranging from $\alpha_{\text{opt}} = 0.4$ for $\overline{R} = 167$ to $\alpha_{\text{opt}} = 0.55$ for $\overline{R} = 254$. For larger values of the Reynolds number $\overline{R} > 250$, the optimal chordwise wavenumber tends towards a constant value $\alpha_{\text{opt}} = 0.6$.

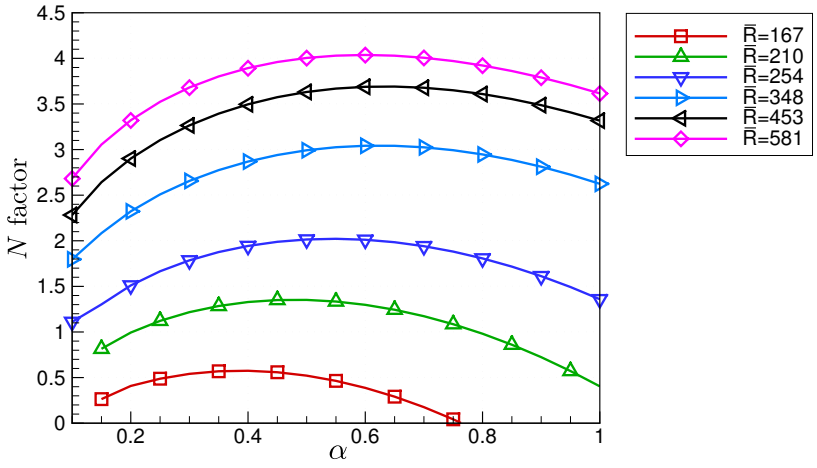


Figure 6.7: $N$ factor curves on the attachment line ($x = 0$) for different chordwise wavenumbers $\alpha$.

A simple criterion based on the value of $\overline{R}$ has been developed for the prediction of attachment-line contamination (Pfenninger, 1965; Poll, 1978) and later extended for high speed flows (Poll, 1985). For low speed flows, contamination can occur when $\overline{R} > 250$ with self-sustained turbulent spots growing until the leading-edge region becomes fully turbulent. We are interested in verifying

[2]Similar results are obtained when the sweep angle is constant and the radius $R$ of the cylinder is modified to change the Reynolds number $\overline{R}$.

this criterion by computing the spatial optimal growth of disturbances along the attachment line. We use the values of the optimal chordwise wavenumber determined previously for various Reynolds numbers.

Stationary optimal perturbations are computed for several sweep angles, from $\Lambda = 20°$ to $40°$. The corresponding Reynolds numbers range from $\overline{R} = 167$ to $\overline{R} = 348$ respectively. Figure 6.8 shows the evolution of the gain for these different Reynolds numbers $\overline{R}$ in the spanwise direction $z$. Large transient growth can be observed for the largest values of $\overline{R}$ which confirms that disturbances can undergo strong non-modal amplification along the attachment line. For comparison, let us recall that for a Blasius boundary layer with $\beta_{\text{opt}} = 0.45$, the gain attains a maximum value $G/Re_L = 2.1 \times 10^{-3}$. The values of the gain at $z_{\text{out}}$ increases when the Reynolds number $\overline{R}$ is more important, and non-modal disturbances become significantly amplified for large Reynolds numbers $\overline{R} > 300$. A possible scenario is that turbulence may be self-sustained when the amplitude of these disturbances reaches a given threshold. However, no major change can be observed when the Reynolds number goes from $\overline{R} < 250$ to $\overline{R} > 250$. Comparing the curves computed for $\overline{R} = 245$ and $\overline{R} = 254$ and 272 reveals a smooth evolution towards larger values of the gain, but no significant change. Physically, it can thus be argued that the mechanism responsible for transient growth along the attachment line does not change when the critical value $\overline{R} = 250$ is crossed. It is important to note that the scaling employed implies that $U$ and $W$ are of the same order, which is a debatable hypothesis along the attachment line.

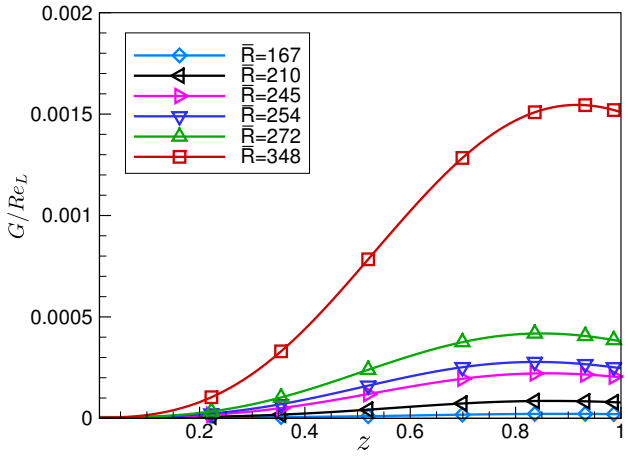


Figure 6.8: Gain curve along the attachment line ($x = 0$) for different Reynolds numbers $\overline{R}$.

Optimal perturbations along the attachment line initially take the form of spanwise counter-rotating vortices which develop further downstream into spanwise streaks. These streaks are aligned with the attachment line $x = 0$. This is illustrated in fig. 6.9 where the initial perturbation at $z_{\text{in}} = 0.01$ and the resulting streaks at $z_{\text{out}} = 1$ are displayed. This result is similar to what can be found in a boundary layer over a flat plate, as postulated by Guégan *et al.* (2008) in a two-dimensional study. This means that transient growth along the attachment line is likely to be due to the lift-up effect.

### 6.2.3 Optimal perturbations close to the attachment line

Finally, the disturbance amplification in the vicinity of the attachment line is also investigated. Two different lines are considered, namely $x = 0.05$ and $x = 0.1$, for a sweep angle $\Lambda = 40°$ that

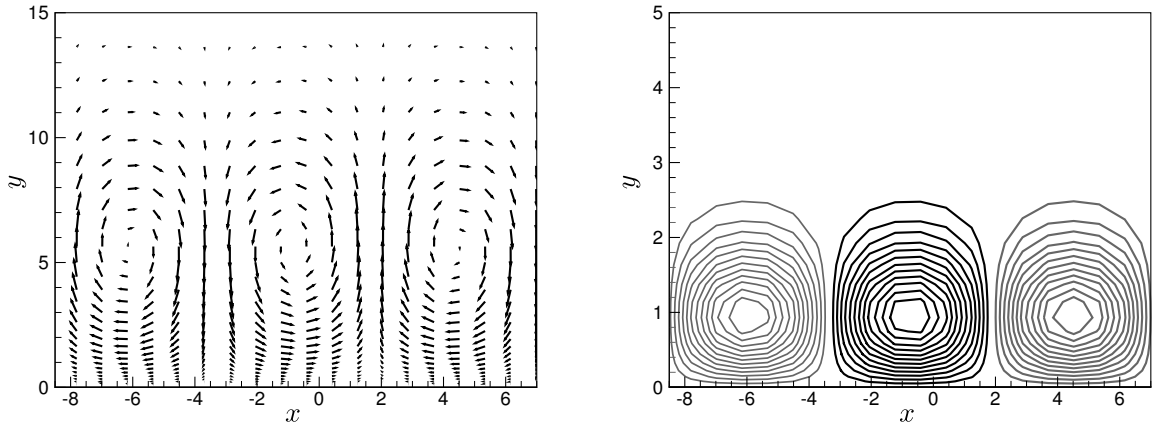


(a) Initial optimal perturbation at $z_{\text{in}} = 0.01$. (b) Resulting disturbances at $z_{\text{out}} = 1$.

Figure 6.9: Vector representation of the optimal perturbation along the attachment line and downstream contours of positive (black) and negative (grey) streamwise disturbance velocity, with $\overline{R} = 348$ ($\Lambda = 40°$).

corresponds to a Reynolds number $\overline{R} = 348$. The principal difference with the computations of the previous section is the importance of the chordwise velocity profile, which increases further away from the attachment line. Figure 6.10 shows the different evolutions of the gain obtained for these parameters. The first observation is that disturbance amplification is smaller when $x \neq 0$ so that the maximum of gain is obtained along the attachment line. When $x = 0.05$, the behaviour is similar to that observed along the attachment line. The major change occurs for $x = 0.1$, where the disturbance amplification is located upstream compared to what can be observed on the other two lines.

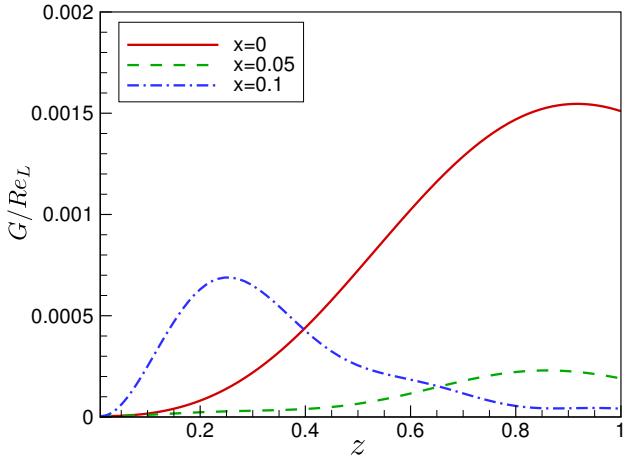


Figure 6.10: Gain curves along ($x = 0$) and close ($x = 0.05$ and $0.1$) to the attachment line for $\overline{R} = 348$ ($\Lambda = 40°$).

Further away from the attachment line, the $N$ factor curve shows that an exponential behaviour is recovered, as illustrated in fig. 6.11. This might be related to the amplification of crossflow vortices that takes place some distance from the leading edge. Mack *et al.* (2008) established the link between attachment-line modes and crossflow modes around a swept parabolic body. However, it is important to keep in mind that the hypothesis regarding the scaling employed, especially concerning the dependence on the chordwise variables, may be too restrictive to draw conclusive interpretations.

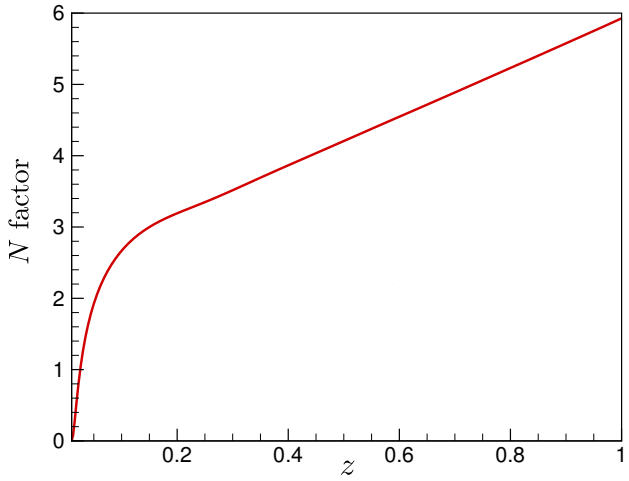


Figure 6.11: Evolution of the $N$ factor further away from the attachment line with $x = 0.2$ and $\overline{R} = 348$ ($\Lambda = 40°$).

The optimal perturbation takes the form of spanwise streaks that propagate away from the attachment line. In a manner similar to what has been described in section 5.4.2, these streaks are initially tilted against the mean chordwise flow. They are later erected and then slightly tilted in the direction of the mean chordwise flow further downstream, with a behaviour that resembles the Orr mechanism.

The influence of transient growth on the amplification of crossflow modes over an airfoil profile has been investigated. Although the region of transient growth is limited, the initial amplitude provided to crossflow modes through non-modal amplification has been highlighted. The sensitivity to transient growth is different for the different modes considered, with some modes showing a larger initial amplitude before exponential amplification. Smaller angles of attack, which correspond to a less accelerated base flow, are found to favour the transient amplification of disturbances. Conversely, the different values of the sweep angle do not strongly affect the results.
The attachment-line boundary layer developing along the leading edge of a swept-cylinder has then been considered. Optimal perturbations have been computed in the three-dimensional boundary layer that develops along the attachment line. The optimal chordwise wavenumber that leads to the maximum value of the gain has been found to evolve towards a constant value for large Reynolds numbers $\overline{R}$. The initial disturbance takes the form of spanwise counter-rotating vortices that evolve into spanwise streaks which are aligned with the attachment line. Finally, disturbance amplification further away from the attachment line has also been investigated. The largest transient growth is found along the attachment line, until some distance further away where exponential amplification is recovered.

# Discussion and conclusions

The present work consisted in the computation of optimal perturbations in boundary-layer flows developing over complex geometries. The influence of transient growth on the exponential amplification of modal instabilities has been of particular interest throughout this study. Both two- and three-dimensional boundary-layer flows have been successively considered.
First, the optimal perturbation theory has been presented in the framework of a Blasius boundary layer. Optimal perturbations refer to the initial disturbances that undergo maximum energy amplification. This disturbance energy is measured using a specific norm and the optimisation problem is solved in a classic way by using successive iterations of the direct and adjoint equations. Two-dimensional compressible boundary layers have first been considered. A set of parabolised equations has been established that accounts for curvature effects. This allowed to compute optimal disturbances in boundary layers over curved surfaces. Computing the optimal perturbations for a flow over a wall with a constant concave curvature has led to the determination of the neutral curve for the Görtler problem. In this case, the neutral curve strongly depends on the form of the initial disturbance that is being propagated. This dependence on the initial condition is removed when using the optimal perturbation approach. A new criterion for the convergence of the gain has been defined that permits the computation of the most amplified disturbances at the shortest chordwise location. This fastest growing optimal perturbation is thus associated with a neutral curve that represents a unique envelope for the unstable domain. Compressible boundary layers have also been considered and results show the stabilising effect of an increasing Mach number on the spatial evolution of Görtler vortices. In order to evaluate the interactions between non-normal modes of the operator, a parallel-flow approximation has been adopted. This allows the computation of the spectrum and pseudospectrum that displays the sensitivity of the eigenvalues. Results show that non-normality effects extend for higher values of the Görtler number, revealing a potential for transient growth that increases when curvature effects become more important. An initial region of transient growth has been identified over the first chordwise locations by computing the $N$ factor based on the most non-normal modes. This initial amplification is not taken into account by classic methods and provides significant values of $N$ factor before recovering an exponential growth. The evolution between Klebanoff modes and Görtler vortices has then been investigated by considering a concave/convex oscillation following a flat plate. The optimal spanwise wavenumber leading to the maximum energy growth is the same for the two disturbances. This means that Klebanoff modes and Görtler vortices describe the same perturbations, with Görtler vortices exhibiting an exponential amplification under the action of centrifugal forces. Transient growth is thus found to provide an initial amplitude prior to the exponential amplification of Görtler vortices. Significant values of $N$ factor can be attained that should not be neglected, in particular when predicting transition locations. This question has been further addressed by considering surfaces with mul-

tiple oscillations, which depict the problem of unintentional surface waviness that can occur in industrial applications. The classic behaviour of Görtler vortices is well reproduced by the optimal perturbation approach, in addition to the initial transient growth. This initial phase of non-modal amplification is reduced when increasing the Mach number but is not impacted by different wall temperatures. Overall, transient growth plays a role in the early development of Görtler vortices and provides initial values of $N$ factor that have to be accounted for in the scope of transition prediction.

The second part of this thesis focused on three-dimensional boundary layers. A set of parabolised equations has been derived to describe the propagation of both modal and non-modal disturbances. This is done by adding terms originating from a boundary-layer scaling to the terms that come from a modal scaling based on the PSE. This allows to describe non-modal growth in addition to the modal amplification captured by the classic PSE. For a fixed chordwise wavenumber, the parabolised equations can be solved using a marching technique. This chordwise wavenumber has to be determined so that it accounts for both the growth and the chordwise periodic variations of the disturbances. In the present work, the chordwise wavenumber has been chosen as a real function, thus only capturing the periodic variations of the disturbances. Although it is possible to consider a complex chordwise wavenumber to also include the growth of the disturbances, computations in this thesis were done with a real function and are thus limited to disturbances that exhibit moderate modal growth. The determination of an adjoint condition to compute the chordwise wavenumber could also be investigated when solving the adjoint system (Pralits *et al.*, 2002). Eventually, non-modal PSE could then be derived that would take both modal and non-modal growth, with a normalisation condition on a complex chordwise wavenumber introduced for both the direct and adjoint systems. In practice, the chordwise wavenumber is determined in order to follow the maximum local disturbance energy. This means that the wavenumber at a given location is chosen to maximise the local disturbance energy at the following location. This method may be related to the ray theory of flow instability where the path of maximum disturbance amplification is computed by solving the eikonal equation, which is a first order differential equation for the phase of the disturbance (Itoh, 1996; Gréa *et al.*, 2005). Solving this equation, which is done by the method of characteristics, gives the ray that may be considered as a path along which the disturbance energy propagates.
The parabolised equations coupled with the determination of the chordwise wavenumber are then used to compute stationary optimal perturbations developing in accelerated and decelerated Falkner-Skan-Cooke boundary layers. As previously, the optimisation problem is solved by employing iterations of the direct and adjoint equations. A parametric study has been conducted to analyse the influence of the inlet and outlet locations as well as the sweep angle. Although the approach employed in this work to specify the chordwise wavenumber was different, this study validated the results presented by Tempelmann *et al.* (2010). The optimal perturbation initially takes the form of streamwise-oriented vortices that are tilted against the mean crossflow shear. As they develop further downstream, these vortices evolve into streaks that are erected and eventually slightly tilted in the direction of the mean crossflow shear. This behaviour resembles the Orr mechanism where structures that are tilted against the shear rise to an upright position by borrowing energy from the mean flow via the action of the disturbance Reynolds stress. The Orr mechanism acts together with the lift-up effect to form streaks that are almost aligned with the external streamline. The connection between these streaks and the development of crossflow vortices has then been particularly investigated. Comparisons between the shape functions of the optimal perturbation and the corresponding eigenfunction downstream the neutral point showed that both disturbances

share the same characteristics. Non-modal streaks are thus found to evolve into crossflow vortices downstream of the neutral point. Computing the $N$ factor with both the classic and modified PSE reveals that the initial region of transient growth provides a significant initial amplitude for the crossflow mode. Based on the computation of the optimal perturbation, modelling the development of non-modal streaks could then be used for practical determination of the transition location in cases of Bypass transition. Following the work of Biau (2006) and Vermeersch (2009), the dynamics of non-modal perturbations could be modelled by solving transport equations in the laminar boundary layer and coupled with a transition criterion to detect the transition to turbulence.

Finally, optimal perturbations have been computed on more complex geometries. The Onera DTP-B profile has been used to determine the influence on transient growth on the development of crossflow vortices on an airfoil. Detailed comparisons between the amplification of optimal perturbations and crossflow vortices have been presented. These computations quantify the initial amplitude provided to crossflow vortices through transient growth, although the initial region of non-modal growth is limited over the geometry considered here. Different modes show different sensitivity to the initial non-modal amplification. Transient growth is also found to play a more important role for smaller angles of attack. However, it is important to keep in mind that initial disturbances occurring in real applications might display suboptimal characteristics. Detailed comparisons with experimental results or direct numerical simulations are thus needed to validate our conclusions.

The attachment-line boundary layer that develops along the leading edge of a swept cylinder has also been investigated from the point of view of transient growth. This type of boundary layer is representative of flow occurring over the leading edge of swept wings. In real applications, large external disturbances coming from the junction between the wing and the fuselage or surface imperfections occurring on the attachment line are likely to result in a transient amplification of disturbances in the boundary layer developing in the spanwise direction. Using the numerical tools developed throughout this thesis, optimal disturbances have been computed along the attachment line. The optimal chordwise wavenumber has been found to evolve towards a constant value when the Reynolds number $\overline{R}$ is large ($\overline{R} > 250$). Based on the determination of these optimal wavenumbers, optimal perturbations have been computed for several values of the Reynolds number $\overline{R}$. The aim was to investigate the practical criterion employed in the case of leading-edge contamination, which is based on the value of the critical Reynolds number $\overline{R} = 250$. This study has revealed the large possible amplification of disturbance through transient growth along the attachment line. Increasing values of the gain have been found at larger Reynolds number $\overline{R}$. However, it was inconclusive in showing a major change when crossing the critical value of this parameter. This arguably means that the physical mechanism responsible for transient growth along the attachment line is not strongly affected by the value of the sweep angle. Optimal perturbations have also been investigated in the vicinity of the attachment line. Higher values of the gain have been found along the attachment line than in its close neighbourhood. Going further away from the attachment line has revealed that a modal amplification can be recovered, although the hypothesis employed in the scaling of the equations are too restrictive to draw definitive conclusions. However, this approach could prove pertinent in the study of the connection between attachment line modes and crossflow modes that has been initiated by Mack *et al.* (2008).

# Outlook

A set of parabolic equations has been derived to take curvature effects into account for two-dimensional compressible boundary layers. The optimal perturbation approach has proven adequate to compute the neutral curve of the Görtler problem. The strong dependence on the form of the initial condition is solved when considering the most rapidly amplified optimal perturbation. The spatial optimal growth of Görtler vortices has been computed over concave surfaces. The potential for transient growth has been found to be more important for larger values of the Görtler number. Considering a periodic oscillation following a flat plate has revealed that Klebanoff modes evolve into Görtler vortices when curvature effects come into play. The initial region of transient growth has been found to provide an initial amplitude prior to the exponential amplification of Görtler vortices. When using practical transition criteria to detect the location of the transition due to surface waviness, it has been show that it is important to account for this initial non-modal growth. Equations governing the amplification of both modal and non-modal disturbances in three-dimensional boundary layers have also been derived. Stationary optimal perturbations in accelerated and decelerated Falkner-Skan-Cooke boundary layers have been investigated through a parametric study. Optimal perturbations have been found to take the form of bent streaks almost aligned with the external streamline that evolve into crossflow vortices downstream the neutral point. It has been shown that transient growth provides an initial amplitude to crossflow mode, both on a flat plate and on a more complex profile.

In the short term, future work should focus on improving the modified PSE approach employed in three-dimensional computations. Considering a complex-valued chordwise wavenumber would allow to capture the disturbance growth in the oscillatory function. This could be done using a normalisation condition similar to what is employed in the classic PSE. Considering a quantity that is representative of the disturbance energy, a condition on the absolute value of this quantity can be derived. The initialisation of the computation of the complex part of the wavenumber would then be based on previous iterations involving a real value that only captures the disturbance oscillations. This would lead to the formulation of a non-modal PSE system that accounts for both modal and transient growth, with a complex-valued chordwise wavenumber determined to follow the maximum disturbance energy.
An adjoint formulation of this non-modal PSE approach could then be derived. Following the work of Pralits *et al.* (2002), auxiliary conditions could be established in order to determine the chordwise wavenumber when propagating the disturbance upstream during the adjoint iterations. The numerical tools developed throughout this thesis to compute optimal perturbations in three-dimensional boundary layers are so far limited to incompressible boundary layers. The extension to account for both compressibility and curvature effects should also be considered to broaden the

domain of applications.

In the long term, the relation between the computed optimal perturbation and real initial disturbances occurring in practical circumstances needs to be evaluated. Suboptimal disturbances may reduce the need to take transient growth into account when considering the growth of modal disturbances. Comparisons with experimental results are needed to assess the validity of the optimal scenario. The influence of transient growth on the subsequent development of modal instability for moderate external disturbance level would then be verified.
Considering a more disturbed external environment, practical transition criteria for Bypass transition in three-dimensional boundary layers could also be investigated. The streaks dynamics could be modelled in a manner similar to what has been done by Vermeersch (2009) for two-dimensional boundary layers. Bypass transition due to surface roughness or external turbulence could then be investigated for realistic three-dimensional cases such as swept-wings. Direct numerical simulations could be employed to better understand the physical mechanisms responsible for transient growth and develop effective criteria for Bypass transition.
Having derived the adjoint equations for the modified parabolised equations, the receptivity problem could also be addressed. In three-dimensional boundary layers, crossflow vortices are receptive to both free-stream turbulence and surface roughness and are thus dependent on the external disturbance environment. Industrial transition criteria overlook this first step of receptivity. The receptivity to surface roughness or free-stream turbulence can be directly computed by accounting for the external disturbances when solving the equations, or it can be predicted using the adjoint solutions of the modified PSE. Again, comparisons with direct numerical simulations and experiments would be needed to validate the results.
Finally, all the results presented in this thesis pertain to the linear regime. For an accurate description of the disturbance dynamics, non-linearities have to be taken into account. Investigating the non-linear regime by relaxing the constraint of infinitesimal disturbances thus constitutes an essential direction for future work.

# Part IV

# Appendices

Appendix A

# Derivation of the adjoint operators

## A.1 Development of the inner product

The direct parabolic system of equations propagating the disturbances downstream may be expressed in operator form as

$$\mathcal{L}\boldsymbol{q} = 0, \tag{A.1}$$

where $\mathcal{L}$ is a linear operator which can be expanded as

$$\mathcal{L} = \mathcal{A} + \mathcal{B}\frac{\partial}{\partial y} + \mathcal{C}\frac{\partial^2}{\partial y^2} + \mathcal{D}\frac{\partial}{\partial x}. \tag{A.2}$$

Considering the inner product $\langle \boldsymbol{a}, \boldsymbol{b} \rangle = \int_{x_{\text{in}}}^{x_{\text{out}}} \int_0^{y_{\max}} \boldsymbol{a}^H \boldsymbol{b}\, \mathrm{d}y\, \mathrm{d}x$, the adjoint operator of $\mathcal{L}$ is defined as

$$\langle \boldsymbol{p}, \mathcal{L}\boldsymbol{q} \rangle = \langle \mathcal{L}^+ \boldsymbol{p}, \boldsymbol{q} \rangle. \tag{A.3}$$

The adjoint operator can be obtained by performing integration by parts on the left inner product in the previous equation, which leads to

$$\begin{aligned}
\int_{x_{\text{in}}}^{x_{\text{out}}} \int_0^{y_{\max}} \boldsymbol{p}^H \left( \mathcal{A}\boldsymbol{q} + \mathcal{B}\frac{\partial \boldsymbol{q}}{\partial y} + \mathcal{C}\frac{\partial^2 \boldsymbol{q}}{\partial y^2} + \mathcal{D}\frac{\partial \boldsymbol{q}}{\partial x} \right) \mathrm{d}y\, \mathrm{d}x = \\
\int_{x_{\text{in}}}^{x_{\text{out}}} \int_0^{y_{\max}} \left( \mathcal{A}^+ \boldsymbol{p} + \mathcal{B}^+ \frac{\partial \boldsymbol{p}}{\partial y} + \mathcal{C}^+ \frac{\partial^2 \boldsymbol{p}}{\partial y^2} + \mathcal{D}^+ \frac{\partial \boldsymbol{p}}{\partial x} \right)^H \boldsymbol{q}\, \mathrm{d}y\, \mathrm{d}x \\
+ \int_{x_{\text{in}}}^{x_{\text{out}}} \left[ \boldsymbol{p}^H \left( \mathcal{B}\boldsymbol{q} + \mathcal{C}\frac{\partial \boldsymbol{q}}{\partial y} - \frac{\partial \mathcal{C}}{\partial y}\boldsymbol{q} \right) - \left( \frac{\partial \boldsymbol{p}}{\partial y} \right)^H \mathcal{C}\boldsymbol{q} \right]_0^{y_{\max}} \mathrm{d}x \\
+ \int_0^{y_{\max}} \left[ \boldsymbol{p}^H \mathcal{D}\boldsymbol{q} \right]_{x_{\text{in}}}^{x_{\text{out}}} \mathrm{d}y,
\end{aligned} \tag{A.4}$$

with

$$\begin{aligned}
\mathcal{A}^+ &= \mathcal{A}^H - \frac{\partial \mathcal{B}^H}{\partial y} + \frac{\partial^2 \mathcal{C}^H}{\partial y^2} - \frac{\partial \mathcal{D}^H}{\partial x}, \\
\mathcal{B}^+ &= -\mathcal{B}^H + 2\frac{\partial \mathcal{C}^H}{\partial y}, \\
\mathcal{C}^+ &= \mathcal{C}^H, \\
\mathcal{D}^+ &= -\mathcal{D}^H.
\end{aligned} \tag{A.5}$$

The first integral on the right-hand side gives the adjoint equation $\mathcal{L}^+\boldsymbol{p} = 0$, where

$$\mathcal{L}^+ = \mathcal{A}^+ + \mathcal{B}^+\frac{\partial}{\partial y} + \mathcal{C}^+\frac{\partial^2}{\partial y^2} + \mathcal{D}^+\frac{\partial}{\partial x} \tag{A.6}$$

The second integral represents boundary terms that are set to zero to give the boundary conditions at $y = 0$ and $y = y_{\max}$ for the adjoint variables. The last integral contributes to the optimality conditions that link the direct and adjoint systems.

## A.2 Lagrangian formulation

In an unconstrained optimisation problem, the aim is to determine the characteristics of a system in order to minimise a real scalar cost or objective function. The system is characterised by its *state*, denoted $\boldsymbol{s}$, which can be *e.g.* the velocity and pressure fields. The minimum of the objective function $J(\boldsymbol{s})$ can be attained in any point in the domain of definition of the state where the gradient $\partial J/\partial \boldsymbol{s}$ vanishes (assuming $J$ continuous with continuous derivatives). Numerically, an unconstrained optimisation problem can be solved using a gradient-based method (*e.g.* the steepest descent method) which requires the determination of the gradient $\partial J/\partial \boldsymbol{s}$, or a gradient-free method which only requires the knowledge of $J$.
In unconstrained optimisation, it is assumed that the state variable $\boldsymbol{s}$ can be directly modified to attain the objective, which is not the case in most situations. The set of parameters which can actually be changed to modify the state is the *control*, denoted $\boldsymbol{c}$. Both the state and the control verify the *state equation* $\mathbf{F}(\boldsymbol{s}, \boldsymbol{c}) = 0$. Hence, the constrained optimisation problem addresses the determination of the control variables $\boldsymbol{c}$ to minimise the objective $J(\boldsymbol{s}, \boldsymbol{c})$ while verifying the constraint $\mathbf{F}(\boldsymbol{s}, \boldsymbol{c}) = 0$.

We consider the simple case where both the state and the control variables are real scalars, and the cost function is $J(s, c) = s^2 + c^2$. The unconstrained minimum of $J$ is zero, attained at the origin of the $s$-$c$ plane. We now consider the state equation $F = s + c - 2$: the aim is to minimise $J$ while ensuring $F = 0$. In the $s$-$c$ plane, the iso-levels of $J$ are concentric circles, while the constraint can be represented by a straight line. The constrained minimum of $J$ corresponds to the point where the line $F = 0$ is tangent to an iso-level of $J$ as illustrated in fig. A.1, which can be formally written as

$$\left\{\frac{\partial J}{\partial s}, \frac{\partial J}{\partial c}\right\} = a\left\{\frac{\partial F}{\partial s}, \frac{\partial F}{\partial c}\right\}. \tag{A.7}$$

From eq. (A.7), the following system of equations for $s$, $c$ and $a$ can be written

$$\frac{\partial J}{\partial s} - a\frac{\partial F}{\partial s} = 0, \tag{A.8a}$$

$$\frac{\partial J}{\partial c} - a\frac{\partial F}{\partial c} = 0, \tag{A.8b}$$

$$F = 0. \tag{A.8c}$$

From these equations, a new cost function can be defined as $\mathscr{L} = J - aF$ so that the constrained optimisation problem of $J$ corresponds to the unconstrained optimisation of $\mathscr{L}$, considering $s$, $c$ and $a$ as independent variables. The constraint is directly ensured in the new cost function, which is called the *Lagrangian* function (and $a$ is referred to as the *Lagrange multiplier* or *adjoint* variable). The generalisation to a vector form leads to

$$\mathscr{L}(\boldsymbol{s}, \boldsymbol{c}, \boldsymbol{a}) = J(\boldsymbol{s}, \boldsymbol{c}) - \boldsymbol{a} \cdot F(\boldsymbol{s}, \boldsymbol{c}), \tag{A.9}$$

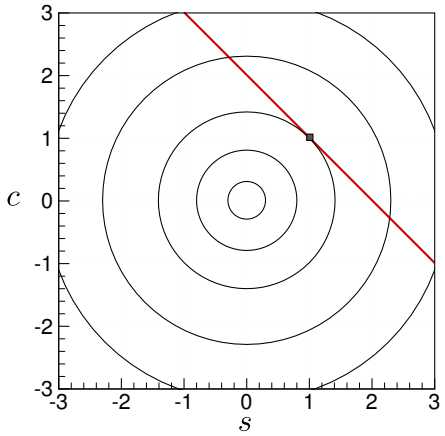


Figure A.1: Example of constrained optimisation in the control-state plane, from Cossu (2013). The circles are iso-levels of the objective function $J(s,c)$ and the straight line represents the state constraint $F(s,c) = 0$. The constrained minimum is the point where the constraint $F$ tangents one iso-level of $J$, represented by the square.

where $\boldsymbol{s}$ and $\boldsymbol{a}$ are $N$-dimensional vectors and $\boldsymbol{c}$ is an $M$-dimensional control vector. The adjoint equation and optimality condition can thus be obtained according to

$$\frac{\partial \mathscr{L}}{\partial \boldsymbol{s}} = 0 \;\Rightarrow\; \left(\frac{\partial F}{\partial \boldsymbol{s}}\right)^T \boldsymbol{a} = \frac{\partial J}{\partial \boldsymbol{s}} \quad \text{(adjoint equation)}, \tag{A.10}$$

$$\frac{\partial \mathscr{L}}{\partial \boldsymbol{c}} = 0 \;\Rightarrow\; \left(\frac{\partial F}{\partial \boldsymbol{c}}\right)^T \boldsymbol{a} = \frac{\partial J}{\partial \boldsymbol{c}} \quad \text{(optimality condition)}, \tag{A.11}$$

$$\frac{\partial \mathscr{L}}{\partial \boldsymbol{a}} = 0 \;\Rightarrow\; F = \boldsymbol{0} \quad \text{(state equation)}. \tag{A.12}$$

Considering state and/or control variables that are functions of a real variable (*e.g.* a spatial coordinate), this formalism can be extended using a variational approach. The dot product is replaced by a scalar product on an associated Euclidian space. Minimising the objective function is done by finding the stationary points of the Lagrangian function, *i.e.* setting to zero the differential

$$\mathrm{d}\mathscr{L} = \frac{\partial \mathscr{L}}{\partial \boldsymbol{s}}\delta\boldsymbol{s} + \frac{\partial \mathscr{L}}{\partial \boldsymbol{c}}\delta\boldsymbol{c} + \frac{\partial \mathscr{L}}{\partial \boldsymbol{a}}\delta\boldsymbol{a} = 0. \tag{A.13}$$

For the differential to render zero, all terms have to be set to zero independently. Considering the gradient with respect to the state variable $\boldsymbol{s}$, eq. (A.9) yields

$$\left\langle \frac{\partial J}{\partial \boldsymbol{s}}, \delta\boldsymbol{s} \right\rangle - \left\langle \boldsymbol{a}, \frac{\partial F}{\partial \boldsymbol{s}}\delta\boldsymbol{s} \right\rangle = \left\langle \frac{\partial J}{\partial \boldsymbol{s}}, \delta\boldsymbol{s} \right\rangle - \left\langle \left(\frac{\partial F}{\partial \boldsymbol{s}}\right)^+ \boldsymbol{a}, \delta\boldsymbol{s} \right\rangle = 0, \tag{A.14}$$

where the adjoint operator has been introduced. For a given linear operator $\mathcal{L}$ and two vectors $\boldsymbol{u}$ and $\boldsymbol{v}$, the adjoint operator $\mathcal{L}^+$ can be defined according to the inner product as

$$\langle \boldsymbol{u}, \mathcal{L}\boldsymbol{v} \rangle = \langle \mathcal{L}^+\boldsymbol{u}, \boldsymbol{v} \rangle. \tag{A.15}$$

The adjoint operator is used to extend the notion of a transpose matrix to linear operators. Setting the inner products in eq. (A.14) to zero for arbitrary $\delta\boldsymbol{s}$ leads to the adjoint equations

$$\frac{\partial J}{\partial \boldsymbol{s}} - \left(\frac{\partial F}{\partial \boldsymbol{s}}\right)^+ \boldsymbol{a} = 0. \tag{A.16}$$

Similarly, the optimal condition and state equation are retrieved by considering the variations of $\mathscr{L}$ with respect to small variations of $\boldsymbol{c}$ and $\boldsymbol{a}$.

Appendix B

# Complements on the discretisation in the wall-normal direction

## B.1 Spectral collocation method for differentiation

The differentiation operators in the wall-normal direction $\partial_y$ and $\partial_{yy}$ are discretised using a spectral collocation method. We start with a function $\Phi$ whose values $\{\Phi(\xi_j)\}_{0\leqslant j\leqslant N}$ are known on a set of pre-defined points $\{\xi_j\}_{0\leqslant j\leqslant N}$ called the *collocation points*. The idea is to interpolate the function on the collocation points and approximate its derivatives by the derivatives of the interpolating polynomial.
A Nth-degree polynomial $(I_N\Phi)$ which interpolates $\Phi$ on the $N+1$ collocation points can be obtained as

$$(I_N\Phi)(\xi) = \sum_{j=0}^{N} \lambda_j(\xi)\Phi(\xi_j), \tag{B.1}$$

where $\lambda_j(\xi)$ is a Nth-degree polynomial satisfying

$$\lambda_j(\xi_k) = \delta_{jk} = \begin{cases} 1 & \text{if } j = k \ ; \\ 0 & \text{otherwise.} \end{cases} \tag{B.2}$$

Hence $(I_N\Phi)$ is a Nth-degree polynomial which interpolates $\Phi$ and verifies, on the collocation points,

$$(I_N\Phi)(\xi_i) = \Phi(\xi_i) \ ; \quad i = 0, ..., N. \tag{B.3}$$

The derivative of the interpolating polynomial is given by

$$(I_N\Phi)'(\xi) = \sum_{j=0}^{N} \lambda_j'(\xi)\Phi(\xi_j), \tag{B.4}$$

which provides a discrete approximation of the derivative of $\Phi$ on the collocation points

$$\Phi'(\xi_i) = (I_N\Phi)'(\xi_i) = \sum_{j=0}^{N} \lambda_j'(\xi_i)\Phi(\xi_j). \tag{B.5}$$

Numerical differentiation can thus be achieved by vector-matrix multiplication, given the vector composed of the function values $\{\Phi(\xi_j)\}_{0\leqslant j\leqslant N}$ and the differentiation matrix $D$ whose elements are $D_{ij} = \lambda_j'(\xi_i)$.

## B.2 Chebyshev collocation method

The Chebyshev collocation method uses the Chebyshev-Gauss-Lobatto collocation points defined on the interval [-1;1] as

$$\xi_i = \cos\left(\frac{\pi i}{N}\right) \; ; \quad i = 0, \dots, N. \tag{B.6}$$

The polynomial $\lambda_j$ is given in this case by

$$\lambda_j(\xi) = \frac{(-1)^{j+1}(1-\xi^2)T_N(\xi_j)}{c_j N^2(\xi - \xi_j)}, \tag{B.7}$$

where $T_N$ is the Nth-degree Chebyshev polynomial and the coefficients $c_j$ are defined as

$$\{c_j = 1 + \delta_{j0} + \delta_{jN}\}_{0 \leqslant j \leqslant N}.$$

The differentiation matrix coefficients on the Gauss-Lobatto points are

$$D = \begin{cases} D_{ij} = \frac{c_i}{c_j}\frac{(-1)^{i+j}}{\xi_i - \xi_j} & \text{if } i \neq j \; ; \\ D_{ii} = -\frac{\xi_i}{2-\xi_i} & \text{if } i = 1, \dots, N-1 \; ; \\ D_{00} = -D_{NN} = \frac{2N^2+1}{6}. \end{cases} \tag{B.8}$$

The differentiation matrix is defined on $[-1;1]$ on the Chebyshev-Gauss-Lobatto collocation points. A mapping between the physical domain $[0;Y_\infty]$ and the domain of definition of $D$ is employed. We use the relation

$$y = \frac{Y_\infty \Upsilon}{2}\frac{1-\xi}{1+\Upsilon-\xi}, \tag{B.9}$$

where $\Upsilon$ is used to refine the number of points close to the wall. In the physical domain, the differentiation matrix $D_y$ is defined as

$$D_y = \frac{-2Y_\infty \Upsilon\,(\Upsilon+2)}{\left(Y_\infty \Upsilon + 2Y\right)^2} D. \tag{B.10}$$

## B.3 Boundary conditions

Enforcing homogeneous Dirichlet boundary conditions is done by simply constructing a matrix without the lines and columns corresponding to the boundary of the domain, where the solution is set to zero. This is the case for instance for chordwise and spanwise velocity disturbances $u$ and $w$, see eq. (2.5).

For other type of boundary conditions, the differentiation matrix is first computed on the interior points of the domain only, and then multiplied by a linear polynomial that enforces the boundary condition. This is the case *e.g.* for the wall-normal velocity and pressure disturbances ($v = 0$ at $y = 0$ and $p = 0$ for $y \to \infty$). The differentiation matrix on the space of $(N-2)$th-degree polynomial can be expressed as

$$\tilde{D_{ij}} = \begin{cases} -\frac{1}{2}\frac{\sin^2\left(\frac{\pi j}{N}\right)}{\sin^2\left(\frac{\pi i}{N}\right)}\frac{(-1)^{i+j}}{\sin\left(\frac{\pi(i+j)}{2N}\right)\sin\left(\frac{\pi(i-j)}{2N}\right)} & \text{if } i \neq j \; ; \\ -\frac{3}{2}\frac{\cos\left(\frac{\pi i}{N}\right)}{\sin^2\left(\frac{\pi i}{N}\right)} & \text{if } 1 \leqslant i = j \leqslant N-1. \end{cases} \tag{B.11}$$

The normal velocity disturbance $v$ is set to zero at the wall, *i.e.* for $y = 0$ which corresponds to $\xi = 1$ on the collocation points. We use the change of variable $v = \tilde{v}(1-\xi)$ where $\tilde{v}$ is equal to $v$

on the interior points of the domain but does not satisfy any boundary condition. The derivative of $v$ is obtained by the matrix-vector multiplication $\partial\tilde{v}/\partial\xi = \tilde{D}\tilde{v}$. This leads to the formulation of the differentiation matrix $D_v$ for $v$,

$$\begin{aligned}\frac{\partial v}{\partial \xi} &= \frac{\partial}{\partial \xi}((1-\xi)\tilde{v}) \\ &= \left((1-\xi)\frac{\partial \cdot}{\partial \xi} - 1\right)\tilde{v} \\ &\underbrace{\left((1-\xi)\tilde{D} - 1\right)\frac{1}{1-\xi}}_{D_v} v.\end{aligned} \tag{B.12}$$

In a similar way, the second-order differentiation matrix for the wall-normal velocity disturbance $D_{2v}$ can be expressed as

$$\frac{\partial^2 v}{\partial \xi^2} = \underbrace{\left((1-\xi)\tilde{D}^2 - 2\tilde{D}\right)\frac{1}{1-\xi}}_{D_{2v}} v. \tag{B.13}$$

The differentiation matrix for the pressure disturbance is computed in a similar fashion. The pressure disturbance $p$ is set to zero for $y \to \infty$, which corresponds to $\xi = -1$ on the collocation points. The change of variable $p = \tilde{p}(1+\xi)$ is used, which leads to the differentiation matrix $D_p$

$$\frac{\partial p}{\partial \xi} = \underbrace{\left((1+\xi)\tilde{D} + 1\right)\frac{1}{1+\xi}}_{D_p} p. \tag{B.14}$$

## B.4 Clenshaw-Curtis method for integration

Integration in the wall-normal direction is done by using the Clenshaw-Curtis method (see Waldvogel, 2006). The integral is replaced by a finite sum, and the discretisation is carried out on the Chebyshev-Gauss-Lobatto points used for differentiation.
The definite integral of a given function $\Phi$ is approximated by the weighted sum

$$\int_{-1}^{1} \Phi(\xi)\,\mathrm{d}\xi = \sum_{k=0}^{N} w_k \Phi(\xi_k) + R_N, \tag{B.15}$$

where $R_N$ is the approximation error. The quadrature weights $w_k$ may be obtained by integrating the Nth-degree polynomial interpolating the $N+1$ discrete points $\{\xi_k, \Phi(\xi_k)\}_{0\leqslant j\leqslant N}$. Using the Chebyshev-Gauss-Lobatto points (eq. (B.6)), the Clenshaw-Curtis weights are given by

$$w_k = \frac{c_k}{N}\left(1 - \sum_{j=1}^{N/2} \frac{b_j}{4j^2-1} cos\,(2j\zeta_k)\right) \quad k = 0, 1, \ldots, N\ ; \tag{B.16}$$

where $\zeta_k = {}^{k\pi}/_{N}$. The coefficients $b_j$ and $c_k$ satisfy

$$b_j = \begin{cases} 1 & \text{if} \quad j = N/2\ ; \\ 2 & \text{if} \quad j < N/2\ ; \end{cases} \qquad \text{and} \qquad c_k = \begin{cases} 1 & \text{if } k = 0\ ; \\ 2 & \text{otherwise.} \end{cases}$$

This leads to a vector $W = \{w_k\}_{k=0,\dots,N}$ containing the integration weights to compute the integral of $\Phi$ with respect to $\xi$ on the interval $[-1;1]$. Equation (B.9) is used to map the domain of definition of $\xi$ to the physical domain $[0;Y_\infty]$, which leads to the integration weights in the physical domain

$$W_y = \frac{Y_\infty \Upsilon \left(\Upsilon + 2\right)}{2\left(1 + \Upsilon + y\right)^2} W. \tag{B.17}$$

Appendix C

# Disturbance equations for flows over curved surfaces

## C.1 Incompressible flow

Using the methodology described in section 3.1.1, we consider a two-dimensional incompressible base flow $\boldsymbol{U} = (U(x,y), V(x,y), 0)^T$ over a curved surface with a radius of curvature $R_c$. Three-dimensional disturbances of the form $\boldsymbol{q}'(x,y,z,t) = \boldsymbol{q}(x,y)\exp(i(\beta z - \omega t))$ are introduced, where $\beta = \beta_d \delta$ is the dimensionless spanwise wavenumber, $\omega = \omega_d U_\infty / L$ is the dimensionless angular frequency, and $\boldsymbol{q}' = (u', v', w', \theta', p')^T$. Using the boundary-layer scaling introduced in section 2.1, the following linear partial differential equations are obtained,

$$\frac{\partial u}{\partial x} + \frac{\partial v}{\partial y} + i\beta w = 0 \tag{C.1a}$$

$$U\frac{\partial u}{\partial x} + V\frac{\partial u}{\partial y} + u\frac{\partial U}{\partial x} + v\frac{\partial U}{\partial y} = \frac{\partial^2 u}{\partial y^2} - \beta^2 u \tag{C.1b}$$

$$U\frac{\partial v}{\partial x} + V\frac{\partial v}{\partial y} + u\frac{\partial V}{\partial x} + v\frac{\partial V}{\partial y} + 2\mathsf{G}Uu = -\frac{\partial p}{\partial y} + \frac{\partial^2 v}{\partial y^2} - \beta^2 v \tag{C.1c}$$

$$U\frac{\partial w}{\partial x} + V\frac{\partial w}{\partial y} = i\beta p + \frac{\partial^2 w}{\partial y^2} - \beta^2 w \tag{C.1d}$$

where, in equation (C.1c), the Görtler number is introduced, defined as

$$\mathsf{G} = \frac{L}{R_c}\sqrt{Re_L}. \tag{C.2}$$

## C.2 Matrix formulation for compressible flows

In section 3.1.1, a two-dimensional compressible flow $\boldsymbol{U} = (U(x,y), V(x,y), 0)^T$ on a curved surface with a radius of curvature $R_c$ is considered. The disturbance equations obtained upon linearizing about the mean flow are written in matrix formulation

$$(A \cdot q)_x = (E \cdot q_y)_x + B \cdot q + C \cdot q_y + D \cdot q_{yy}, \tag{C.3}$$

where the matrix coefficients at leading order are as follows,

Matrix A:

$$a_{11} = \rho$$
$$a_{14} = -\frac{\rho U}{T}$$
$$a_{21} = 2\rho U$$
$$a_{24} = -\frac{\rho U^2}{T}$$
$$a_{31} = \rho V + \frac{2}{3}\frac{\partial \mu}{\partial y}$$
$$a_{34} = -\frac{\rho U V}{T} - \frac{\mathrm{d}\mu}{\mathrm{d}T}\frac{\partial U}{\partial y}$$
$$a_{43} = -\rho U$$
$$a_{44} = -\frac{1}{3} i\beta\mu\frac{U}{T}$$
$$a_{51} = \rho T$$

Matrix B:

$$b_{12} = -\frac{\partial p}{\partial y}$$
$$b_{13} = -i\beta\rho$$
$$b_{14} = \frac{\partial}{\partial y}\left(\frac{\rho V}{T}\right) - i\omega\frac{\rho}{T}$$
$$b_{21} = -\frac{\partial \rho V}{\partial y} - \mu\beta^2$$
$$b_{22} = -\frac{\partial \rho U}{\partial y}$$
$$b_{23} = -i\beta\rho U$$
$$b_{24} = \frac{\partial}{\partial y}\left(\frac{\mathrm{d}\mu}{\mathrm{d}T}\frac{\partial U}{\partial y}\right) + \frac{\partial}{\partial y}\left(\frac{\rho U V}{T}\right) - i\omega\rho\frac{U}{T}$$
$$b_{31} = \frac{2}{3}\frac{\partial^2 \mu}{\partial x \partial y} - m_{12}\rho U$$
$$b_{32} = -2\frac{\partial \rho V}{\partial y} + i\omega\rho - \beta^2\mu$$
$$b_{33} = -\frac{2}{3} i\beta\frac{\partial \mu}{\partial y}$$
$$b_{34} = \frac{4}{3}\frac{\partial}{\partial y}\left(\frac{\mathrm{d}\mu}{\mathrm{d}T}\frac{\partial V}{\partial y}\right) - \frac{2}{3}\frac{\partial}{\partial y}\left(\frac{\mathrm{d}\mu}{\mathrm{d}T}\frac{\partial U}{\partial x}\right) + \frac{\partial}{\partial y}\left(\frac{\rho V}{T}\right) + \frac{m_{12}}{2}\frac{\rho U^2}{T} - i\omega\frac{\rho V}{T}$$
$$b_{41} = i\beta\frac{\partial \mu}{\partial x} - \frac{1}{3} i\beta\frac{\mu}{\rho}\frac{\partial \rho}{\partial x}$$
$$b_{42} = -\frac{1}{3} i\beta\frac{\mu}{\rho}\frac{\partial \rho}{\partial y} + i\beta\frac{\partial \mu}{\partial y}$$
$$b_{43} = i\omega\rho - \frac{\partial \rho V}{\partial y} - \beta^2\mu$$
$$b_{44} = -\frac{1}{3} i\beta\frac{\rho U}{T}\frac{\partial \frac{\mu}{\rho}}{\partial x} - \frac{2}{3} i\beta\frac{\mathrm{d}\mu}{\mathrm{d}T}\left(\frac{\partial U}{\partial x} + \frac{\partial V}{\partial y}\right) + \frac{1}{3} i\beta\frac{\mu}{\rho}\frac{\partial}{\partial y}\left(\frac{\rho V}{T}\right) + \frac{1}{3}\beta\omega\frac{\mu}{T}$$
$$b_{45} = -i\beta$$
$$b_{51} = \frac{\gamma - 1}{\gamma}\frac{\partial P}{\partial x}$$
$$b_{53} = -i\beta\rho T$$
$$b_{54} = \frac{1}{Pr}\frac{\partial}{\partial y}\left(\frac{\mathrm{d}\mu}{\mathrm{d}T}\frac{\partial T}{\partial y}\right) - \frac{1}{Pr}\beta^2\mu + (\gamma - 1)M^2\frac{\mathrm{d}\mu}{\mathrm{d}T}\left(\frac{\partial U}{\partial y}\right)^2$$

Matrix C:

$$
\begin{aligned}
c_{12} &= -\rho \\
c_{14} &= \frac{\rho V}{T} \\
c_{21} &= -\frac{\partial \rho V}{\partial y} - \mu\beta^2 \\
c_{22} &= -\rho U \\
c_{24} &= \frac{\mathrm{d}\mu}{\mathrm{d}T}\frac{\partial U}{\partial y} + \frac{\rho U V}{T} \\
c_{31} &= \frac{2}{3}\frac{\partial \mu}{\partial x} \\
c_{32} &= -2\rho V + \frac{4}{3}\frac{\partial \mu}{\partial y}
\end{aligned}
\qquad
\begin{aligned}
c_{33} &= \frac{1}{3} i\beta\mu \\
c_{34} &= \frac{4}{3}\frac{\mathrm{d}\mu}{\mathrm{d}T}\frac{\partial V}{\partial y} + \frac{\rho V^2}{T} - \frac{2}{3}\frac{\mathrm{d}\mu}{\mathrm{d}T}\frac{\partial U}{\partial x} \\
c_{35} &= -1 \\
c_{43} &= -\rho V + \frac{\partial \mu}{\partial y} \\
c_{44} &= \frac{1}{3} i\beta\frac{\mu V}{T} \\
c_{51} &= 2(\gamma - 1)M^2\mu\frac{\partial U}{\partial y} \\
c_{52} &= -\rho T \\
c_{54} &= \frac{2}{Pr}\frac{\partial \mu}{\partial y}
\end{aligned}
$$

Matrix D:

$$
\begin{aligned}
d_{21} &= \mu \\
d_{32} &= \frac{4}{3}\mu
\end{aligned}
\qquad
\begin{aligned}
d_{43} &= \mu \\
d_{54} &= \frac{\mu}{Pr}
\end{aligned}
$$

Matrix E:

$$e_{31} = \frac{\mu}{3}$$

with $m_{12} = \dfrac{1}{h1}\dfrac{\partial h_1}{\partial y}$. This coefficient can be linked to the Görtler number according to $m_{12} = -\mathsf{G}/Re_L$.

Appendix D

# Complements on three-dimensional boundary layers

## D.1 Similarity solutions

Falkner and Skan (1931) proposed a self-similar solution for two-dimensional boundary-layer flows subject to a pressure gradient. This solution was latter extended by Cooke (1950) to describe three-dimensional boundary layers over swept bodies. Further details regarding self-similar boundary-layer solutions may also be found in Schlichting (1979) and Schmid and Henningson (2001).

### D.1.1 Falkner-Skan boundary layers

We consider velocity profiles of the form

$$U_\infty = Cx^m, \tag{D.1}$$

which depends on the pressure gradient through the acceleration parameter $m$. The mean pressure gradient and velocity profile are linked through the relation

$$\frac{\mathrm{d}P_\infty}{\mathrm{d}x} = -U_\infty \frac{\mathrm{d}U_\infty}{\mathrm{d}x}. \tag{D.2}$$

To reduce the partial differential boundary-layer equations into an ordinary differential equation, the independent variables are linked to similarity variables defined as

$$\eta = \sqrt{\frac{m+1}{2}\frac{Re_L \nu}{U_\infty x^{m-1}}}\, y \qquad \text{and} \qquad \xi = \frac{x}{L}. \tag{D.3}$$

In these equations, $L$ is a characteristic length scale and $Re_L$ is the Reynolds number based on $L$, $Re_L = U_\infty L/\nu$. A stream function $\psi$ is also introduced,

$$\psi = \sqrt{\frac{2U_\infty \nu x}{m+1}} f(\eta), \tag{D.4}$$

with

$$u = \frac{\partial \psi}{\partial y} \qquad \text{and} \qquad v = -\frac{\partial \psi}{\partial x}. \tag{D.5}$$

Inserting eq. (D.5) into Prandtl's boundary-layer equations and using the definition given by eq. (D.4) leads to a nonlinear differential equation for the function $f$, known as the Falkner-Skan equation,

$$f''' + ff' + \beta_H(1 - f'^2) = 0, \tag{D.6}$$

where $\beta_H = 2m/(1+m)$ is the *Hartree parameter*. The parameter $m$ denotes a dimensionless pressure gradient characterizing the acceleration of the flow (accelerated if $m > 0$, decelerated if $m < 0$). This equation has to be solved subject to the boundary conditions

$$\begin{aligned} &f = f' = 0 \quad \text{at } \eta = 0\,; \\ &\lim_{\eta\to\infty} f'(\eta) = 1. \end{aligned} \tag{D.7}$$

### D.1.2 Falkner-Skan-Cooke boundary layers

When considering three-dimensional boundary layers, the incoming velocity can be decomposed into a chordwise and a spanwise component (perpendicular and parallel to the leading edge respectively). Cooke (1950) extended the Falkner-Skan solutions to add an equation accounting for the spanwise velocity profile.
In a manner similar to the previous section, similarity variables and a stream function $\psi$ are introduced. A spanwise velocity component is also introduced according to

$$w = W_\infty g(\eta). \tag{D.8}$$

An ordinary differential equation is then obtained for the non-dimensional similarity solution $g$ that describes the crossflow profile (while eq. (D.6) remains valid),

$$g'' + fg' = 0, \tag{D.9}$$

together with the boundary conditions

$$\begin{aligned} &g = 0 \quad \text{at } \eta = 0\,; \\ &\lim_{\eta\to\infty} g(\eta) = 1. \end{aligned} \tag{D.10}$$

Solving eqs. (D.6) and (D.9) give the Falkner-Skan-Cooke mean velocity profiles,

$$\begin{aligned} U(y) &= f'[\eta(y)]\,; \\ W(y) &= \frac{W_\infty}{U_\infty} g[\eta(y)]\,, \end{aligned} \tag{D.11}$$

with the base flow

$$\begin{aligned} &\frac{U_\infty}{Q_\infty} = \left(\frac{x}{L}\right)^m\,; \\ &W_\infty = \text{cste}. \end{aligned} \tag{D.12}$$

## D.2 Operators of the direct equations

In section 5.1.2, the parabolic equations for the spatial evolution of disturbances in three-dimensional boundary layers have been introduced. The equations can be expressed in compact operator form as

$$\mathcal{L}\boldsymbol{q} = 0, \tag{D.13}$$

where $\boldsymbol{q} = (u, v, w, p)^T$ represents the vector of the disturbances and $\mathcal{L}$ is a linear operator of the form

$$\mathcal{L} = \mathcal{A} + \mathcal{B}\frac{\partial}{\partial y} + \mathcal{C}\frac{\partial^2}{\partial y^2} + \mathcal{D}\frac{\partial}{\partial x}. \tag{D.14}$$

The operators $\mathcal{A}$, $\mathcal{B}$, $\mathcal{C}$ and $\mathcal{D}$ can be expanded as

$$\mathcal{A} = \begin{pmatrix} i\alpha Re_\delta & 0 & i\beta Re_\delta & 0 \\ C + U_x & U_y & 0 & \frac{i\alpha}{Re_\delta} \\ V_x & C + V_y & 0 & 0 \\ W_x & W_y & C & \frac{i\beta}{Re_\delta} \end{pmatrix}, \tag{D.15}$$

$$\mathcal{B} = \begin{pmatrix} 0 & 1 & 0 & 0 \\ V & 0 & 0 & 0 \\ 0 & V & 0 & 1 \\ 0 & 0 & V & 0 \end{pmatrix}, \tag{D.16}$$

$$\mathcal{C} = \begin{pmatrix} 0 & 0 & 0 & 0 \\ -1 & 0 & 0 & 0 \\ 0 & -1 & 0 & 0 \\ 0 & 0 & -1 & 0 \end{pmatrix}, \tag{D.17}$$

$$\mathcal{D} = \begin{pmatrix} 1 & 0 & 0 & 0 \\ U & 0 & 0 & 0 \\ 0 & U & 0 & 0 \\ 0 & 0 & U & 0 \end{pmatrix}, \tag{D.18}$$

with $C = -i\omega + iRe_\delta\alpha U + iRe_\delta\beta W + (\alpha^2 + \beta^2)$.

# Bibliography


Airiau, C. (1994). *Stabilité linéaire et faiblement non linéaire d'une couche limite laminaire incompressible par un système d'équations parabolisé (PSE)*. PhD thesis, ENSAE. (Cited on pages 15, 16 and 85.)

Akervik, E., Ehrenstein, U., Gallaire, F. and Henningson, D. S. (2008). Global two-dimensional stability measures of the flat plate boundary-layer flow. *Eur. J. of Mech. B/Fluids*, 27:501–513. doi:10.1016/j.euromechflu.2007.09.004. (Cited on page 27.)

Andersson, P., Berggren, M. and Henningson, D. S. (1999). Optimal disturbances and bypass transition in boundary layers. *Phys. Fluids*, 11(1):134–150. doi:10.1063/1.869908. (Cited on pages 2, 28, 30, 42 and 84.)

Arnal, D. (1993). Boundary layer transition predictions based on linear theory. AGARD FDP/VKI Special Course on Progress in Transition Modelling – AGARD Report 793. (Cited on page 14.)

Arnal, D. and Casalis, G. (2000). Laminar-turbulent transition prediction in three-dimensional flows. *Progress in Aerospace Sciences*, 36(2):173–191. doi:10.1016/S0376-0421(00)00002-6. (Cited on page 10.)

Arnal, D., Casalis, G. and Houdeville, R. (2008a). Pratical transition prediction methods: subsonic and transonic flows. *In RTO-AVT/VKI Lectures Series 'Advances in Laminar-Turbulent Transition Modelling'*, VKI, Brussels, Belgium. (Cited on pages 13 and 14.)

Arnal, D., Perraud, J. and Seraudie, A. (2008b). Attachment line and surface imperfection problems. *In RTO-AVT/VKI Lectures Series 'Advances in Laminar-Turbulent Transition Modelling'*, VKI, Brussels, Belgium. (Cited on page 21.)

Bagheri, S. and Hanifi, A. (2007). The stabilizing effect of streaks on Tollmien-Schlichting and oblique waves : A parametric study. *Phys. Fluids*, 19(7). doi:10.1063/1.2746047. (Cited on page 84.)

Bassom, A. P. and Hall, P. (1991). Vortex instabilities in three-dimensional boundary layers: the relationship between Görtler and crossflow vortices. *J. Fluid Mech.*, 232:647–680. doi:10.1017/S0022112091003841. (Cited on page 20.)

Bassom, A. P. and Seddougui, S. O. (1995). Receptivity mechanisms for Görtler vortex modes. *Theoretical and Computational Fluid Dynamics*, 7(5):317–339. doi:10.1007/BF00312412. (Cited on page 21.)

Bertolotti, F. P., Herbert, T. and Spalart, P. R. (1992). Linear and nonlinear stability of the Blasius boundary layer. *J. Fluid Mech.*, 242:441–474. doi:10.1017/S0022112092002453. (Cited on page 15.)

Biau, D. (2006). *Etude des structures longitudinales dans la couche limite laminaire et de leur lien avec la transition*. PhD thesis, ENSAE. (Cited on pages 2, 28 and 109.)

Bippes, H. (1990). Instability features appearing on swept wing configurations. *In* Arnal, D. and Michel, R., editors: *Laminar-Turbulent Transition*, IUTAM. Springer Berlin Heidelberg. (Cited on pages 11 and 22.)

Bippes, H. and Görtler, H. (1972). Three-dimensional disturbances in the boundary layer along a concave wall. *Acta Mechanica*, 14(4):251–267. doi:10.1007/BF01387373. (Cited on page 17.)

Bonnet, A. and Luneau, J. (1989). *Théorie de la dynamique des fluides*. Cepadues. (Cited on page 52.)

Bottaro, A. and Luchini, P. (1999). Görtler vortices: are they amenable to local eigenvalue analysis? *Eur. J. of Mech. B/Fluids*, 18(1):47–65. doi:10.1016/S0997-7546(99)80005-3. (Cited on page 19.)

Breuer, K. S. and Kuraishi, T. (1994). Transient growth in two- and three-dimensional boundary layers. *Phys. Fluids*, 6(6):1983–1993. doi:10.1063/1.868205. (Cited on page 30.)

Butler, K. M. and Farrell, B. F. (1992). Three-dimensional optimal perturbations in viscous shear flow. *Phys. Fluids*, 4(8):1637–1650. doi:10.1063/1.858386. (Cited on pages 26 and 27.)

Byström, M. G. (2007). *Optimal disturbances in boundary layer flows*. PhD thesis, KTH. (Cited on pages 30, 31 and 32.)

Cooke, J. C. (1950). The boundary layer of a class of infinite yawed cylinders. *Math. Proc. Camb. Phil. Soc.*, 46:645–648. doi:10.1017/S0305004100026220. (Cited on pages 82, 127 and 128.)

Copie, M. L. (1996). *Stabilité linéaire et faiblement non-linéaire d'une couche limite pour un fluide incompressible, avec l'approche PSE*. PhD thesis, Institut National Polytechnique de Toulouse. (Cited on page 52.)

Corbett, P. and Bottaro, A. (2000). Optimal perturbations for boundary layers subject to stream-wise pressure gradient. *Phys. Fluids*, 12(1):120–130. doi:10.1063/1.870287. (Cited on page 30.)

Corbett, P. and Bottaro, A. (2001). Optimal linear growth in swept boundary layers. *J. Fluid Mech.*, 435:1–23. doi:10.1017/S0022112001003627. (Cited on pages 30, 91 and 93.)

Cossu, C. (2013). A rough introduction to constrained optimization. Flow-Nordita Summer School Lecture Notes. (Cited on page 117.)

Cossu, C., Chomaz, J.-M., Huerre, P. and Costa, M. (2000). Maximum spatial growth of Görtler vortices. *Flow Turb. Combust.*, 65:369–392. doi:10.1023/A:1011489309543. (Cited on pages 21, 29, 40, 55 and 56.)

Crouch, J. D., Kosorygin, V. S. and Ng, L. L. (2006). Modeling the effects of steps on boundary-layer transition. *In* Govindarajan, R., editor: *IUTAM Symposium on Laminar-Turbulent Transition*, volume 78 of *Fluid Mechanics and Its Applications*, pages 37–44. Springer Netherlands. doi:10.1007/1-4020-4159-4_4. (Cited on page 68.)

Day, H. P., Herbert, T. and Saric, W. S. (1990). Comparing local and marching analyses of Görtler instability. *AIAA Journal*, 28(6):1010–1015. doi:10.2514/3.25158. (Cited on page 19.)

Denier, J. P., Hall, P. and Seddougui, S. O. (1991). On the receptivity problem for Görtler vortices: vortex motions induced by wall roughness. *Philosophical Transactions of the Royal Society of London. Series A: Physical and Engineering Sciences*, 335(1636):51–85. doi:10.1098/rsta.1991.0036. (Cited on page 21.)

Dorsselaer, J. L. M. V. (1996). Pseudospectra for matrix pencils and stability of equilibria. *BIT Numerical Mathematics*, 37(4):833–845. doi:10.1007/BF02510354. (Cited on page 61.)

Ellingsen, T. and Palm, E. (1975). Stability of linear flow. *Phys. Fluids*, 18(4):487. doi:10.1063/1.861156. (Cited on pages 1 and 26.)

Falkner, V. M. and Skan, S. W. (1931). Solutions of the boundary-layer equations. *Philosophical Magazine Series 7*, 12(80):865–896. doi:10.1080/14786443109461870. (Cited on page 127.)

Farrell, B. F. (1988). Optimal excitation of perturbations in viscous shear flow. *Phys. Fluids*, 31(8):2093–2102. doi:10.1063/1.866609. (Cited on page 27.)

Finnis, M. V. and Brown, A. (1997). The linear growth of Görtler vortices. *International Journal of Heat and Fluid Flow*, 18(4):389–399. doi:10.1016/S0142-727X(97)00022-2. (Cited on page 17.)

Floryan, J. M. (1986). Görtler instability of boundary layers over concave and convex walls. *Phys. Fluids*, 29(8):2380–2386. doi:10.1063/1.865531. (Cited on page 20.)

Floryan, J. M. and Saric, W. S. (1982). Stability of Görtler vortices in boundary layers. *AIAA Journal*, 20(3):316–324. doi:10.2514/3.51076. (Cited on pages 18 and 71.)

Gaster, M. (1962). A note on the relation between temporally increasing and spatially increasing disturbances in hydrodynamic stability. *J. Fluid Mech.*, 14:222–224. doi:10.1017/S0022112062001184. (Cited on page 12.)

Goulpié, P., Klingmann, B. G. B. and Bottaro, A. (1996). Görtler vortices in boundary layers with streamwise pressure gradient: linear theory. *Phys. Fluids*, 8(2):451–459. doi:10.1063/1.868799. (Cited on page 19.)

Gregory, N., Stuart, J. T. and Walker, W. S. (1955). On the stability of three-dimensional boundary layers with application to the flow due to a rotating disk. *Philosophical Transactions of the Royal Society of London. Series A, Mathematical and Physical Sciences*, 248(943):155–199. doi:10.1098/rsta.1955.0013. (Cited on page 11.)

Gréa, B. J., Luchini, P. and Bottaro, A. (2005). Ray theory of flow instability and the formation of caustics in boundary layers. Technical report, IMFT. (Cited on page 108.)

Gulyaev, A. N., Kozlov, V. E., Kuznetsov, V. R., Mineev, B. I. and Sekundov, A. N. (1989). Interaction of a laminar boundary layer with external turbulence. *Fluid Dynamics*, 24(5):700–710. doi:10.1007/BF01051722. (Cited on page 27.)

Gustavsson, L. H. (1991). Energy growth of three-dimensional disturbances in plane Poiseuille flow. *J. Fluid Mech.*, 224:241–260. doi:10.1017/S002211209100174X. (Cited on page 27.)

Guégan, A., Huerre, P. and Schmid, P. J. (2007). Optimal disturbances in swept Hiemenz flow. *J. Fluid Mech.*, 578:223–232. doi:10.1017/S0022112007005162. (Cited on pages 22 and 101.)

Guégan, A., Schmid, P. J. and Huerre, P. (2006). Optimal energy growth and optimal control in swept Hiemenz flow. *J. Fluid Mech.*, 566:11–45. doi:10.1017/S0022112006001303. (Cited on pages 22 and 101.)

Guégan, A., Schmid, P. J. and Huerre, P. (2008). Spatial optimal disturbances in swept attachment-line boundary layers. *J. Fluid Mech.*, 603:179–188. doi:10.1017/S0022112008001067. (Cited on pages 23, 101 and 104.)

Görtler, H. (1941). Instabilität laminarer Grenzschichten an konkaven Wänden gegenüber gewissen dreidimensionalen Störungen. *Z. Angew Math. Mech.*, 21(4):250–252. doi:10.1002/zamm.19410210408. (Cited on page 16.)

Hall, P. (1982). Taylor-Görtler vortices in fully developed or boundary-layer flows: linear theory. *J. Fluid Mech.*, 124:475–494. doi:10.1017/S0022112082002596. (Cited on pages 17, 19 and 57.)

Hall, P. (1983). The linear development of Görtler vortices in growing boundary layers. *J. Fluid Mech.*, 130:41–58. doi:10.1017/S0022112083000968. (Cited on pages 19, 56 and 57.)

Hall, P. (1985). The Görtler vortex instability mechanism in three-dimensional boundary layers. *Proceedings of the Royal Society of London. A. Mathematical and Physical Sciences*, 399(1816):135–152. doi:10.1098/rspa.1985.0051. (Cited on page 20.)

Hall, P. (1990). Görtler vortices in growing boundary layers: the leading edge receptivity problem, linear growth and the nonlinear breakdown stage. *Mathematika*, 37:151–189. doi:10.1112/S0025579300012894. (Cited on page 21.)

Hall, P. and Fu, Y. (1989). On the Görtler vortex instability mechanism at hypersonic speeds. *Theoretical and Computational Fluid Dynamics*, 1(3):125–134. doi:10.1007/BF00417916. (Cited on page 20.)

Hall, P. and Malik, M. (1989). The growth of Görtler vortices in compressible boundary layers. *Journal of Engineering Mathematics*, 23:239–251. doi:10.1007/BF02383571. (Cited on pages 20 and 59.)

Hall, P., Malik, M. R. and Poll, D. I. A. (1984). On the stability of an infinite swept attachment line boundary layer. *Proceedings of the Royal Society of London. A. Mathematical and Physical Sciences*, 395(1809):229–245. doi:10.1098/rspa.1984.0099. (Cited on page 22.)

Hanifi, A., Schmid, P. J. and Henningson, D. S. (1996). Transient growth in compressible boundary layer flow. *Phys. Fluids*, 8(3):826–837. doi:10.1063/1.868864. (Cited on pages 28 and 42.)

Hennequin, Y. (1993). *Etude numérique de l'instabilité de Görtler : application à la définition d'une soufflerie supersonique silencieuse*. PhD thesis, ENSAE. (Cited on pages 19 and 68.)

Henningson, D. S. (1996). Comment on "Transition in shear flows. Nonlinear normality versus non-normal linearity". *Phys. Fluids*, 8(8):2257–2258. doi:10.1063/1.869011. (Cited on page 23.)

Henningson, D. S., Lundbladh, A. and Johansson, A. V. (1993). A mechanism for bypass transition from localized disturbances in wall-bounded shear flows. *J. Fluid Mech.*, 250:169–207. doi:10.1017/S0022112093001429. (Cited on page 27.)

Herbert, T. (1993). Parabolized Stability Equations. *AGARD Report*, (793). (Cited on page 15.)

Hill, D. C. (1995). Adjoint systems and their role in the receptivity problem for boundary layers. *J. Fluid Mech.*, 292:183–204. doi:10.1017/S0022112095001480. (Cited on page 30.)

Hultgren, L. S. and Gustavsson, L. H. (1981). Algebraic growth of disturbances in a laminar boundary layer. *Phys. Fluids*, 24(6):1000–1004. doi:10.1063/1.863490. (Cited on page 27.)

van Ingen, J. L. (1956). A suggested semi-empirical method for the calculation of the boundary layer transition region. *Rept. UTH-74, Univ. of Techn., Dept. of Aero. Eng., Delft.* (Cited on page 13.)

Itoh, N. (1996). Development of wedge-shaped disturbances originating from a point source in a three-dimensional boundary layer. *Fluid Dynamics Research*, 18(6):337. doi:10.1016/0169-5983(96)00021-4. (Cited on page 108.)

Jallade, S. (1990). *Etude théorique et numérique de l'instabilité de Görtler*. PhD thesis, Institut National Polytechnique de Toulouse. (Cited on pages 20 and 52.)

Kalburgi, V., Mangalam, S. M. and Dagenhart, J. R. (1988a). A comparative study of theoretical methods on Görtler instability. *AIAA Paper*, (88-0407). (Cited on page 19.)

Kalburgi, V., Mangalam, S. M. and Dagenhart, J. R. (1988b). Görtler instability on an airfoil: Comparison of marching solution with experimental observations. *AGARD CP No. 438, Paper No. 8.* (Cited on pages 19, 69 and 71.)

Kendall, J. M. (1985). Experimental study of disturbances produced in a pre-transitional laminar boundary layer by weak freestream turbulence. *AIAA Paper*, 85–1695. doi:10.2514/6.1985-1695. (Cited on page 26.)

Klebanoff, P. S. (1971). Effect of free-stream turbulence on a laminar boundary layer. *Bulletin of the American Physical Society*, 16. (Cited on page 27.)

Klebanoff, P. S., Tidstrom, K. D. and Sargent, L. M. (1962). The three-dimensional nature of boundary-layer instability. *J. Fluid Mech.*, 12:1–34. doi:10.1017/S0022112062000014. (Cited on page 27.)

Kosorygin, V. S. and Polyakov, N. P. (1990). Laminar boundary layers in turbulent flows. *In* Arnal, D. and Michel, R., editors: *Laminar-Turbulent Transition*, IUTAM, pages 573–578. Springer Berlin Heidelberg. doi:10.1007/978-3-642-84103-3_53. (Cited on page 9.)

Landahl, M. T. (1980). A note on an algebraic instability of inviscid parallel shear flows. *J. Fluid Mech.*, 98(2):243–251. doi:10.1017/S0022112080000122. (Cited on pages 1, 26 and 58.)

Lessen, M. and Koh, P. H. (1985). Instability and turbulent bursting in the boundary layer. *In* Kozlov, V. V., editor: *Laminar-Turbulent Transition*, IUTAM, pages 39–51. Springer Berlin Heidelberg. doi:10.1007/978-3-642-82462-3_5. (Cited on page 20.)

Levin, O. and Henningson, D. S. (2003). Exponential vs algebraic growth and transition prediction in boundary layer flow. *Flow Turb. Combust.*, 70:183–210. doi:10.1023/B:APPL.0000004918.05683.46. (Cited on pages 30, 84 and 88.)

Li, F. and Malik, M. R. (1996). On the nature of PSE approximation. *Theoretical and Computational Fluid Dynamics*, 8(4):253–273. doi:10.1007/BF00639695. (Cited on page 85.)

Lucas, J. M., Vermeersch, O. and Arnal, D. (2013). Spatial optimal growth of Görtler vortices in two-dimensional compressible boundary layers. 31st AIAA Applied Aerodynamics Conference, San Diego. doi:10.2514/6.2013-2814. (Cited on page 3.)

Lucas, J. M., Vermeersch, O. and Arnal, D. (2014). Transient growth of Görtler vortices in two-dimensional compressible boundary layers. Application to surface waviness. *Eur. J. of Mech. B/Fluids*. doi:10.1016/j.euromechflu.2014.11.005. (Cited on page 3.)

Luchini, P. (2000). Reynolds-number-independent instability of the boundary layer over a flat surface: optimal perturbation. *J. Fluid Mech.*, 404:289–309. doi:10.1017/S0022112099007259. (Cited on pages 2, 28, 30, 37, 42, 43 and 84.)

Luchini, P. and Bottaro, A. (1998). Görtler vortices: a backward-in-time approach to the receptivity problem. *J. Fluid Mech.*, 363:1–23. doi:10.1017/S0022112098008970. (Cited on page 21.)

Mack, C. J. and Schmid, P. J. (2011). Global stability of swept flow around a parabolic body: the neutral curve. *J. Fluid Mech.*, 678:589–599. doi:10.1017/jfm.2011.158. (Cited on page 23.)

Mack, C. J., Schmid, P. J. and Sesterhenn, J. L. (2008). Global stability of swept flow around a parabolic body: connecting attachment-line and crossflow modes. *J. Fluid Mech.*, 611:205–214. doi:10.1017/S0022112008002851. (Cited on pages 23, 105 and 109.)

Mack, L. M. (1969). Boundary-layer stability theory. J.P.L. Report 900-277, California Inst. of Technology, Pasadena. (Cited on page 42.)

Mack, L. M. (1977). Transition prediction and linear stability theory. *In AGARD Conf. Proc. No 224, Paris*. (Cited on page 13.)

Mack, L. M. (1984). Boundary-layer stability theory. *AGARD Report*, (709):3–1–3–8. (Cited on page 10.)

Mangalam, S. M., Dagenhart, J. R., Hepner, T. E. and Meyers, J. F. (1985). The Görtler instability on an airfoil. *AIAA Paper*, (85-0491). (Cited on page 18.)

Matsubara, M. and Alfredsson, P. H. (2001). Disturbance growth in boundary layers subjected to free-stream turbulence. *J. Fluid Mech.*, 430:149–168. doi:10.1017/S0022112000002810. (Cited on pages 27 and 28.)

Morkovin, M. V. (1969). On the many faces of transition. *In* Wells, C. S., editor: *Viscous Drag Reduction*, pages 1–31. Plenum, New York. (Cited on pages 1 and 8.)

Morkovin, M. V., Reshotko, E. and Herbert, T. (1994). Transition in open flow systems – A reassessment. *Bulletin of the American Physical Society*, 39:1882. (Cited on pages 8 and 9.)

Obrist, D. and Schmid, P. J. (2003). On the linear stability of swept attachment-line boundary layer flow. Part 2. Non-modal effects and receptivity. *J. Fluid Mech.*, 493:31–58. doi:10.1017/S0022112003005780. (Cited on pages 22 and 101.)

Orr, W. M. F. (1907). The stability or instability of the steady motions of a perfect liquid and of a viscous liquid. *Proc. Royal Irish Acad. A*, 27:69–138. (Cited on page 27.)

Pascal, L. (2013). *Acoustique modale et stabilité linéaire par une méthode numérique avancée. Cas d'un conduit traité acoustiquement en présence d'un écoulement*. PhD thesis, ISAE. (Cited on page 44.)

Perraud, J. and Arnal, D. (2013). Laminar-turbulent transition prediction in the presence of surface imperfection. 48$^{\text{th}}$ International Symposium of Applied Aerodynamics, Saint-Louis. (Cited on page 68.)

Perraud, J., Vermeersch, O. and Houdeville, R. (2011). Descriptif et mode d'emploi du code 3C3D. Technical report RT 1/18325, ONERA DMAE. (Cited on page 43.)

Pfenninger, W. (1965). Flow phenomena at the leading edge of swept wings. *AGARDograph 97*, Part 4. (Cited on pages 22 and 103.)

Poll, D. I. A. (1978). Some aspects of the flow near a swept attachment line with particular reference to boundary layer transition. Technical report 7805/K, Cranfield, College of Aeronautics. (Cited on pages 22 and 103.)

Poll, D. I. A. (1985). Boundary layer transition on the windward face of space shuttle during re-entry. *AIAA Paper*, 85-0899. doi:10.2514/6.1985-899. (Cited on page 103.)

Pralits, J. O., Byström, M. G., Hanifi, A. and Henningson, D. S. (2007). Optimal disturbances in three-dimensional boundary layer flows. *ERCOFTAC Bull.*, 74:23–31. (Cited on page 30.)

Pralits, J. O., Hanifi, A. and Henningson, D. S. (2002). Adjoint-based optimization of steady suction for disturbance control in incompressible flows. *J. Fluid Mech.*, 467:129–161. doi:10.1017/S0022112002001301. (Cited on pages 108 and 111.)

Rayleigh, L. (1879). On the stability, or instability, of certain fluid motions. *Proceedings of the London Mathematical Society*, s1-11(1):57–72. doi:10.1112/plms/s1-11.1.57. (Cited on page 11.)

Reddy, S. C. and Henningson, D. S. (1993). Energy growth in viscous channel flows. *J. Fluid Mech.*, 252:209–238. doi:10.1017/S0022112093003738. (Cited on page 27.)

Reed, H. L. and Saric, W. S. (1989). Stability of three-dimensional boundary layers. *Ann. Rev. Fluid Mech.*, 21(1):235–284. doi:10.1146/annurev.fl.21.010189.001315. (Cited on page 11.)

Reed, H. L., Saric, W. S. and Arnal, D. (1996). Linear stability theory applied to boundary layers. *Ann. Rev. Fluid Mech.*, 28(1):389–428. doi:10.1146/annurev.fl.28.010196.002133. (Cited on page 8.)

Reshotko, E. (2001). Transient growth: A factor in bypass transition. *Phys. Fluids*, 13(5):1067–1075. doi:10.1063/1.1358308. (Cited on page 8.)

Reshotko, E. (2008). Paths to transition in wall layers. *In RTO-AVT/VKI Lectures Series 'Advances in Laminar-Turbulent Transition Modelling'*, VKI, Brussels, Belgium. (Cited on page 8.)

Reynolds, O. (1883). An experimental investigation of the circumstances whether the motion of water shall be direct and sinuous, and the law of resistance in parallel channels. *Philosophical Transactions of the Royal Society of London*, 174:935–982. (Cited on page 8.)

Saric, W. S. (1994). Görtler vortices. *Ann. Rev. Fluid Mech.*, 26:379–409. doi:10.1146/annurev.fl.26.010194.002115. (Cited on page 16.)

Saric, W. S. and Benmalek, A. (1991). Görtler vortices with periodic curvature. *In Proc. symposium on boundary layer stability and transition to turbulence*. 1st ASME-JSME fluid engineering conference, Portland. (Cited on pages 19, 20, 58, 68, 71 and 76.)

Saric, W. S., Reed, H. L. and White, E. B. (2003). Stability and transition of three-dimensional boundary layers. *Ann. Rev. Fluid Mech.*, 35(1):413–440. doi:10.1146/annurev.fluid.35.101101.161045. (Cited on page 11.)

Schlichting, H. (1979). *Boundary-layer theory*. McGraw-Hill, 7th edition. (Cited on page 127.)

Schmid, P. and Henningson, D. (2001). *Stability and Transition in Shear Flows*. Number 142 of Applied Mathematical Sciences. Springer New York. (Cited on pages 23, 24 and 127.)

Schmid, P. J. (2001). Tools for nonmodal stability analysis. *Notes from a Ladhyx Tutorial*. (Cited on page 24.)

Schmid, P. J. (2007). Nonmodal stability theory. *Ann. Rev. Fluid Mech.*, 39:129–162. doi:10.1146/annurev.fluid.38.050304.092139. (Cited on pages 25 and 26.)

Schrader, L., Brandt, L. and Zaki, T. A. (2011). Receptivity, instability and breakdown of Görtler flow. *J. Fluid Mech.*, 682:362–396. doi:10.1017/jfm.2011.229. (Cited on pages 21 and 30.)

Schubauer, G. and Skramstad, H. (1948). Laminar boundary-layer oscillations and transition on a flat plate. Technical report 909, NACA. (Cited on page 10.)

Simen, M. (1992). Local and nonlocal stability theory of spatially varying flows. *In Instability, Transition and Turbulence*, pages 181–201. Springer-Verlag. (Cited on page 15.)

Smith, A. M. O. and Gamberoni, N. (1956). Transition, pressure gradient and stability theory. Technical report ES 26388, Douglas Aircraft Co., El Segundo, CA. (Cited on page 13.)

Squire, H. (1933). On the stability for three-dimensional disturbances of viscous fluid flow between parallel walls. *Proceedings of the Royal Society of London A*, 142:621–628. (Cited on page 12.)

Tempelmann, D., Hanifi, A. and Henningson, D. S. (2010). Spatial optimal growth in three-dimensional boundary layers. *J. Fluid Mech.*, 646:5–37. doi:10.1017/S0022112009993260. (Cited on pages 32, 84, 85, 88, 90 and 108.)

Tempelmann, D., Hanifi, A. and Henningson, D. S. (2012). Spatial optimal growth in three-dimensional compressible boundary layers. *J. Fluid Mech.*, 704:251–279. doi:10.1017/jfm.2012.235. (Cited on page 32.)

Theofilis, V. (1995). Spatial stability of incompressible attachment-line flow. *Theoretical and Computational Fluid Dynamics*, 7(3):159–171. doi:10.1007/BF00312360. (Cited on page 22.)

Trefethen, L. N. (1991). Pseudospectra of matrices. *In* Griffiths, D. F. and Watson, G. A., editors: *Numerical analysis, 1991*, volume 260, page 292, Harlow, Essex. Longman Scientific and Technical. (Cited on page 25.)

Trefethen, L. N. (1997). Pseudospectra of linear operators. *SIAM Rev*, pages 383–406. (Cited on pages 23, 25 and 61.)

Trefethen, L. N. (1999). Computation of pseudospectra. *Acta Numerica*, 8:247–295. doi:10.1017/S0962492900002932. (Cited on page 26.)

Trefethen, L. N. and Embree, M. (2005). *Spectra and pseudospectra: the behavior of nonnormal matrices and operators*. Princeton University Press. (Cited on pages 24 and 25.)

Trefethen, L. N., Trefethen, A. E., Reddy, S. C. and Driscoll, T. A. (1993). Hydrodynamic stability without eigenvalues. *Science*, 261(5121):578–584. doi:10.1126/science.261.5121.578. (Cited on page 23.)

Tumin, A. and Ashpis, D. E. (2003). Optimal disturbances in boundary layers subject to streamwise pressure gradient. *AIAA Journal*, 41(11):2297–2300. doi:10.2514/2.6825. (Cited on page 28.)

Tumin, A. and Reshotko, E. (2001). Spatial theory of optimal disturbances in boundary layers. *Phys. Fluids*, 13(7):2097–2104. doi:10.1063/1.1378070. (Cited on pages 28 and 64.)

Tumin, A. and Reshotko, E. (2003). Optimal disturbances in compressible boundary layers. *AIAA Journal*, 41(12):2357–2363. doi:10.2514/2.6860. (Cited on page 29.)

Vermeersch, O. (2009). *Étude et modélisation du phénomène de croissance transitoire pour des couches limites incompressibles et compressibles*. PhD thesis, ISAE. (Cited on pages 2, 29, 42, 60, 88, 90, 109 and 112.)

Waldvogel, J. (2006). Fast construction of the Fejèr and Clenshaw-Curtis quadrature rules. *BIT Numerical Mathematics*, 43(1):195–202. doi:10.1007/s10543-006-0045-4. (Cited on pages 45 and 121.)

Waleffe, F. (1995). Transition in shear flows. Nonlinear normality versus non-normal linearity. *Phys. Fluids*, 7(12):3060–3066. doi:10.1063/1.868682. (Cited on page 23.)

Wie, Y. S. and Malik, M. R. (1998). Effect of surface waviness on boundary-layer transition in two-dimensional flow. *Computers & Fluids*, 27(2):157–181. doi:10.1016/S0045-7930(97)00024-8. (Cited on page 68.)

Zuccher, S. and Tumin, A. (2005). Optimal disturbances in compressible boundary layers - Complete energy norm analysis. *AIAA Paper*, 2005-5314. doi:10.2514/6.2005-5314. (Cited on page 43.)

Zuccher, S., Tumin, A. and Reshotko, E. (2006). Parabolic approach to optimal perturbations in compressible boundary layers. *J. Fluid Mech.*, 556:189–216. doi:10.1017/S0022112006009451. (Cited on page 45.)

Le document suivant constitue un résumé des travaux effectués dans le cadre de cette thèse. La version anglaise, intitulée *Spatial optimal perturbations for transient growth analysis in three-dimensional boundary layers*, contient l'ensemble des résultats et doit être consultée pour plus de détails.

# Table des matières

# Introduction

L'étude de la stabilité de la couche limite et de la transition du régime laminaire au régime turbulent constitue un enjeu majeur de l'aérodynamique moderne. La transition vers la turbulence est caractérisée par d'importantes modifications des propriétés de l'écoulement. Si un écoulement laminaire est ordonné et non perturbé, un écoulement turbulent présente un caractère tourbillonnaire marqué par des fluctuations tridimensionnelles et aléatoires de vitesse. D'un point de vue industriel, ces modifications peuvent avoir un caractère bénéfique, par exemple en augmentant la capacité de mélange ou les transferts de chaleur. Cependant, en aéronautique, la transition vers la turbulence s'accompagne d'une forte augmentation du coefficient de frottement, responsable en grande partie de la traînée totale d'un avion. L'amélioration des performances aérodynamiques passe par la réduction de cette traînée de façon à réduire la consommation en carburant, et ce en augmentant l'étendue de la région laminaire au niveau des ailes. Cela passe par le design spécifique des ailes des futurs avions ou par l'utilisation de techniques de contrôle afin de repousser le point de transition vers le bord de fuite. La bonne compréhension des mécanismes de transition vers la turbulence est donc nécessaire pour une prévision fiable des performances aérodynamiques.
La première étape du processus de transition pour des écoulements faiblement perturbés est l'étape de réceptivité, au cours de laquelle les perturbations présentes dans l'environnement extérieur vont venir impacter l'écoulement pour donner naissance à des instabilités au sein de la couche limite. Ces instabilités peuvent alors être amplifiées de façon linéaire avant de conduire à la turbulence par interactions non-linéaires. La plupart des critères de transition employés actuellement se basent sur la théorie de stabilité linéaire, qui décrit l'amplification du mode le moins stable. La transition dite naturelle est déclenchée lorsque l'amplitude de ce mode atteint une valeur donnée. Cependant, de nombreuses expériences ont montré que la transition pouvait avoir lieu dans certains cas d'écoulements cisaillés pour des nombres de Reynolds nettement inférieurs à ceux prévus par la théorie de stabilité linéaire. Ces observations suggèrent l'existence d'un autre mécanisme d'amplification des perturbations au sein des couches limites. Ce mécanisme a été mis en évidence pour la première fois par Ellingsen et Palm (1975) qui ont étudié l'évolution d'une perturbation transverse introduite dans un écoulement cisaillé. Ils ont montré que de telles perturbations pouvaient être amplifiées et engendrer des fluctuations de vitesse longitudinales appelées stries ou modes de Klebanoff. Ces stries peuvent être amplifiées au cours d'un intervalle de temps ou d'espace avant d'être dissipées sous l'effet de la viscosité : c'est le phénomène de croissance transitoire. Une transition prématurée par rapport à la transition naturelle peut être déclenchée si l'énergie des stries est suffisamment amplifiée par la croissance transitoire. C'est la transition Bypass, signifiant que le phénomène classique d'amplification modale a été court-circuité. Contrairement à la théorie de stabilité linéaire qui se concentre sur le calcul du mode le moins stable, l'étude de la croissance transitoire passe par la détermination de la perturbation optimale. Ce terme désigne l'instabilité initiale qui maximise

l'énergie des perturbations au sein de la couche limite. L'étude de l'évolution spatiale des perturbations optimales a débuté avec Andersson *et al.* (1999) et Luchini (2000) pour une couche limite de Blasius. Ils ont montré que le maximum de croissance transitoire est associé à des perturbations transversales stationnaires qui conduisent à la formation de stries alternées de vitesse. Utilisant la théorie des perturbations optimales, les travaux de Biau (2006) et Vermeersch (2009) ont permis de mettre en place des critères pour la transition Bypass. Dans de tels cas, l'écoulement extérieur est tellement perturbé que la croissance transitoire pilote entièrement le déclenchement de la transition. Cependant, lorsque le taux de turbulence extérieure est plus modéré, la croissance transitoire et le phénomène d'amplification modale peuvent cohabiter. Cela pose la question de l'influence de la croissance transitoire sur l'amplification modale des perturbations.

C'est dans ce contexte que se situe cette thèse qui vise à étendre les outils numériques permettant le calcul des perturbations optimales à des écoulements plus complexes afin de quantifier l'influence de la croissance transitoire sur l'amplification modales des perturbations. Tout au long de l'étude, le lien avec les critères de transition classiques employés dans de telles configurations est étudié.

La première partie de cette thèse présente les principaux mécanismes de transition que l'on peut rencontrer au sein des couches limites. Le phénomène de croissance transitoire ainsi que les études précédentes concernant l'étude des perturbations optimales pour des couches limites bidimensionnelles et tridimensionnelles sont également détaillés afin de préciser le contexte de l'étude (chapitre 1). La technique de calcul des perturbations optimales est ensuite introduite dans le cas général d'une couche limite bidimensionnelle incompressible. En particulier, la méthode d'optimisation de l'énergie des perturbations basée sur la résolution itérative des équations parabolisées directes et adjointes est présentée (chapitre 2).
Les outils numériques présentés sont ensuite appliqués à la détermination des perturbations optimales pour des couches limites bidimensionnelles et compressibles se développant sur des parois courbes. Pour cela, un système d'équations paraboliques est établi afin de prendre en compte les effets de courbure. Un nouveau critère est proposé afin de spécifier la perturbation optimale la plus rapidement amplifiée. Le calcul de ces perturbations optimales pour des couches limites se développant sur des parois concaves est effectué afin de définir la courbe neutre du problème de Görtler. L'amplification spatiale des tourbillons de Görtler est étudiée et les effets de compressibilité sont analysés. L'hypothèse d'écoulement parallèle est ensuite adoptée afin de calculer le spectre et le pseudospectre des opérateurs. Le pseudospectre permet de mesurer le degré de non-normalité et de quantifier l'effet de la courbure sur les interactions entre les modes non-normaux. L'amplification des perturbations est ensuite calculée par une approche multi-modale basée sur les modes non-normaux afin d'étudier le potentiel de croissance transitoire avant l'amplification exponentielle des tourbillons de Görtler (chapitre 3). Après avoir considéré une paroi à courbure constante, la transition pour des couches limites compressibles sur des parois à oscillations multiples, caractéristiques d'ondulations de surface rencontrées dans des applications industrielles, est étudiée. L'évolution des modes de Klebanoff vers les tourbillons de Görtler est d'abord analysée pour une courbure périodique. Le lien entre la croissance transitoire et l'amplitude exponentielle des tourbillons de Görtler est ensuite précisé. Pour cela, l'amplification des perturbations est calculée par l'approche optimale et comparée au résultat obtenu par la méthode PSE (Parabolised Stability Equations). L'importance de la prise en compte des effets de croissance transitoire dans les critères de transition classiques pour des ondulations de surface est finalement quantifiée (chapitre 4). Les résultats de ces deux derniers chapitres ont fait l'objet de communications lors de deux congrès internationaux ainsi que d'une publication soumise (Lucas *et al.*, 2013a,b).

La dernière partie de cette thèse est consacrée au phénomène de croissance transitoire au sein de couches limites tridimensionnelles caractéristiques d'écoulements sur des ailes en flèche. Une modification des équations PSE, utilisées dans la détermination des modes transversaux, est présentée afin de considérer l'évolution de perturbations modales et non-modales. Les perturbations optimales stationnaires se développant dans des couches limites de Falkner-Skan-Cooke sont alors étudiées avec cette méthode. L'évolution de la perturbation optimale vers le mode transversal correspondant en aval de la position neutre est particulièrement examinée dans le cadre de cette thèse. Pour cela, l'amplification et les fonctions d'amplitude de la perturbation optimale et de la fonction propre associée sont comparées. L'influence de la croissance transitoire sur l'amplitude initiale du mode transversal est quantifiée pour des couches limites accélérées et décélérées (chapitre 5). Cette amplification initiale potentielle du mode transversal sous l'effet de la croissance transitoire est ensuite analysée pour des couches limites se développant sur des géométries plus complexes. Le profil Onera DTP-B est considéré et des comparaisons détaillées entre croissance modale et non-modale sont effectuées. Enfin, la couche limite se développant le long de la ligne de partage d'un cylindre en flèche d'envergure infinie, représentatif de l'écoulement au niveau du bord d'attaque d'une aile d'avion, est envisagée. Le critère de transition utilisé pour la détection du phénomène de contamination du bord d'attaque est considéré du point de vue de la croissance transitoire. Pour cela, la perturbation optimale se développant sur et au voisinage de la ligne de partage est déterminée pour différentes configurations (chapitre 6).
Les principaux résultats obtenus sont finalement rassemblés et discutés afin de tirer les conclusions de l'étude réalisée au cours de cette thèse et de dégager des perspectives en vue de futurs travaux qui permettront d'améliorer la compréhension du phénomène de transition au sein des couches limites.

Chapitre 1

# État de l'art

Ce chapitre traite du processus de transition au sein des couches limites bidimensionnelles et tridimensionnelles. Les différents scénarios conduisant à la turbulence sont détaillés afin de préciser le contexte de l'étude. Selon les caractéristiques de la couche limite et de l'environnement extérieur, différents types d'instabilités vont se développer. L'étude de ces instabilités se fait par les méthodes de stabilité linéaire locale ou non qui sont ici rappelées. Pour des écoulements perturbés, le phénomène de croissance transitoire, lié aux interactions entre des modes non normaux, peut aussi intervenir. Les études précédentes portant sur ce processus d'amplification linéaire des instabilités dans les couches limites sont aussi résumées.

## 1.1 Différentes routes vers la turbulence

La transition entre le régime laminaire et le régime turbulent est due à une instabilité de l'écoulement de base. Dans l'étude du processus de transition, la première étape cherche à décrire la naissance de ces instabilités dans la couche limite : c'est l'étape de réceptivité (Morkovin, 1969). Selon les caractéristiques de l'écoulement, ces instabilités vont ensuite s'amplifier pour conduire à la transition, ou décroître. L'étude de la transition passe donc par la connaissance des mécanismes d'amplification des perturbations.
Reshotko (2008) présente différentes routes possibles du régime laminaire au régime turbulent, représentées sur la figure 1.1 en fonction de l'amplitude des perturbations extérieures. En effet, le processus de transition dépend de nombreux paramètres, tels que l'état de surface, le bruit ou le taux de turbulence extérieure $Tu$. Ces perturbations extérieures vont être filtrées par la couche limite pour y générer des instabilités lors de l'étape de réceptivité. Le processus de transition peut alors emprunter différents chemins.

- Le chemin A correspond au mécanisme classique de transition par amplification modale (Reed *et al.*, 1996). Ce scénario est caractéristique d'écoulements peu perturbés où la croissance modale joue un rôle important. L'amplification des ondes de Tollmien-Schlichting (TS) en 2D, ou des modes transversaux (ou *crossflow* en anglais, noté CF) pour des couches limites tridimensionnelles sur ailes en flèche, conduit à la transition. Les instabilités de Görtler pour des écoulements sur surfaces concaves suivent également ce chemin. Dans ce cas, la transition est gouvernée par l'amplification du mode le moins stable, dont la croissance est bien décrite par la théorie de stabilité linéaire.

– Lorsque l'amplitude des perturbations extérieures augmente, le phénomène de croissance transitoire apparaît. Pour le chemin B, l'amplitude des perturbations extérieures reste suffisamment faible pour que les phénomènes de croissance modale et transitoire cohabitent. La croissance transitoire fournit une amplitude initiale aux perturbations avant la phase d'amplification exponentielle. Une illustration possible de ce scénario est à trouver dans la phase de croissance transitoire qui précède l'amplification des tourbillons de Görtler. Ce cas sera détaillé plus précisément dans les chapitres 3 et 4. Pour les couches limites tridimensionnelles, le lien entre croissance transitoire et modes crossflow relève également de ce chemin, comme détaillé dans les chapitres 5 et 6.

– Pour le chemin C, l'amplitude des perturbations extérieures est suffisante pour que le phénomène de croissance transitoire prédomine devant l'amplification modale. La théorie des perturbations optimales montre que les perturbations initiales correspondant à des tourbillons longitudinaux entraînent la formation de stries, aussi appelées modes de Klebanoff, dans la couche limite. Ces stries peuvent être amplifiées de façon importante jusqu'à être déstabilisées.

– Pour le chemin D comme pour le chemin C, les perturbations extérieures pénètrent dans la couche limite au niveau du bord d'attaque pour donner naissance à des stries. Pour le chemin C, la transition est due à une instabilité secondaire de l'écoulement de couche limite modifié par la propagation de ces stries. Pour le chemin D, le filtrage des hautes fréquences de la turbulence extérieure n'a pas lieu car les stries atteignent une amplitude critique dans une région proche du bord d'attaque. Ces hautes fréquences interagissent alors avec les modes de Klebanoff pour précipiter la transition.

– Le chemin E caractérise des écoulements fortement perturbés. Le forçage de la couche limite par les perturbations extérieures est tel qu'il n'y a plus de régime linéaire. La couche limite est pleinement turbulente dès sa formation et la notion même de transition est remise en question.

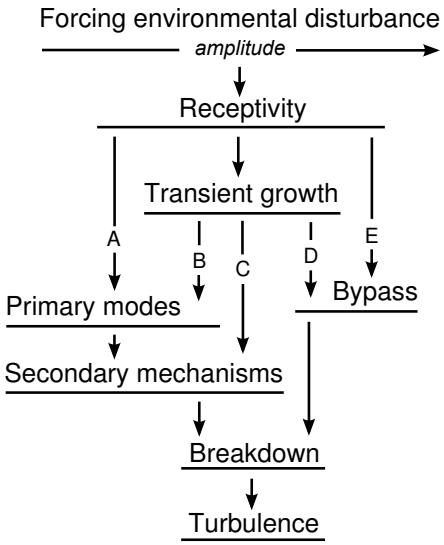


Figure 1.1 : Différentes routes vers la turbulence (Morkovin *et al.*, 1994).

## 1.2 Instabilités de couche limite

### 1.2.1 Instabilités modales

Tollmien (1929) et Schlichting (1933) ont déterminé pour la première fois l'amplification des perturbations les moins stables pour un écoulement de couche limite bidimensionnel. Ces instabilités visqueuses, appelées ondes de Tollmien-Schlichting (TS), furent observées par Schubauer et Skramstad (1948). La figure 1.2 montre l'évolution des ondes TS dans une couche limite observée dans une cuve hydraulique à basse vitesse. Ces ondes peuvent être décrites par la théorie de stabilité linéaire locale.

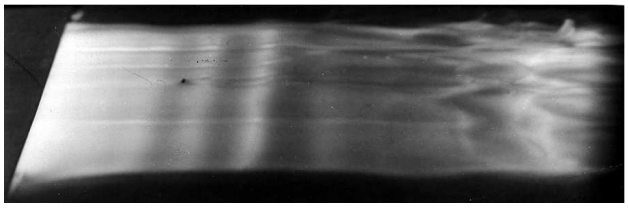

Figure 1.2 : Propagation des ondes TS dans une couche limite bidimensionnelle incompressible (Werlé, ONERA, 1980). L'écoulement se fait de la gauche vers la droite.

Pour les couches limites tridimensionnelles, comme par exemple sur les ailes en flèche d'un avion, le profil de vitesse de l'écoulement de base peut se décomposer en une composante longitudinale $U$ et une composante transversale $W$, comme illustré sur la figure 1.3. Le profil de vitesse $W$ présente un point d'inflexion qui génère une instabilité appelé mode transverse, ou crossflow (CF) (Reed et Saric, 1989; Saric *et al.*, 2003).

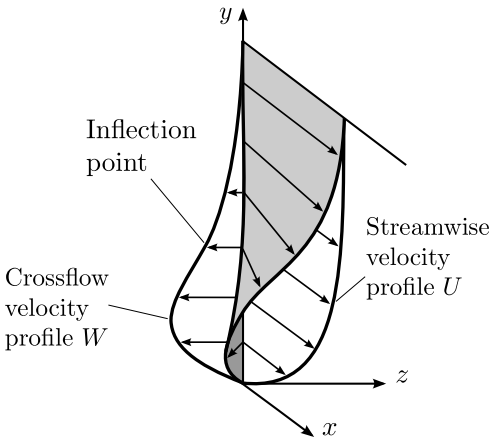


Figure 1.3 : Profils de vitesse pour une couche limite tridimensionnelle (Saric *et al.*, 2003).

Les modes CF sont instables dans les régions où l'écoulement est accéléré dans la direction longitudinale, comme par exemple dans la région proche du bord d'attaque pour une aile en flèche. On peut observer des perturbations stationnaires ou non stationnaires, la transition étant généralement liée à l'amplification d'un seul de ces types d'ondes. Les modes stationnaires sont prédominants pour des écoulements faiblement perturbés (faible $Tu$), tandis que les ondes non stationnaires, plus amplifiées selon la théorie de stabilité linéaire, dominent quand l'amplitude des perturbations extérieures est plus élevée. Du point de vue de la réceptivité, les modes stationnaires

sont initiés par des micro-rugosités de surface, tandis que les ondes non stationnaires sont dues à la turbulence extérieure.

### 1.2.2 Analyse de stabilité modale

#### 1.2.2.1 Stabilité locale

Les perturbations sont introduites dans les équations de Navier-Stokes qui sont ensuite linéarisées. En adoptant l'hypothèse d'écoulement parallèle avec $(U(y), V(y) = 0, W(y))^T$, les perturbations sont introduites sous la forme de modes normaux,

$$\boldsymbol{q}'(x, y, z, t) = \boldsymbol{q}(y) \exp[i(\alpha x + \beta z - \omega t)], \tag{1.1}$$

où $\alpha$ et $\beta$ sont respectivement les nombres d'onde dans les directions longitudinale et transverse, et où $\omega$ est la pulsation temporelle. La résolution du système d'équations linéarisées constitue alors un problème aux valeurs propres. Les solutions non triviales sont obtenues pour des combinaisons particulières de ($\alpha$,$\beta$,$\omega$) données par la relation de dispersion.

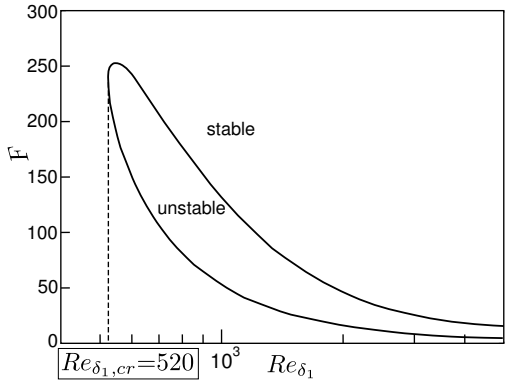


Figure 1.4 : Courbe neutre pour la couche limite de Blasius.

Le taux d'amplification des perturbations est relié à la partie imaginaire du nombre d'onde longitudinal d'après la relation

$$\frac{1}{A}\frac{\mathrm{d}A}{\mathrm{d}x} = -\alpha_i. \tag{1.2}$$

Pour une fréquence $F$ donnée, l'onde est d'abord atténuée, puis amplifiée à l'intérieur de la courbe neutre, puis atténuée de nouveau, comme illustré sur la figure 1.4. Si l'on note $A_0$ l'amplitude de la perturbation au point $x_0$ d'intersection avec la branche inférieure de la courbe neutre, on peut exprimer le rapport total d'amplification comme

$$\ln(A/A_0) = \int_{x_0}^{x} -\alpha_i(\xi, f)\,\mathrm{d}\xi. \tag{1.3}$$

Calculer ce rapport d'amplification pour différentes fréquences conduit à la définition du facteur $N$, qui représente l'enveloppe des différentes courbes intégrales,

$$N(x) = \max_f \left(\ln(A/A_0)\right). \tag{1.4}$$

La figure 1.5 représente les taux d'amplification pour différentes fréquences et la courbe enveloppe du facteur $N$ pour une couche limite de Blasius. La méthode du $e^N$ suppose que la transition se

produit pour une valeur prédéfinie du facteur $N$, notée $N_T$ (van Ingen, 1956; Smith et Gamberoni, 1956). Cela signifie que la transition se produit lorsque l'onde la plus instable a été amplifiée d'un facteur $e^{N_T}$. La relation proposée par Mack (1977) permet de relier le seuil de transition au taux de turbulence extérieure $Tu$ pour des écoulement bidimensionnels à basse vitesse,

$$N_T = -8.43 - 2.4\ln(Tu) \quad \text{pour } 10^{-3} < Tu < 10^{-2}. \tag{1.5}$$

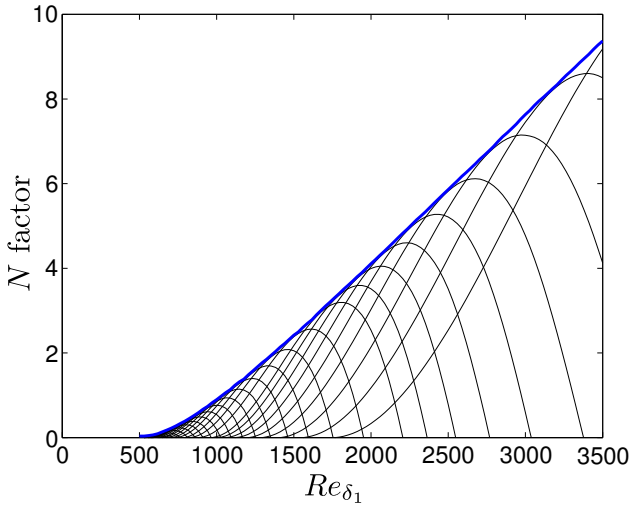


Figure 1.5 : Taux d'amplification (——) et courbe enveloppe (——) pour une couche limite de Blasius.

#### 1.2.2.2 Approche non locale : système d'équations parabolisées (PSE)

Afin de s'affranchir de l'hypothèse d'écoulement parallèle et de prendre en compte les effets liés à l'épaississement de la couche limite, Simen (1992) et Bertolotti *et al.* (1992); Herbert (1993) ont proposé une nouvelle formulation pour l'analyse de stabilité qui repose sur un système d'équations parabolisées : c'est la méthode PSE (parabolised stability equations). Cette méthode s'applique par exemple dans les cas d'écoulements de couches limites ou de jets. L'idée de la méthode PSE est que les grandeurs considérées comme locales sous l'hypothèse d'écoulement parallèle peuvent maintenant dépendre faiblement de la coordonnée longitudinale $x$.
Les perturbations sont écrites comme le produit d'une fonction d'amplitude $\boldsymbol{q}$ lentement variable en $x$ et d'une fonction d'onde $\Theta$,

$$\boldsymbol{q}'(x,y,z,t) = \boldsymbol{q}(x,y)\exp(i\Theta(x,z,t)), \tag{1.6a}$$

$$\Theta(x,z,t) = \int_{x_0}^{x} \alpha(\xi)\,\mathrm{d}\xi + \beta z - \omega t. \tag{1.6b}$$

Les perturbations sont introduites dans les équations de Navier-Stokes qui sont ensuite linéarisées. Une fois le gradient de fluctuation de pression longitudinal négligé, le système d'équations aux dérivées partielles obtenu est parabolique et peut donc être résolu par une technique de marche vers l'aval. La résolution permet d'obtenir les fonctions d'amplitude $\boldsymbol{q}(x,y)$ pour un nombre d'onde longitudinal complexe $\alpha$ fixé mais encore inconnu.
Sous l'hypothèse d'écoulement parallèle, ce nombre d'onde est déterminé par la relation de dispersion. La méthode PSE ajoute une nouvelle équation, appelée condition de normalisation, qui constitue une relation de fermeture permettant la détermination de $\alpha$. Cette condition doit lever l'ambiguïté de la

double dépendance en $x$ de la fonction d'amplitude et de la fonction d'onde dans l'équation (1.6a). Une extension de l'analyse de stabilité locale conduit à la relation de normalisation,

$$\int_0^\infty \boldsymbol{q}^H \frac{\partial \boldsymbol{q}}{\partial x}\,\mathrm{d}y = 0, \tag{1.7}$$

qui assure une évolution lente de la fonction d'amplitude dans la direction longitudinale (Airiau, 1994).

### 1.2.3 Tourbillons de Görtler

Les tourbillons de Görtler sont des tourbillons longitudinaux contra-rotatifs et stationnaires qui se développent dans les couches limites sur paroi concave (Görtler, 1941). Dans de telles configurations, l'écoulement est soumis à un déséquilibre entre les forces centrifuges et le gradient de pression normal qui déstabilise la couche limite et entraîne la formation de tourbillons longitudinaux, comme illustré sur la figure 1.6.

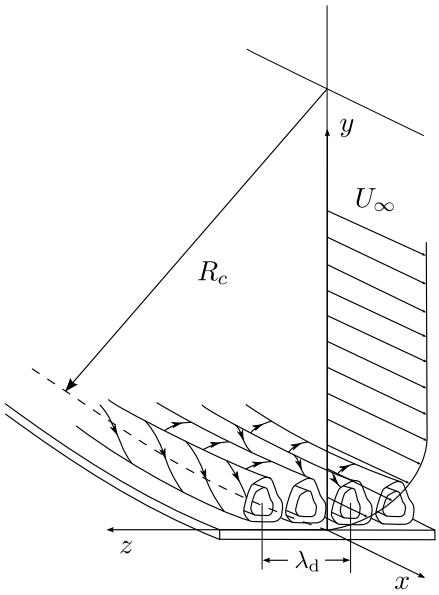


Figure 1.6 : Formation de tourbillons de Görtler dans une couche limite se développant sur une surface concave de rayon de courbure $R_c$ (Saric, 1994).

L'étude des couches limites se développant sur des parois concaves a débuté avec les travaux de Görtler, qui se basent sur la théorie de stabilité linéaire locale. La courbe neutre pour une couche limite de Blasius sur une paroi courbe a été calculée notamment par Hämmerlin (1955) et Smith (1955), mais les résultats obtenus divergent.
Les travaux de Hall (1982) ont montré que l'hypothèse d'écoulement parallèle n'est pas valable lorsque la longueur d'onde des tourbillons est de l'ordre de l'épaisseur de la couche limite. La résolution des équations paraboliques par une technique de marche vers l'aval montre en particulier que la courbe neutre n'est pas unique et qu'elle dépend des perturbations initiales (Hall, 1983). Plus de détails concernant les études portant sur le développement des tourbillons de Görtler sont fournis dans la version anglaise du manuscrit (voir chapitre 1, paragraphe 1.2.3).

### 1.2.4 Transition sur la ligne de partage

Pour des géométries simples, la ligne de partage peut être vue comme la ligne de courant qui divise l'écoulement en une partie se développant sur l'intrados et une partie sur l'extrados. De façon plus précise, il s'agit de la ligne dans la direction transverse sur laquelle la pression statique est maximale (Arnal *et al.*, 2008). Cette ligne est représentée sur la figure 1.7 pour un cylindre d'envergure infinie en flèche. La vitesse à l'infini amont $Q_\infty$ peut être décomposée en une composante longitudinale $U_\infty = Q_\infty \cos(\phi)$ normale au bord d'attaque et une composante transverse $W_\infty = Q_\infty \sin(\phi)$ parallèle au bord d'attaque.

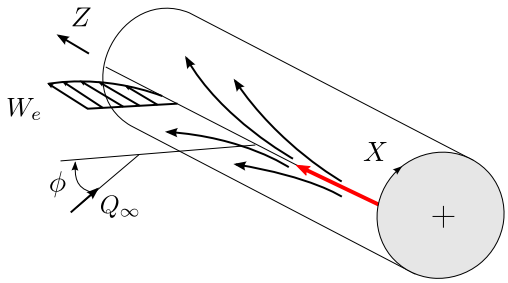


Figure 1.7 : Ligne de partage pour un cylindre en flèche d'envergure infinie.

Le long de la ligne de partage, on peut définir les composantes de vitesse extérieure $U_e$ et $W_e$,

$$U_e = kX \quad \text{et} \quad W_e = W_\infty = \text{constante}, \tag{1.8}$$

où $k$ est le gradient de vitesse extérieure dans la direction $X$. L'écoulement le long de la ligne de partage est caractérisé par le nombre de Reynolds $\overline{R}$,

$$\overline{R} = \frac{W_e \eta}{\nu_e} \quad \text{avec } \eta = (\nu_e/k)^{1/2}, \tag{1.9}$$

où $\nu_e$ est la viscosité.

Deux types de phénomènes peuvent être identifiés le long de la ligne de partage : la transition naturelle et la contamination du bord d'attaque.
La transition naturelle se produit quand la ligne de partage n'est pas soumise à de fortes perturbations extérieures. Une couche limite laminaire se développe alors dans la direction transverse $Z$ qui peut ensuite devenir turbulente plus en aval. La transition vers la turbulence est alors due à un mécanisme d'amplification des perturbations, de façon similaire à ce que l'on peut observer pour une couche limite se développant sur une plaque plane.

A l'inverse, le phénomène de contamination du bord d'attaque est dû à la présence de fortes perturbations extérieures à la naissance de la ligne de partage. C'est le cas par exemple de l'écoulement sur le bord d'attaque d'une aile d'avion qui est susceptible d'être contaminé par la turbulence provenant de la jonction de l'aile avec le fuselage. Des spots turbulents sont alors convectés le long de la ligne de partage ; ils peuvent ensuite grossir jusqu'à ce que l'écoulement soit entièrement turbulent.
En régime subsonique et transsonique, un critère basé sur la valeur de $\overline{R}$ a été développé pour prévoir la transition (Pfenninger, 1965; Poll, 1978). Si $\overline{R} < 250$, les spots turbulents sont dissipés lors de leur convection le long de la ligne de partage. Si $\overline{R} > 250$, les spots turbulents sont auto-entretenus et grossissent jusqu'à ce que la région du bord d'attaque soit entièrement turbulente.

La présence de fortes perturbations dans l'écoulement extérieur ou d'imperfections de surface dans le cas de la contamination du bord d'attaque pose la question de la croissance transitoire le long de la ligne de partage. Obrist et Schmid (2003) puis Guégan *et al.* (2006, 2007) ont mis en évidence une forte amplification transitoire des perturbations dans le domaine temporel. Dans le domaine spatial, Guégan *et al.* (2008) ont montré que l'amplification des perturbations est due à l'effet lift-up, où des perturbations longitudinales de vitesse donnent lieu à des stries se développant dans la direction transverse de façon similaire aux modes de Klebanoff observés dans une couche limite de Blasius.

## 1.3 Croissance transitoire

La théorie de stabilité linéaire fournit un paramètre critique (par exemple le nombre de Reynolds) au-dessus duquel une perturbation infinitésimale est amplifiée exponentiellement. Il existe cependant des écoulements pour lesquels le paramètre critique donné par la stabilité linéaire diffère des observations expérimentales. Ces différences sont dues à un phénomène d'amplification linéaire, appelé croissance transitoire ou croissance algébrique, qui est attribué à la non normalité des opérateurs (Trefethen, 1991). La non orthogonalité des fonctions propres conduit à des interactions possibles entre plusieurs modes, ce qui peut alors entraîner une augmentation significative de l'énergie des perturbations (Schmid et Henningson, 2001). Ce phénomène est illustré de façon schématique sur la figure 1.8.

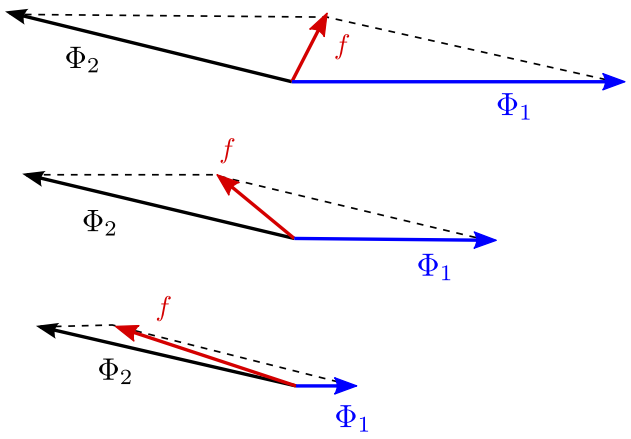


Figure 1.8 : Illustration de la croissance transitoire due à la combinaison de deux fonctions propres non orthogonales. Le vecteur $f$ est défini comme la somme des vecteurs propres $\Phi_1 + \Phi_2$ : bien que $\Phi_1$ et $\Phi_2$ diminuent au cours du temps ou de la propagation spatiale (de haut en bas sur le schéma), la norme du vecteur $f$ augmente (Schmid et Henningson, 2001).

La première analyse du phénomène de croissance transitoire a été réalisée par Ellingsen et Palm (1975) qui ont introduit une perturbation transversale dans un écoulement non visqueux cisaillé. Ils ont montré que des fluctuations longitudinales de vitesse apparaissaient alors, qui peuvent croître linéairement pour donner naissance à des stries de haute et basse vitesse alternées dans la direction transversale. Le mécanisme physique responsable de la formation de ces stries est donné par Landahl (1980) : c'est l'effet "lift-up", illustré sur la figure 1.9. Hultgren et Gustavsson (1981) ont montré que des fluctuations longitudinales de vitesse peuvent aussi être amplifiées dans un écoulement visqueux, où elles décroissent finalement sous l'effet de la viscosité. De nombreuses expériences montrent que ces stries de vitesse, aussi appelées modes de Klebanoff, jouent un rôle dans le processus de transition (Klebanoff, 1971; Matsubara et Alfredsson, 2001).

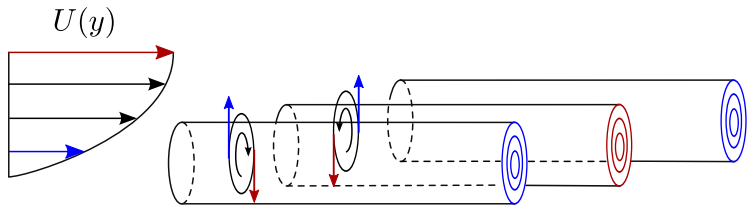


Figure 1.9 : Illustration de l'effet "lift-up" : interaction entre le cisaillement de l'écoulement de base et un tourbillon longitudinal conduisant à la formation de stries de haute (lignes rouges) et basse (lignes bleues) vitesse.

L'étude de la croissance transitoire passe par la détermination de la perturbation optimale (Butler et Farrell, 1992). Ce terme désigne la perturbation initiale qui va engendrer les instabilités les plus énergétiques dans la couche limite au bout d'une certaine distance (ou d'un certain temps). La perturbation optimale représente donc le pire scénario vis-à-vis de la transition, maximisant l'énergie des perturbations se propageant dans la zone laminaire.
Andersson *et al.* (1999) et Luchini (2000) ont étudié la stabilité d'une couche limite incompressible en incluant les effets de non parallélisme. La technique d'optimisation consiste à rechercher la perturbation initiale en procédant à des itérations successives du système direct et du système adjoint. La perturbation optimale obtenue correspond à des tourbillons longitudinaux stationnaires responsables de la formation de stries dans la couche limite (voir les figures 1.10 et 1.11). Tumin et Reshotko (2003) ont étendu ces travaux pour des couches limites compressibles et ont montré que la perturbation optimale est là encore formée de tourbillons longitudinaux produisant des stries de vitesse et de température.

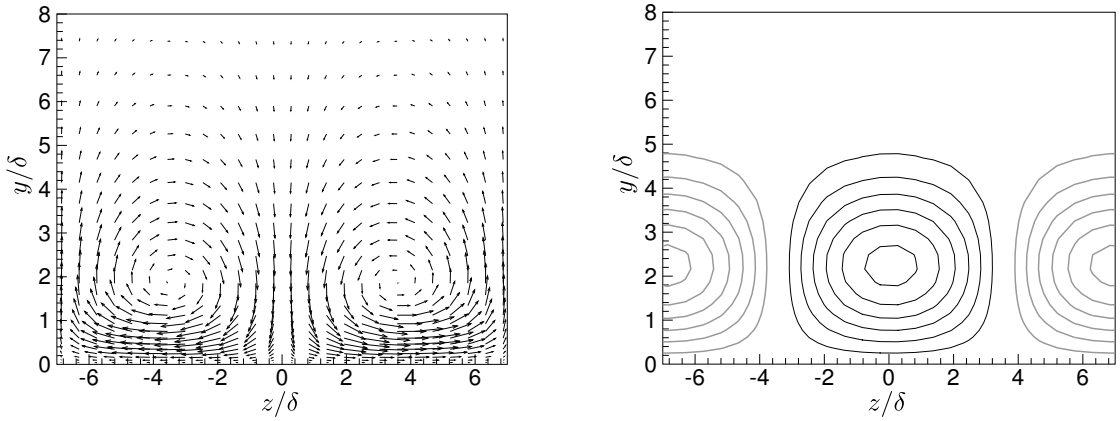


(a) Tourbillons initiaux en $x_{\text{in}} = 0$.

(b) Iso-contours de vitesse longitudinale (positif en noir, négatif en gris) en $x_{\text{out}} = 1$.

Figure 1.10 : Perturbation initiale en $x_{\text{in}} = 0$ et perturbation résultante en $x_{\text{out}} = 1$ dans le plan $(z,y)$ pour une couche limite de Blasius avec $\beta = 0.45$ et $\omega = 0$.

Cossu *et al.* (2000) ont employé la théorie des perturbations optimales pour calculer l'amplification spatiale des tourbillons de Görtler. Leur étude fait notamment ressortir les similitudes entre les perturbations optimales obtenues sur une plaque plane et dans le cas avec courbure.

L'étude de la croissance transitoire dans les couches limites tridimensionnelles a débuté récemment avec les travaux de Corbett et Bottaro (2001) dans le domaine temporel. La différence majeure avec le cas bidimensionnel est que la croissance transitoire et la croissance modale sont

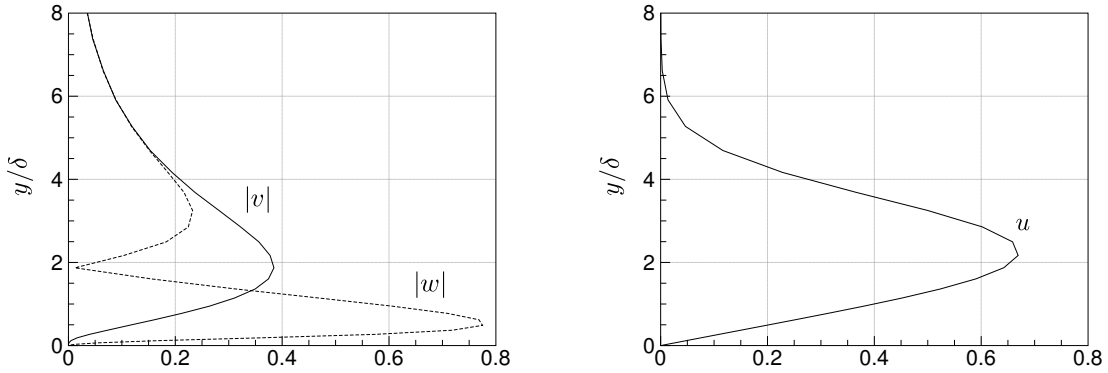


(a) Perturbation initiale en $x_{\text{in}} = 0$, $u = 0$

(b) Perturbation résultante en $x_{\text{out}} = 1$, $v = w = 0$.

Figure 1.11 : Profils de vitesse de la perturbation initiale en $x_{\text{in}} = 0$ et de la perturbation résultante en $x_{\text{out}} = 1$ pour une couche limite de Blasius avec $\beta = 0.45$ et $\omega = 0$.

observées pour des perturbations similaires. Celles-ci prennent la forme de tourbillons quasiment alignés avec la ligne de courant qui évoluent ensuite vers des stries. La ressemblance avec l'instabilité transversale (CF) laisse supposer que les deux phénomènes de croissances transitoire et modale sont complémentaires.

Dans le domaine spatial, Byström (2007), puis Tempelmann *et al.* (2010) utilisent un système d'équations parabolisées pour décrire l'évolution des perturbations dans une couche limite de Falkner-Skan-Cooke soumise à un gradient de pression favorable ou défavorable. Dans les deux cas, les perturbations prennent la forme de tourbillons contra-rotatifs dans le plan transversal et inclinés par rapport à un axe normal à la paroi. La perturbation évolue ensuite vers l'aval sous forme d'une strie quasiment alignée avec la ligne de courant extérieure, se redressant par rapport à l'axe normal. Le mécanisme de croissance transitoire pour une couche limite tridimensionnelle semble donc être basé sur une combinaison de l'effet "lift-up" et du mécanisme de Orr. La ressemblance entre les instabilités non modales et les instabilités transversales est là aussi soulignée.

Différents types d'instabilités peuvent être recensés au sein des couches limites. Pour chacune de ces instabilités, la théorie de stabilité linéaire décrit l'évolution du mode le moins stable qui caractérise l'écoulement aux temps longs. La méthode $e^N$ de prévision de la transition se base sur cette approche. Cependant, quand l'amplitude des perturbations extérieures est suffisante, le phénomène de croissance transitoire joue un rôle dans le processus de transition. Ce phénomène est dû à de possibles interactions entre des modes non normaux qui entraînent une amplification des perturbations. Cette thèse vise à étudier l'influence de la croissance transitoire sur l'amplification modale des perturbations dans le cas de géométries complexes telles que des couches limites se développant sur des parois courbes ou des configurations fortement tridimensionnelles. Un scénario possible qui sera en particulier abordé dans la suite de cette thèse consiste en une phase initiale de croissance transitoire précédant l'amplification exponentielle des instabilités. La relation entre les modes de Klebanoff et les tourbillons de Görtler sera ainsi étudiée. La question de la détermination de la courbe neutre pour le problème de Görtler, qui a été soulignée dans ce chapitre, sera considérée du point de vue de la croissance transitoire. La relation entre les instabilités transversales et la croissance transitoire dans les couches limites tridimensionnelles sera aussi envisagée.

Chapitre 2

# Théorie des perturbations optimales

Ce chapitre décrit la méthode de calcul des perturbations optimales, c'est-à-dire des perturbations initiales qui conduisent à l'amplification maximale des perturbations dans la couche limite. Les équations de Navier-Stokes pour un écoulement bidimensionnel sont pour cela adimensionnées puis linéarisées de façon à obtenir un système d'équations paraboliséees. La détermination de la perturbation optimale est présentée dans le cas général d'un écoulement non parallèle avec une méthode de résolution basée sur des itérations successives du système direct/adjoint. Numériquement, les équations sont discrétisées dans la direction longitudinale et dans la direction normale, puis résolues par une méthode de marche vers l'aval.

## 2.1 Équations des perturbations

La transition dans la couche limite est due à l'amplification des perturbations. L'évolution de ces perturbations est décrite par les équations de Navier-Stokes linéarisées autour d'un écoulement de base $\boldsymbol{Q} = (U, V, W, P)^T$. Ces équations sont ensuite rendues sans dimension en utilisant les échelles de Prandtl : la coordonnée longitudinale $x$ est adimensionnée par une longueur de référence $L$ (par exemple la corde), tandis que les coordonnées normale et transversale $y$ et $z$ sont adimensionnées par une grandeur représentative de l'épaisseur de la couche limite $\delta = L\sqrt{Re_L}$, où $Re_L = {}^{U_\infty L}/_{\nu}$ est le nombre de Reynolds basé sur $L$. La vitesse longitudinale $U$ et la perturbation associée $u'$ sont adimensionnées par $U_\infty$. L'équation de continuité implique alors que $V$ et $W$, ainsi que leurs perturbations associées $v'$ et $w'$, soient adimensionnées par $U_\infty/\sqrt{Re_L}$. La perturbation de pression $p'$ est quant à elle adimensionée par $\rho_\infty U_\infty^2/Re_L$. Par ailleurs, les termes de diffusion dans la direction $x$ sont négligés, ainsi que le gradient de fluctuation de pression longitudinal. L'écoulement de base étant stationnaire et bidimensionnel, on peut écrire les perturbations $\boldsymbol{q'} = (u', v', w', p')^T$ sous la forme

$$\boldsymbol{q'}(x, y, z, t) = \boldsymbol{q}(x, y)e^{i(\beta z - \omega t)}. \tag{2.1}$$

En introduisant les perturbations dans le système d'équations paraboliques, on obtient

$$u_x + v_y + i\beta w = 0, \tag{2.2a}$$
$$-i\omega u + Uu_x + Vu_y + uU_x + vU_y = u_{yy} - \beta^2 u, \tag{2.2b}$$
$$-i\omega v + Uv_x + Vv_y + uV_x + vV_y + p_y = v_{yy} - \beta^2 v, \tag{2.2c}$$
$$-i\omega w + Uw_x + Vw_y + i\beta p = w_{yy} - \beta^2 w, \tag{2.2d}$$

qui peut s'écrire

$$\mathcal{L}\boldsymbol{q} = 0. \tag{2.3}$$

Les conditions aux limites sont données par

$$u = v = w = 0 \quad \text{en } y = 0, \tag{2.4a}$$
$$u = w = p = 0 \quad \text{en } y = y_{\max}. \tag{2.4b}$$

## 2.2 Perturbation optimale et maximisation du gain

Déterminer la perturbation optimale revient à chercher la perturbation initiale qui va maximiser le gain, c'est-à-dire le rapport entre l'énergie finale en $x_{\text{out}}$ et l'énergie initiale en $x_{\text{in}}$ des perturbations. La perturbation initiale est donc recherchée de manière à maximiser

$$G_{\max} = \max_{\boldsymbol{q}_{\text{in}}} \frac{\|\boldsymbol{q}_{\text{out}}\|^2}{\|\boldsymbol{q}_{\text{in}}\|^2}, \tag{2.5}$$

où $\|\boldsymbol{q}\|$ désigne la norme associée au produit scalaire $(\boldsymbol{q}, \boldsymbol{q})$, tandis que l'énergie des perturbations s'écrit $E(\boldsymbol{q}) = \|\boldsymbol{q}\|^2$. La maximisation du gain est un problème d'optimisation contraint par les équations de couche limite parabolisées et les conditions aux limites associées. L'utilisation de la fonction lagrangienne permet de se ramener à un problème d'optimisation sans contrainte. La fonction objectif s'exprime

$$J(\boldsymbol{q}) = \frac{\|\boldsymbol{q}_{\text{out}}\|^2}{\|\boldsymbol{q}_{\text{in}}\|^2}, \tag{2.6}$$

où l'énergie des perturbations est mesurée en $x_{\text{out}}$ et $x_{\text{in}}$ respectivement. La lagrangienne s'écrit alors

$$\mathscr{L}(\boldsymbol{q}, \boldsymbol{p}, \lambda_0) = J(\boldsymbol{q}) - \langle \boldsymbol{p}, \mathcal{L}\boldsymbol{q} \rangle - \lambda_0 \left( \|\boldsymbol{q}_{\text{in}}\|^2 - E_{\text{in}} \right), \tag{2.7}$$

où les multiplicateurs de Lagrange $\boldsymbol{p}$ permettent de vérifier les contraintes. Le problème étant linéaire, on ajoute une contrainte supplémentaire d'énergie initiale unitaire $E_{\text{in}} = 1$.
Le problème d'optimisation est résolu en déterminant les points stationnaires de la lagrangienne,

$$\mathrm{d}\mathscr{L} = \left\langle \frac{\partial \mathscr{L}}{\partial \boldsymbol{q}}, \delta\boldsymbol{q} \right\rangle + \left\langle \frac{\partial \mathscr{L}}{\partial \boldsymbol{p}}, \delta\boldsymbol{p} \right\rangle = 0 \tag{2.8}$$

La variation de $\mathscr{L}$ par rapport aux multiplicateurs de Lagrange $\boldsymbol{p}$ redonne l'équation du problème direct. La variation par rapport aux variables d'état $\boldsymbol{q}$ donne le système adjoint. Comme le système direct, le système adjoint est parabolique, mais propage l'information dans le sens opposé à l'écoulement de, $x_{\text{out}}$ à $x_{\text{in}}$. Les conditions d'optimalité, qui relient le système direct et le système adjoint en $x_{\text{in}}$ et $x_{\text{out}}$, sont données par les variations de $\mathscr{L}$ par rapport à $\boldsymbol{q}_{\text{in}}$ et $\boldsymbol{q}_{\text{out}}$.
Le calcul est initialisé par une perturbation arbitraire introduite à la station $x_{\text{in}}$. La perturbation optimale qui maximise le gain est alors déterminée par itérations successives du système direct/système adjoint de façon à maximiser le gain en $x_{\text{out}}$.

Dans le cas simplifié d'un écoulement parallèle, le calcul du gain se réduit à une décomposition en valeurs singulières. Plus de détails sont donnés dans la version anglaise du manuscrit (voir chapitre 2, paragraphe 2.2).

## 2.3 Définition d'une norme

Afin de déterminer la perturbation initiale qui va maximiser l'amplification de l'énergie des instabilités, la définition d'une mesure de cette énergie est nécessaire. Le choix d'une quantité représentative de l'énergie des perturbations n'est cependant pas unique. Pour un écoulement incompressible, Andersson *et al.* (1999) ont utilisé l'énergie cinétique basée sur les trois composantes de vitesse,

$$E = \int_0^\infty u^2 + Re_L^{-1}(v^2 + w^2)\,\mathrm{d}y. \tag{2.9}$$

Dans l'équation (2.9), le nombre de Reynolds provient de l'adimensionnement utilisé et présenté au paragraphe 2.1. Luchini (2000) a réduit cette expression pour ne prendre en compte que $v$ et $w$ dans le calcul de l'énergie de la perturbation initiale et $u$ dans le calcul de l'énergie finale. Le mécanisme de formation des stries par effet "lift-up" est donc ici supposé a priori. Les deux approches fournissent des résultats similaires dans la limite d'un nombre de Reynolds infini (en pratique $Re_L > 10^4$). L'expression du gain est réduite à

$$G_{\max} = Re_L \max_{\boldsymbol{q}_{\mathrm{in}} \neq 0} \frac{\int_0^\infty u^2\,\mathrm{d}y\ |_{x=x_{\mathrm{out}}}}{\int_0^\infty v^2 + w^2\,\mathrm{d}y\ |_{x=x_{\mathrm{in}}}}. \tag{2.10}$$

Le choix est plus délicat pour un écoulement compressible, où l'énergie cinétique seule ne suffit pas. Il est nécessaire de prendre en compte les fluctuations de température et de masse volumique dues aux effets de compressibilité. On utilise alors la norme de Mack (1969) qui donne l'expression de l'énergie des perturbations,

$$E = \int_0^\infty \left[\rho\left(u^2 + \frac{1}{Re_L}\left(v^2 + w^2\right)\right) + \frac{P\theta^2}{(\gamma - 1)\,T^2 M^2}\right]\mathrm{d}y. \tag{2.11}$$

où $(u, v, w)$ sont les perturbations de vitesse, et $\theta$ est la variation de température $T$. La masse volumique de l'écoulement de base est notée $\rho$, $\gamma$ est le coefficient adiabatique et $M$ est le nombre de Mach.

## 2.4 Approche numérique

A chaque station $x$ pour un écoulement non parallèle, les équations de couche limite parabolisées sont résolues selon la normale $y$ en utilisant une méthode de collocation spectrale.
Les matrices de dérivation sont calculées sur les $N_y$ points de collocation de Gauss-Lobatto, en se ramenant ensuite au domaine physique. Les conditions aux limites vérifiées par les fluctuations de vitesse (ainsi que de température et de masse volumique en écoulement compressible) en $y_{\max}$ sont implicitement contenues dans les matrices de dérivation.
L'intégration selon la normale $y$, utilisée en particulier dans le calcul de l'énergie, est effectuée par la méthode de Clenshaw-Curtis. L'intégrale est calculée sur les points de collocation de Gauss-Lobatto déjà utilisés pour le calcul des opérateurs de dérivation.

La discrétisation dans la direction longitudinale $x$ est effectuée de manière à raffiner le nombre de points aux extrémités $x_{\mathrm{in}}$ et $x_{\mathrm{out}}$. Par ailleurs, le système direct étant parabolique dans la direction $x$, les dérivées longitudinales sont évaluées par un schéma aux différences finies d'ordre 2. L'initialisation du calcul à la première station se fait par un schéma d'Euler d'ordre 1. Les équations pour le problème adjoint sont discrétisées de façon similaire.

Dans le cas général d'un écoulement bidimensionnel non parallèle, la perturbation optimale et le gain correspondant sont déterminés par itérations système direct/système adjoint. Une norme appropriée pour mesurer l'énergie des perturbations doit également être choisie.
Le prochain chapitre traite de couches limites se développant sur des surfaces présentant un rayon de courbure non nul. Les perturbations optimales sur des parois concaves et convexes seront déterminées en employant la méthode décrite dans ce chapitre.

Chapitre 3

# Effets de courbure sur la croissance transitoire

Ce chapitre est consacré à la détermination des perturbations optimales sur des parois concaves à rayon de courbure constant. Dans un premier temps, les équations régissant un écoulement sur une paroi courbe sont détaillées. La perturbation optimale est ensuite calculée par itérations direct/adjoint, et un nouveau critère de convergence est proposé pour calculer la perturbation optimale amplifiée le plus rapidement. Cette approche permet de calculer la courbe neutre pour le problème de Görtler. Une analyse multi-modale est enfin proposée pour mettre en évidence les effets de la courbure sur les interactions entre modes non normaux.

## 3.1 Mise en équations

On s'intéresse à l'écoulement sur une paroi présentant un rayon de courbure $R_c$ grand devant la longueur de référence de la couche limite $\delta$. On part des équations de Navier-Stokes pour un écoulement bidimensionnel compressible.

L'écriture dans un système de coordonnées généralisées se fait par l'introduction du tenseur métrique dont les coefficients sont

$$h_1 = 1 - \frac{y}{R_c} \; ; \qquad h_2 = h_3 = 1. \tag{3.1}$$

Les perturbations de la forme $\boldsymbol{q}'(x,y,z,t) = \boldsymbol{q}(x,y)\exp(i(\beta z - \omega t))$ sont introduites dans les équations, avec $\boldsymbol{q}' = (u', v', w', \theta', p')^T$ pour un écoulement compressible. Comme précédemment, les équations sont linéarisées et rendues sans dimension en utilisant les échelles de Prandtl. On obtient finalement, en notation matricielle,

$$(A \cdot q)_x = (E \cdot q_y)_x + B \cdot q + C \cdot q_y + D \cdot q_{yy}. \tag{3.2}$$

Les coefficients intervenant dans l'équation (3.2) pour un écoulement compressible sont détaillés dans la partie anglaise du manuscrit (voir paragraphe 3.1.1 et annexe C.2). En supposant que le rayon de courbure $R_c$ et la longueur de référence $L$ sont grands devant la longueur de référence de la couche limite $\delta$, les effets de courbure sont pris en compte au travers du seul terme

$$m_{12} = \frac{1}{h_1 h_2}\frac{\partial h_1}{\partial x_2}. \tag{3.3}$$

Ce terme peut être relié à un nombre sans dimension, appelé nombre de Görtler, qui est défini par

$$\mathsf{G} = \frac{L}{R_c}\sqrt{Re_L}. \tag{3.4}$$

Pour un écoulement incompressible, le système obtenu s'écrit alors

$$\frac{\partial u}{\partial x} + \frac{\partial v}{\partial y} + i\beta w = 0 \ ; \tag{3.5a}$$

$$U\frac{\partial u}{\partial x} + V\frac{\partial u}{\partial y} + u\frac{\partial U}{\partial x} + v\frac{\partial U}{\partial y} = \frac{\partial^2 u}{\partial y^2} - \beta^2 u \ ; \tag{3.5b}$$

$$U\frac{\partial v}{\partial x} + V\frac{\partial v}{\partial y} + u\frac{\partial V}{\partial x} + v\frac{\partial V}{\partial y} + 2\mathsf{G}Uu = -\frac{\partial p}{\partial y} + \frac{\partial^2 v}{\partial y^2} - \beta^2 v \ ; \tag{3.5c}$$

$$U\frac{\partial w}{\partial x} + V\frac{\partial w}{\partial y} = i\beta p + \frac{\partial^2 w}{\partial y^2} - \beta^2 w. \tag{3.5d}$$

Une fois le système d'équations parabolisées mis en place, l'objectif est de déterminer les perturbations optimales sur des parois courbes. Pour ce faire, on utilise la méthodologie mise en place lors du chapitre précédent. La norme utilisée pour mesurer l'énergie des perturbations est la norme de Mack. La perturbation optimale est déterminée par itérations successives du système direct/système adjoint.

L'objectif est ici de déterminer l'effet de la courbure sur la croissance transitoire. On s'intéresse plus particulièrement à la croissance optimale des tourbillons de Görtler et à la détermination de la courbe neutre.
Pour résoudre ce problème, un nouveau critère de convergence est proposé pour déterminer la perturbation optimale. La courbe neutre sépare le domaine en une région stable et une région instable. Les perturbations qui sont amplifiées le plus rapidement possible (c'est-à-dire à l'abscisse la plus petite) doivent être déterminées. Le nouveau critère de convergence maximise donc le gain au niveau de la première position neutre, de façon à assurer que la perturbation optimale calculée correspond à la perturbation amplifiée le plus rapidement possible.

## 3.2 Parois à courbure constante

On cherche à déterminer la courbe neutre pour le problème de Görtler, dans le cas où la paroi est concave avec un rayon de courbure constant. La position neutre est définie comme la première station où la dérivée longitudinale de l'énergie s'annule, $\mathrm{d}E/\mathrm{d}x = 0$. A chaque station où cette condition est vérifiée, on peut définir un nombre de Görtler local $\mathsf{G}_x$ et un nombre d'onde transversal local $\beta_x$,

$$\mathsf{G}_x = \mathsf{G} \times x^{3/2}, \tag{3.6}$$

$$\beta_x = \beta \times x^{1/2}. \tag{3.7}$$

Hall (1983) a montré que pour de faibles valeurs du nombre d'onde transversal, la courbe neutre dépend fortement des conditions initiales. Il a introduit différentes perturbations initiales qui sont ensuite propagées vers l'aval pour déterminer la courbe neutre correspondante. La détermination de la perturbation optimale associée au nouveau critère de convergence établi précédemment permet de s'affranchir de cette dépendance aux conditions initiales. En effet, la courbe neutre calculée

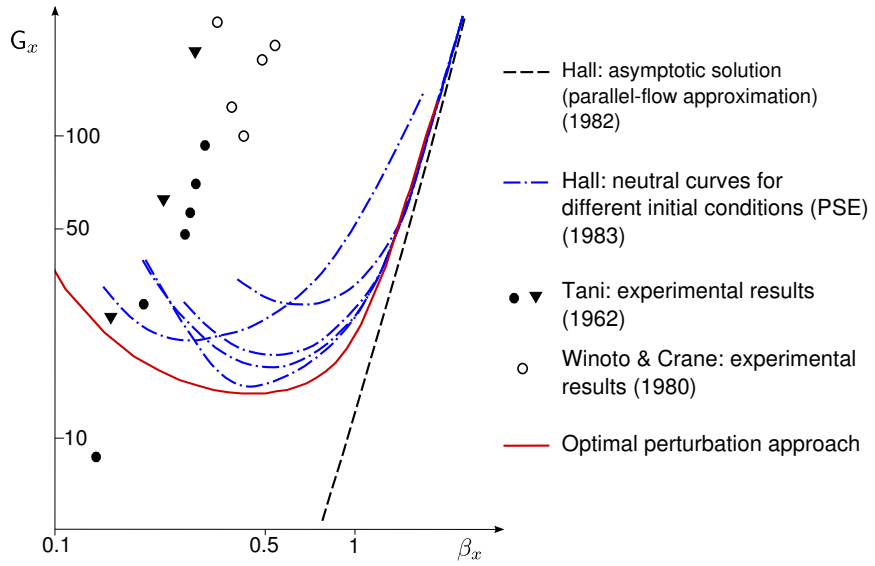


Figure 3.1 : Comparaison entre les différentes courbes neutres calculées par Hall (1983) pour différentes perturbations initiales introduites en $x_{\text{in}} = 50$ (-·-·-), la courbe neutre asymptotique développée par Hall (1982) (- - -), les résultats expérimentaux de Tani (1962) (• et ▼) et Winoto & Crane (1980) (∘) en présence de tourbillons de Görtler, et la courbe neutre associée à la perturbation optimale introduite en $x_{\text{in}} = 50$ (——).

correspond à la perturbation amplifiée le plus rapidement possible et définit par conséquent la courbe enveloppe du domaine instable, comme illustré sur la figure 3.1.

La courbe neutre de la figure 3.1 présente un minimum en $(0.45; 14.5)$ dans le plan $(\beta_x, \mathsf{G}_x)$. Ce minimum correspond à un nombre de Görtler $\mathsf{G} = 0.025$. La figure 3.2 montre les profils de fluctuations de vitesse pour la perturbation optimale introduite en $x_{\text{in}} = 50$ qui correspond à ce minimum (avec $\eta = y/2\sqrt{x}$).

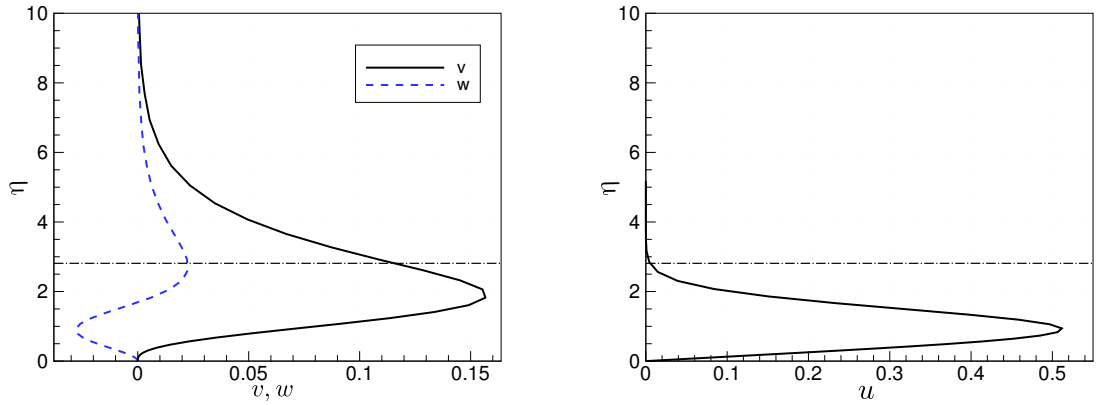


(a) Profils de vitesse normale et transversale de la perturbation optimale en $x_{\text{in}} = 50$, avec $u = 0$.

(b) Profil de vitesse longitudinale de la perturbation optimale en $x = 240$.

Figure 3.2 : Perturbation optimale introduite en $x_{\text{in}} = 50$ qui correspond au minimum de la courbe neutre (la figure 3.2a) et profils de vitesse de la perturbation propagée en $x = 240$ (la figure 3.2b). La ligne en pointillés indique la frontière de la couche limite.

La figure 3.3 représente les tourbillons initiaux et les iso-contours de vitesse longitudinale des stries pour la même perturbation optimale dans un plan transverse.

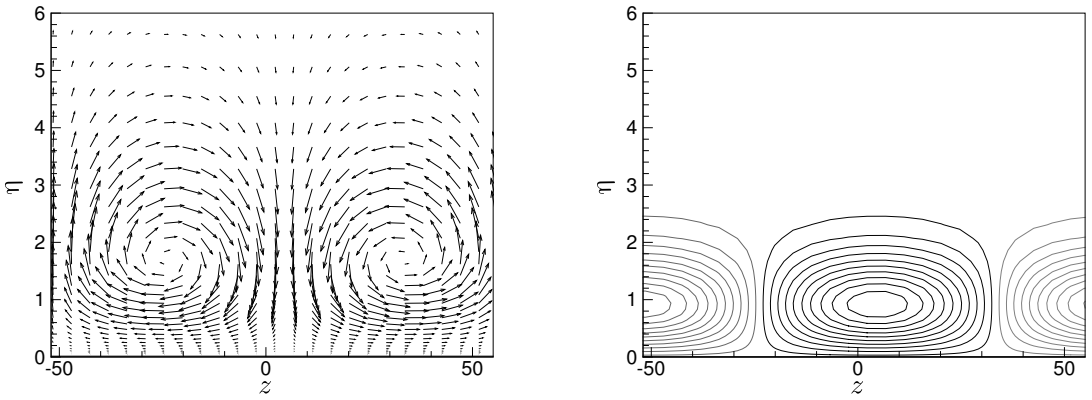


(a) $x = 50$ (b) $x = 240$

Figure 3.3 : Tourbillons initiaux en $x = 50$ correspondant au minimum de la courbe neutre (a) et iso-contours de vitesse longitudinale (les lignes grises correspondent à des valeurs négatives) de la perturbation résultante en $x = 240$ (b) dans le plan transverse $\eta - z$.

La détermination de la courbe neutre pour un écoulement compressible révèle que la couche limite est plus stable lorsque le nombre de Mach augmente. La figure 3.4 montre que les courbes neutres sont déplacées vers le haut pour $\beta_x \geqslant 0.4$, ce qui correspond à un accroissement de la région stable.

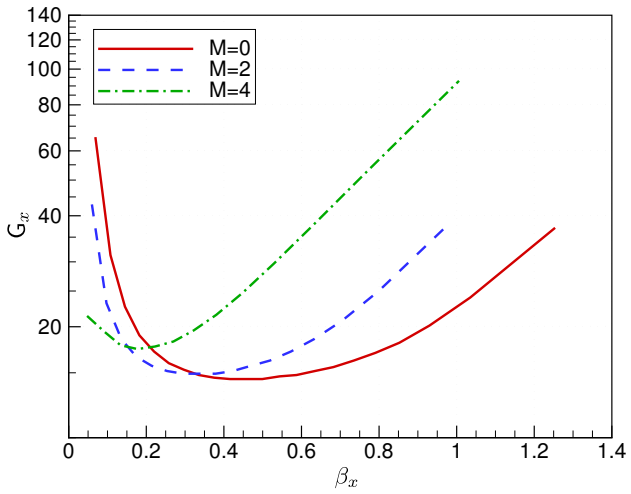


Figure 3.4 : Courbes neutres pour différents nombres de Mach, avec $x_{\text{in}} = 50$, $x_{\text{out}} = 200$ et $\mathsf{G} = 0.025$.

## 3.3 Analyse spectrale

Afin de déterminer l'influence de la courbure sur le spectre des opérateurs, l'hypothèse d'écoulement parallèle est ici adoptée. Bien que trop restrictive, cette méthode permet d'effectuer une analyse multi-modale afin de mettre en évidence les interactions entre modes non normaux et l'influence des termes de courbure sur la croissance transitoire.

On introduit les perturbations sous la forme d'une somme de modes,

$$\begin{aligned} \boldsymbol{q}'(x,y,z,t) &= \boldsymbol{q}(x,y)e^{i(\beta z-\omega t)}, \\ \boldsymbol{q}(x,y) &= \sum_k \hat{\boldsymbol{q}}_k(y)e^{i\alpha_k x}. \end{aligned} \tag{3.8}$$

Les équations de Navier-Stokes linéarisées conduisent alors à un problème aux valeurs propres généralisées qui permet de déterminer le spectre des opérateurs,

$$\forall k, \quad \mathcal{A}(y,\beta,\omega)\ \hat{\boldsymbol{q}}_k(y) = \mathcal{B}(y,\beta,\omega)\ \alpha_k\ \hat{\boldsymbol{q}}_k(y), \tag{3.9}$$

Afin de déterminer les interactions entre modes non normaux, on détermine également le pseudo-spectre pour le problème (3.9). Le pseudospectre est calculé en déterminant la plus petite valeur singulière $\sigma_{\min}$ de $z\mathcal{B}-\mathcal{A}$ pour $z \in \mathbb{C}$,

$$\Lambda_\epsilon(\mathcal{A},\mathcal{B}) = \{z \in \mathbb{C} : \sigma_{\min}(z\mathcal{B}-\mathcal{A}) \leqslant \epsilon\}. \tag{3.10}$$

Le pseudospectre donne une mesure de la sensibilité des valeurs propres à des perturbations de l'opérateur. D'après la figure 3.5, les interactions non modales sont prises en compte en considérant la branche supérieure du spectre dans le calcul de la perturbation optimale. Par ailleurs, la détermination du pseudospectre pour différents nombres de Görtler montre que le degré de non normalité augmente pour de plus grandes valeurs du nombre de Görtler. Le potentiel de croissance transitoire est donc plus important pour des nombres de Görtler élevés.

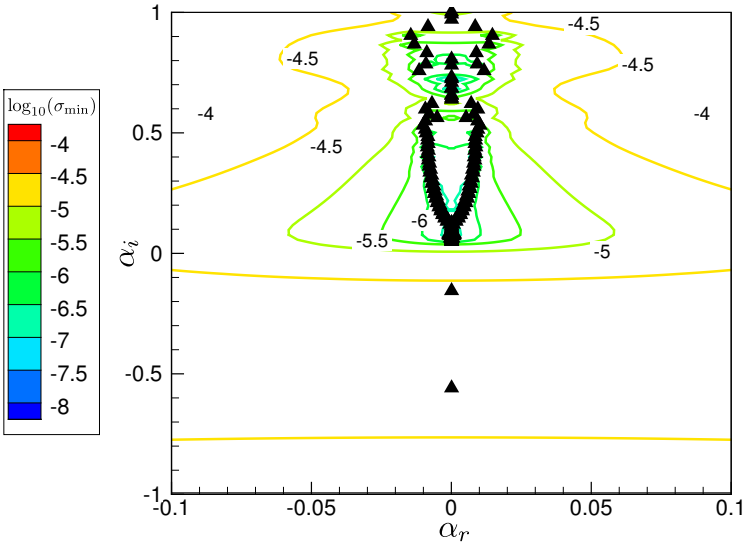


Figure 3.5 : Spectre et pseudospectre (iso-contours de $\log_{10}(\sigma_{\min})$) à $x = 20$, avec $\mathsf{G} = 4$ et $\beta = 0.22$.

En prenant en compte les modes non normaux de la branche supérieure où les interactions sont possibles, on peut déterminer la courbe du gain, ou de façon équivalente l'évolution du facteur $N$, sous l'hypothèse d'écoulement parallèle. Cette hypothèse conduit à une sur-estimation du facteur $N$, comme illustré sur la figure 3.6.

Comparer l'approche multi-modale à la stabilité linéaire locale montre que la prise en compte des interactions entre les modes non normaux est nécessaire pour la bonne détermination du facteur $N$, notamment aux premières stations de calcul où la croissance transitoire induit un accroissement du facteur $N$ significatif. Cet effet est également visible en comparant l'approche PSE à la théorie

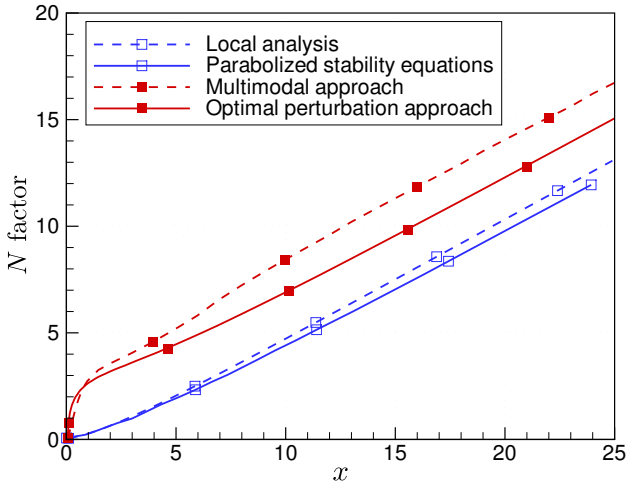


Figure 3.6 : Facteur $N$ calculé en utilisant seulement le mode le moins stable (stabilité linéaire locale, - -⊟- -), avec la méthode de stabilité linéaire non locale (PSE, —⊟—), l'approche multi-modale (- -■- -) et la théorie de perturbation optimale (—■—).

de perturbation optimale. L'importance de la prise en compte de la croissance transitoire pour la prévision de la transition est ici soulignée. La question de l'évolution des modes de Klebanoff vers les tourbillons de Görtler et de la similarité des deux types d'instabilité sera abordée dans le chapitre suivant.

L'approche optimale, couplée à un nouveau critère de convergence pour calculer la perturbation initiale amplifiée le plus rapidement possible, permet donc de déterminer la courbe neutre pour le problème de Görtler. La détermination de la perturbation optimale pour un écoulement supersonique montre l'effet stabilisant de l'augmentation du nombre de Mach. Une analyse de réceptivité, présentée dans la version anglaise du manuscrit, montre que les instabilités sont localisées plus près de la paroi lorsque la station où les perturbations sont introduites s'éloigne du bord d'attaque. Une étude paramétrique montre également que la couche limite est plus susceptible d'être déstabilisée lorsque les perturbations sont introduites près du bord d'attaque.
En adoptant une hypothèse d'écoulement parallèle, il est possible de calculer le spectre et le pseudospectre des opérateurs. La prise en compte des interactions entre les modes non normaux se fait avec une approche multi-modale pour le calcul du facteur $N$. Cette approche montre que la croissance transitoire joue un rôle aux premières stations de calcul avec un accroissement significatif du facteur $N$. Le chapitre suivant se concentre notamment sur l'évolution continue des modes de Klebanoff vers les tourbillons de Görtler, avant de considérer le problème de la transition sur des parois présentant des oscillations de surface.

Chapitre 4

# Application aux ondulations de surface

La position de la transition dépend fortement de l'état de la surface qui peut présenter des imperfections. Ce chapitre explore le processus de transition pour des couches limites compressibles se développant sur des parois présentant des défauts de type ondulations de surface. La perturbation optimale amplifiée le plus rapidement possible est déterminée selon la méthode développée dans les chapitres précédents.

## 4.1 Des modes de Klebanoff aux tourbillons de Görtler

La croissance transitoire pour un écoulement se développant sur une plaque plane est caractérisée par des stries alternées de vitesse appelées modes de Klebanoff. Le passage d'une plaque plane à une paroi concave pose la question de l'évolution de ces modes de Klebanoff vers les tourbillons de Görtler. On étudie donc l'écoulement sur une paroi constituée d'un plaque plane, suivie d'une partie concave puis convexe, définie par la relation suivante,

$$\begin{cases} \dfrac{1}{R_c} = 0 \text{ pour } x < 0.3\,\mathrm{m}\,; \\ \dfrac{1}{R_c} = 4\sin\left(\dfrac{2\pi(x-0.3)}{0.7}\right) \text{ pour } x \geqslant 0.3\,\mathrm{m}. \end{cases} \tag{4.1}$$

Un calcul de perturbation optimale sur cette surface montre que les perturbations sont d'abord amorties sur la partie plane, puis fortement amplifiées sur la partie concave, avant d'être de nouveau amorties après le point d'inflexion de la paroi. Ce résultat illustre l'effet déstabilisant d'une surface concave, et inversement l'effet stabilisant d'une surface convexe. Plus de détails sont disponibles dans la version anglaise du manuscrit (chapitre 4, paragraphe 4.1.1).

On détermine la perturbation optimale sur la géométrie définie par l'équation (4.1). La station où le gain est maximisé varie de manière à étudier l'évolution du nombre d'onde transversal optimal pour l'amplification des modes de Klebanoff et des tourbillons de Görtler. On considère la fin de la partie plane $x_{\mathrm{out}} = 0.3$ où les modes de Klebanoff sont développés, la fin de la partie concave $x_{\mathrm{out}} = 0.65$ et la fin de la partie convexe $x_{\mathrm{out}} = 1$ où les tourbillons de Görtler sont présents. Le nombre d'onde dimensionné $\beta_{\mathrm{d}}$ est rendu sans dimension par $\delta$ qui correspond à la longueur de référence de la couche limite en $x_{\mathrm{out}}$.

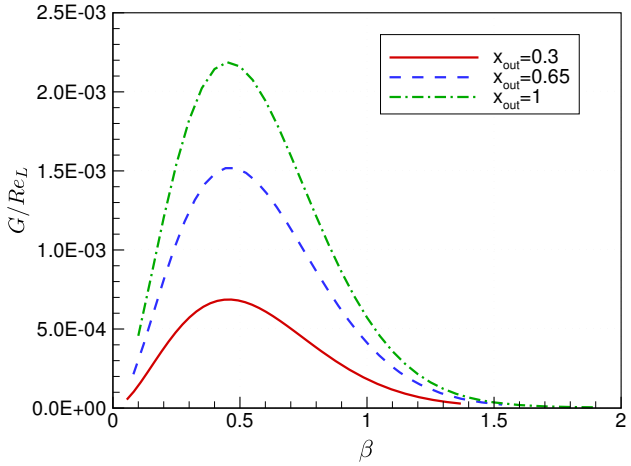


Figure 4.1 : Nombre d'onde transversal optimal $\beta$ pour différentes stations $x_{\text{out}}$.

Le nombre d'onde optimal est le même pour les modes de Klebanoff et les tourbillons de Görtler, comme illustré sur la figure 4.1. Ce résultat montre qu'il y a une évolution continue des modes de Klebanoff vers les tourbillons de Görtler, les deux types de perturbations étant constitués de structures similaires. La différence entre une paroi concave et une plaque plane vient des forces centrifuges qui alimentent les tourbillons, amenant l'amplification exponentielle des tourbillons de Görtler.

## 4.2 Multiples oscillations de surface

On se place dans la suite des travaux de Saric et Benmalek (1991) qui ont déterminé l'amplification des perturbations sur des parois à courbure variable par la méthode PSE. Le nombre de Görtler est défini par

$$\mathsf{G} = 2\mathsf{G}_0^2 \cos\left(2\pi m \frac{x-1}{x_{\text{out}}-1}\right), \tag{4.2}$$

avec $\mathsf{G}_0$ le nombre de Görtler à la station $x_{\text{in}} = 1$ où les perturbations sont introduites et $x_{\text{out}} = 25$. Le paramètre $m$ caractérise le nombre d'oscillations de la courbure.

Le long de la surface concave, les tourbillons de Görtler se déplacent vers la paroi et s'amplifient. Quand la courbure diminue, les tourbillons ont tendance à s'éloigner de la paroi et, quand l'écoulement arrive sur la partie convexe, une seconde paire de tourbillons contra-rotative par rapport à celle déjà présente se forme à la paroi. La paire de tourbillons initiale est progressivement éjectée et amortie. Ce processus est répété pour chaque oscillation de la courbure.

L'amplification des instabilités est calculée sur la base du maximum selon la normale de vitesse longitudinale des perturbations,

$$\begin{aligned} A(x) &= |u(x, y_{\max})|\,; \\ N &= \ln(A(x)/A_0)\,. \end{aligned} \tag{4.3}$$

La figure 4.2 montre l'évolution du facteur $N$ pour $\mathsf{G}_0 = 2$ et $\beta = 0.22$. On considère le cas d'une paroi concave à courbure constante ($m = 0$) et d'une paroi à courbure variable ($m = 0.5$). Les résultats sont comparés aux calculs PSE effectués par Saric et Benmalek (1991). Le facteur $N$

correspondant à la perturbation optimale présente une région de forte amplification transitoire aux premières stations de calcul. A la fin de cette région, l'amplification des perturbations a atteint un niveau significatif ($N \simeq 3.5$) qui n'est pas pris en compte par les méthodes classiques. L'amplification exponentielle des instabilités est ensuite retrouvée.

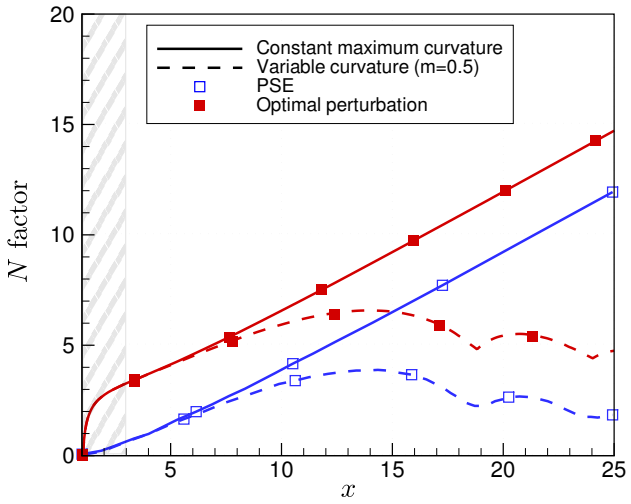


Figure 4.2 : Facteur $N$ pour une paroi concave à courbure constante ($m = 0$, ——) et une paroi à courbure variable ($m = 0.5$, - - - ) avec $\mathsf{G}_0 = 2$ et $\beta = 0.22$. Comparaison entre l'approche PSE (□) et l'approche optimale (■). La zone hachurée représente la région où la croissance transitoire joue un rôle.

Quand le nombre d'oscillations de la paroi augmente, le facteur $N$ subit une amplification initiale moins importante, comme illustré sur la figure 4.3. Globalement, l'amplification des perturbations sur une paroi à courbure variable est toujours plus faible que sur une paroi concave à courbure constante, ce qui montre que les parties convexes ont un effet globalement stabilisant.

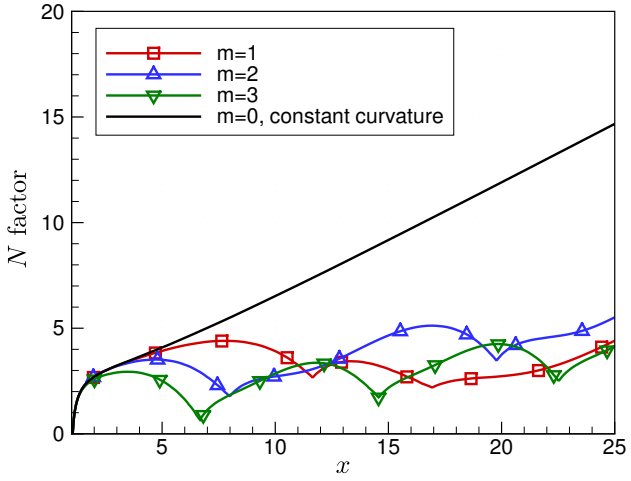


Figure 4.3 : Facteur $N$ pour différentes valeurs de $m$, avec $\mathsf{G} = 2$ et $\beta = 0.22$.

Quand les effets de compressibilité sont pris en compte et que le nombre de Mach augmente, l'amplification des perturbations est atténuée. D'une part la région où la croissance transitoire joue un rôle est réduite, et d'autre part l'amplification exponentielle des instabilités est moins importante. Cependant, la croissance transitoire conduit toujours à une amplification des perturbations aux premières stations de calcul avant l'amplification modale.

## 4.3 Courbure périodique superposée à une courbure constante

Les parois courbes peuvent elles-mêmes présenter des imperfections ou des ondulations de surface. On considère le cas d'une courbure périodique superposée à une courbure concave constante. L'écart à cette courbure concave $\kappa_0$ est défini par

$$\kappa = \kappa_0 \left[ 1 + \gamma \sin \left( 2\pi m \frac{x - 1}{x_{\text{out}} - 1} \right) \right] . \tag{4.4}$$

Pour $|\gamma| < 1$, il n'y a pas de partie convexe et l'ondulation de surface superposée n'a quasiment pas d'influence sur l'évolution du facteur $N$. Augmenter la valeur de $\gamma$ conduit à des valeurs plus faibles pour le facteur $N$, comme illustré sur la figure 4.4. Il est donc nécessaire d'avoir une partie concave afin d'observer un changement significatif. Les premières stations de calcul montrent toujours une phase d'amplification due à la croissance transitoire, qui n'est pas affectée pas la valeur de $\gamma$.

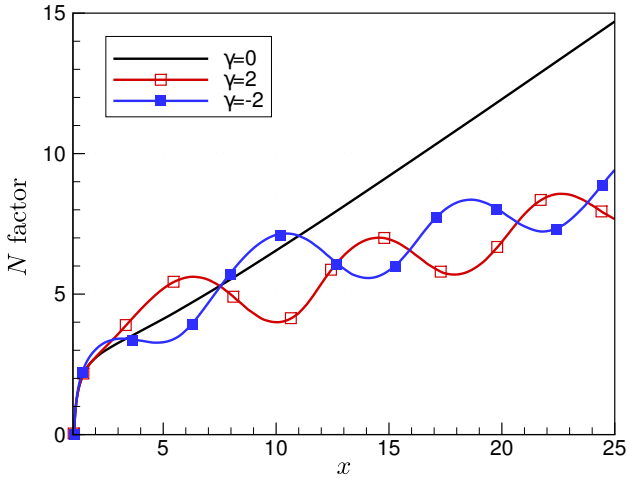


Figure 4.4 : Facteur $N$ pour une courbure périodique superposée à une courbure concave constante, avec $m = 3$, $\mathsf{G}_0 = 2$ et $\beta = 0.22$.

Le passage d'une plaque plane à une paroi concave, puis convexe, a été envisagé. Les modes de Klebanoff et les tourbillons de Görtler représentent les mêmes perturbations, les tourbillons de Görtler étant amplifiés exponentiellement sous l'effet des forces centrifuges. La croissance transitoire des tourbillons de Görtler précédant cette phase d'amplification exponentielle est capturée par l'approche optimale. L'amplification non modale aux premières stations de calcul conduit à des valeurs de facteur $N$ significatives. La croissance transitoire doit donc être prise en compte dans l'objectif d'une prévision précise de la position de transition.

Chapitre 5

# Croissance transitoire dans les couches limites tridimensionnelles

La théorie des perturbations optimales est maintenant étendue aux couches limites tridimensionnelles. Pour cela, on écrit les équations qui régissent l'évolution des perturbations dans une couche limite de Falkner-Skan-Cooke. Ces équations sont paraboliques et peuvent être résolues par une technique classique de marche vers l'aval pour un nombre d'onde longitudinal fixé. Ce nombre d'onde doit donc être déterminé, et une nouvelle méthode de calcul basée sur le suivi du maximum d'énergie pour les perturbations est proposée. Comme précédemment, la perturbation optimale est calculée par itérations direct/adjoint. Cette méthode est ensuite appliquée au calcul des perturbations optimales stationnaires dans une couche limite tridimensionnelle et plus particulièrement à l'étude du lien entre croissance transitoire et amplification exponentielle des modes transversaux.

## 5.1 Équations des perturbations

De façon similaire à ce qui a été présenté dans le chapitre 2, on cherche à décrire l'évolution des perturbations à partir des équations de Navier-Stokes linéarisées autour d'un écoulement de base. Pour une couche limite tridimensionnelle, cet écoulement de base est représenté par les solutions de similitudes de Falkner-Skan-Cooke, détaillées dans la version anglaise du manuscrit (paragraphe 5.1.1 et annexe D.1).
Les perturbations sont d'abord décomposées de la même façon que dans l'approche PSE,

$$\boldsymbol{q}'(x,y,z,t) = \boldsymbol{q}(x,y)\exp(i\Theta(x,z,t))\,; \tag{5.1a}$$

$$\Theta(x,z,t) = \int_{x_0}^{x} \alpha(\xi)\,\mathrm{d}\xi + \beta z - \omega t\,, \tag{5.1b}$$

où $\boldsymbol{q} = (u,v,w,p)^T$ est la fonction d'amplitude et $\Theta$ est la fonction d'onde. Les nombres d'onde longitudinaux et transversaux sont respectivement notés $\alpha$ et $\beta$, et la pulsation temporelle est notée $\omega$. La méthode PSE classique utilise une condition de normalisation,

$$\int_0^\infty \boldsymbol{q}^H \frac{\partial \boldsymbol{q}}{\partial x}\,\mathrm{d}y = 0 \tag{5.2}$$

qui assure que les variations de la fonction d'amplitude dans la direction longitudinale sont faibles. Cette condition permet alors de déterminer le nombre d'onde longitudinal $\alpha$. Cette méthode n'est

cependant pas applicable à l'étude la croissance transitoire des perturbations, notamment en raison de l'initialisation du calcul PSE par un mode propre donné par la stabilité locale. Dans le paragraphe suivant, deux méthodes sont présentées pour modifier la condition de normalisation PSE et calculer $\alpha$.
Afin de comparer les ordres de grandeurs des différents termes, deux adimensionnements, détaillés dans table 5.1, sont appliqués aux différentes grandeurs. Les termes écartés doivent être négligeables vis-à-vis de ces deux adimensionnements.

| | $x$, $z$ | $y$ | $U$, $W$ | $V$ | $u$, $w$ | $v$ | $p$ | $\alpha$ | $\beta$ | $\omega$ |
|---|---|---|---|---|---|---|---|---|---|---|
| Non-modal | $L$ | $\delta$ | $U_\infty$ | $U_\infty\delta/L$ | $U_\infty$ | $U_\infty\delta/L$ | $\rho U_\infty^2\delta^2/L^2$ | $1/\delta$ | $1/\delta$ | $U_\infty/L$ |
| Modal | $\delta$ | $\delta$ | $U_\infty$ | $U_\infty$ | $U_\infty$ | $U_\infty$ | $\rho U_\infty^2$ | $1/\delta$ | $1/\delta$ | $U_\infty/\delta$ |

TABLE 5.1 : Adimensionnements de type couche limite (non modal) et PSE (modal) appliqués à l'écoulement de couche limite tridimensionnelle incompressible.

Les termes d'ordre $\mathcal{O}(1)$ et $\mathcal{O}(Re_\delta^{-1})$ donnent alors les équations aux perturbations en adimensionnement non modal,

$$u_x + iRe_\delta\alpha u + v_y + iRe_\delta\beta w = 0, \tag{5.3a}$$

$$(U_x + iRe_\delta\alpha U + iRe_\delta\beta W - i\omega)u + Uu_x + Vu_y + U_y v + \frac{p_x}{Re_\delta^2} + \frac{i\alpha p}{Re_\delta} = u_{yy} - k^2 u, \tag{5.3b}$$

$$(V_y + iRe_\delta\alpha U + iRe_\delta\beta W - i\omega)v + Uv_x + Vv_y + V_x u + p_y = v_{yy} - k^2 v, \tag{5.3c}$$

$$(iRe_\delta\alpha U + iRe_\delta\beta W - i\omega)w + Uw_x + Vw_y + uW_x + vW_y + \frac{i\beta p}{Re_\delta} = w_{yy} - k^2 w, \tag{5.3d}$$

avec $k^2 = \alpha^2+\beta^2$. Le terme $uV_x$ dans l'équation (5.3c) est négligeable vis-à-vis de l'adimensionnement modal mais doit être pris en compte par rapport à l'adimensionnement de type couche limite. Physiquement, cela revient à conserver les termes représentatifs de la croissance transitoire avec les termes décrivant l'amplification modale des perturbations. Le gradient de fluctuation de pression longitudinal est négligé afin de rendre le système parabolique. Le système (5.3) peut alors être résolu par une technique de marche vers l'aval. Les conditions aux limites spécifiées sont

$$u = v = w = 0 \quad \text{pour } y = 0, \tag{5.4a}$$

$$u = w = p = 0 \quad \text{quand } y \to \infty. \tag{5.4b}$$

## 5.2 Détermination du nombre d'onde longitudinal

A ce stade, les inconnues sont le nombre d'onde longitudinal $\alpha$ et les fonctions d'amplitude $\boldsymbol{q} = (u, v, w, p)^T$. La résolution du système (5.3) permet de déterminer les fonctions d'amplitude pour un nombre d'onde $\alpha$ fixé, mais encore inconnu.
Sous l'hypothèse d'écoulement parallèle, ce nombre d'onde est donné par la relation de dispersion. La méthode PSE utilise une condition de normalisation comme relation de fermeture permettant de déduire $\alpha$. On présente ici la modification proposée par Tempelmann *et al.* (2010) pour déterminer $\alpha$ dans le cadre de l'étude de la croissance transitoire. Une nouvelle méthode est ensuite présentée, qui détermine $\alpha$ sur la base du maximum d'énergie pour les perturbations. Cette méthode sera ensuite appliquée dans le reste de ces travaux.

### 5.2.1 Méthode de phase constante (Tempelmann *et al.*, 2010)

Dans l'approche proposée par Tempelmann *et al.* (2010), le nombre d'onde longitudinal est considéré réel. En introduisant une nouvelle amplitude complexe $A(x)$ de phase $\vartheta$, la fonction d'amplitude peut se réécrire

$$\boldsymbol{q}(x,y) = A(x)\tilde{\boldsymbol{q}}(x,y), \tag{5.5}$$

et les perturbations prennent alors la forme

$$\begin{aligned}\boldsymbol{q}'(x,y,z,t) &= |A(x)|\exp(i\vartheta(x))\boldsymbol{q}(x,y)\exp\left(i\Theta(x,z,t)\right)\\ &= |A(x)|\boldsymbol{q}'(x,y)\ \exp\left(i\Theta'(x,z,t)\right),\end{aligned}$$

avec

$$\Theta'(x,z,t) = \vartheta(x_0) + \int_{x_0}^{x}\left(\alpha(x) + \frac{\partial\vartheta}{\partial x}\right)dx + \beta z - \omega t.$$

On cherche à capturer l'oscillation des perturbations dans la fonction d'onde ($\alpha \in \mathbb{R}$), ce qui impose

$$\vartheta = cste \Leftrightarrow \frac{\partial\vartheta}{\partial x} = 0. \tag{5.6}$$

Cette condition est assurée globalement de façon itérative,

$$\alpha^{(k+1)} = \alpha^{(k)} + \frac{\partial\vartheta}{\partial x}. \tag{5.7}$$

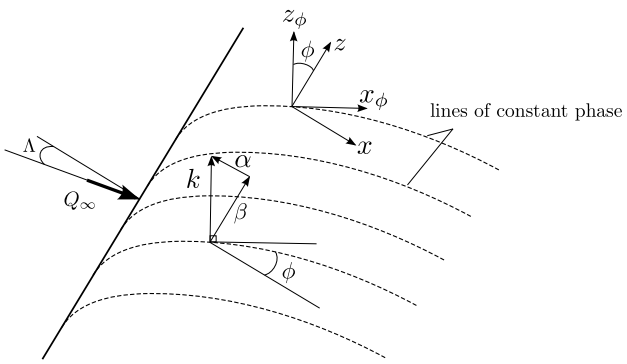


Figure 5.1 : Lignes de phase constante pour une couche limite tridimensionnelle. Le vecteur d'onde $\boldsymbol{k} = (\alpha,\beta)^T$ est également représenté.

Le choix de la fonction d'amplitude se porte sur la composante de vitesse tangentielle à la ligne de phase constante et quasiment alignée avec la ligne de courant extérieure (voir la figure 5.1), qui représente la perturbation de vitesse la plus importante,

$$A(x) = \max_y(u_\phi(x,y)). \tag{5.8}$$

En théorie non-locale, on peut écrire le nombre d'onde réel physique sous la forme

$$\tilde{\alpha}(x,y) = \alpha(x) - \Re\left(i\frac{1}{A}\frac{\partial A}{\partial x}\right), \tag{5.9}$$

où $\mathfrak{R}$ représente la partie réelle. La condition (5.6) s'interprète alors comme une condition de normalisation au sens de la méthode PSE.

Cette méthode est limitée à l'étude des perturbations dont les lignes de phase constante sont quasiment alignées avec la ligne de courant extérieure. En outre, la restriction à un nombre d'onde réel ne permet de considérer que des perturbations dont la croissance exponentielle est modérée.

### 5.2.2 Méthode à $\alpha_r$ fixé développée au cours de cette thèse

Dans cette thèse, une nouvelle approche a été développée pour déterminer le nombre d'onde $\alpha$. Cette méthode est similaire à la méthode dite à $\beta$ fixé employée en étude de stabilité locale, où le taux d'amplification des perturbations est calculé pour des valeurs fixées de la fréquence et du nombre d'onde $\beta$, puis maximisé par rapport à ces deux paramètres pour donner une courbe enveloppe.

Comme précédemment, le nombre d'onde est choisi réel, $\alpha = \alpha_r(x)$. Le système (5.3) est résolu jusqu'à une station donnée $x_i$. A cette station, $\alpha_r$ est déterminé de façon à maximiser l'énergie locale des perturbations à la station suivante $x_{i+1}$. Le nombre d'onde longitudinal à $x_i$ est déterminé de façon itérative en se basant sur la valeur en $x_{i-1}$. L'énergie locale des perturbations est définie par

$$E(x) = \int_0^{y_{\max}} (u^2 + v^2 + w^2)\,\mathrm{d}y, \tag{5.10}$$

pour un écoulement incompressible. Les trois composantes de vitesse des perturbations sont utilisées de façon à capturer les perturbations les plus amplifiées aux premières stations de calcul où les stries ne sont pas complètement formées. La première itération se base sur un nombre d'onde déterminé à partir de la ligne de courant extérieure,

$$\alpha = -\tan(\phi)\beta, \tag{5.11}$$

où $\phi$ est défini par $\phi = \arctan(W_e/U_e)$, avec $U_e$ et $W_e$ les vitesses à la frontière de la couche limite dans la direction longitudinale et transverse respectivement. Le nombre d'onde longitudinal est donc déterminé de façon à obtenir le maximum d'énergie pour les perturbations à la station suivante. Cela signifie que $\alpha$ capture la plus grande partie des oscillations dans la fonction d'onde. Contrairement à la méthode précédente, le nombre d'onde est calculé de façon locale : on détermine $\alpha$ de façon à suivre le maximum d'énergie pour les perturbations à chaque station avant de résoudre les équations parabolisées à la station suivante.

## 5.3 Perturbations optimales dans des couches limites de Falkner-Skan-Cooke

Le système d'équations paraboliques (5.3) peut être résolu avec le nombre d'onde longitudinal déterminé selon la méthode décrite au paragraphe 5.2.2. On peut donc décrire l'évolution de perturbations modales et non modales dans une couche limite tridimensionnelle soumise à un gradient de pression. Comme précédemment, la perturbation optimale est calculée par itérations du système direct/adjoint.

Une étude paramétrique sur les perturbations optimales stationnaires dans une couche limite de Falkner-Skan-Cooke est réalisée. Le nombre de Reynolds est fixé à $Re_L = 10^6$ et l'écoulement peut être accéléré ($\beta_H = 0.1$) ou décéléré ($\beta_H = -0.05$). Les résultats de cette étude sont résumés

dans le paragraphe suivant, plus de détails étant disponibles dans la version anglaise du manuscrit (paragraphe 5.4.1).

L'influence des stations initiales et finales $x_{\text{in}}$ et $x_{\text{out}}$ est étudiée. Les résultats obtenus sont cohérents en comparaison des conclusions de Tempelmann *et al.* (2010), bien que la détermination du nombre d'onde longitudinal se fasse de façon différente. Dans le cas où la station finale varie, le nombre d'onde transverse qui donne la plus importante amplification des perturbations décroît pour de grandes valeurs de $x_{\text{out}}$. La station initiale optimale est ensuite déterminée en faisant varier $x_{\text{in}}$ : comme dans le cas bidimensionnel, elle est située en aval du bord d'attaque.

On étudie ensuite la dépendance à l'angle de flèche $\Lambda$ pour les valeurs $\Lambda = 45°$, $\Lambda = 35°$ et $\Lambda = 25°$. On observe une croissance transitoire plus importante pour les écoulements ralentis, ce qui est cohérent avec l'étude temporelle de Corbett et Bottaro (2001) et les résultats obtenus pour des couches limites bidimensionnelles. Dans le cas d'un écoulement ralenti, les instabilités transversales sont moins importantes ; la croissance transitoire peut alors compenser cet effet en donnant une amplitude initiale plus importante aux instabilités CF avant la phase d'amplification modale.
Le maximum d'amplification est par ailleurs atteint pour $\Lambda = 45°$. Cependant, si l'on compare l'amplification modale seule à l'amplification prenant en compte la croissance transitoire, on constate que la croissance transitoire est plus importante pour de faibles angles de flèche. De même que pour le gradient de pression, cet effet pourrait compenser les instabilités transversales moins amplifiées pour des angles de flèche plus faibles mais avec une amplitude initiale des instabilités plus importante avant l'amplification modale.

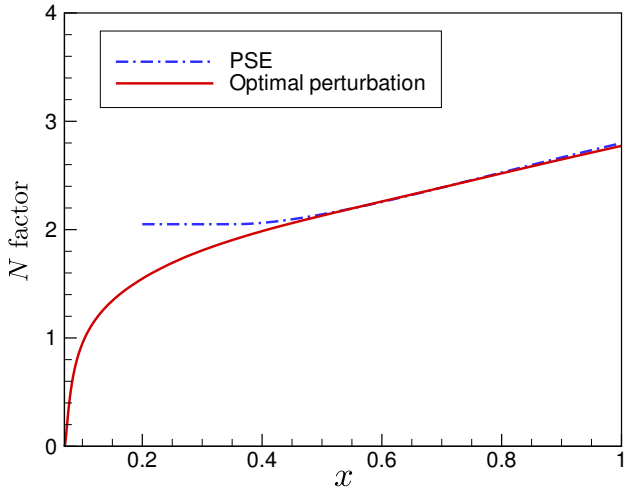


Figure 5.2 : Courbe de facteur $N$ pour la perturbation optimale (ligne continue) et pour le mode transverse par la méthode PSE (ligne en pointillés) avec $x_{\text{in}} = 0.07$, $x_{\text{out}} = 1$, $\beta_H = 0.1$, $\Lambda = 45°$, $\omega = 0$ et $\beta = 0.38$. Cette dernière courbe est décalée pour correspondre au niveau atteint par la perturbation optimale en $x_{\text{out}}$.

On s'intéresse ensuite plus particulièrement au lien entre les instabilités transversales et la phase de croissance transitoire. La figure 5.2 montre la courbe de facteur $N$ pour laquelle la croissance transitoire et modale sont présentes au sein d'une couche limite accélérée. La croissance transitoire résulte en une forte augmentation du facteur $N$ aux premières stations de calcul, de façon similaire à ce qui a été décrit dans le cas des tourbillons de Görtler (chapitre 3). L'amplification exponentielle du mode transverse est ensuite retrouvée en aval de la position neutre ($x \geqslant 0.4$). Sur cette figure, le

facteur $N$, défini comme $N = 0.5\ln(G/Re_L)$, a été divisé par un facteur 2 pour coïncider avec la définition utilisée par la méthode PSE. La croissance transitoire donne donc une amplitude initiale plus importante au mode transverse.

Pour étudier plus finement la relation entre les modes transversaux et la croissance transitoire, on compare les profils de vitesse de la perturbation optimale aux fonctions propres du mode transverse correspondant. La figure 5.3 montre cette comparaison pour deux stations différentes. La première station $x = 0.4$ correspond au début de l'amplification modale, tandis que la seconde $x = 0.8$ est située plus en aval.

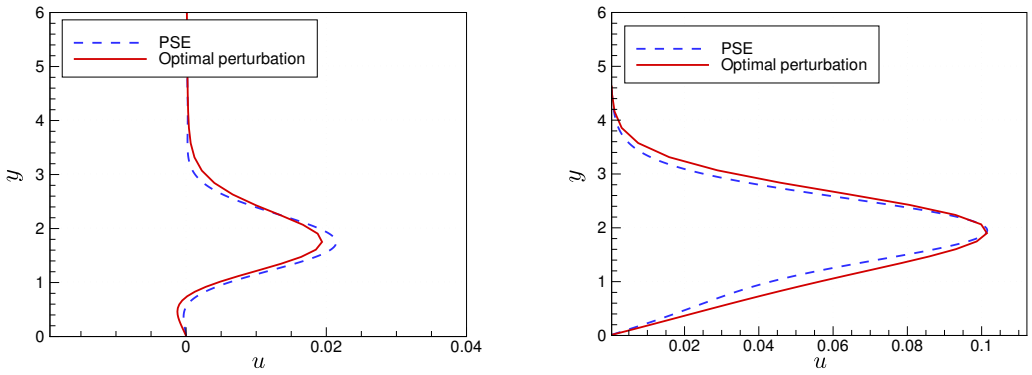


(a) $x = 0.4$ (b) $x = 0.8$

Figure 5.3 : Fonction d'amplitude $u$ de la perturbation optimale (ligne continue) et fonction propre du mode transverse correspondant donnée par la méthode PSE (ligne en pointillés) en $x = 0.4$ (début de l'amplification modale, voir la figure 5.2) et $x = 0.8$.

Les fonctions d'amplitude de la perturbation optimale et du mode propre associé coïncident aux deux stations, ce qui signifie que la propagation vers l'aval de la perturbation optimale correspond à l'évolution du mode transverse associé. Ce résultat a été souligné par Corbett et Bottaro (2001) dans le domaine temporel.

La projection de la perturbation optimale en régime sous-critique (croissance transitoire seulement) et super-critique (croissance transitoire suivie d'une amplification modale) dans un repère perpendiculaire à la ligne de propagation des perturbations confirme cette observation (voir les figures 5.4 and 5.5 pour un écoulement accéléré). La perturbation optimale est initialement inclinée contre le cisaillement de l'écoulement de base, avant de se redresser et de s'incliner dans le sens opposé plus en aval. Le phénomène physique de croissance transitoire dans les couches limites tridimensionnelles est donc une combinaison de l'effet "lift-up" et du mécanisme de Orr.

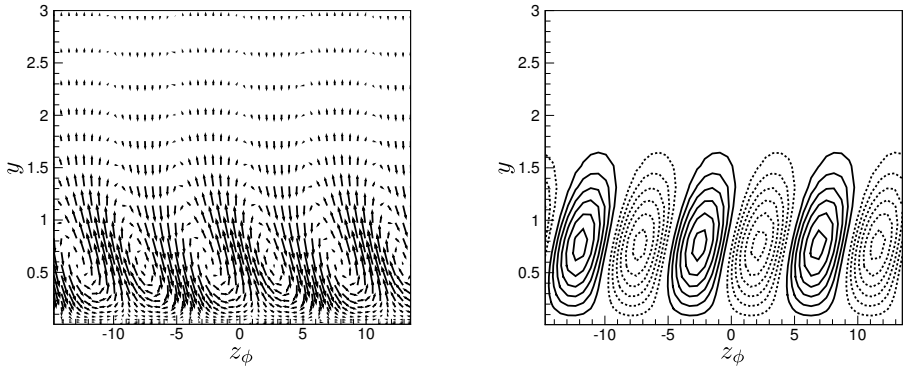


(a) Vecteurs $v$ et $w_\phi$ (b) Iso-contours de $u_\phi$

Figure 5.4 : Perturbation optimale en $x_{\text{in}} = 0.01$ et propagée en $x_{\text{out}}$ en régime sous critique ($\beta = 0.82$, $x_{\text{out}} = 0.13$), avec $\Lambda = 45°$ et $\beta_H = 0.1$.

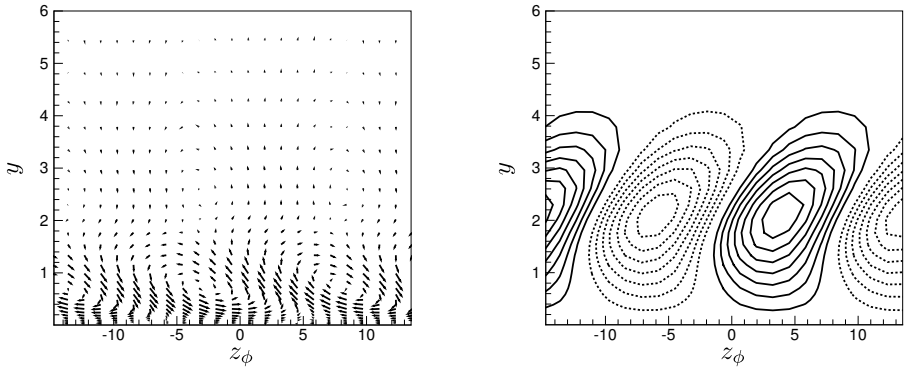


(a) Vecteurs $v$ et $w_\phi$ (b) Iso-contours de $u_\phi$

Figure 5.5 : Perturbation optimale en $x_{\text{in}} = 0.01$ et propagée en $x_{\text{out}}$ en régime super-critique ($\beta = 0.38$, $x_{\text{out}} = 1$), avec $\Lambda = 45°$ et $\beta_H = 0.1$.

Nous avons établi un système d'équations parabolisées permettant de décrire l'évolution des perturbations modales et non modales dans les couches limites tridimensionnelles. Une nouvelle méthode de calcul du nombre d'onde longitudinal a de plus été développée, qui se base sur le suivi du maximum d'énergie des perturbations.
L'étude des perturbations optimales dans les couches limites de Falkner-Skan-Cooke révèle que la perturbation est initialement inclinée contre le cisaillement de l'écoulement de base, avant d'être redressée puis inclinée dans le sens opposé plus en aval. La formation des stries dans les couches limites tridimensionnelles se fait donc par une combinaison de l'effet "lift-up" et du mécanisme de Orr. La comparaison de la perturbation optimale et de l'instabilité transverse à l'aval de la position neutre montre que les phénomènes de croissance transitoire et d'amplification modale sont complémentaires. La croissance transitoire initie donc le mode propre correspondant et les stries évoluent vers des tourbillons crossflow. Le potentiel d'amplification initiale des instabilités transversales par la croissance transitoire est développé dans le dernier chapitre sur des géométries plus complexes.

Chapitre 6

# Applications à des géométries complexes

Ce chapitre a pour objectif d'appliquer les outils de calcul des perturbations optimales pour des couches limites tridimensionnelles développés précédemment à des géométries plus complexes. Dans un premier temps, l'amplification des perturbations sur le profil d'aile Onera DTP-B est étudiée. L'amplification des tourbillons transversaux est calculée en prenant en compte ou non la région initiale de croissance non modale. L'influence de la croissance transitoire sur l'amplitude initiale des modes est ainsi quantifiée pour différents modes identifiés sur ce profil. Dans un second temps, le potentiel de croissance transitoire pour des couches limites se développant le long de la ligne de partage d'un cylindre en flèche est évalué. Le problème de la contamination du bord d'attaque est étudié. Pour ce faire, on calcule la perturbation optimale le long de la ligne de partage pour différents angles de flèche (ou, de façon équivalente, différents nombres de Reynolds). Enfin, l'amplification des perturbations au voisinage de la ligne de partage est également déterminée.

## 6.1 Amplification modale et non modale sur un profil d'aile

On considère le profil d'aile Onera DTP-B, qui est caractérisé par une longueur de corde $L = 0.7\,\mathrm{m}$, une épaisseur maximale de 94 mm et une envergure de 2.5 m. L'angle de flèche varie entre 35° et 45° et l'angle d'attaque est compris entre 5° et 7°. La vitesse à l'infini amont est fixée à $70\,\mathrm{m\,s^{-1}}$ pour un nombre de Reynolds basé sur la corde $Re_c = 3.2 \times 10^6$. La figure 6.1 représente le coefficient de pression $K_p$ pour les différents angles d'attaque considérés et un angle de flèche $\Lambda = 40°$. Sur la majorité du profil, on observe un gradient de pression négatif favorable au développement des modes transversaux.

On compare les courbes de facteur $N$ calculées pour différents modes par la méthode PSE classique et la méthode PSE modifiée introduite au chapitre précédent. La figure 6.2 présente les courbes d'amplification pour différents modes. De façon similaire à ce qui a été détaillé dans le chapitre précédent, une phase de croissance transitoire peut être observée aux premières stations de calcul. La position neutre est cependant située très proche du bord d'attaque, ce qui signifie que la région où la croissance transitoire joue un rôle est très réduite. L'écoulement est de plus accéléré sur une grande partie du profil, ce qui est moins favorable à l'amplification non modale. Cependant, lorsque la croissance transitoire est prise en compte dans le calcul, on observe une amplitude initiale supérieure des modes transversaux avant l'amplification exponentielle.

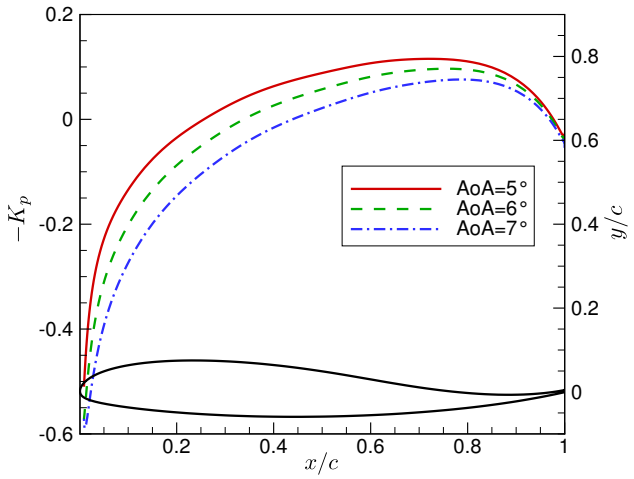


Figure 6.1 : Coefficients de pression et géométrie du profil DTP-B, pour un angle de flèche de 40° et les différents angles d'attaque considérés.

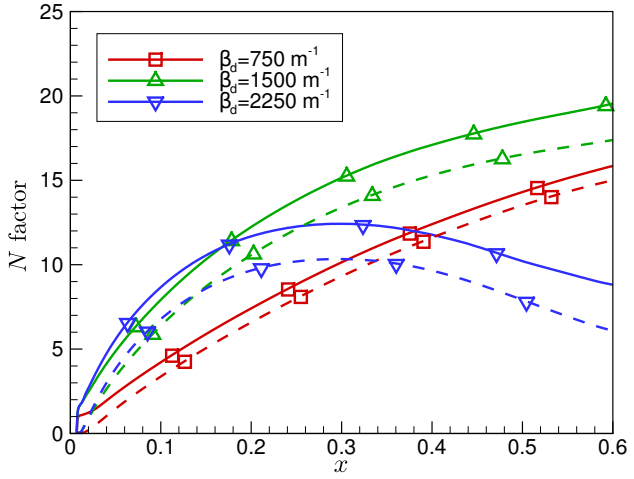


Figure 6.2 : Facteurs $N$ des modes principaux calculés par la méthode PSE classique (- - - ) et l'approche modifiée pour tenir compte de la croissance transitoire (——). L'angle de flèche est $\Lambda = 40°$ et l'angle d'attaque est fixé à 6°.

L'amplitude initiale des modes transversaux est plus importante quand le nombre d'onde transversal dimensionné $\beta_\mathrm{d}$ augmente. Cela signifie que les différents modes transversaux ne sont pas tous affectés de la même façon par l'étape de croissance transitoire initiale. L'amplification modale des perturbations est ensuite retrouvée, et l'écart $\Delta N$ dû à la croissance transitoire reste constant.

L'influence de l'angle d'attaque est ensuite évaluée. La figure 6.3 montre l'amplification du mode le moins stable, c'est-à-dire pour $\beta_\mathrm{d} = 1500\,\mathrm{m}^{-1}$, pour trois angles d'attaque différents. L'amplitude initiale du mode transversal diminue lorsque l'angle d'attaque augmente. Bien que l'amplification maximale soit atteinte pour l'angle d'attaque le plus grand, l'amplitude initiale due à la croissance transitoire est plus importante pour l'angle d'attaque le plus faible, qui correspond à un écoulement plus faiblement accéléré. La croissance transitoire joue donc un rôle plus important pour de faibles angles d'attaque.

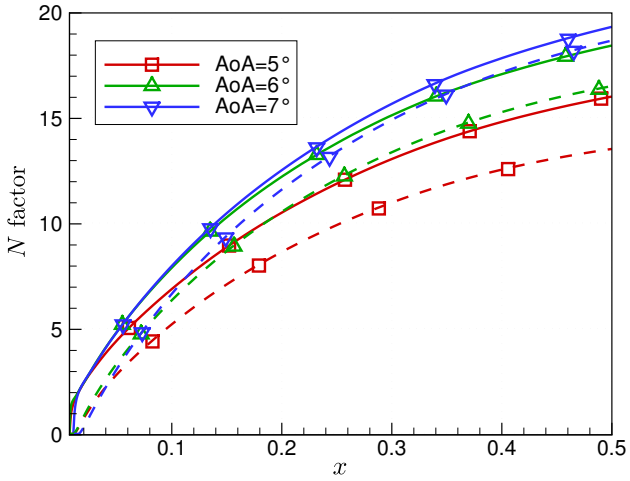


Figure 6.3 : Facteurs $N$ du mode le plus amplifié ($\beta_d = 1500\,m^{-1}$) sur le profil DTP-B pour différents angles d'attaque et $\Lambda = 40°$, calculés avec la méthode PSE classique (- - -) et modifiée pour tenir compte de la croissance transitoire (——).

La figure 6.4 présente les courbes de facteurs $N$ pour le mode le plus amplifié $\beta_d = 1500\,m^{-1}$ en fonction de trois angles de flèche, $\Lambda$=35°, 40° et 45°. L'amplification maximale est obtenue pour l'angle de flèche le plus grand, ce qui correspond physiquement à l'écoulement transverse le plus important. Pour les différents angles de flèche considérés ici, l'amplitude initiale du mode transversal est la même. Cela signifie que pour le mode propre étudié $\beta_d = 1500\,m^{-1}$, l'angle de flèche n'influe pas sur l'étape de croissance transitoire. Cela est dû au fait que la position neutre est située très proche du bord d'attaque et n'est elle-même que peu influencée par la valeur de l'angle de flèche.

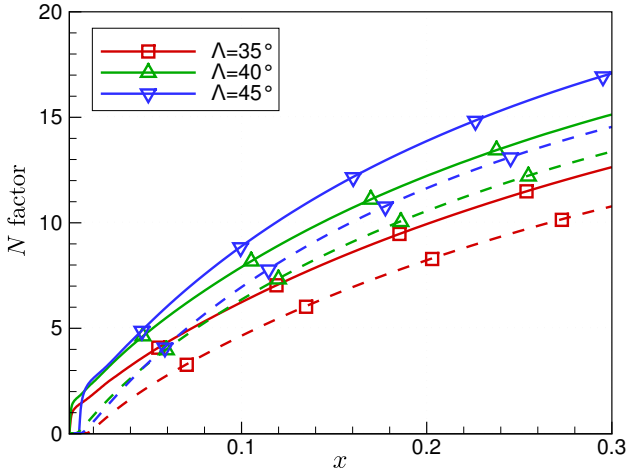


Figure 6.4 : Facteurs $N$ du mode le plus amplifié ($\beta_d = 1500\,m^{-1}$) sur le profil DTP-B pour différents angles de flèche et un angle d'attaque de 6°, calculés avec la méthode PSE classique (- - -) et modifiée pour tenir compte de la croissance transitoire (——)

.

Dans l'ensemble, même si la région de croissance transitoire est très réduite sur ce profil, la croissance transitoire fournit une amplitude initiale significative avant l'amplification exponentielle des modes transversaux. Cette amplitude est en particulier plus importante pour des angles d'attaque faibles.

## 6.2 Croissance transitoire sur la ligne de partage

On s'intéresse ici au problème de la ligne de partage, détaillée au paragraphe 1.2.4, dans le cas d'un écoulement sur un cylindre en flèche infini. L'écoulement extérieur peut être décomposé en une composante longitudinale $U_\infty = Q_\infty \cos(\Lambda)$ dans la direction $X$ et une composante transversale $W_\infty = Q_\infty \sin(\Lambda)$ dans la direction $Z$, pour un angle de flèche $\Lambda$. Les composantes de vitesse extérieure $U_e$ et $W_e$ sont définies par

$$U_e = kX \quad \text{et} \quad W_e = W_\infty = \text{constante}, \tag{6.1}$$

où $k$ est le gradient de vitesse extérieure dans la direction $X$. L'écoulement le long de la ligne de partage est caractérisé par le nombre de Reynolds $\overline{R}$,

$$\overline{R} = \frac{W_e \eta}{\nu_e} \quad \text{avec } \eta = (\nu_e/k)^{1/2}. \tag{6.2}$$

Les composantes de l'écoulement de base, constantes dans la direction $Z$, sont de la forme

$$U = \frac{x}{\overline{R}} \bar{u}(y)\,; \quad V = \frac{1}{\overline{R}} \bar{v}(y)\,; \quad W = \bar{w}(y). \tag{6.3}$$

Les vitesses $(\bar{u}, \bar{v}, \bar{w})$ sont solutions d'un système d'équations différentielles par rapport à $y = Y/\eta$ de type Falkner-Skan-Cooke. Les solutions de similitude pour l'écoulement de base sont présentées sur la figure 6.5, plus de détails étant disponibles dans la version anglaise du manuscrit (chapitre 6, paragraphe 6.2.1).

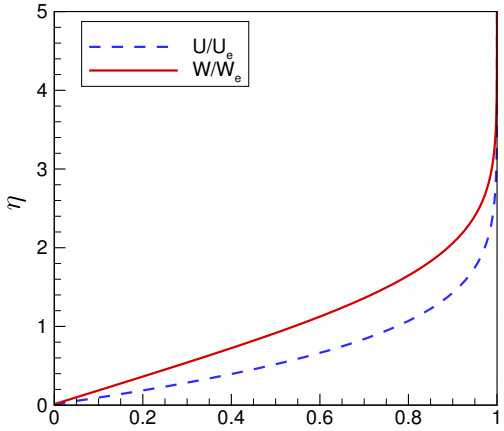


Figure 6.5 : Distributions de vitesses le long de la ligne de partage.

Pour être cohérent avec les variables d'adimensionnement employées jusqu'à maintenant dans cette thèse, les vitesses sont adimensionnées par $W_\infty = Q_\infty \sin\Lambda$, et le nombre de Reynolds est redéfini en conséquence,

$$Re_L = \frac{Q_\infty \sin(\Lambda) R}{\nu}, \tag{6.4}$$

où $R$ est le rayon du cylindre, choisi comme longueur de référence. La longueur de référence de la couche limite est alors $\delta = \sqrt{\nu R/(Q_\infty \sin\Lambda)}$. Le nombre de Reynolds défini par l'équation (6.4) est différent de $\overline{R}$ mais tient compte de l'angle de flèche et du gradient de vitesse extérieure $k = 2U_\infty/R$.

L'écoulement considéré est représenté sur la figure 6.6, la couche limite se développant dans la direction $z$ avec une vitesse transversale extérieure constante $W_e = W_\infty$. Le nombre d'onde

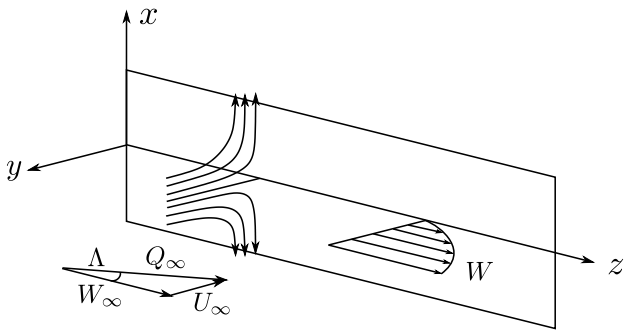


Figure 6.6 : Système de coordonnées $(x, y, z)$ pour l'écoulement le long de la ligne de partage, avec un angle de flèche $\Lambda$ et une vitesse infinie amont $Q_\infty$.

longitudinal est fixé et le nombre d'onde transversal est déterminé selon la procédure décrite au paragraphe 5.2.2.

Dans un premier temps, on cherche à déterminer le nombre d'onde longitudinal optimal $\alpha_{\text{opt}}$ qui conduit au maximum du gain en $z_{\text{out}} = 1$. Les différentes courbes de gain obtenues pour différents nombres de Reynolds $\overline{R}$ correspondant à des angles de flèches compris entre $\Lambda = 20°$ et $60°$ [1] sont représentées sur la figure 6.7. Le nombre d'onde longitudinal optimal augmente pour des valeurs plus importantes du nombre de Reynolds, avant d'atteindre une valeur constante $\alpha_{\text{opt}} = 0.6$ pour des nombres de Reynolds $\overline{R} > 250$.

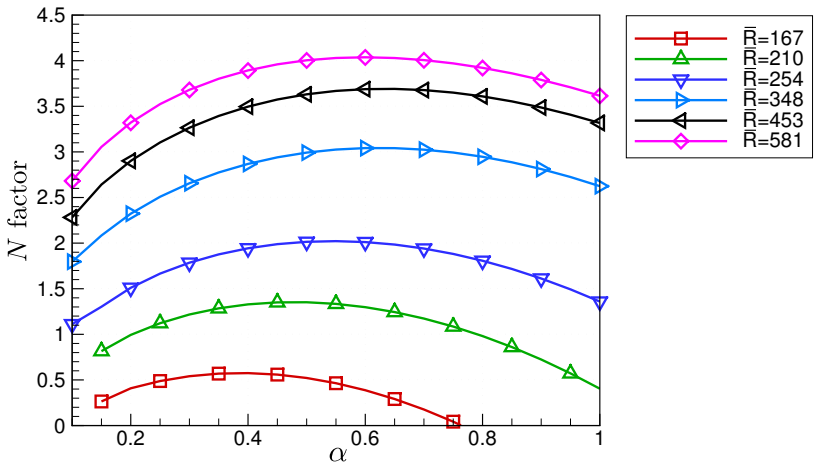


Figure 6.7 : Facteur $N$ en fonction du nombre d'onde longitudinal $\alpha$ le long de la ligne de partage ($x = 0$).

Une fois que le nombre d'onde longitudinal optimal a été spécifié, la perturbation optimale peut être déterminée le long de la ligne de partage pour différents nombres de Reynolds. L'objectif est d'étudier l'amplification non modale des perturbations en regard du critère utilisé pour la contamination du bord d'attaque (Pfenninger, 1965; Poll, 1978). Ce critère est basé sur une valeur critique du nombre de Reynolds $\overline{R} = 250$. La perturbation optimale est donc déterminée pour différents nombres de Reynolds $\overline{R}$ et les courbes correspondantes de gain sont reportées sur la figure 6.8. On observe que l'amplification non modale des perturbations est possible le long de la ligne de partage pour tous les nombres de Reynolds considérés. A titre de comparaison, pour une couche

1. Ces résultats sont retrouvés si l'on fixe l'angle de flèche et que l'on modifie le rayon du cylindre $R$ pour changer le nombre de Reynolds $\overline{R}$.

limite de Blasius avec $\beta_{\text{opt}} = 0.45$, le gain atteint la valeur maximale $G/Re_L = 2.1 \times 10^{-3}$. Les valeurs du gain augmentent par ailleurs pour des valeurs plus élevées de $\overline{R}$. Cependant, l'évolution d'une valeur inférieure à $\overline{R} = 250$ vers des valeurs plus élevées se fait de façon continue et sans changement drastique de comportement. Il est cependant important de remarquer que l'adimensionnement employé suppose que $U$ et $W$ sont du même ordre de grandeur, ce qui n'est a priori pas justifié sur la ligne de partage.

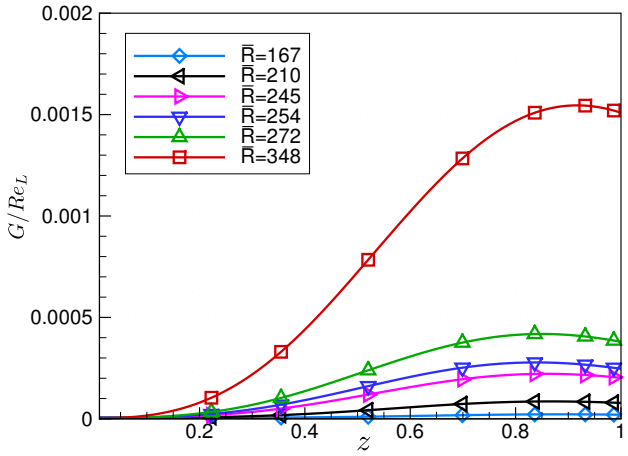


Figure 6.8 : Courbes de gain pour les perturbations optimales sur la ligne de partage ($x = 0$) pour différents nombres de Reynolds $\overline{R}$.

On considère l'amplification des perturbations dans le voisinage proche de la ligne de partage. A la différence des calculs précédents, le profil de vitesse longitudinal est plus important alors que l'on s'éloigne de la ligne de partage. La figure 6.9 présente les courbes de gains obtenues sur la ligne de partage ($x = 0$) et dans son voisinage ($x = 0.05$ et $0.1$) pour un angle de flèche $\Lambda = 40°$ correspondant à un nombre de Reynolds $\overline{R} = 348$. L'amplification des perturbations est plus importante le long de la ligne de partage en $x = 0$ qu'au voisinage. Pour $x = 0.05$, le comportement est similaire à ce qui se passe sur la ligne de partage. Un changement intervient pour $x = 0.1$ où l'amplification des perturbations se fait plus en amont.

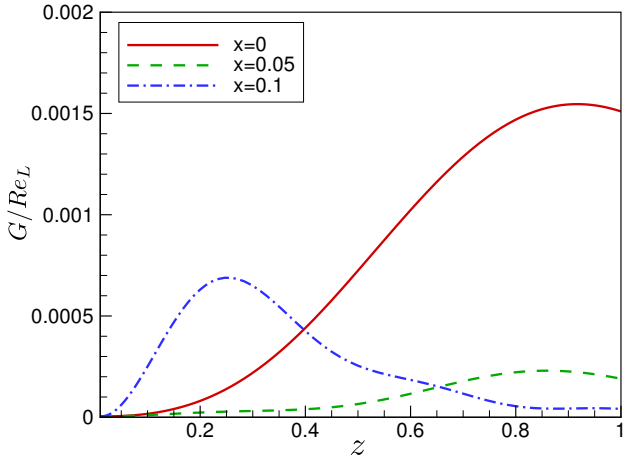


Figure 6.9 : Courbes de gain sur la ligne de partage ($x = 0$) et dans son voisinage ($x = 0.05$ et $0.1$) pour $\overline{R} = 348$ ($\Lambda = 40°$).

Si l'on s'éloigne encore de la ligne de partage, on observe que les perturbations sont amplifiées de façon exponentielle, comme illustré sur la figure 6.10. Cette observation peut être reliée à l'amplification des tourbillons transversaux qui s'opère à une certaine distance du bord d'attaque.

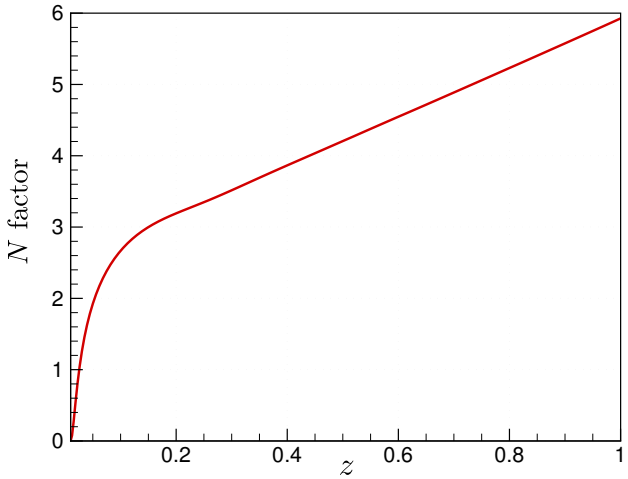


Figure 6.10 : Facteur $N$ en $x = 0.2$ et $\overline{R} = 348$ ($\Lambda = 40°$).

L'influence de la croissance transitoire sur l'amplification des modes transversaux se développant sur un profil d'aile a été étudiée. Bien que la région en amont de la position neutre soit réduite, la croissance transitoire fournit une amplitude initiale avant l'amplification modale. Les différents modes considérés ne sont cependant pas également affectés pas cette étape. Des angles d'attaque plus faibles, qui conduisent à un écoulement plus faiblement accéléré, favorisent l'amplification non-modale. La valeur de l'angle de flèche n'influence pas quant à elle les résultats du fait de la localisation très en amont de la position neutre.
L'écoulement le long de la ligne de partage d'un cylindre en flèche a ensuite été considéré. Le nombre d'onde longitudinal optimal qui conduit à la valeur maximale du gain a été déterminé, puis utilisé pour calculer la perturbation optimale le long de la ligne de partage. L'amplification des perturbations dans le voisinage de la ligne de partage a également été étudiée.

# Conclusions et perspectives

Cette thèse a été consacrée à l'étude de la croissance transitoire dans les couches limites bidimensionnelles et tridimensionnelles. L'influence de la croissance transitoire sur l'amplification modale des perturbations a été en particulier étudiée dans les différents cas.
La théorie des perturbations optimales a été présentée dans le cas général d'une couche limite de Blasius. La perturbation optimale correspond à la perturbation initiale qui engendre les perturbations les plus énergétiques dans la couche limite. La mesure de cette énergie passe par le choix d'une norme adaptée et le problème d'optimisation est résolu par itérations du système d'équations de couche limite parabolisées et de son système adjoint.
Dans un premier temps, l'étude a porté sur les couches limites bidimensionnelles se développant sur des parois courbes. Les équations régissant l'évolution des perturbations ont été établies afin de prendre en compte les effets de courbure. Cela a permis de déterminer la perturbation optimale dans le cas d'une paroi à courbure concave et de définir la courbe neutre pour le problème de Görtler. Cette courbe neutre dépend normalement fortement de la forme de la perturbation initiale. Cette dépendance aux conditions initiales est levée par l'emploi de l'approche optimale. Pour cela, un nouveau critère pour la convergence du gain a été développé afin de sélectionner la perturbation optimale la plus rapidement amplifiée. La courbe neutre associée représente alors l'enveloppe du domaine instable. L'extension de cette étude à des couches limites compressibles a montré l'effet stabilisant d'un nombre de Mach croissant sur l'amplification des tourbillons de Görtler. Afin d'évaluer les interactions entre modes non-normaux, l'hypothèse d'écoulement parallèle a été ensuite adoptée. Cette hypothèse permet de calculer le spectre et le pseudospectre des opérateurs et de quantifier le degré de non-normalité des valeurs propres. Les résultats montrent que le degré de non-normalité augmente pour des valeurs plus élevées du nombre de Görtler. La croissance transitoire est donc plus marquée lorsque la courbure est plus importante. L'amplification des perturbations a ensuite été calculée par une approche multi-modale basée sur les modes non-normaux. Cela a permis d'identifier une phase initiale de croissance transitoire aux premières stations de calcul avant une phase d'amplification exponentielle. L'évolution des modes de Klebanoff vers les tourbillons de Görtler a ensuite été étudiée en considérant une plaque plane suivie d'une paroi concave puis convexe. Le nombre d'onde transversal optimal qui conduit au gain maximal est le même pour les deux perturbations. Cela signifie que les modes de Klebanoff et les tourbillons de Görtler représentent la même instabilité, l'amplification exponentielle des tourbillons de Görtler provenant de l'action des forces centrifuges. La croissance transitoire conduit donc à une amplitude initiale significative avant de basculer vers l'amplification exponentielle des tourbillons de Görtler. Ces valeurs initiales de facteur $N$ fournies par la croissance transitoire doivent être prises en compte dans l'objectif d'une prévision précise de la position de la transition. Le lien avec les critères de transition employés dans des cas d'oscillations de surface est ensuite étudié en considérant une paroi avec de multiples

oscillations. Le comportement classique des tourbillons de Görtler est correctement décrit par l'approche optimale et la phase de croissance transitoire est en plus capturée. Cette phase initiale de croissance transitoire est réduite quand le nombre de Mach augmente, mais la température de paroi n'influence aucunement les résultats. Dans tous les cas, la croissance transitoire joue un rôle dans le développement initial des tourbillons de Görtler et fournit une amplitude initiale qu'il est important de prendre en compte avant l'amplification exponentielle.

La seconde partie de cette thèse a été consacrée aux couches limites tridimensionnelles. Un système d'équations parabolique a été établit pour décrire à la fois l'évolution des perturbations modales et non-modales. Cela est rendu possible par l'emploi de deux systèmes d'adimensionnement, qui permettent de prendre en compte les termes responsables de la croissance transitoire au sein du système d'équations PSE. Pour un nombre d'onde longitudinal donné, ces équations peuvent être résolues par une technique de marche vers l'aval. Ce nombre d'onde longitudinal doit être déterminé de façon à capturer les oscillations des perturbations. En pratique, la détermination se fait par une méthode locale afin de suivre le maximum d'énergie des perturbations.
Ce système d'équations PSE modifié a alors permis de déterminer la perturbation optimale pour des couches limites accélérées et décélérées de Falkner-Skan-Cooke. Comme précédemment, le problème d'optimisation est résolu par itérations du système direct/adjoint. Une étude paramétrique a été effectuée pour étudier l'influence de la station initiale et finale ainsi que de l'angle de flèche sur l'amplification non-modale des perturbations. Même si l'approche employée dans cette thèse pour spécifier le nombre d'onde longitudinale est différente, cette étude a permis de confirmer les résultats présentés par Tempelmann *et al.* (2010). La perturbation optimale prend initialement la forme de tourbillons longitudinaux contra-rotatifs inclinés contre le cisaillement de l'écoulement transverse. Plus en aval, ces tourbillons se développent en stries qui sont redressées, puis inclinées dans le sens du cisaillement de l'écoulement transverse et quasiment alignées avec la ligne de courant extérieure. Le mécanisme physique responsable de la formation de ces stries consiste en une combinaison de l'effet lift-up et du mécanisme de Orr. La relation entre les stries et le développement des modes transversaux a ensuite été particulièrement étudiée. Les comparaisons entre les fonctions d'amplitude de la perturbation optimale et des modes transversaux correspondant en aval de la position neutre montrent que les deux instabilités partagent la même structure. Les stries non-modales évoluent donc vers l'aval vers les modes transversaux. Le calcul de l'amplification des perturbations par la méthode des PSE classiques et modifiées montre que la région initiale de croissance transitoire fournit une amplitude initiale significative au mode transversal.
Enfin, le potentiel d'amplification non modale des perturbations est étudié pour des géométries plus complexes. Dans un premier temps, on considère le profil d'aile Onera DTP-B pour étudier l'influence de la croissance transitoire sur l'amplification des modes transversaux. Des comparaisons entre les facteurs $N$ calculés par la méthode PSE classique et modifiée montrent que la croissance transitoire fournit là encore une amplitude initiale aux modes transversaux, bien que la région en amont de la position neutre soit restreinte sur ce profil. Les différents modes étudiés ne sont pas influencé de la même façon par l'étape de croissance transitoire. Cette étape fournit par ailleurs une amplitude initiale plus importante pour de faibles angles d'attaque. Dans un deuxième temps, la couche limite qui se développe le long de la ligne de partage d'un cylindre d'envergure infini en flèche est étudiée. Ce type de configuration est représentatif de l'écoulement le long du bord d'attaque d'une aile en flèche. Dans des applications aérodynamiques, l'écoulement peut être très perturbé, par exemple par des défauts de surface, ce qui peut entrainer une amplification importante des perturbations. On a cherché à déterminer la perturbation optimale à l'aide des outils mis en place au cours de cette thèse. Le nombre d'onde longitudinal qui permet d'obtenir le gain maximal

a d'abord été déterminé pour différents nombres de Reynolds, puis a été utilisé pour calculer la perturbation optimale sur la ligne de partage. L'amplification transitoire des perturbations est possible pour tous les nombres de Reynolds considérés, et les valeurs de gain obtenues sont plus importantes pour de plus grandes valeurs de ce paramètre. Cependant, l'étude présentée ici n'a pas permis de retrouver le critère de contamination du bord d'attaque basé sur une valeur critique du nombre de Reynolds $\overline{R} = 250$. La perturbation optimale se développant au voisinage de la ligne de partage a également été considérée. L'amplification des perturbations est plus importante le long de la ligne de partage que dans son voisinage. Cependant, suffisamment loin de la ligne de partage, les perturbations sont amplifiées de façon exponentielle. Cette observation est à mettre en regard avec l'amplification des modes transversaux qui débute à une certaine distance du bord d'attaque. Cependant, les hypothèses faites sur l'adimensionnement employé ne permettent pas de tirer de conclusions définitives de cette étude.

Comme on l'a vu, la méthode des PSE modifiée peut être améliorée à court terme en considérant un nombre d'onde longitudinal complexe qui prenne en compte la croissance des perturbations. Une condition de normalisation similaire à la méthode PSE classique pourrait être employée sur la base d'itérations préalables avec un nombre d'onde réel. Cela conduirait à une formulation non modale des PSE permettant de capturer la croissance modale et non modale des perturbations. Une formulation adjointe de ces équations PSE modifiées pourrait également être établie afin de déterminer le nombre d'onde longitudinal lors de la résolution des équations vers l'amont.
L'un des objectifs de cette thèse était d'étendre les outils disponibles pour des couches limites tridimensionnelles. Une suite logique à ce travail est de continuer à améliorer ces outils en considérant les effets de courbure et de compressibilité afin d'élargir le domaine d'applications.
A plus long terme, la relation entre les perturbations optimales et les perturbations observées dans des cas d'applications réels a besoin d'être évaluée. Ces dernières perturbations peuvent en effet présenter un caractère suboptimal qui réduit alors l'influence de la croissance transitoire sur l'amplification modale. Des comparaisons avec des résultats expérimentaux ou issus de simulations numériques directes sont donc nécessaires afin de déterminer la validité des scénarios présentés dans cette thèse.
En considérant des environnements plus perturbés, des critères de transition Bypass peuvent être développés pour des couches limites tridimensionnelles. En se basant sur le calcul et la propagation des perturbations optimales, la dynamique des stries peut être modélisée de façon similaire à ce qui existe pour des couches limites bidimensionnelles (Vermeersch, 2009). Des critères de transition Bypass pour des couches limites tridimensionnelles se développant sur des ailes en flèche pourraient ainsi être établis.
Enfin, on peut envisager traiter le problème de la réceptivité des couches limites en déterminant les solutions adjointes du système PSE modifiées. Les critères de transition actuels utilisés dans un cadre industriel ignorent cette étape. Pourtant, au sein des couches limites tridimensionnelles, le phénomène de réceptivité à la turbulence extérieure ou aux rugosités de surface est crucial pour le développement des modes transversaux. Là encore, des comparaisons fines entre les résultats théoriques et des relevés expérimentaux ou des résultats issus de simulations numériques directes seront nécessaires pour valider les résultats obtenus.